FOSSIL ENERGY

A NOVEL APPROACH TO MODELING
UNSTABLE EOR DISPLACEMENTS

Final Report

By
Ekwere J. Peters

April 1994

The University of Texas at Austin
Austin, Texas

**Bartlesville Project Office
U. S. DEPARTMENT OF ENERGY
Bartlesville, Oklahoma**

DISCLAIMER

A NOVEL APPROACH TO MODELING UNSTABLE EOR DISPLACEMENTS

Final Report

By
Ekwere J. Peters

April 1994

Prepared for
U.S. Department of Energy
Assistant Secretary for Fossil Energy

Jerry D. Ham, Project Manager
Metairie Site Office
900 Commerce Road, East
New Orleans, LA 70123

Prepared by
The University of Texas at Austin
Center for Petroleum and Geosystems Engineering
Austin, TX 78712

EXECUTIVE SUMMARY

This is the final report of a three-year research project that was aimed at developing a methodology for predicting the performance of unstable displacements in heterogeneous reservoirs. A performance prediction approach that combines numerical modeling with laboratory imaging experiments has been developed.

Most enhanced oil recovery (EOR) schemes involve the displacement of one fluid by another fluid in a heterogeneous porous medium. In the majority of cases, the injected fluid is less viscous and less dense than the displaced fluid. This situation has long been recognized as having the potential to create hydrodynamic instabilities in the forms of viscous fingering and gravity override or underride. These instabilities not only impair the displacement efficiency, they also make the displacement performance more difficult to model mathematically, and, therefore, more difficult to predict. A further complication in the displacement is caused by the presence of heterogeneities within the porous medium whose magnitude and distribution are usually unknown. The interaction of heterogeneities with hydrodynamic instabilities can significantly reduce the displacement efficiency and result in low oil recovery.

Since hydrodynamic instabilities and reservoir heterogeneities can severely limit the success of many enhanced oil recovery projects, there is considerable interest within the EOR community to (1) develop increased understanding of the physics of unstable displacements, (2) develop accurate mathematical models to predict the performance of unstable displacements, (3) develop geostatistical models to better characterize reservoir heterogeneities, and (4) develop mobility control measures to prevent viscous instability. This research addressed the first three of these EOR issues through flow visualization experiments combined with geostatistical and high-resolution numerical modeling.

Flow visualization experiments were conducted using X-ray computed tomography (CT) imaging and a video imaging workstation to (a) gain new insights into the dynamics of unstable displacements, (b) acquire detailed quantitative experimental image data for calibrating numerical models of unstable displacements and (c) image and characterize heterogeneities in laboratory cores geostatistically. High-resolution numerical models modified for use on vector-architecture supercomputers were used to replicate the image data. Geostatistical models of reservoir heterogeneity were incorporated in the numerical models in order to study the interaction of hydrodynamic instability and heterogeneity in reservoir displacements. Finally, a systematic methodology for matching the experimental

data with the numerical models and scaling the laboratory results to other systems were developed. The outcome of the research is a new method for predicting the performance of unstable EOR displacements in the field based on small-scale displacements in the laboratory.

The research was organized into four major tasks: (1) Flow visualization experiments with CT scanner; (2) Flow visualization experiments with video imaging workstation; (3) Model development and testing; and (4) History-matching of the flow visualization experiments. All project tasks and subtasks were successfully completed except for a subtask on CT measurements in consolidated cores which could not be performed because of CT equipment malfunction in the final year of the research. Two PhD dissertations and one MS thesis were completed in the course of the research. Other deliverables include ten technical publications in scientific journals and conference proceedings and fourteen oral presentations at technical meetings and research seminars.

The results of our visualization experiments and mathematical modeling show that, in the absence of significant gravity segregation, unstable miscible and immiscible displacements and their mathematical models are self-similar processes, a fact that greatly enhances the ability to model and scale them from one system to another. When presented in terms of an appropriate similarity transformation variable, the spatial and temporal saturation data collapsed into one dimensionless response curve that was easier to model than the original data. The results further show how laboratory displacements in relatively homogeneous media can be scaled to predict expected field performance in heterogeneous reservoirs. A technique for characterizing the small-scale heterogeneities in laboratory cores geostatistically through imaging was also developed.

The methodology developed in this research is general and can applied to forecast the performance of most industrial processes that involve fluid flow and transport in porous media. Therefore, this research should be of interest to those involved in forecasting the performance of enhanced oil recovery processes and the spreading of contaminants in heterogeneous acquifers.

ABSTRACT

This is the final report of a three-year research project that was aimed at developing a methodology for predicting the performance of unstable displacements in heterogeneous reservoirs. A performance prediction approach that combines numerical modeling with laboratory imaging experiments has been developed.

Most enhanced oil recovery (EOR) schemes involve the displacement of a more dense and more viscous oil by a less dense and less viscous fluid in a heterogeneous porous medium. The interaction of heterogeneity with the several competing forces, namely, viscous, capillary, gravitational, and dispersive forces, can conspire to make the displacements unstable and difficult to model and to predict. The objective of this research was to develop a systematic methodology for modeling unstable fluid displacements in heterogeneous media.

Flow visualization experiments were conducted using X-ray computed tomography (CT) imaging and a video imaging workstation to (a) gain new insights into the dynamics of unstable displacements, (b) acquire detailed quantitative experimental image data for calibrating numerical models of unstable displacements and (c) image and characterize heterogeneities in laboratory cores geostatistically. High-resolution numerical models modified for use on vector-architecture supercomputers were used to replicate the image data. Geostatistical models of reservoir heterogeneity were incorporated in the numerical models in order to study the interaction of hydrodynamic instability and heterogeneity in reservoir displacements. Finally, a systematic methodology for matching the experimental data with the numerical models and scaling the laboratory results to other systems were developed. The outcome of the research is a new method for predicting the performance of unstable EOR displacements in the field based on small-scale displacements in the laboratory.

The results of our visualization experiments and mathematical modeling show that, in the absence of significant gravity segregation, unstable miscible and immiscible displacements and their mathematical models are self-similar processes, a fact that greatly enhances the ability to model and scale them from one system to another. When presented in terms of an appropriate similarity transformation variable, the spatial and temporal saturation data collapsed into one dimensionless response curve that was easier to model than the original data. The results further show how laboratory displacements in relatively homogeneous media can be scaled to predict expected field performance in heterogeneous

reservoirs. A technique for characterizing the small-scale heterogeneities in laboratory cores geostatistically through imaging was also developed.

The methodology developed in this research is general and can applied to forecast the performance of most industrial processes that involve fluid flow and transport in porous media. Therefore, this research should be of interest to those involved in forecasting the performance of enhanced oil recovery processes and the spreading of contaminants in heterogeneous acquifers.

Table of Contents

List of Tables

List of Figures

xi

1 INTRODUCTION

1.1 Problem Statement

Most enhanced oil recovery (EOR) schemes involve the displacement of one fluid by another fluid in a heterogeneous porous medium. In the majority of cases, the injected fluid is less viscous and less dense than the displaced fluid. This situation has long been recognized as having the potential to create hydrodynamic instabilities in the forms of viscous fingering and gravity override or underride (Engelberts and Klinkenberg, 1951). These instabilities not only impair the displacement efficiency, they also make the displacement performance more difficult to model mathematically, and, therefore, more difficult to predict. A further complication in the displacement is caused by the presence of heterogeneities within the porous medium whose magnitude and distribution are usually unknown. The interaction of heterogeneities with hydrodynamic instabilities can significantly reduce the displacement efficiency resulting in low oil recovery.

Since hydrodynamic instabilities and reservoir heterogeneities can severely limit the success of many enhanced oil recovery projects, there is considerable interest within the EOR community to (1) develop increased understanding of the physics of unstable displacements, (2) develop accurate mathematical models to predict the performance of unstable displacements, (3) develop geostatistical models to better characterize reservoir heterogeneities, and (4) develop mobility control measures to prevent viscous instability. This research addressed the first three of these EOR issues through innovative flow visualization experiments combined with geostatistical and high-resolution numerical modeling.

1.2 Objectives

The goal of this research was to develop a methodology for predicting the performance of unstable EOR displacements in heterogeneous reservoirs. A novel performance prediction approach that combined numerical modeling with laboratory imaging experiments was to be developed. The specific objectives were:

1. To conduct flow visualization experiments in the laboratory using X-ray computed tomography (CT) scanner and a video imaging workstation to (a) gain new insights into the dynamics of unstable displacements, (b) acquire detailed quantitative experimental image data for calibrating numerical models of unstable displacements and (c) image and characterize heterogeneities in laboratory cores.

2. To adapt existing numerical models where possible or develop new models if necessary to simulate the laboratory displacement experiments uniquely.

3. To develop a systematic procedure for history-matching the laboratory displacement experiments with numerical models in order to accurately simulate the performance of unstable displacements.

4. To scale the laboratory experiments to predict their expected performance in heterogeneous porous media.

The outcome of the research will be a method for predicting the performance of unstable EOR displacements in heterogeneous reservoirs based on small-scale laboratory tests conducted on homogeneous or mildly heterogeneous cores.

1.3 Literature Review

1.3.1 Modeling Unstable Displacements

The first approach to modeling unstable displacements was concerned with performing stability analysis on the differential equations of the displacements to predict the conditions for the onset of instability (Chuoke *et al.*, 1959; Perrine, 1963; Rachford, 1964; Schowalter, 1965; Heller, 1966; Hagoort, 1974; Peters, 1979; Peters and Flock, 1981; Peters *et al.*, 1984; Jerauld *et al.*, 1984; Gardner and Ypma, 1984; King and Scher, 1985; Mui and Miller, 1985; Lee *et al.*, 1984; Tan and Homsy, 1986). Although stability analysis has been successful in identifying the conditions for the onset of instability, it is not capable of providing information about the subsequent performance of the unstable displacement. Moreover, it is usually not possible to explicitly incorporate the effect of heterogeneity into a stability analysis except to assume that heterogeneity creates the perturbations in the displacements that ultimately grow into viscous fingers.

A second approach to modeling unstable displacements is the use of empirical models to match the recovery performance of unstable displacements (Koval, 1963; Dougherty, 1963; Todd and Longstaff, 1972; Fayers, 1984; Fayers and Newly, 1987, Odeh, 1989). This approach makes no attempt to model the details of the instabilities. Instead, adjustable parameters are used in a simple 1-D model to match the recovery performance of the displacement. The problem with this approach is that it is not based on the actual physics of flow and as a result, the adjustable parameters, in most cases, often have no physical significance.

A third approach to modeling unstable displacements is that in which an attempt is made to simulate the dynamics of the unstable displacement in detail using fine mesh or high-resolution numerical models. Pioneered by Peaceman and Rachford in 1962, this approach has enjoyed a resurgence of interest in recent years (Peaceman and Rachford, 1962; Giordano, *et al.*, 1985; Peters and Kasap, 1986; Christie and Bond, 1987; Christie, 1989; Tan and Homsy, 1988; Hatziavramidis, 1987; Araktingi and Orr, 1988; Kelkar and

Gupta, 1991; Khataniar and Peters, 1990; Christie *et al.*, 1989). This interest is due to the availability of faster and larger computers in recent years than were available to Peaceman and Rachford in 1962. Using supercomputers, it is now possible to develop and run high-resolution numerical models at a reasonable cost. The advantage of this modeling approach is that it is based on sound physical principles of multiphase flow in porous media as currently understood. Furthermore, heterogeneities can easily be incorporated into the model using geostatistical techniques. Thus, high-resolution numerical modeling of laboratory data is likely to become the preferred tool of the future for the design, performance prediction and scale-up of enhanced oil recovery processes. This is the modeling approach that we sought to further develop in this research.

1.3.2 Quantitative Experiments of Unstable Displacements

A major handicap in the development of high-resolution numerical models of unstable displacements is the lack of quantitative experimental data with which to calibrate the models. Clearly, our computational ability has outrun our ability to perform detailed quantitative experiments of unstable displacements. As a result, the efforts to calibrate high-resolution models of unstable displacements in recent studies have concentrated on matching the recovery curves from the first-contact miscible experiments of Blackwell et al. (Blackwell et al., 1959; Christie and Bond, 1987; Christie, 1989; Araktingi and Orr, 1988; Kelkar and Gupta, 1991). Unfortunately, matching the recovery curves of an unstable displacement is no guarantee that the displacement was correctly simulated. This is because there are usually enough adjustable parameters in the model to match most recovery curves without necessarily matching the fluid flow field in the porous medium. The best way to calibrate a high-resolution model of an unstable displacement would be to attempt to replicate the actual fluid flow field by matching the fluid saturation distribution in the porous medium in time and space. If the fluid saturation in the porous medium is matched, the recovery curve is automatically matched as well. The converse is not true.

Matching the fluid saturation in the porous medium in an experiment is more challenging than matching the effluent recovery curve. However, it leads to a more unique simulation of the displacement than matching the recovery curve. The development of a strategy for matching fluid saturations in the porous medium in laboratory experiments is one of the innovations of this research.

The lack of suitable experimental data in the literature for calibration of high-resolution numerical models of unstable displacements is not accidental. Until recently, the acquisition of such detailed quantitative data was difficult. However, the availability of high-resolution computer imaging technologies to enhanced oil recovery researchers in recent years has made the acquisition of such experimental data now feasible (Peters *et al.*,

1987). X-ray computed tomography (CT) and nuclear magnetic resonance (NMR) imaging, long used in medical diagnoses, can now be used to obtain detailed quantitative data on laboratory corefloods. CT and NMR systems can be used to image the fluid saturations in a coreflood in time and space (Wang *et al.*, 1984; Wellington and Vinegar, 1985; Hove *et al.*, 1987; Vinegar and Wellington, 1987; Withjack, 1987; Withjack and Akervoll, 1988; Hardham, 1988; Peters and Hardham, 1989; Peters and Hardham, 1990). They also can be used to visualize the spatial distribution of heterogeneities within the porous medium (Vinegar, 1986; Bergosh *et al.*, 1985; Honarpour *et al.*, 1986; Hunt *et al.*, 1988). These are precisely the type of experimental data needed to calibrate high-resolution numerical models of unstable displacements in heterogeneous media. The use of CT and other imaging technologies to obtain detailed quantitative experimental data for calibrating numerical models is another innovation of this research. The combination of laboratory imaging experiments with high-resolution numerical modeling is a novel approach to modeling unstable EOR displacements.

1.4 Experimental Equipment and Procedure

Our flow visualization experiments were performed with an X-ray CT scanner and a high-resolution video imaging workstation. Image processing of the experimental data and numerical simulations were performed on a number of mainframe computers at The University of Texas.

1.4.1 X-Ray CT Scanner

Our CT scanner is a Radapt CS scanner manufactured by Bio-Imaging Research Incorporated specifically for core analysis. It is a second-generation scanner in which the object to be imaged rotates while the X-ray source and detectors translate back and forth. This design results in a very compact scanner with the entire assembly housed in a 234 cm x 140 cm x 126 cm radiation cabinet. The scanner has an extremely accurate positioning mechanism that allows the same volume elements (voxels) to be scanned repeatedly during the course of an experiment. Multiple scans of the same voxels are required to calculate fluid saturation and porosity from CT scanning. The scanner has a resolution of 1 mm^3 which is more than adequate to resolve fingering and gravity override or underride which were of interest in this research.

The procedure for CT imaging of a coreflood has been presented by Peters and Hardham (1990). A typical imaging sequence was as follows. After preparation, the porous medium, which could be a sandpack or a consolidated core, was mounted horizontally in the scanner for an initial scan of the dry medium. The coreholder for the sandpacks was made of PVC pipe whereas the coreholder for consolidated cores was made

of aluminum pipe. PVC and aluminum were used as coreholders because of their low X-ray attenuation coefficients. For a 2 ft core, we typically imaged fifty slices of 5 mm thickness, spaced 5 mm apart. After scanning the dry porous medium, it was saturated with the displaced fluid and scanned again at exactly the same voxels as before. Next, a predetermined pore volume of the displacing fluid was injected at a constant rate. The coreflood was then shut in and scanned. It was necessary to shut in the flood because the process of scanning fifty slices of the core lasted about two hours. The processes of flooding, shutting in and scanning were repeated several times in order to follow the progress of the coreflood.

For a porous medium saturated with two fluids, the following equations apply in each voxel (Peters and Hardham, 1990):

$$S_w + S_o = 1 \tag{1.1}$$

$$\psi_m(1 - \phi) + \psi_a\phi = \psi_1 \tag{1.2}$$

$$\psi_m(1 - \phi) + \psi_o\phi = \psi_2 \tag{1.3}$$

$$\psi_m(1 - \phi) + (\psi_w S_w + \psi_o S_o)\phi = \psi_3 \tag{1.4}$$

Solving Eqs. 1.1 to 1.4 gives the porosity, fluid saturation and X-ray absorption coefficient of the rock matrix (mineralogy) in each voxel as

$$\phi = \frac{\psi_2 - \psi_1}{\psi_o - \psi_a} \tag{1.5}$$

$$S_w = \frac{\psi_3 - \psi_2}{\phi(\psi_w - \psi_o)} \tag{1.6}$$

and

$$\psi_m = \frac{\psi_2 - \psi_o\phi}{1 - \phi} \tag{1.7}$$

The large data files generated by CT scanning were processed off-line on a VAX 6520 mainframe computer and presented as saturation and porosity images along three orthogonal viewing planes as shown in Fig. 1.1. The saturation data also were presented as 1-D saturation profiles along the core as is customary in numerical simulation.

1.4.2 Video Imaging Workstation

This workstation was designed and built by our research group to visualize 2-D fluid flow fields. Described in detail by Peters and Reid (1990), the workstation consists of the following hardware: an IBM PC-AT with 1 MB RAM and a 20 MB hard disk, an image digitizer board that plugs into one of the expansion slots of the PC, a Tecmar graphics board having an image resolution of 640 x 400 x 16, IBM color graphics and monochrome monitors, a Hewlett Packard Paint Jet graphics printer and a video camera. It was used to visualize fluid flow in a thin bed of glass beads sandwiched between two clear acrylic plates.

Image acquisition with the workstation is simple and automated. After the saturated porous medium model is illuminated, the video camera is turned on and focused. Next, the image acquisition software is invoked. After the displacement experiment is initiated, the image acquisition program is run on automatic image capture mode. Images are then captured automatically, displayed and saved on disk at the frequency specified by the user.

The major advantage of the video imaging workstation over the CT scanner is the speed and frequency of image acquisition. Image acquisition on the CT scanner is slow. Therefore, a coreflood can only be scanned at a few time steps. To scan a 2 feet coreflood at seven times with our CT scanner required at least fifteen hours. In contrast, the video workstation can acquire images of the entire flow field at rates as rapid as every half second. The major disadvantage of the video workstation is that its images are qualitative compared to the quantitative images of the CT scanner. Nevertheless, the video workstation provided qualitative 2-D data which were useful for areal sweep efficiency studies and which complemented the quantitative 3-D data from the CT scanner.

1.4.3 Computational Facilities

Preliminary numerical simulations were done on an in-house VAX 6520 mainframe computer. Final numerical simulations and history-matching of the experimental CT data with high-resolution numerical models were done on a Cray Y-MP supercomputer at The University of Texas Center for High Performance Computing.

1.5 Organization of the Research

The research was organized into the following tasks and subtasks:

Task 1:   Flow visualization experiments with CT scanner

          Subtask 1.1: Visualization of displacements in homogeneous porous media

          Subtask 1.2: Characterization of reservoir cores

Subtask 1.3: Visualation of displacements in heterogeneous media

Task 2:   Flow visualization experiments with video imaging workstation

Task 3:   Model development and testing

Task 4:   History-match of the flow visualization experiments

      Subtask 4.1: Image processing of flow visualization data

      Subtask 4.2: Geostatistical generation of displacement parameters

      Subtask 4.3: Development of history-matching methodology

This report is organized by task and presents the accomplishments of the various research tasks and subtasks.

2 TASK 1: FLOW VISUALIZATION EXPERIMENTS WITH CT SCANNER

The objective of this task was to conduct 3-D flow visualization experiments using the CT scanner to (1) obtain quantitative experimental data with which to calibrate high-resolution numerical models, (2) gain additional insights into the physics of unstable displacements and (3) characterize the small-scale heterogeneities in laboratory cores.

2.1 Subtask 1.1: Visualization of Displacements in Homogeneous Media

2.1.1 Objective

The objective of this subtask was to obtain experimental data on unstable miscible and immiscible displacements in ideal porous media free of heterogeneities. Consequently, these tests were performed in unconsolidated, relatively homogeneous sandpacks.

2.1.2 Experiments

Several unstable miscible and immiscible displacements in homogeneous sandpacks were performed in the course of this research. In this section, we present the results from three representative experiments (Experiments 2.1, 2.2 and 2.3) to show the major characteristics of unstable displacements. Experiment 2.1 was an unstable first-contact miscible displacement in which water was used to displace a mixture of glycerin and water at a viscosity ratio of 54. Experiments 2.2 and 2.3 were waterfloods (immiscible displacements) in which water was used to displace a mineral oil (Dow Corning Oil) at a viscosity ratio of 91. In Experiment 2.2, the sandpack was rendered oil-wet by saturating it first with the silicon-based mineral oil whereas in Experiment 2.3, the sandpack was rendered water-wet by first saturating it with water and then displacing the water with the mineral oil to establish an initial oil saturation before the waterflood. The objective was to visualize and measure the effect of wettability on the waterflood performance. Because of the high viscosity ratios (mobility ratios) and displacement rates used in the experiments, all three displacements were unstable and resulted in viscous fingering. All the experiments were conducted at room temperature.

Table 2.1 shows the sandpack and fluid properties as well as other useful information about the experiments. The experiments were characterized by their stability and gravity numbers defined as:

$$N_s = \frac{(M-1)U\mu_w d^2}{C^* \sigma k} \qquad (2.1)$$

$$N_s = 2\frac{(M-1)Ud^2}{(M+1)D^*} \qquad (2.2)$$

$$N_g = \frac{kg(\rho_w - \rho_o)d}{U\mu_o L} \qquad (2.3)$$

Equations 2.1 and 2.2 give the stability numbers for immiscible and miscible displacements, respectively. The stability numbers are dimensionless numbers which indicate the degree of instability. If the stability number of a coreflood exceeds 13.56, the displacement will be unstable and subject to viscous fingering (Peters and Flock, 1981; Peters et al., 1984). The higher the stability number, the more severe will be the viscous fingering. The gravity number as defined in Eq. 2.3 is the ratio of gravity to viscous forces for the displacement (Stalkup, 1983). High values of this number for an unstable displacement indicate that gravity segregation will occur in addition to viscous fingering, whereas low values indicate that viscous fingering will predominate and gravity segregation will be suppressed. A negative gravity number indicates gravity override whereas a positive gravity number indicates gravity underride.

2.1.3 Results and Discussion

The results of these experiments are comprehensive quantitative experimental data that will be used to calibrate the numerical models of the unstable displacements (Task 4). Three types of data were obtained: oil recovery curves, 1-D saturation profiles and 3-D saturation images.

Figure 2.1 presents the oil recovery curves from the three experiments which show that the miscible displacement was the most efficient and the immiscible waterflood in the oil-wet medium was the least efficient of the three displacements. The efficiency of the waterflood in the water-wet medium was intermediate between that of the miscible displacement and the waterflood in the oil-wet medium.

It can be observed on Fig. 2.1 that below 1.0 pore volume injected, the miscible displacement was less efficient than the waterflood in the water-wet medium. Based on the recovery curves alone, this anomalous behavior of the miscible displacement is difficult to explain. However, as will be seen in the saturation images later, this anomalous behavior was caused by gravity override in the miscible displacement. This points to the necessity

of having the image data in addition to the recovery data to fully describe and understand a displacement behavior.

Oil recovery curves such as shown in Fig. 2.1 have traditionally been used to calibrate numerical models in the literature. Although the recovery curves give the overall performance of the displacements, they are not unique descriptors of the displacements. Therefore, matching the recovery curve alone in an unstable displacement is not a guarantee that the unstable displacement mechanisms were correctly simulated inside the porous medium. A more unique approach to modeling the displacement would be to match the fluid saturation distribution within the porous medium. This is the modeling strategy adopted in this study. The 1-D saturation profiles acquired by CT imaging of the corefloods provide an opportunity for the implementation of this modeling approach.

Figures 2.2, 2.3 and 2.4 show the 1-D displacing fluid saturation profiles for the three experiments. For the miscible displacement involving incompressible fluids (Experiment 2.1), the saturation profiles are the same as the solvent concentration profiles. For the immiscible displacement in the water-wet medium (Experiment 2.3), the saturation profiles have been normalized to account for the initial water saturation. The saturation profiles show very interesting features. All contain fluctuations. This is a mark of the instability of the displacements. However, the fluctuations in the profiles of the miscible displacement appear to propagate down the core with time (Fig. 2.2) whereas those in the immiscible displacements remain stationary with time (Figs. 2.3 and 2.4). This feature points to a fundamental difference in the processes of miscible and immiscible displacements which have implications for the mathematical modeling of these displacements.

A comparison of the saturation profiles in the oil-wet and water-wet media (Figs. 2.3 and 2.4) shows that (1) the saturation levels are higher in the water-wet medium than in the oil-wet medium at the same timestep, (2) the flood front has advanced further in the oil-wet medium than in the water-wet medium at each timestep before breakthrough, and (3) the frontal saturation is higher in the water-wet medium than in the oil-wet medium. These observations point to the higher displacement efficiency in the water-wet medium than in the oil-wet medium. Clearly, significantly different displacement parameters will be required to model the unstable waterfloods in the oil-wet and water-wet media.

The saturation profiles are 1-D averages of the 3-D saturation data from the coreflood. They provide more unique information about the displacement process than the recovery curve because they give an indication of the fluid distribution in the porous medium at each stage of the coreflood. Because fluid saturation often is one of the

dependent variables calculated in a numerical model of a displacement, the saturation profiles provide one means of comparing a numerical model with an experiment. In our numerical modeling, we focused on matching the saturation profiles rather than the recovery curves of the unstable displacements. Like the recovery curve, the 1-D saturation profiles cannot reveal all aspects of the displacement. For example, they cannot reveal the presence of gravity override or underride. Thus, the saturation profiles, though superior to the recovery curves in their information content, give still an incomplete picture of the displacement.

The 3-D image data provide the most complete and unique information about the displacement. Because they are high-resolution physical models of the displacement, they show all aspects of the displacement such as viscous fingering, gravity override or underride and channeling due to permeability heterogeneities. If the 3-D image data could be replicated by a numerical model of the displacement, then the saturation profiles and the recovery curve would automatically be replicated as well. However, the image data are much too dense to be modeled numerically on a voxel by voxel basis. For example, each of the experiments reported here contained 685,000 voxels, corresponding to 685,000 saturation image data points at each time step. This is too fine a grid system for a numerical model of the displacement even on a supercomputer. Therefore, the image data were used in a somewhat qualitative manner in the numerical modeling. Our numerical modeling focused on replicating the saturation profiles in the porous medium, with the saturation image data being used qualitatively to ensure that the major displacement mechanisms such as viscous fingering and gravity override or underride revealed by the image data were accounted for in the numerical model.

Figures 2.5 and 2.6 show the saturation (solvent concentration) images from the miscible displacement (Experiment 2.1) at 0.25 and 2.0 pore volumes injected. The images show the injected fluid saturation distribution in a vertical slice through the center of the sandpack. The images clearly show evidence of hydrodynamic instabilities in the forms of viscous fingering and gravity override. This gravity override problem caused the anomalous displacement behavior seen in Fig. 2.1. A comparison of Figs. 2.5 and 2.6 shows that regions of the sandpack initially bypassed by viscous fingering have been swept by subsequently injected fluid. This ability to mobilize and displace the oil from regions that were initially bypassed accounts for the propagating nature of the fluctuations in the saturation profiles in miscible displacements. It also accounts for the high displacement efficiency of the miscible displacement. In fact, given enough time, an unstable first-contact miscible displacement will recover 100% of the original oil in place.

Figures 2.7 and 2.8 show the saturation images from the waterflood in the oil-wet sandpack (Experiment 2.2) at 0.10 and 2.0 pore volumes injected. The figures show a fragmented, chaotic and rather complex displacement pattern with low water saturations propagating rapidly through the sandpack. The fragmented nature of the displacement is caused by the oil wetness of the sandpack. There is evidence of gravity underride in Fig. 2.8 which shows a higher water saturation in the lower half of the sandpack than in the upper half. It should be noted that the oil initially bypassed in the upper part of the sandpack at 0.10 pore volume injected remained largely trapped at 2.0 pore volumes injected. Subsequently injected fluid flowed through the channels created by the initial viscous fingers, avoiding the trapped oil. This displacement behavior is more evident in Fig. 2.9 which shows the image at 3.0 pore volumes injected. A comparison of the images in Figs. 2.8 and 2.9 shows them to be very similar, indicating that very little additional oil displacement occurred from 2.0 to 3.0 pore volumes injected. This tendency of the injected fluid to flow through only the previously swept channels accounts for the stationary nature of the fluctuations observed in the saturation profiles of the immiscible displacements. It also partly accounts for the relative inefficiency of the immiscible displacements compared to the miscible displacement in which initially bypassed oil was easily mobilized and subsequently displaced. Of course, there is residual oil saturation in the swept areas of the immiscible displacements due to capillary trapping which further adds to their inefficiency.

Figures 2.10 and 2.11 show the saturation images from the waterflood in the water-wet sandpack (Experiment 2.3) at 0.10 and 0.25 pore volumes injected. They show the displacement pattern to be fairly uniform and free from severe viscous fingering in contrast to the pattern observed in the oil-wet medium. Apparently, the water wetness of the sandpack has resulted in the uniform spreading of the injected water, significantly enhancing the displacement efficiency of the waterflood in the water-wet sandpack. It has also eliminated the gravity underride problem observed in the waterflood of the oil-wet medium. The uniform spreading of the injected fluid coupled with the absence of gravity override or underride caused this waterflood to be initially more efficient than the miscible displacement. Because of the uniform nature of the displacement in the water-wet medium, one can anticipate that it would be easier to model the displacement in the water-wet medium with a partial differential equation that admits of smooth solutions than in the oil-wet medium in which the saturation distribution was highly fragmented. Although masked by the initial uniform spreading of the injected fluid, the tendency of bypassed oil to remain trapped exists even in the water-wet medium. This is evident from the stationary nature of the fluctuations in the saturation profiles observed in Fig. 2.4.

In addition to providing quantitative experimental data for calibrating numerical models, the CT experiments have resulted in additional qualitative insights into the displacement mechanisms in unstable miscible and immiscible displacements. They show that there is a fundamental difference in the displacement mechanisms in unstable miscible and immiscible displacements. The fluctuations in the saturation profiles in the miscible displacement appeared to propagate along the core with time whereas those in the immiscible displacements were stationary. This suggests that miscible displacements have wave-like characteristics whereas immiscible displacements do not. These observations have implications for the mathematical modeling of the displacements. Miscible displacements are best modeled by a diffusion-convection equation which has wave-like or hyperbolic characteristics whereas immisicible displacements are best modeled by a diffusion-type equation which is parabolic in nature and lacks the wave-like characteristic.

The saturation images show why unstable miscible displacements are much more efficient than their immiscible counterparts. The images show that in a miscible displacement, the oil previously bypassed due to viscous fingering can be subsequently mobilized and displaced by continued fluid injection. By contrast, in an immiscible displacement, the oil bypassed by viscous fingering remains largely trapped and is not easily mobilized by subsequent fluid injection. Finally, the images show why a waterflood in an oil-wet medium is significantly less efficient than in a water-wet medium. They show the displacement pattern in the oil-wet medium to be fragmented, chaotic and subject to severe viscous fingering. In contrast, they show the displacement pattern in the water-wet medium to be uniform, with very little fingering. Clearly, these qualitative observations indicate that different numerical model parameters will be needed to simulate the waterfloods in the oil-wet and water-wet media.

2.1.4 Conclusions

The following conclusions may be drawn from the results of this subtask:

1.   Unstable miscible displacements are more efficient that their immiscible counterparts because of a fundamental difference in their displacement mechanisms.

2.   Wettability has a significant impact on the displacement efficiency of an immiscible displacement.

3.   Everything else being equal, a waterflood in a water-wet porous medium will be more efficient than in an oil-wet medium.

4.   CT imaging is a powerful tool for obtaining quantitative experimental data as well as for gaining qualitative insights into displacement phenomena.

2.2 Subtask 1.2: Characterization of Reservoir Rocks

2.2.1 Objectives

One of the major difficulties in modeling fluid displacements in permeable media is the inability to properly characterize the heterogeneous permeable media. The objectives of this subtask were to develop techniques to (1) characterize the small-scale heterogeneities in laboratory cores and (2) determine the dispersion coefficients of laboratory cores.

2.2.2 Characterization of Core Heterogeneities

We have developed a procedure to characterize the porosity and permeability heterogeneities in cores. The porosity heterogeneities are imaged directly, but the permeability heterogeneities are obtained indirectly by imaging a stable miscible displacement in the core. Our permeability estimation procedure is based on tracking the displacement front along streamtubes in the core and estimating the streamtube permeabilities from a theoretical model of the displacement.

The procedure consists of the following steps: (1) image the dry core sample for mineralogy; (2) image the porosity distribution; (3) image the progress of a stable, first-contact miscible displacement in the core at several times; (4) calculate the permeability distribution from the saturation image data and (5) perform geostatistical analyses of the X-ray absorption coefficient and porosity distributions to characterize their variability quantitatively. The 3-D data generated by the procedure can be presented as images, histograms and variograms. The outcome of the procedure is a geostatistical characterization of the heterogeneities in the core.

Theory

Bahralolom and Heller (1989) presented an indirect method for estimating the transverse permeability distribution in a core by CT imaging under certain restrictive conditions. They approximated the core as a bundle of streamtubes along which one-dimensional flows occurred in the direction of bulk flow. By observing the arrival times of an injected solvent at the end of the core for each streamtube in a CT experiment, they were able to calculate the average permeability of each streamtube using Eq. 2.4 which was presented in their paper.

$$k_i = \frac{\mu \phi_i L^2}{t \, \Delta P}.$$
(2.4)

Withjack et al. (1990) used the same procedure to characterize laboratory cores, further demonstrating the usefulness of this method. Because this indirect method of permeability

measurement assumes one-dimensional linear flow along the streamtubes, the method should work well in cores with severe layering in the direction of bulk flow in which the flow is essentially one-dimensional along the layers.

In this research, we derived a generalized theoretical basis for the above method of permeability estimation and extended it to estimate the permeability variation along the direction of bulk flow as well.

Consider a stable displacement in a heterogeneous porous medium that is divided into volume elements or voxels as shown in Fig. 2.12. Contiguous voxels in series along the length of the porous medium constitute a streamtube. These streamtubes are joined in parallel to form the porous medium. Assuming incompressible fluids, mass conservation law applied to the entire porous medium gives

$$q_T = \Sigma q_i. \qquad (2.5)$$

For steady-state, single-phase flow, Darcy's law applied to the entire medium gives

$$q_T = \frac{k_T A_T \Delta P}{\mu L}. \qquad (2.6)$$

The total permeability of the porous medium in the direction of bulk flow can be determined from Eq. 2.6 as

$$k_T = \frac{q_T \mu L}{A_T \Delta P}. \qquad (2.7)$$

Darcy's law for steady-state flow along each streamtube gives

$$q_i = \frac{k_i A_i \Delta P}{\mu L}. \qquad (2.8)$$

The average permeability of each streamtube can be determined from Eq. 2.8 as

$$k_i = \frac{q_i \mu L}{A_i \Delta P}. \qquad (2.9)$$

Combining Eqs. 2.5 to 2.9 gives the total permeability of the porous medium in terms of the streamtube permeabilities as

$$k_T = \frac{\Sigma k_i A_i}{A_T}. \qquad (2.10)$$

Equation 2.10 results from combining the average streamtube permeabilities in parallel. This equation can be used to check that the estimated average streamtube permeabilities are consistent with the average permeability of the whole core.

Let us now focus on the displacement along a streamtube. Because the displacement is stable, it can be approximated as a piston-like displacement. Of course, in reality, there is a transition zone that is usually small in comparison to the length of the porous medium (Fig. 2.13). In the most general case, we consider an immiscible displacement in which only the injected fluid flows behind the front and the displaced fluid flows ahead of the front. We allow for initial and residual saturations. The miscible displacement case will be derived as a special case of the immiscible displacement. If we treat the displacement as a moving boundary problem, then the instantaneous rate of advance of the displacement front is given by (Collins, 1962)

$$\frac{dx_{fi}}{dt} = \frac{q_i}{A_i \phi_i (1 - S_{wi} - S_{or})}.$$

(2.11)

Darcy's law and mass conservation law give

$$\frac{\partial^2 P_w}{\partial x^2} = 0, \quad 0 < x < x_{fi}$$

(2.12)

and

$$\frac{\partial^2 P_o}{\partial x^2} = 0, \quad x_{fi} < x < L$$

(2.13)

At the interface,

$$P_w = P_o$$

(2.14)

$$\frac{k_{wr}}{\mu_w} \frac{\partial P_w}{\partial x} = \frac{k_{or}}{\mu_o} \frac{\partial P_o}{\partial x}.$$

(2.15)

At the inlet,

$$P_w = P_1. \quad x = 0.$$

(2.16)

At the outlet,

$$P_o = P_2, \quad x = L.$$

(2.17)

Integrating Eqs. 2.12 and 2.13 gives

$$P_w = ax + b$$

(2.18)

and

$$P_o = a'x + b', \quad (2.19)$$

where a, b, a' and b' are integration constants defined below. Applying the boundary conditions at the ends and at the interface leads to

$$b = P_1 \quad (2.20)$$

$$a = -\frac{\Delta P}{M^o L + (1 - M^o)x_{fi}} \quad (2.21)$$

$$a' = -\frac{M^o \Delta P}{M^o L + (1 - M^o)x_{fi}} \quad (2.22)$$

$$b' = -\frac{(1 - M^o)x_{fi}\Delta P}{M^o L + (1 - M^o)x_{fi}} + P_1 \quad (2.23)$$

where

$$\Delta P = P_1 - P_2 \quad (2.24)$$

and M is the end point mobility ratio given by

$$M^o = \frac{k_{wr}\,\mu_o}{k_{or}\,\mu_w}. \quad (2.25)$$

Applying Darcy's law to the invaded zone yields

$$\frac{q_i}{A_i} = -\frac{k_{wr}}{\mu_w}\frac{\partial P_w}{\partial x} = -\frac{k_{wr}a}{\mu_w}. \quad (2.26)$$

Substituting Eq. 2.26 into 2.11 gives

$$\frac{dx_{fi}}{dt} = \frac{k_{wr}\Delta P}{\mu_w\phi_i(1 - S_{wi} - S_{or})}\frac{1}{[M^o L + (1 - M^o)x_{fi}]} \quad (2.27)$$

for the rate of advance of the front. Integrating Eq. 2.27 with $x_{fi} = 0$ at $t = 0$ gives the time required for the front to advance from $x = 0$ to $x = x_{fi}$ as

$$t = \frac{\mu_w\phi_i(1 - S_{wi} - S_{or})[M^o \, x_{fi} + 0.5(1 - M^o)\,x_{fi}^2]}{k_{wr}\,\Delta P}. \quad (2.28)$$

Equation 2.28 can be rearranged to calculate the average permeability of the streamtube behind the front,

$$k_{wr} = \frac{\mu_w\phi_i(1-S_{wi}-S_{or})[M^o Lx_{fi} + 0.5(1-M^o)x_{fi}^2]}{t\Delta P}. \tag{2.29}$$

Equation 2.29 is a generalized equation for calculating the permeability behind the front for each streamtube. By monitoring the front positions for each streamtube at successive times during a displacement, the average streamtube permeabilities behind the front can be calculated for different positions of the front. Since the successive averages represent permeabilities in series, the permeabilities for various segments of the streamtube can be computed. Thus, imaging the progress of a stable coreflood at multiple times provides the necessary data to estimate the permeability variation along the core. This approach is an extension of the permeability determination method of Bahralolom and Heller (1989). The front positions in each streamtube can easily be monitored in a CT experiment.

In the special case of a miscible displacement at a mobility ratio of unity, $M^o = 1$, $S_{wi} = S_{or} = 0$, $\mu_w = \mu_o = \mu$, and $k_{wr} = k_{or} = k_i$, and Eq. 2.29 simplifies to

$$k_i = \frac{\mu\phi_i Lx_{fi}}{t\Delta P}. \tag{2.30}$$

This is the same as Eq. 2.4 for $x_{fi} = L$. Thus, we have demonstrated that Eq. 2.4 presented by Bahralolom and Heller is a special case of a more general equation for the estimation of permeabilities from CT imaging based on the assumption of one-dimensional flow.

Experiments

Two CT imaging experiments are presented to demonstrate our core characterization procedure. In the first experiment (Experiment 2.4), we characterized a laboratory sandpack. The sandpack was prepared by pouring 60 to 120 mesh sand, a little at a time, into a cylindrical plastic coreholder and tamping the side of the coreholder with a rubber mallet to compact the sand. This process was repeated until the packing was completed. In the second experiment (Experiment 2.5), we characterized a Berea sandstone. Both experiments were stable first-contact miscible displacements (tracer tests) in which brine with an X-ray contrast agent was used to displace pure brine. Each displacement was imaged at several times before solvent breakthrough. Table 2.2 provides additional information about the experiments.

Results and Discussion

Figures 2.14 and 2.15 show the CT images of a typical transaxial slice and a longitudinal vertical slice through the center of the dry sandpack. The CT number, which is related to the X-ray attenuation coefficient of the sandpack, is expressed here in arbitrary units. The images clearly show that the sandpack is not uniform. Our packing method has introduced an unintended ring structure into the sandpack.

Figures 2.16 and 2.17 show the porosity images for the same transaxial and longitudinal slices. Radial porosity heterogeneities are clearly apparent throughout the length of the sandpack but there is variability along the sandpack as well. Islands of relatively low porosity occur at certain sections of the sandpack, reflecting closely the packing history of the sandpack. The medium was packed by pouring the sand into the coreholder a little at a time and tamping the coreholder with a rubber mallet to compact the sand. This process of pouring and compacting the sand was repeated a number of times to complete the sandpack. The different porosity segments visible in Fig. 2.17 show this packing history. These low porosity features may be expected to affect fluid flow through the sandpack.

Figure 2.18 shows saturation (solvent concentration) images at three of the nine times used to calculate the streamtube permeabilities behind the front. Several interesting features may be noted. First, the displacement is very efficient as may be expected for a stable, first-contact miscible displacement. Second, the growth in the transition zone as the displacement progresses is clearly evident. This is due to hydrodynamic dispersion. Finally, we note the tendency for the flood front to advance further near the edge than in the middle of the sandpack. This is due to the higher porosity (and consequently, higher permeability) of the sandpack near the wall of the coreholder that was evident in the porosity images.

Equation 2.30 was used in conjunction with the saturation image data to estimate the average streamtube permeabilities at successive stages of the displacement. Average permeabilities were computed at nine times. Figure 2.19 shows the computed permeability image for a vertical slice through the center of the sandpack. As may be expected for a sandpack, the overall permeability variation is small. The brick-shaped permeability distribution is caused by the fact that the permeability estimates were calculated at a few large time steps. The permeability estimates can be further refined by imaging the displacement at smaller time steps than was done in this experiment. It is of interest to note that the resultant absolute permeability obtained by our characterization procedure was within 5% of the absolute permeability of the sandpack obtained by application of Darcy's law for single phase flow.

To quantify the heterogeneities in the sandpack, we resort to normal and geostatistics. Figure 2.20 shows the porosity histogram for the 685,000 voxels in the sandpack. It shows an essentially normal distribution with an average porosity of 29.7% and a standard deviation of 2.5%. As may be expected for a "uniform" sandpack, the variability of the porosity is small as indicated by the low standard deviation. The average porosity of 29.7% obtained by CT compared favorably with the 31.3% obtained by material balance.

To examine the spatial structure of the heterogeneities in the sandpack, we computed semivariograms (or variograms) of the CT numbers of the dry sandpack and the porosity in three orthogonal directions of the sandpack. The variogram is a geostatistical tool for assessing the spatial continuity of a regionalized variable in a particular direction (Clark, 1979; Kerbs, 1986; Hohn, 1988; Isaaks and Srivastava, 1989). It is computed with the following equation:

$$\gamma(h) = \frac{\Sigma[z(x) - z(x+h)]^2}{2N_h}, \tag{2.31}$$

where $z(x)$ is the value of the regionalized variable at location x, $z(x+h)$ is the value of the same variable at a distance h from x and N_h is the number of data pairs.

Figure 2.21 shows the the variograms of the CT numbers of the dry sandpack along two perpendicular transaxial directions. The variograms were computed over the entire length of the sandpack. The two variagrams are nearly identical which is consistent with the near radial symmetry in the CT images of Figs. 2.14 and 2.15. Figure 2.22 shows the variogram in longitudinal direction of the sandpack. We note the sinusoidal feature in the variogram known as a trend surface. This is caused by the unintentional structure built into the sandpack by our packing method. Thus, the variagram is clearly able to detect and show this heterogeneity in the sandpack.

Figures 2.23 and 2.24 show the corresponding porosity variograms for the sandpack. These variograms are similar in appearance to those of the CT numbers of the dry sandpack indicating that the X-ray absorption data of the dry sample and the porosity data provide similar structural information about the dominant heterogeneities in the sandpack. Although there were insufficient data to perform a meaningful calculation of permeability variograms, we speculate that the permeability variograms will be qualitatively similar to the porosity and X-ray absorption variograms.

Figures 2.25 and 2.26 show the CT images of a typical transaxial slice and a longitudinal vertical slice through the center of the Berea sandstone. Clearly, the images

show a highly layered sandstone structure. Figures 2.27 and 2.28 show the porosity images for the same transaxial and longitudinal slices. The porosity images show the same layered structure seen in the CT images of the dry core. From these images, we conclude that the dominant heterogeneity in this sandstone is layering.

Figure 2.29 shows saturation (solvent concentration) images at three of the nine times used to calculate the streamtube permeabilities behind the front. Again, spreading of the injected solvent caused by hydrodynamic dispersion is apparent. At 0.5 pore volume injected, the flood front has advanced further in the lower half of the core than in the upper half. This is due to the higher permeability in the lower half of the core than in the upper half.

Figure 2.30 shows the computed permeability image for a vertical slice through the center of the Berea sandstone core. In this case, the resultant absolute permeability obtained by our characterization procedure was within 1% of the absolute permeability of the Berea core.

Figure 2.31 shows the porosity histogram for the Berea sandstone core. It shows an essentially normal distribution with an average porosity of 17.3% and a low standard deviation of 2.0%. After all, Berea sandstones often are considered to be uniform. The average porosity of 17.3% obtained by CT compared favorably with the 19.1% obtained by material balance. The dominant heterogeneity of layering is invisible in a histogram.

Figure 2.32 shows the the variograms of the CT numbers of the dry Berea sandstone along two perpendicular transaxial directions. The Y-direction is normal to the bedding planes whereas the Z-direction is parallel to the bedding planes. The fact that the Y-direction variogram is higher than the Z-direction variogram means that the core is more heterogeneous in the Y-direction than in the Z-direction. More significantly, the Y-direction variogram shows a trend surface caused by the layering in this direction. Thus, the variogram is able to reveal the layered nature of the core. The Z-direction variogram shows no trend surface because this direction is parallel to the bedding planes. Figure 2.33 shows the variogram in the X-direction which also is parallel to the bedding planes in the direction of bulk flow. It shows the classical shape of a correlated field with a correlation length of about 40 cm.

Figures 2.34 and 2.35 show the corresponding porosity variograms for the Berea sandstone. Like the CT variograms, Fig. 2.34 shows that the porosity is more heterogeneous normal to the bedding planes than parallel to the bedding planes. However, the heterogeneity in the calculated porosity is not as layered as the CT numbers. Therefore, there is no trend surface in the porosity variogram in the Y-direction. Figure 2.35 shows

that in the direction of bulk flow (X-direction), the porosity distribution has a correlation length of about 5 cm compared to 40 cm for the CT numbers.

2.2.3 Determination of Dispersion Coefficients of Cores

One of the fundamental issues in modeling miscible displacements is the quantitative description of the mixing or dispersion that occurs in miscible displacements and the attendant problem of measuring the dispersion coefficient for the porous medium. In this section, we present an improved method for determining the longitudinal dispersion coefficient of a porous medium from CT imaging of a tracer test in the medium. The method is demonstrated by determining the dispersion coefficients for the sandpack and Berea sandstone of Experiments 2.4 and 2.5. Our method allows the effects of dispersion and heterogeneity to be distinguished.

Theory

In order to focus attention on the dispersion phenomenon, we consider a tracer test consisting of a stable, first-contact miscible displacement of two incompressible fluids having equal viscosities and densities in a homogeneous porous medium. For such a displacement, viscous and gravity instabilities are absent and only dispersion will manifest itself. The mathematical model for this displacement in one dimension consists of the continuity equation, Darcy's law and the convection-dispersion equation:

$$\frac{\partial u}{\partial x} = 0 \tag{2.32}$$

$$u = -\frac{k}{\mu} \frac{\partial P}{\partial x} \tag{2.33}$$

$$\frac{\partial C}{\partial t} + \frac{u}{\phi R_f} \frac{\partial C}{\partial x} - \frac{K_L}{R_f} \frac{\partial^2 C}{\partial x^2} = 0 \tag{2.34}$$

In the above equations, u is the superficial velocity (Darcy velocity) and R_f is a retardation factor that accounts for the adsorption of the tracer by the porous medium. If there is no adsorption of the tracer by the porous medium, the retardation factor is unity whereas if there is adsorption, the retardation factor is greater than unity. It can be seen from Eq. 2.34 that the effect of the retardation factor is to reduce u and the K_L for the displacement. Thus, the speed of the solvent concentration is retarded and the effective dispersion coefficient is reduced by adsorption.

For a constant rate injection, Eqs. 2.32 and 2.33 lead to the following solution for the superficial velocity

$$u = \frac{k}{\mu} \frac{\Delta P}{L} = U \qquad (2.35)$$

where ΔP is the pressure drop across the porous medium, L is the length of the porous medium and U is the constant solvent injection flux. Therefore, the interstitial velocity is given by

$$\frac{u}{\phi} = \frac{k}{\mu} \frac{\Delta P}{\phi L} = \frac{U}{\phi} \qquad (2.36)$$

Equation 2.36 can then be substituted into Eq. 2.34 to describe the longitudinal dispersion of the solvent in the porous medium. To solve Eq. 2.34 for the case of continuous injection of the solvent, we apply the following initial and boundary conditions:

$$C(x,0) = 0 \quad x > 0 \qquad (2.37)$$

$$C(0,t) = C_i \quad t \geq 0 \qquad (2.38)$$

$$C(\infty,t) = 0 \quad t \geq 0 \qquad (2.39)$$

The analytical solution to Eq. 2.34 for the initial and boundary conditions given by Eqs. 2.37 to 2.39 is (Ogata and Banks, 1961)

$$C(x,t) = \frac{C_i}{2}\left[\text{erfc}\left(\frac{x - \frac{Ut}{\phi R_f}}{2\sqrt{(K_L/R_f)t}} \right) + \exp\left(\frac{vx}{K_L}\right) \text{erfc}\left(\frac{x + \frac{Ut}{\phi R_f}}{2\sqrt{(K_L/R_f)t}} \right) \right] \qquad (2.40)$$

where erfc is the complementary error function, an integral that is tabulated in mathematical handbooks. An approximate analytical solution normally used to determine the dispersion coefficient from breakthrough data is

$$C(x,t) = \frac{C_i}{2}\left[\text{erfc}\left(\frac{x - \frac{Ut}{\phi R_f}}{2\sqrt{(K_L/R_f)t}} \right) \right] \qquad (2.41)$$

In dimensionless form, Eq. 2.41 becomes

$$C(x_D,t_D) = \frac{C_i}{2}\left\{ \text{erfc}\left[\sqrt{N_{Pe}}\left(\frac{x_D - (t_D/R_f)}{2\sqrt{t_D/R_f}}\right) \right] \right\} \qquad (2.42)$$

where the dimensionless variables are defined as

$$x_D = \frac{x}{L} \qquad (2.43)$$

$$t_D = \frac{Ut}{\phi L} \qquad (2.44)$$

$$N_{Pe} = \frac{UL}{\phi K_L} \tag{2.45}$$

Equation 2.45 defines a Peclet number which is the ratio of convective to dispersive transports. Eq. 2.42 suggests a self-similarity transformation variable for first-contact miscible displacement of the form

$$\xi = \frac{x_D - \left(\frac{t_D}{R_f}\right)}{\sqrt{\frac{t_D}{R_f}}} \tag{2.46}$$

Defining a mixing zone length as the distance between C = 0.1 and C = 0.9, it can be shown from Eq. 2.42 that the growth of the mixing zone is given in dimensionless form by (Lake, 1989)

$$\Delta x_D = 3.625\sqrt{\frac{t_D}{N_{Pe}R_f}} \tag{2.47}$$

or in dimensional form by

$$\Delta x = 3.625\sqrt{\frac{K_L t}{R_f}} \tag{2.48}$$

Thus, by measuring the length of the mixing zone as a function of time, Eq. 2.48 can be used to calculate the longitudinal dispersion coefficient for the porous medium. The length of the mixing zone can easily be measured by imaging the experiment.

The longitudinal dispersion coefficient consists of a diffusion term and a mechanical dispersion term, as shown in the following equation (Perkins and Johnston, 1963):

$$K_L = \frac{D_o}{F\phi} + \alpha_L v \tag{2.49}$$

In Eq. 2.49, D_o is the molecular diffusion coefficient, F is the formation electrical resistivity factor, ϕ is the porosity, and α_L is the longitudinal dispersivity. At interstitial velocities greater than about 3.5×10^{-5} cm/s, the mechanical dispersion term ($\alpha_L v$) dominates the molecular diffusion term ($D_o/F\phi$) (Lake and Hirasaki, 1981). Therefore, at a sufficiently high displacement rate or Peclet number, Eq. 2.49 can be used to estimate the longitudinal dispersivity from the dispersion coefficient by neglecting the molecular diffusion term.

Assuming a linear sorption isotherm, the retardation factor is related to the distribution coefficient, K_d, as (Domenico and Schwartz, 1990):

$$R_f = \left[1 + \frac{(1-\phi)}{\phi} \rho_g K_d \right] \qquad (2.50)$$

where ρ_g is the grain density of the porous medium. The distribution coefficient can be calculated from Eq. 2.50.

Traditionally, the longitudinal dispersion coefficient is normally determined by measuring the solvent concentration at the outlet end of the porous medium (breakthrough curve) for a tracer test and then applying Eq. 2.41 at the outlet end to calculate K_L or more correctly K_L/R_f if retardation is not explicitly accounted for. This method gives an average K_L that includes the effects of hydrodynamic dispersion and heterogeneity. We present herein a method of determining K_L that allows the effects of dispersion and heterogeneity to be distinguished. This is accomplished by imaging the tracer test experiment in time and space. We use Eq. 2.41 to determine the average K_L (due to dispersion and heterogeneity) and R_f by history-matching the average concentration profiles and use Eq. 2.48 to determine the component of K_L that is due to dispersion only by measuring the length of the mixing zone with time from the image data.

We demonstrate our method by calculating the longitudinal dispersion coefficients for the sandpack and Berea sandstone of Experiments 2.4 and 2.5.

Results and Discussion

Figure 2.18 shows a distortion in the mixing zone caused by inhomogeneities in the sandpack of Experiment 2.4. Such distortions or heterogeneities serve to increase the average dispersion coefficient determined by the traditional breakthrough curve method.

Figure 2.36 compares the experimental and calculated solvent concentration profiles based on Eq. 2.41 using an average longitudinal dispersion coefficient of 100×10^{-5} cm^2/s and a retardation factor of unity. We see that the agreement between the experimental and calculated profiles is good at early times but poor at late times. At late times, the calculated profiles traveled farther than the experimental profiles. However, the experimental and calculated profiles are essentially parallel at late times, indicating that the average longitudinal dispersion coefficient is correct but the retardation factor of unity is incorrect. Figure 2.37 compares of the experimental and calculated profiles with the same average dispersion coefficient but with a retardation factor of 1.04. The agreement between the experiment and Eq. 2.41 is good at all times. It should be noted that the dispersion coefficient estimated from the average solvent concentration profiles contains the effect of heterogeneity in the sandpack and is equivalent to the dispersion coefficient that would be obtained with a breakthrough curve. The average dispersivity for the sandpack was estimated to be 0.098 cm.

Figure 2.38 shows the growth of the mixing zone length with time for the sandpack experiment. The average mixing zone length at each time step was measured from the three-dimensional CT images of the tracer test. Thus, the effect of the distortion of the mixing zone caused by heterogeneity in the sandpack was excluded from the mixing zone length. We see that the mixing zone grows linearly with the square root of time as predicted by Eq. 2.47 or 2.48. From the slope of the straight line of Fig. 2.38, K_L/R_f was calculated to be 78.5×10^{-5} cm^2/s. Thus, the dispersion coefficient without the effect of heterogeneity in the packing is 82×10^{-5} cm^2/s. Therefore, heterogeneity accounts for about 18% of the total dispersivity of the sandpack.

Figure 2.29 shows a distortion in the mixing zone caused by heterogeneity in the Berea sandstone which increases the average dispersion coefficient of the core. The lower half of the sandstone was more permeable than the upper half.

Figure 2.39 compares the experimental and calculated solvent concentration profiles based on Eq. 2.41 using an average dispersion coefficient of 600×10^{-5} cm^2/s and a retardation factor of unity. We see that the calculated profiles travel farther than the experimental profiles at all times, the separation of the two profiles increasing with time. The results indicate a satisfactory average dispersion coefficient but an incorrect retardation factor. Figure 2.40 compares the experimental and calculated profiles with the same dispersion coefficient but with a retardation factor of 1.11. The agreement between the experiment and Eq. 2.41 is excellent at all times. The average dispersivity for the Berea sandstone was estimated to be 0.379 cm.

Figure 2.41 shows the growth of the mixing zone length with time for the Berea sandstone experiment. We see that the mixing zone grows linearly with the square root of time as predicted by Eq. 2.47 or 2.48. From the slope of the straight line of Fig. 2.41, K_L/R_f was calculated to be 388×10^{-5} cm^2/s. Thus, the dispersion coefficient without the effect of heterogeneity in the porous medium is 431×10^{-5} cm^2/s. Therefore, heterogeneity accounts for about 28% of the total dispersivity of the Berea sandstone.

Table 2.3 summarizes the results for the sandpack and the Berea sandstone. As may be expected, the Berea sandstone which is a natural porous medium has a higher dispersion coefficient (dispersivity) and a higher retardation factor than the clean sandpack. The effect of heterogeneities in the porous medium is to increase the average dispersion coefficient over that which would be obtained in a homogeneous medium.

Figure 2.42 shows the solvent concentration data at all times for the two experiments plotted against the self-similarity variable given by Eq. 2.46. As expected from Eq. 2.42, the data transform into unique dimensionless response curves characteristic

of the two miscible displacements. The curve for the sandpack is steeper than for the sandstone, a reflection of the higher Peclet number in the sandpack experiment (N_{Pe} = 554) than in the sandstone experiment (N_{Pe} = 159). Similarity transformations such as demonstrated here are extremely useful and will be employed in Section 5 to develop a strategy for modeling laboratory coreflood experiments.

2.2.4 Conclusions
Based on the results presented in this section, the following conclusions may be drawn:

1. A method for characterizing the small-scale heterogeneities in laboratory cores by CT imaging has been demonstrated. The structure in the spatial variations in X-ray absorption coefficient (mineralogy), porosity and permeability in the core can be imaged and characterized geostatistically.

2. Sandpacks may not be as uniform as normally assumed. Their uniformity depends critically on the packing method employed.

3. A method for determining the longitudinal dispersion coefficients (dispersivities) of laboratory cores by CT imaging has been demonstrated. The method allows for the contributions of heterogeneity and hydrodynamic dispersion to the total dispersion coefficients to be estimated.

2.3 Subtask 1.2:   Visualization of Displacements in Heterogeneous Media

2.3.1 Objective
Petroleum reservoir rocks are nearly always heterogeneous. The objective of this subtask was to conduct flow visualization studies in heterogeneous consolidated cores which more closely approximate reservoir rocks. The goal was to image unstable miscible and immiscible displacements in these cores by CT to obtain data comparable to those obtained in homogeneous sandpacks.

2.3.2 Status
The objective of this subtask could not be achieved because of equipment malfunction. Our CT scanner developed a significant drift problem in the last year of the project that made it difficult to obtain reliable quantitative results. Attempts to repair the drift problem by the equipment manufacturer were unsuccessful. Therefore, further work on this subtask was suspended. The suspension of this subtask due to equipment malfunction was the only major problem encountered in this research.

3 TASK 2: FLOW VISUALIZATION EXPERIMENTS WITH VIDEO IMAGING WORKSTATION

3.1 Objective

The objective of this task was to acquire 2-D saturation image data of unstable displacements in an areal model to gain additional insights into the physics of unstable displacements. These 2-D data from the video workstation were needed to complement the 3-D data from the CT scanner. The 3-D CT data were acquired on linear, cylindrical systems whereas the 2-D video data were acquired on a quarter five-spot areal model which more closely approximates the displacement geometry in field projects.

3.2 Experiments

Several unstable first-contact miscible and immiscible displacements were visualized to examine the effects of viscosity ratio, injection rate, gravity segregation and wettability on the displacements. The porous media used in the experiments were unconsolidated packs of 30/25-mesh glass beads sandwiched between two acrylic plates, with an average porosity of 40% and an average permeability of about 20 darcies. The model simulated a quarter five-spot injection pattern of dimensions 40cm x 40cm x 0.32cm, with the injection well at one corner and the production well at the diagonally opposite corner.

The injected fluid was colored distilled water whereas the displaced fluids were mixtures of glycerin and water for the miscible displacements and mineral oil (Dow Corning Oil) for the immiscible displacements. Thirty images were typically captured in each experiment, with half the total number being captured before injected fluid breakthrough. Each image consisted of 350x350 picture elements (pixels).

3.3 Results and Discussion

The results from fourteen experiments are presented in this section. The first six experiments (Experiments 3.1 to 3.6) were unstable first-contact miscible displacements with the model oriented horizontally to eliminate the effect of gravity. The next six experiments (Experiments 3.7 to 3.12) were also unstable first-contact miscible displacements but with the model oriented vertically to take advantage of the effect of

gravity. The last two experiments (Experiments 3.13 and 3.14) were unstable immiscible displacements. In Experiment 3.13, the glass beadpack was first saturated with the mineral oil thereby rendering it oil-wet whereas in Experiment 3.14, the beadpack was first saturated with distilled water thereby making it water-wet. Table 3.1 provides additional information on the fourteen experiments.

3.3.1 Unstable Miscible Displacements in a Horizontal Model

Figures 3.1, 3.2 and 3.3 show the solvent concentration images for Experiments 3.1 to 3.6 at 0.10, 0.15 and 1.0 pore volumes injected. The images show the irregular viscous fingering patterns normally associated with unstable displacements with the most unstable displacement at the highest rate and viscosity ratio (Experiment 3.1) showing more fingering than the others. The variation in the solvent concentration caused by mixing is clearly evident in the images although the concentration could not be easily quantified at early times as in the CT images of Section 2. At late times, the solvent concentration is essentially 1.0 in the middle of the model, with a small mixing zone bodering the major solvent channel from the injector to the producer (Fig. 3.3).

We examined the viscous fingering patterns before solvent breakthrough for evidence of fractal behavior. This was done because fractal growth models have been proposed for modeling viscous fingering (van Damme et al., 1986; Nittman et al., 1985, 1986; Daccord et al., 1986; Maloy et al., 1985, 1986). To test for fractal behavior, we plotted the areal sweep efficiencies of each experiment against the maximum finger radius from the injector at several times before breakthrough. The areal sweep efficiency, defined as the fraction of the pattern area contacted by the injected fluid, is a useful performance index for a pattern flood. Figure 3.4 shows the areal sweep efficiency versus maximum finger length plot on a log-log scale for all six experiments. Remarkably, all the data plot as a straight line indicating that the areal sweep efficiencies in these experiments may be described by an equation of the form:

$$\ln (E_a) = D \ln (r_d) + \ln B \qquad (3.1)$$

or

$$E_a = B r_d^D \qquad (3.2)$$

where E_a is the areal sweep efficiency, B is a constant, r_d is a dimensionless maximum finger radius and D is a non integral exponent. This result shows that the areal sweep efficiencies of the unstable displacements obey a power law model or a fractal scaling law with a fractal dimension D. For the limited number of experiments shown on Figure 3.4, B = 0.80 and D = 1.96. Thus, it would appear that viscous fingering could be described by a fractal growth model. Because of its simplicity, such a model would be an attractive

-29-

alternative model for describing unstable EOR displacements. This approach to modeling unstable displacements could be the subject of future research.

A closer look at the images for Experiments 3.1 to 3.6 shows that high injection rate and high viscosity ratio are detrimental to the displacment efficiency whereas low injection rate and low viscosity ratio are beneficial to the displacement efficiency. These observations are most apparent in Fig.3.3 which shows the solvent concentration images at 1.0 pore volume injected. We see that at 1.0 pore volume injected, Experiment 1 at an injection rate of 320 cc/hour and a viscosity ratio of 100 had the least areal sweep efficiency whereas Experiment 3.6 at an injection rate of 100 cc/hour and a viscosity ratio of 50 had the largest areal sweep efficiency.

Figures 3.5 and 3.6 shows the effect of injection rate on the areal sweep efficiencies at viscosity ratios of 100 and 50 more quantitatively. The beneficial effect of low injection rate is apparent at both viscosity ratios although the beneficial effect is greater at the lower viscosity ratio than at the higher viscosity ratio.

Figures 3.7, 3.8 and 3.9 show the combined effects of viscosity ratio and injection rate on the performance of the unstable miscible displacements. At 100 cc/hour, the areal sweep efficiency after breakthrough at a viscosity ratio of 50 was significantly higher than that at a viscosity ratio of 100. However, as the injection rate increased, the difference in the sweep efficiencies at the two viscosity ratios diminished until at 320 cc/hour, the areal sweep efficiencies at both viscosity ratios were essentially the same.

3.3.2 Unstable Miscible Displacements in a Vertical Model

In Experiments 3.7 to 3.12, the five-spot model was oriented vertically to promote gravity segregation. The less dense solvent was injected at the top left corner of the model while fluids were produced from the bottom right corner of the model. The experiments were designed to investigate the degree of gravity stabilization that can be achieved by appropriate choice of injection scheme.

Figures 3.10, 3.11 and 3.12 show the solvent concentration images for Experiments 3.7 to 3.12 at 0.10, 0.15 and 1.0 pore volumes injected. We see the beneficial effect of gravity stabilization achieved by injecting the less dense solvent up structure and producing the oil down structure. The displacement efficiency is enhanced at all the rates and viscosity ratios. We note the spreading of the solvent from the left top corner, the injection point, to the right top corner that did not have an injection well, especially at the low injection rate of 100 cc/hour. Clearly, gravity can act as a double-edged sword in a displacement. In Experiment 2.1 in which the lighter solvent was injected horizontally to displace a more dense oil, gravity override of the oil by the solvent

led to a premature breakthrough of the solvent, thereby reducing the displacement efficiency. In Experiments 3.7 to 3.12 in which the lighter solvent was injected on top of the more dense oil to displace the oil downward, gravity segregation improved the displacement efficiency.

To quantify the benefit of gravity stabilization to the displacements, we present Figs. 3.13 and 3.14 which show the oil recovery curves for the displacements at viscosity ratios of 100 and 50 with and without gravity stabilization. In each case, the oil recovery with gravity stabilization was significantly greater than without gravity stabilization.

3.3.3 Unstable Immiscible Displacements in a Horizontal Model

Figures 3.15 and 3.16 show the saturation images for the unstable immiscible displacements in the oil-wet and water-wet beadpacks. The images for the displacement in the oil-wet beadpack show a highly branched displacement pattern similar to that normally associated with capillary driven displacements. The images for the displacement in the water-wet beadpack shows less branching than in the oil-wet beadpack. This is a reflection of the beneficial effect of water-wetness on the displacement in sandpacks that was observed in the CT images of Section 2. However, because of the low initial water saturation of 5% in the beadback compared to the 15% in the sandpack, we suspect that the beadpack was not as strongly water-wet as the sandpack. Therefore, the spreading tendency of the injected water in the water-wet beadpack (Experiment 3.14) was not as strong as in the water-wet sandpack (Experiment 3.3).

Figure 3.17 compares the areal sweep efficiencies for the displacements in the oil-wet and water-wet beadpacks. As was apparent from the saturation images, the areal sweep efficiency after breakthrough is greater in the water-wet medium than in the oil-wet medium. Figure 3.18 compares the oil recovery curves for an unstable first-contact miscible displacement (Experiment 3.1) and the immiscible displacements (Experiments 3.13 and 3.14) at the same injection rate and viscosity ratio. The results show that the miscible displacement is the most efficient whereas the immiscible displacement in the oil-wet medium is the least efficient of the three displacements. The efficiency of the immiscible displacement in the water-wet medium was intermediate between those of the miscible displacement and the immiscible displacement in the oil-wet medium. The oil recovery behavior in the quarter five-spot model (Fig. 3.18) is similar to that observed in cylindrical sandpacks in Section 2 (Fig. 2.1).

3.4 Conclusions

A large database of qualitative saturation image data of unstable miscible and immiscible displacements in an areal quarter five-spot model was acquired in this research. Based on the results of this task, the following conclusions may be drawn:

1. High displacement rates and high viscosity ratios are detrimental to the displacement efficiency of unstable miscible displacements.

2. The viscous fingering patterns in unstable miscible displacements before solvent breakthrough appears to obey a fractal scaling law indicating the potential for describing unstable displacements with a simple fractal growth model.

3. Gravity stabilization of unstable miscible displacements has been visualized and demonstrated.

4. Gravity stabilization can be used to enhance the efficiencies of miscible displacements by suitable choice of solvent density, injection rate and the locations of injection and production wells.

5. In general, miscible displacements are more efficient than their immiscible counterparts.

6. Immiscible displacements in a water-wet medium is more efficient than in an oil-wet medium.

4 TASK 3: MODEL DEVELOPMENT AND TESTING

4.1 Objective

The objective of this task was to develop fast and accurate high-resolution numerical models of selected EOR displacements for use in the numerical modeling task of the research (Task 4).

4.2 Preliminary Testing

To avoid duplication of previous research, we performed preliminary simulations with several existing numerical models at the University of Texas to bench-mark them for possible use in this research. The simulators tested include the first-contact miscible displacement numerical model developed by Peters and Kasap (1986), the immiscible displacement model developed by Khataniar and Peters (1991) and UTCHEM, a chemical flood simulator developed by Pope *et al.* (1990). We found that UTCHEM was the fastest of all the numerical simulators tested and was therefore well suited for the fine-mesh numerical simulations required in this research. Therefore, UTCHEM was used in all the simulation subtasks of this research.

4.3 Overview of UTCHEM Numerical Simulator

4.3.1 General Description

UTCHEM (Version 5.03) is a three-dimensional, three-phase, finite difference chemical flood simulator developed at the University of Texas at Austin by Pope *et al.* (1990). The simulator has evolved over many years (1978 to present) and has been tested extensively by others over this long period. It is now being used by many oil companies worldwide that have subjected it to further testing.

The simulator, which consists of more than fifteen thousand lines of FORTRAN code, is highly vectorized, thereby making it very efficient for fine-mesh simulation on the CRAY-Y/MP supercomputer. It can be used to simulate several types of fluid displacements including immiscible displacements and first-contact miscible displacements. Some of the components implemented in the simulator include water, oil, surfactant, polymer, anions, divalent cations, alcohols, tracers and gel. The phases include oleic, aqueous and microemulsion. More detailed information on the simulator may be found in the dissertation by Saad (1989).

The solution scheme in UTCHEM is analogous to IMPES, where the grid pressures are solved for implicitly using physical properties based on current phase

compositions, while the component material balances (concentrations), rather than the phase saturations, are solved for explicitly from the components mass conservation equations. A total variation diminishing third order method (TVD) is used to reduce numerical dispersion and grid orientation effects. The Jacobi-Conjugate-Gradient (JCG) method is used to solve the pressure equation. This method is highly recommended for a simulations with a large number of grid blocks, which were the cases in this research.

The physical properties modeled in UTCHEM include dispersion, dilution effects, adsorption, interfacial tension, relative permeability, capillary trapping, cation exchange, capillary pressure, phase densities, compositional phase viscosity, phase behavior, alcohol partitioning, shear thinning of polymer, inaccessible pore volume to polymer, permeability reductions of polymer and of gel.

4.3.2 Physical Property Relationships

Relative Permeability and Capillary Pressure

Details of the relative permeability and capillary pressure relationships used in UTCHEM to simulate immiscible displacements are given in Camilleri *et al.* (1987) and Saad (1989). For this research, the following relative permeability and capillary pressure models were used to simulate immiscible displacements:

$$k_{rw} = k_{wr} \left(\frac{S_w - S_{wi}}{1 - S_{wi} - S_{or}} \right)^{n_w} \tag{4.1}$$

$$k_{ro} = k_{or} \left(\frac{S_o - S_{or}}{1 - S_{wi} - S_{or}} \right)^{n_o} \tag{4.2}$$

$$P_c = C_{pc} \left(1 - \frac{S_o - S_{or}}{1 - S_{wi} - S_{or}} \right)^{e_{pc}} \tag{4.3}$$

where k_{wr}, n_w, k_{or}, n_o, C_{pc}, e_{pc} are constants specified as input parameters to the simulator.

Dispersion Coefficients

In UTCHEM, the dispersion coefficients needed to simulate first-contact miscible displacements are calculated accurately as elements of the tensor:

$$\vec{K}_{ij} = \begin{bmatrix} K_{xxij} & K_{xyij} & K_{xzij} \\ K_{yxij} & K_{yyij} & K_{yzij} \\ K_{zxij_{ij}} & K_{zyij} & K_{zzij} \end{bmatrix} \tag{4.4}$$

The elements of $\vec{K}_{ij}$ contain contributions from molecular diffusion and mechanical dispersion as given in the following equations:

$$K_{xxij} = \frac{D_{ij}}{\tau} + \frac{\alpha_{Lj}}{\phi S_j}\frac{u_{xj}^2}{|u_j|} + \frac{\alpha_{Tj}}{\phi S_j}\frac{u_{yj}^2}{|u_j|} + \frac{\alpha_{Tj}}{\phi S_j}\frac{u_{zj}^2}{|u_j|} \qquad (4.5)$$

$$K_{yyij} = \frac{D_{ij}}{\tau} + \frac{\alpha_{Lj}}{\phi S_j}\frac{u_{yj}^2}{|u_j|} + \frac{\alpha_{Tj}}{\phi S_j}\frac{u_{xj}^2}{|u_j|} + \frac{\alpha_{Tj}}{\phi S_j}\frac{u_{zj}^2}{|u_j|} \qquad (4.6)$$

$$K_{zzij} = \frac{D_{ij}}{\tau} + \frac{\alpha_{Lj}}{\phi S_j}\frac{u_{zj}^2}{|u_j|} + \frac{\alpha_{Tj}}{\phi S_j}\frac{u_{yj}^2}{|u_j|} + \frac{\alpha_{Tj}}{\phi S_j}\frac{u_{xj}^2}{|u_j|} \qquad (4.7)$$

$$K_{xyij} = K_{yxij} = \frac{(\alpha_{Lj} - \alpha_{Tj})}{\phi S_j}\frac{u_{xj}u_{yj}}{|u_j|} \qquad (4.8)$$

$$K_{xzij} = K_{zxij} = \frac{(\alpha_{Lj} - \alpha_{Tj})}{\phi S_j}\frac{u_{xj}u_{zj}}{|u_j|} \qquad (4.9)$$

$$K_{yzij} = K_{zyij} = \frac{(\alpha_{Lj} - \alpha_{Tj})}{\phi S_j}\frac{u_{yj}u_{zj}}{|u_j|} \qquad (4.10)$$

where

$$|u_j| = \left(u_{xj}^2 + u_{yj}^2 + u_{zj}^2\right)^{1/2} \qquad (4.11)$$

Darcy's law is used to calculate the fluxes, u_{xj}, u_{yj}, u_{zj} as

$$\vec{u_j} = -\vec{k}.\lambda_{rj}(\nabla P_j - \gamma_j \nabla z) \qquad (4.12)$$

Viscosity

A quarter-power mixing rule was used to calculate fluid viscosities for simulating first-contact miscible displacements. The mixture viscosity, μ_m, is calculated from the following equation:

$$\left[\frac{1}{\mu_m}\right]^{1/4} = C_s\left[\frac{1}{\mu_s}\right]^{1/4} + C_o\left[\frac{1}{\mu_o}\right]^{1/4} \qquad (4.13)$$

where C_s and C_o are the solvent and oil concentrations, respectively. This form of the mixture viscosity was used in the simulations because it has been found to match line-drive displacements well (Koval 1963).

4.3.3 Automatic Time-Step Selector

UTCHEM contains an automatic time-step selector. The purpose of a time-step selector in a simulator is to automatically select the time step size to avoid numerical instability, and to save the expense and effort in selecting a suitable time-step size by trial-and-error. UTCHEM employs the method of relative changes for selecting the time-step size. The automatic time-step selector was based on a maximum allowable absolute concentration change per time-step for each grid block. The following equation was used to select the time-step size:

$$\Delta t^{n+1} = \Delta t^n \cdot \min_{k=1}^{n_c} \left(\frac{\Delta C_{lim,k}}{\min\limits_{i=1}^{n_b} |\Delta C_{i,k}|} \right) \tag{4.15}$$

The maximum allowable concentration change, ΔC_{lim}, of the displaced fluid in each reservoir grid block for each time-step was one-tenth of the initial concentration. This value was found to be strict enough in the simulation to eliminate the need to further reduce the time-step size.

4.3.4 Maximum Time-Step Size

The maximum time-step size was based on the maximum Courant number allowed for the injection grid blocks. The Courant number for the injection grid blocks for multiphase flow was defined in our simulations as:

$$N_{cour} = \frac{(q_{ij})_{max}\Delta t}{\Delta x \; \Delta y \; \Delta z \; S_j \phi_i} \tag{4.16}$$

where $(q_{ij})_{max}$ is the maximum injection rate of a phase allowed in an injection grid block. This injection rate corresponds to an injection grid block with the maximum permeability value since injection into each injection grid block is proportional to the permeability of the grid block. In all the simulation runs, the maximum time-step size was chosen such that the maximum Courant number for each injection grid block was 0.10.

4.3.5 Grids and Boundary Conditions

All the simulations in this research were performed in two-dimensional vertical cross-sectional porous media with 53x122 mesh. The number of grid blocks was chosen

to coincide with the resolution of a two-dimensional slice from our CT experiments. The x-direction was the direction of bulk flow. Fifty-three blocks were used in this direction whereas 122 grid blocks were used in the y-direction. Fluid was injected at one side of the porous medium and produced at the other side. In every case, the displacement was linear from left to right. A constant injection rate and a constant production pressure boundary conditions were used in the simulations.

4.4 Typical Simulation Results from UTCHEM

To demonstrate the capabilites of UTCHEM, we present typical simulation results for an unstable immiscible displacement and an unstable first-contact miscible displacement.

4.4.1 Typical Immiscible Displacement Simulation

An immiscible displacement was simulated in a porous medium characterized by a random permeability distribution (Run 4.1). Fluid injection was maintained through the 122 grid blocks in the z-direction at a constant rate of 0.15 cm^3/s with the injection rate into each grid block being proportional to its permeability. This flow rate resulted in a gravity number, Ng, of 1.251×10^{-3}. Production, constrained by a constant outlet pressure of 1 atm, occurred through the 122 grid blocks at the outlet end of the core.

The permeability distribution was random, uncorrelated and log-normally distributed with an average permeability of 9.26 darcies and a Dykstra-Parsons coefficient of 0.55 (Dykstra and Parsons, 1950). Figure 4.1 shows a map of the permeability distribution.

The relative permeability and capillary pressure models given in Eqs. 4.1 to 4.3 wer used in the simulation with $k_{rw} = 0.9$, $n_w = 3.5$, $k_{or} = 0.9$, $n_o = 0.50$, $C_{pe} = 0.01$ $e_{pc} = 2.0$, $S_{wi} = 0.15$ and $S_{or} = 0.20$. The resulting relative permeability curves are shown in Fig. 4.2. Other pertinent input data for the simulation are given in Table 4.1.

Results and Discussion

Figure 4.3 shows the calculated water saturation maps for Run 4.1 at 0.05, 0.10 and 0.25 pore volumes injected. These water saturation maps have been normalized to account for the initial water saturation as:

$$S = \frac{S_w - S_{wi}}{1 - S_{wi}} \qquad (4.17)$$

The study of such spatial fluid distribution maps in addition to the more traditional recovery curves can provide valuable insights into the displacement mechanisms. The maps show diffuse water saturation with saturation bands that stretch with time qualitatively similar to

those observed in the CT experiments (Experiments 2.2 and 2.3). There is no gravity segregation in the simulated results. Several fingers develop at the displacing fluid front. However, none of these fingers is more dominant than the others. This is because the total randomness in the permeabilities prevents runaway finger growth.

The normalized water saturation profiles for Run 4.1 at six times are shown in Figure 4.4. The saturation profiles are qualitatively similar to those observed in Experiment 2.3 (Fig. 2.4). Figure 4.5 shows the same saturation profiles replotted as a function of the self-similarity variable, x_D/t_D. Remarkably, the saturation data collapse into one response curve that is characteristic of the simulated unstable displacement. We will use similarity transformations and the resulting response curves in developing simulation strategies for our laboratory coreflood experiments. Figure 4.6 shows the simulated recovery curve. Breakthrough of the injected fluid occurred at about 0.45 pore volume injected.

4.4.2 Typical First-Contact Miscible Displacement Simulation

An unstable miscible displacement was simulated in another porous medium characterized by a random permeability distribution (Run 4.2). The injection rate in this case was 0.76 cm^3/s resulting in a gravity number of -6.3×10^{-5}. The negative sign in the gravity number indicates that the injected solvent was less dense that the displaced oil.

The permeability distribution was random, uncorrelated and log-normally distributed with an average permeability of 9.5 darcies and a Dykstra-Parsons coefficient of 0.05, a relatively homogeneous porous medium compared to that used in Run 4.1. The displacement of a more viscous fluid by a less viscous fluid was simulated at a viscosity ratio of 54. Other pertinent input data for the simulation are given in Table 4.2.

Results and Discussion

Figure 4.7 shows the calculated solvent concentration maps for Run 4.2 at 0.10, 0.25 and 0.50 pore volumes injected. From the concentration maps, the unstable nature of the displacement is clearly evident with the development of viscous fingers. The solvent concentration profiles for Run 4.2 are shown in Fig. 4.8. We note the propagating nature of the disturbances in the saturation profiles qualitatively similar to that of Experiment 2.1. Figure 4.9 shows the calculated solvent concentration profiles presented as a function of the similarity transformation variable for first-contact miscible displacement. We note that even though the displacement was very unstable with significant viscous fingering, the solvent concentration profiles collapsed into one dimensionless response function that is characteristic of the miscible displacement. The similarity of the calculated response curve to the experimental response curves of Fig. 2.42 is noteworthy. The calculated oil recovery curve for Run 4.2 is shown in Fig. 4.10.

-38-

4.5 Conclusions

1.   Preliminary simulation runs have shown that UTCHEM, a chemical flood simulator developed at the University of Texas, is ideally suited for the numerical simulation tasks of this research.

2.   With appropriate input data, UTCHEM can be used to simulate either a first-contact miscible displacement or an immiscible displacement.

5 TASK 4: HISTORY MATCH OF FLOW VISUALIZATION EXPERIMENTS

The objective of this task was to replicate the flow visualization experiments from the CT scanner with a high-resolution numerical model to a degree never before attempted. Instead of matching the oil recovery curve as is traditionally done in the literature, we attempted to match the insitu fluid saturation distribution in the porous medium. This task was divided into the following subtasks.

5.1: Subtask4.1: Image Processing of Flow Visualization Data

5.1.1 Objective

CT imaging of a coreflood gives rise to an extremely large data set. For example, each of the coreflood experiments reported in this research consisted of 128x128x53 or 868,352 voxels. This means that there are 868,352 porosity values and the same number of saturation data at each time step of the experiment. Thus, to model the coreflood experiment numerically at the same resolution as the CT data would require 868,352 grid points. This is too high a resolution even on a supercomputer.

The objective of this subtask was to develop a procedure for processing the massive experimental data obtained by CT imaging of laboratory corefloods in order to make them easier to match with numerical models. This objective is achieved in this section for immiscible and first-contact miscible displacements. The mathematical models for immiscible and miscible displacements are presented. Inspectional analysis is used to derive the dimensionless scaling groups and a self-similarity transformation for the displacements. The dimensionless groups are useful for scaling our laboratory coreflood experiments to systems other than those used to acquire the data. The self-similarity transformation allows the massive saturation or solvent concentration data obtained by CT imaging of corefloods to be transformed into a dimensionless response curve that is characteristic of the displacement and is easier to match than the original data. The power of the transformation is demonstrated with a number of coreflood experiments.

5.1.2 Immiscible Displacement Equations

The partial differential equations for immiscible displacement in porous media are obtained by combining three types of equations—Darcy's law for multiphase flow, mass conservation equations (continuity equations) and the equations of state for the fluids.

Darcy's Law for Two-Phase Flow

The law of simultaneous flow of two immiscible fluids in porous media is given by a generalized form of Darcy's law. Let the two fluids be denoted as oil and water, where the water displaces the oil. For a homogeneous and anisotropic porous medium, Darcy's law, applied to the water and oil phases gives

$$\vec{u_w} = -\lambda_{rw} \, \vec{k}.(\nabla P_w + \rho_w g \nabla z') \tag{5.1}$$

and

$$\vec{u_o} = -\lambda_{ro} \, \vec{k}.(\nabla P_o + \rho_o g \nabla z') \tag{5.2}$$

where the z' direction is vertical and is positive upwards.

There are fourteen dependent variables in Eqs. 5.1 and 5.2. These are u_{wx}, u_{wy}, u_{wz}, u_{ox}, u_{oy}, u_{oz}, P_w, P_o, S_w, S_o, ρ_w, ρ_o, μ_w, and μ_o. To complete the mathematical formulation of the displacement model, eight more equations are required to supplement the six provided by Eqs. 5.1 and 5.2.

Continuity Equations

Two additional equations are obtained from the law of mass conservation applied to the water and oil phases in a region free of sources and sinks.

$$\frac{\partial(S_w \rho_w \phi)}{\partial t} + \nabla.(\rho_w \vec{u_w}) = 0 \tag{5.3}$$

and

$$\frac{\partial(S_o \rho_o \phi)}{\partial t} + \nabla.(\rho_o \vec{u_o}) = 0 \tag{5.4}$$

Other Equations

For isothermal flow, the following equations of state apply:

$$\rho_w = \rho_w(P_w) \tag{5.5}$$

$$\rho_o = \rho_o(P_o) \tag{5.6}$$

$$\mu_w = \mu_w(P_w) \tag{5.7}$$

$$\mu_o = \mu_o(P_o) \tag{5.8}$$

Next, a capillary pressure function is defined as:

$$P_o - P_w = (P_c) \tag{5.9}$$

and the oil and water saturations must , of course, sum to unity:

$$S_w + S_o = 1 \qquad (5.10)$$

The above fourteen equations provide in principle a complete mathematical description of two-phase immiscible displacement at the macroscopic level. To obtain a solution for a particular displacement of interest, the equations must be augmented with appropriate initial and boundary conditions.

The rock-fluid interactive properties—the relative permeability curves and the capillary pressure function—must be determined experimentally. Often, analytical models such as those presented in Section 4 are used.

Homogeneous Incompressible Fluids

If the fluids are homogeneous and incompressible, then their densities and viscosities are constant. Furthermore, in a non-deformable, homogeneous porous medium, the porosity is also constant. In this case, the continuity equations simplify to:

$$\phi\frac{\partial S_w}{\partial t} + \nabla\cdot\vec{u_w} = 0 \qquad (5.11)$$

and

$$\phi\frac{\partial S_o}{\partial t} + \nabla\cdot\vec{u_o} = 0 \qquad (5.12)$$

Adding Eqs. 5.11 and 5.12 and using Eq. 5.10, one obtains

$$\nabla\cdot\left(\vec{u_w} + \vec{u_o}\right) = \nabla\cdot\vec{u} = 0 \qquad (5.13)$$

where

$$\vec{u} = \vec{u_w} + \vec{u_o} \qquad (5.14)$$

Various alternative forms of the immiscible displacement equations that will be found useful later are now derived.

Water Saturation Equation

Equations 5.1 and 5.2 may be rewritten as

$$\frac{\vec{u_w}}{\lambda_{rw}} = -\overleftrightarrow{k}\cdot(\nabla P_w + \rho_w g \nabla z') \qquad (5.15)$$

and

$$\frac{\vec{u_o}}{\lambda_{ro}} = -\overleftrightarrow{k}\cdot(\nabla P_o + \rho_o g \nabla z') \qquad (5.16)$$

Subtracting Eq. 5.16 from 5.15 gives

$$\frac{\overrightarrow{u_w}}{\lambda_{rw}} - \frac{\overrightarrow{u_o}}{\lambda_{ro}} = \overrightarrow{k}.(\nabla P_c - \Delta \rho g \nabla z') \tag{5.17}$$

where

$$\Delta \rho = \rho_w - \rho_o \tag{5.18}$$

Using Eq. 5.14 to eliminate u_o from Eq. 5.17, one obtains

$$\frac{\overrightarrow{u_w}}{\lambda_{rw}} - \frac{\overrightarrow{u} - \overrightarrow{u_w}}{\lambda_{ro}} = \overrightarrow{k}.(\nabla P_c - \Delta \rho g \nabla z') \tag{5.19}$$

which upon rearrangement leads to

$$\overrightarrow{u_w}\left[\frac{1}{\lambda_{rw}} + \frac{1}{\lambda_{ro}}\right] = \frac{\overrightarrow{u}}{\lambda_{ro}} + \overrightarrow{k}.(\nabla P_c - \Delta \rho g \nabla z') \tag{5.20}$$

Let

$$F_w(S_w) = \frac{1}{1 + \lambda_{ro}/\lambda_{rw}} \tag{5.21}$$

Substituting Eq. 5.21 into 5.20 and rearranging give

$$\overrightarrow{u_w} = F_w \overrightarrow{u} + \left[\frac{1}{\lambda_{rw}} + \frac{1}{\lambda_{ro}}\right]^{-1} \overrightarrow{k}.(\nabla P_c - \Delta \rho g \nabla z') = 0 \tag{5.22}$$

Substituting Eq. 5.22 into Eq. 5.11 gives

$$\phi \frac{\partial S_w}{\partial t} + \nabla.(F_w \overrightarrow{u}) + \nabla.\left[\left[\frac{1}{\lambda_{rw}} + \frac{1}{\lambda_{ro}}\right]^{-1} \overrightarrow{k}.(\nabla P_c - \Delta \rho g \nabla z')\right] = 0 \tag{5.23}$$

Noting that for incompressible fluids

$$\nabla.(F_w \overrightarrow{u}) = F_w \nabla.\overrightarrow{u} + \overrightarrow{u}.\nabla F_w \tag{5.24}$$

Eq. 5.23 simplifies to

$$\phi \frac{\partial S_w}{\partial t} + \overrightarrow{u}.\nabla F_w + \nabla.[F_w \lambda_{ro} \overrightarrow{k}.(\nabla P_c - \Delta \rho g \nabla z')] = 0 \tag{5.25}$$

Since F_w, P_c, λ_{ro} and λ_{rw} are functions of S_w only, Eq. 5.25 may be further modified to give the following saturation equation:

$$\phi \frac{\partial S_w}{\partial t} + \frac{dF_w}{dS_w}\left(\overrightarrow{u}.\nabla S_w\right) + \nabla.[F_w \lambda_{ro} \overrightarrow{k}.(\nabla P_c - \Delta \rho g \nabla z')] = 0 \tag{5.26}$$

Fractional Flow Formula

Dividing every term of Eq. 5.22 by the modulus of the total velocity vector yields the water fractional flow formula:

$$\vec{f_w} = \frac{\vec{u_w}}{|\vec{u}|} = F_w\frac{\vec{u}}{|\vec{u}|} + [\frac{F_w\lambda_{ro}}{|\vec{u}|}\vec{k}.(\nabla P_c - \Delta\rho g\nabla z')] = 0 \qquad (5.27)$$

Written in terms of the fractional flow of water, Eq. 5.11 becomes

$$\frac{\phi}{|\vec{u}|}\frac{\partial S_w}{\partial t} + \nabla.\vec{f_w} = 0 \qquad (5.28)$$

Eq. 5.28 is a generalized form of the Buckley-Leverett immiscible displacement model (Buckley and Leverett, 1942). This equation and its modifications play a dominant role in the numerical simulation as well as scaling of immiscible displacements.

Dimensionless Form of the Displacement Equations

When cast in dimensionless form, the immiscible displacement equation can be applied either to a laboratory model or to a field prototype. Moreover, the dimensionless groups that emerge naturally from the process of non-dimensionalization serve as scaling or similarity groups that may be employed to relate the results of laboratory displacements to those of the prototypes.

To facilitate the dimensionless formulation, we assume that the displacement occurs in a two-dimensional, vertical cross-section that is homogeneous and anisotropic. In addition, we assume that the porous medium in inclined at a dip angle α measured from the horizontal. Figure 5.1 shows the geometrical setting for the two-dimensional displacement.

To complete the mathematical model, the boundary and initial conditions must be considered. For this research, a constant injection rate, a constant production pressure and no-flow boundary conditions at y=0 and y=H are used. In addition, the porous medium had an initial water saturation, S_{wi}.

The following dimensionless and normalized variables are defined. First, dimensionless coordinates are defined as

$$x_D = \frac{x}{L}, \, y_D = \frac{y}{H} \quad 0 \le x_D \le 1 \quad 0 \le y_D \le 1 \qquad (5.29)$$

where L and H are the length and the height of the porous medium (Fig. 5.1). Second, a normalized water saturation is defined as

$$S_n = \frac{S_w - S_{wi}}{1 - S_{wi} - S_{or}}, \quad 0 \le S_n \le 1 \tag{5.30}$$

Third, a dimensionless time is defined as

$$t_D = \frac{|\vec{u}|t}{\phi L} \tag{5.31}$$

Fourth, a dimensionless relative permeability is defined as

$$k_{rj} = k_{jr}k_{rjD} \quad 0 \le k_{rjD} \le 1 \tag{5.32}$$

where k_{jr} is the end-point relative permeability to phase j. Finally, a generalized capillary pressure function based on Leverett's J-function (Leverett, 1941) is defined as

$$P_c = \frac{\sigma f(\theta)}{\sqrt{k_x/\phi}} J(S_n) \tag{5.33}$$

Based on the above definitions, the water saturation equation, Eq. 5.26, takes on the following dimensionless form:

$$\frac{\partial S_n}{\partial t_D} + \left[\frac{u_x}{|\vec{u}|} \frac{\partial S_n}{\partial x_D} + \left[\frac{L}{H}\right] \frac{\partial S_n}{\partial x_D} \frac{u_y}{|\vec{u}|}\right] \frac{dF_w}{dS_n}$$

$$+ \left[\frac{k_{or}\sigma\sqrt{k_x\phi}}{|\vec{u}|\mu_o L}\right] [f(\theta)] \frac{\partial}{\partial x_D}\left[F_w k_{roD} \frac{dJ}{dS_n} \frac{dS_n}{dx_D}\right]$$

$$+ \left[\frac{k_{or}\sigma\sqrt{k_x\phi}}{|\vec{u}|\mu_o L}\right] \left[\frac{L^2}{H^2} \frac{k_y}{k_x}\right] [f(\theta)] \frac{\partial}{\partial y_D}\left[F_w k_{roD} \frac{dJ}{dS_n} \frac{dS_n}{dy_D}\right]$$

$$- \left[\frac{k_x k_{or}\Delta\rho\, g}{|\vec{u}|\mu_o}\right] [\sin\alpha] \frac{d(F_w k_{roD})}{dS_n} \frac{\partial S_n}{\partial x_D}$$

$$- \left[\frac{k_x k_{or}\Delta\rho\, g}{|\vec{u}|\mu_o}\right] [\cos\alpha] \left[\frac{H}{L}\right]\left[\frac{L^2}{H^2} \frac{k_v}{k_x}\right] \frac{d(F_w k_{roD})}{dS_n} \frac{\partial S_n}{\partial y_D} = 0 \tag{5.34}$$

where

-45-

$$F_w(S_n) = \frac{M^o \, k_{rwD}}{M^o \, k_{rwD} + k_{roD}} \tag{5.35}$$

In Eq. 5.35, M^o is the end-point mobility ratio.

Equation 5.34 is a general form of the water saturation equation that describes immiscible displacement of oil by water in a homogeneous, anisotropic, two-dimensional, inclined porous medium. It shows that immiscible displacements in porous media are controlled by convection or advection, capillarity, and gravity. Equation 5.34 provides the scaling groups for immiscible displacements in porous media. From Equation 5.34, the following dimensionless variables and scaling groups for two-dimensional immiscible displacements are derived. The dimensionless independent variables are x_D, y_D, and t_D. The dimensionless similarity or scaling groups are: M^o, A_r, $f(\theta)$, N_c, N_g, α, and R_L. The groups are defined as:

$$A_r = \frac{L}{H} \tag{5.36}$$

$$M^o = \frac{k_{wr} \, \mu_o}{k_{or} \, \mu_w} \tag{5.37}$$

$$N_c = \frac{k_{or} \, \sigma \, \sqrt{\phi k_x}}{\mu_o \, L \, |\bar{u}|} \tag{5.38}$$

$$N_g = \frac{k_x \, k_{or} \, \Delta\rho \, g}{\mu_o \, |\bar{u}|} \tag{5.39}$$

$$R_L = \frac{L}{H} \sqrt{\frac{k_y}{k_x}} \tag{5.40}$$

M^o is the mobility ratio; A_r is the aspect ratio; $f(\theta)$ is the wettability number; N_c is the capillary number; N_g is the gravity number; α is the dip angle and R_L is the effective aspect ratio. Using these scaling groups, the normalized water saturation equation may be rewritten in the following generalized form:

$$S_n = f_{2D} \, (x_D, \, y_D, \, t_D, \, M^o, \, A_r, \, f(\theta), \, N_c, \, N_g, \, \alpha, \, R_L) \tag{5.41}$$

Equation 5.41 applies to geometrically similar porous media either in the laboratory or in the field. It shows the similarity groups that must be the same in the model and the

prototype in order to properly scale unstable immiscible displacements in porous media. Matching these dimensionless scaling groups and the petrophysical properties (i.e. relative permeability ratio (k_{ro}/k_{rw}) and $J(S_n)$) will yield identical dimensionless results for two geometrically similar porous media.

The scaling group M^o, the mobility ratio, has long been recognized as controlling the areal sweep efficiency of an immiscible displacement. When this group is less than unity, the displacement arrangement is said to be favorable and the areal sweep efficiency will be high. When this group is greater than unity, the displacement arrangement is said to be unfavorable and the sweep efficiency will be low.

The scaling group, N_c, the ratio of capillary to viscous forces, is a measure of the influence of surface or capillary forces on the displacement. This influence is strongest at low displacement rates in which the surface forces promote the displacement efficiency of the nonwetting phase by the wetting phase (Benner et al., 1938; Bentsen, 1978; Fayers and Sheldon, 1959; Graham and Richardson, 1959; Handy, 1960; Hassler et al., 1944; Hovanessian and Fayers, 1961; Kyte and Rapoport, 1958; Leverett, 1941; Miller and Miller, 1956; Mungan, 1966, 1981; Perkins, 1957).

The scaling group $f(\theta)$ is a wettability number that is a measure of the tendency of one of the immiscible fluids to preferentially wet the surface of the porous medium. The scaling group $f(\theta)$ requires that the laboratory experiment must be done in a medium with wetting characteristics identical to the prototype. Wettability and its measurement have preoccupied petroleum researchers for many years, as shown by the extensive literature on the subjects (Amott, 1959; Anderson, 1986, 1987; Bobek et al., 1958; Brown and Fatt, 1956; Cuiec, 1977, 1990; Donaldson et al., 1969; Fatt and Klikoff, 1959; Morrow, 1990; Mungan, 1981; Newcombe et al., 1955; Raza et al., 1968; Treiber et al., 1972). However, in spite of the extensive research on the subject, a quantitative characterization of wettability remains somewhat elusive. The difficulty about characterizing wettability was best summed up by Mungan (1981) when he said "it had become common, indeed almost fashionable, for engineers and researchers to blame all unexplained reservoir and coreflood behavior on wettability".

Based on stability analysis, Peters and Flock (1981) obtained an estimate for $f(\theta)$ of 5.45 for a strongly oil-wet medium and 306 for a strongly water-wet medium. Recently, Haugen (1991) has combined these estimates with an Amott test to obtain the wettability number for a porous medium with intermediate wettability. In an Amott test, the wettability index for a strongly oil-wet medium is -1.0 whereas that for a strongly water-wet medium is +1.0. These correspond to Peters and Flock's wettability numbers of 5.45 and 306. By

measuring the Amott wettability index for a porous medium, he used linear interpolation to scale the Amott wettability index to the corresponding Peters and Flock wettability number. From his study, the wettability number for an intermediate-wet medium was estimated as 150. This number successfully predicted the onset of instability in his intermediate-wet porous media.

The gravity number, N_g, is the ratio of gravitational to viscous forces in the displacement. This group controls the problem of gravity override or underride that is a form of hydrodynamic instability. Like the capillary force, the gravity force is independent of the displacement rate and will therefore manifest itself most strongly at low displacement rates, when the viscous and pressure forces are low. The magnitude of the gravity number determines the degree of gravity instability whereas the sign determines whether the instability is gravity override or underride. If the gravity number is negative, the problem is override whereas if the number is positive, the problem is underride. The gravity number is an important scaling group which should always be considered because the immiscible displacement in the laboratory or in the reservoir occurs in the earth's gravitational field. The only occasion for neglecting gravity would be when the fluid densities are equal or if the coreflood experiment were performed in outer space!. It should be noted that the gravity force is a double-edged sword. It can lead to premature breakthrough of the displacing fluid by gravity override or underride. However, it can be harnessed by suitable choice of fluids, injection arrangement, and injection rate to obtain a gravity-stable efficient displacement.

Self-Similarity Transformation of Laboratory Corefloods

In a laboratory coreflood, it is useful to examine the displacement process in time and space through one-dimensional saturation profiles. Consider that the core has a zero dip angle and that vertical equilibrium is a good assumption. It should be noted from Eq. 5.34 that under vertical equilibrium assumption, R_L will be absent from the dimensionless scaling groups. This is so because, under vertical equilibrium, the pressure gradient of each phase is independent of the y-direction. Then, for a coreflood, Eq. 5.41 may be written as:

$$S = f_{1D} (x_D, t_D, M^o, A_r, f(\theta), N_c, N_g) \qquad (5.42)$$

where now S is the cross-sectional average of the normalized water saturation.

In Eqs. 5.41 and 5.42, the dimensionless response functions f_{2D} and f_{1D} are unknown but can be obtained from experiments or from numerical solutions of the displacement equations. In this study, f_{1D} was obtained from CT imaging experiments and from numerical simulations with UTCHEM. From Eq. 5.42, for a given set of similarity

-48-

groups, it is apparent that f_{1D} is a function of the two independent variables x_D and t_D. This dependence of f_{1D} on two independent variables obscures the true nature of the response function. It would be better if the dimensionless response function could be made to depend on only one independent variable. This can be done by subjecting the saturation equation to a self-similar transformation (Baker et al., 1991; Barenblatt, 1979; Barenblatt et al., 1990; David and Nolle, 1982; Gukham, 1965; Szucs, 1980).

According to Barenblatt (1979), a phenomenon or process is self-similar if the spatial distributions of its properties at various moments of time can be obtained from one another by a similarity transformation. Establishing self-similarity has always represented progress for a researcher: self-similarity has simplified computations and the representation of the characteristics of the phenomena under investigation. In handling experimental data, self-similarity has reduced what would seem to be a random cloud of empirical points so as to lie on a single curve or surface, constructed using self-similar variables chosen in some special way. Self-similarity of the solutions of partial differential equations has allowed their reduction to ordinary differential equations, which often simplifies the investigation. Therefore, with the help of self-similar solutions, researchers have attempted to envision the characteristic properties of new phenomena. Self-similar solutions have also served as standards in evaluating approximate methods of solving more complicated problems.

The self-similarity variable for immiscible displacement in a coreflood can be derived from Eq. 5.28 written in the following dimensionless form:

$$1 + \frac{\nabla \cdot \vec{f_w}}{\dfrac{\phi}{|\vec{u}|} \dfrac{\partial S_w}{\partial t}} = 0 \tag{5.43}$$

From Eq. 5.43, the self-similar dimensionless variable can be easily derived from dimensional considerations as follows:

$$\frac{\left[\nabla \cdot \vec{f_w}\right]}{\left[\dfrac{\phi}{|\vec{u}|} \dfrac{\partial S_w}{\partial t}\right]} \Rightarrow \frac{1/x}{\dfrac{\phi}{|\vec{u}|}(1/t)} \Rightarrow \frac{|\vec{u}|t}{\phi\, t} \Rightarrow \frac{t_D}{x_D} \text{ or } \frac{x_D}{t_D} \tag{5.44}$$

Thus, the self-similar dimensionless variable for immiscible displacement in a coreflood is x_D/t_D. Equation 5.42 may now be written as:

$$S = \tilde{f}\left(\frac{x_D}{t_D}, M^o, A_r, f(\theta), N_c, N_g\right) \tag{5.45}$$

where $\tilde{f}$ is now one dimensionless response curve that is characteristic of the immiscible displacement for the given dimensionless similarity groups. Later, it will be shown that this simple self-similar transformation is a powerful technique for gaining a deeper insight into the displacement as well as for simulating the displacement numerically. Furthermore, since $\tilde{f}$ reveals the true nature of the displacement, it can be used as the basis for comparing the performance of corefloods for various values of the similarity scaling groups.

It can be shown from Buckley-Leverett theory that the rate of advance of a particular water saturation is given by

$$\left[\frac{x_D}{t_D}\right]_S = \frac{df_w}{dS} \tag{5.46}$$

Thus, a graph of S versus x_D/t_D (the response curve) is the same as a graph of S versus df_w/dS. Therefore, the dimensionless response curve for an immiscible displacement is related to the derivative of the fractional flow curve. In fact, the fractional flow curve can be obtained by integrating the response curve.

Experimental Verification of Self-Similarity Transformation

We use the results from Experiments 2.2 and 2.3 to demonstrate the validity of the self-similarity transformation (x_D/t_D). Extensive validation of the similarity transformation with a variety of experiments may be found in a recent paper by Peters, Afzal and Gharbi (1993). We recall that Experiments 2.2 and 2.3 were unstable waterfloods in unconsolidated sandpacks. Experiment 2.2 was conducted in an oil-wet medium, whereas Experiment 2.3 was conducted in a water-wet medium.

The saturation profiles from the two experiments (Figs. 2.3 and 2.4) were replotted as functions of the self-similarity variable, x_D/t_D. Figures 5.2 and 5.3 show the resulting response curves. Clearly, the saturation profiles from the two experiments collapse into unique response curves that are characteristic of the displacements. Thus, both the calculated and experimental saturation profiles for unstable immiscible displacements are self-similar and can be transformed to give the response curve for the displacement.

It is interesting to compare the performances of Experiments 2.2 and 2.3. This can easily be done quantitatively using their respective response curves. Figure 5.4 compares the dimensionless response curves from the two experiments. The response curve in the water-wet medium (Experiment 2.3) has a well-developed, Buckley-Leverett displacement front whereas that in the oil-wet medium (Experiment 2.2) lacks such a well-defined front. Therefore, the displacement in the water-wet medium is more efficient than in the oil-wet medium. It should also be observed that the velocities of the low saturations in the oil-wet

medium are considerably higher than those in the water-wet medium, whereas the velocities of the high saturations are higher in the water-wet medium than in the oil-wet medium. These are due to the tendency for severe viscous fingering to occur in the oil-wet medium resulting in the rapid propagation of low injected fluid saturations through the medium. Thus, the dimensionless response curves are very effective in providing insights into the quantitative behavior of the unstable displacements in the two media.

Figure 5.5 shows the same response curves as in Fig. 5.4 but on a semilog scale. This presentation emphasizes the response curves at low values of the self-similarity variable or the late-time data. The late-time data are useful for determining the residual oil saturations for the displacements. It should be noted that on a semilog scale, the dimensionless response curves in the water-wet and oil-wet media can be approximated by three linear segments: a horizontal segment at low values of x_D/t_D, an intermediate segment, and a frontal segment. From the horizontal segments, the normalized residual oil saturation is found to be 15% in the water-wet medium and 38% in the oil-wet medium. These residual saturations will be incorporated in the relative permeability curves used to simulate Experiments 2.2 and 2.3 in Section 5.3.2.

Figure 5.6 shows the fractional flow curves for Experiments 2.2 and 2.3 obtained by integrating their respective response curves. It is interesting to note that the full fractional flow curve is obtained rather than the S-shaped curve typically obtained by neglecting capillary and gravity effects. Thus, the combined theoretical analysis and imaging experiments presented in this section provide, for the first time, a direct method for measuring the fractional flow curve for an immiscible displacement.

5.1.3 First-Contact Miscible Displacement Equations

In this section, the mathematical model for multidimensional miscible displacement is presented. Inspectional analysis is used to derive the dimensionless similarity scaling groups for miscible displacements. CT experiments for unstable first-contact miscible displacements are presented to demonstrate the effects of some of the similarity groups on the displacement performance. A self-similarity transformation variable is suggested for miscible displacements.

Theory

The mathematical model for a first-contact miscible displacement in a heterogeneous porous medium consists of the following mass transport, continuity, flow and state equations:

$$\frac{\partial(\phi C)}{\partial t} + \nabla.(\vec{u}C) - \nabla.(\phi \vec{K}\nabla C) = 0 \qquad (5.47)$$

-51-

$$\frac{\partial(\phi\rho)}{\partial t} + \nabla \cdot (\rho\vec{u}) = 0 \tag{5.48}$$

$$\vec{u} = -\frac{\vec{k}}{\mu}\nabla(P \pm \rho gh) \tag{5.49}$$

$$\rho = \rho(C) \tag{5.50}$$

$$\mu = \mu(C) \tag{5.51}$$

To simplify the model, we consider a two-dimensional displacement in a medium of length L and width H oriented in space as shown in Figure 5.1. Let us assume (a) a homogeneous and anisotropic medium, (b) incompressible fluids, (c) ideal mixing of the solvent and oil, (d) constant-rate injection of the solvent at the inlet (x = 0), and (e) coordinate axes that coincide with the principal axes of the permeability and dispersion coefficient tensors. Under these conditions, Eqs. 5.47 to 5.51 can be written in scalar forms with the appropriate initial and boundary conditions as:

$$\phi\frac{\partial C}{\partial t} + u\frac{\partial C}{\partial x} + v\frac{\partial C}{\partial y} - \phi K_L\frac{\partial^2 C}{\partial x^2} - \phi K_T\frac{\partial^2 C}{\partial y^2} = 0 \tag{5.52}$$

$$\frac{\partial u}{\partial x} + \frac{\partial v}{\partial y} = 0 \tag{5.53}$$

$$u = -\frac{k_x}{\mu}\left(\frac{\partial P}{\partial x} + \rho g\sin\alpha\right) \tag{5.54}$$

$$v = -\frac{k_y}{\mu}\left(\frac{\partial P}{\partial y} + \rho g\cos\alpha\right) \tag{5.55}$$

$$\rho = \rho_o + C\Delta\rho \tag{5.56}$$

$$\mu = \mu_o + C\Delta\mu \tag{5.57}$$

where $\Delta\rho = (\rho_s - \rho_o)$ and $\Delta\mu = (\mu_s - \mu_o)$.

Initial Condition:

$$C(x,y,t) = 0 \quad \text{at} \quad t = 0 \tag{5.58}$$

Boundary Conditions

$$C(x,y,t) = 1 \quad \text{at} \quad x = 0 \tag{5.59}$$

$$u(x,y,t) = U \quad \text{at} \quad x = 0 \tag{5.60}$$

$$\phi\frac{\partial C}{\partial t} + u\frac{\partial C}{\partial x} + v\frac{\partial C}{\partial y} = 0 \quad \text{at} \quad x = L \tag{5.61}$$

$$P(x,y,t) = P_1 - \int_0^y \rho g \cos \alpha\, d\xi \quad \text{at} \quad x = L \tag{5.62}$$

$$\frac{\partial C}{\partial y} = 0 \quad \text{at} \quad y = 0 \tag{5.63}$$

$$v(x,y,t) = 0 \quad \text{at} \quad y = 0 \tag{5.64}$$

$$\frac{\partial C}{\partial y} = 0 \quad \text{at} \quad y = H \tag{5.65}$$

$$v(x,y,t) = 0 \quad \text{at} \quad y = H \tag{5.66}$$

Equations 5.52 through 5.66 can put in dimensionless forms by defining the following dimensionless variables based on the initial and boundary conditions:

$$x_D = \frac{x}{L}, \; y_D = \frac{y}{H}, \; u_D = \frac{u}{U}, \; v_D = \frac{vL}{UH}, \; P_D = \frac{k_x P}{\mu_o UL}, \; \rho_D = \frac{\rho}{\rho_o}, \; \mu_D = \frac{\mu}{\mu_o} \tag{5.67}$$

Substituting Eq. 5.67 into Eqs. 5.52 through 5.66 gives the following dimensionless equations:

$$\frac{\partial C}{\partial t_D} + u_D\frac{\partial C}{\partial x_D} + v_D\frac{\partial C}{\partial y_D} - \left[\frac{\phi K_L}{UL}\right]\frac{\partial^2 C}{\partial x_D^2} - \left[\frac{\phi K_T L}{UH^2}\right]\frac{\partial^2 C}{\partial y_D^2} = 0 \tag{5.68}$$

$$\frac{\partial u_D}{\partial x_D} + \frac{\partial v_D}{\partial y_D} = 0 \tag{5.69}$$

$$u_D = -\frac{1}{\mu_D}\left(\frac{\partial P_D}{\partial x_D} + \left[\frac{k_x \rho_o g}{\mu_o U}\right]\rho_D \sin[\alpha]\right) \tag{5.70}$$

$$v_D = -\frac{1}{\mu_D}\left[\frac{k_y L^2}{k_x H^2}\right]\left(\frac{\partial P_D}{\partial y_D} + \left[\frac{k_x \rho_o g H}{\mu_o U L}\right]\rho_D \cos[\alpha]\right)$$ (5.71)

$$\rho_D = 1 + C\left[\frac{\Delta\rho}{\rho_o}\right]$$ (5.72)

$$\mu_D = 1 + C\left(\left[\frac{\mu_s}{\mu_o}\right] - 1\right)$$ (5.73)

$$C(x_D, y_D, t_D) = 0 \quad \text{at} \quad t_D = 0$$ (5.74)

$$C(x_D, y_D, t_D) = 1 \quad \text{at} \quad x_D = 0$$ (5.75)

$$u_D(x_D, y_D, t_D) = 1 \quad \text{at} \quad x_D = 0$$ (5.76)

$$\frac{\partial C}{\partial t_D} + u_D \frac{\partial C}{\partial x_D} + v_D \frac{\partial C}{\partial y_D} = 0 \quad \text{at} \quad x_D = 1$$ (5.77)

$$P_D(x_D, y_D, t_D) = P_{1D} - \left[\frac{k_x \rho_o g H}{\mu_o U L}\right]\int_0^{y_D} \rho_D \cos[\alpha] d\xi_D \quad \text{at} \quad x_D = 1$$ (5.78)

$$\frac{\partial C}{\partial y_D} = 0 \quad \text{at} \quad y_D = 0$$ (5.79)

$$v_D = 0 \quad \text{at} \quad y_D = 0$$ (5.80)

$$\frac{\partial C}{\partial y_D} = 0 \quad \text{at} \quad y_D = 1$$ (5.81)

$$v_D = 0 \quad \text{at} \quad y_D = 1$$ (5.82)

The terms in square brackets in Eqs. 5.68 to 5.82 are dimensionless numbers that will be the same at corresponding points in similar systems. These dimensionless similarity scaling groups control the performance of miscible displacements. Based on the above inspectional analysis, we identify the following dimensionless similarity groups for miscible displacements:

$$G_1 = \frac{\phi K_L}{UL} \tag{5.83}$$

$$G_2 = \frac{\phi K_T L}{UH^2} \tag{5.84}$$

$$G_3 = \frac{k_x \rho_o g}{\mu_o U} \tag{5.85}$$

$$G_4 = \alpha \tag{5.86}$$

$$G_5 = \frac{k_y L^2}{k_x H^2} \tag{5.87}$$

$$G_6 = \frac{k_x \rho_o g H}{\mu_o UL} \tag{5.88}$$

$$G_7 = \frac{\Delta \rho}{\rho_o} \tag{5.89}$$

$$G_8 = \frac{\mu_s}{\mu_o} \tag{5.90}$$

There are several things to note about the dimensionless scaling groups G1 to G8. First, they are dimensionless power products which could have been obtained from dimensional analysis of the displacement problem. Second, they may not be linearly independent and can therefore be further manipulated to obtain the minimum set of independent dimensionless groups needed to describe the displacement. Third, they are not unique and can therefore be combined to form other legitimate dimensionless groups. It can be shown from linear algebra theory that the above groups do form a complete set of independent dimensionless numbers (Shook *et al.*, 1992; Gharbi, 1993).

The dimensionless groups can be further manipulated to obtain the following more familiar dimensionless numbers (Gharbi, 1993):

$$N_{PeL} = \frac{1}{G_1} = \frac{UL}{\phi K_L} = \text{Longitudinal Peclet Number} \tag{5.91}$$

$$N_d = \sqrt{\frac{G_2}{G_1}} = \frac{L}{H}\sqrt{\frac{K_T}{K_L}} = \text{Dispersion Number} \tag{5.92}$$

$$A_r = \frac{G_6}{G_3} = \frac{H}{L} = \text{Aspect Ratio} \tag{5.93}$$

$$N_\alpha = G_4 = \alpha = \text{Dip Angle} \tag{5.94}$$

$$R_L = \sqrt{G_5} = \frac{L}{H} \sqrt{\frac{k_y}{k_x}} = \text{Effective Aspect Ratio} \tag{5.95}$$

$$N_g = G_6 \times G_7 = \frac{k_x \Delta\rho g H}{\mu_o U L} = \text{Gravity (Buoyancy) Number} \tag{5.96}$$

$$N_\rho = G_7 = \frac{\Delta\rho}{\rho_o} = \text{Density Number} \tag{5.97}$$

$$M = \frac{1}{G_8} = \frac{\mu_o}{\mu_s} = \text{Viscosity Ratio} \tag{5.98}$$

The performance of an unstable miscible displacement is determined by the above dimensionless groups. The effects of the groups on the displacement performance may be obtained experimentally or by solving Eqs. 5.68 to 5.82 for various values of the dimensionless numbers. It can be shown by a simple stability analysis that the conditions for a perturbation at the flood front to diminish or grow with time are given by the following inequalities (Bear, 1972; Hill, 1952; and Marle, 1981).

$$(M - 1)(U - U_c) < 0 \quad \text{Stable Displacement} \tag{5.99}$$

$$(M - 1)(U - U_c) > 0 \quad \text{Unstable Displacement} \tag{5.100}$$

where U_c is a critical velocity given by

$$U_c = \frac{k_x(\rho_s - \rho_o)g\sin\alpha}{\mu_o - \mu_s} \approx \frac{N_g \sin\alpha}{A_r} U \tag{5.101}$$

If the solvent is less dense and less viscous than the oil, as is normally the case in practice, then $M > 1$, $U_c < 0$ and $(M - 1)(U - U_c) > 0$, indicating that the displacement will always be unstable. The instability will manifest itself as viscous fingering and/or gravity override.

Self-Similarity Transformation Variable

The one-dimensional, diffusion-convection model for miscible displacement presented in Section 2.2.3 is a special case of the above miscible displacement mathematical model. The solution to the 1-D model showed that the appropriate similarity transformation

variable for miscible displacement is as given in Eq. 2.46 if retardation is considered or as given in Eq. 5.102 if the retardation factor is unity.

$$\xi = \frac{x_D - t_D}{\sqrt{t_D}} \qquad (5.102)$$

For stable first-contact miscible displacements, it was shown that the proposed similarity transformation variable was effective in transforming the solvent concentration data into one dimensionless response curve that was representative of the displacement performance (see Fig. 2.42). It was also shown through numerical simulation that the similarity variable was useful for transforming the solvent concentration data for an unstable miscible displacement free from significant gravity segregation (see Fig. 4.9). In this section, we show through CT experiments that the similarity transformation is less effective in displacements with significant gravity segregation.

Experimental Verification of Self-Similarity Transformation

Two CT experiments of unstable first-contact miscible displacements in unconsolidated sandpacks are presented to demonstrate the similarity transformation for unstable miscible displacements and to examine the effects of some of the controlling dimensionless scaling groups (Experiments 2.1 and 5.1). Experiment 2.1 with a gravity number of -2.7×10^{-5} was presented and discussed in Section 2. Experiment 5.1 was conducted at a higher gravity number of -1.4×10^{-4} than Experiment 2.1. Table 5.1 compares the pertinent experimental data and the values of the various dimensionless groups for the two experiments. Because the magnitude of the gravity number for Experiment 5.1 was about five times that for Experiment 2.1, it may be expected that the tendency for gravity override of the oil by the solvent would be greater in Experiment 5.1 than Experiment 2.1.

Figures 5.7 and 5.8 show the solvent concentration images for Experiments 2.1 and 5.1 at 0.5, 1.0 and 2.0 pore volumes injected. The images show a vertical slice through the center of the coreflood experiments. It is apparent from the images that the two experiments were affected by hydrodynamic instabilities in the forms of viscous fingering and gravity override. However, the gravity override problem is more severe in Experiment 5.1 than Experiment 2.1 as expected from their gravity numbers. Because of its higher gravity number (and higher mobility ratio), Experiment 5.1 was less efficient than Experiment 2.1 at the same pore volumes injected.

Figure 5.9 shows the solvent concentration profiles of Experiment 2.1 (Fig. 2. 2) replotted as a function of the self-similarity variable given by Eq. 5.102. We see that at early times (from 0.05 to 1.0 pore volumes injected) the solvent concentration data

collapsed essentially into one dimensionless response curve. However, the late-time data which were significantly affected by the gravity override problem deviated from the early-time response curve. Thus, gravity segregation destroys the self-similarity of the displacement thereby making the similarity transformation less useful in gravity-dominated displacements.

Figure 5.10 shows the solvent concentration profiles for Experiment 5.1. We note the wavelike characteristics of the profiles similar to those for Experiment 2.1 discussed in Section 2. Figure 5.11 shows the solvent concentration profiles plotted against the similarity transformation variable. We note a significant departure of the late-time data from the early-time response curve. This is a reflection of the severe gravity override encountered in this experiment.

5.1.4. Conclusions

This subtask was aimed at developing a procedure for averaging the massive CT data from laboratory corefloods in order to make them easier to simulate numerically. An averaging technique that subjects the data to a similarity transformation was developed theoretically and verified experimentally. Based on the results of this section, the following conclusions can be drawn:

1. Miscible and immiscible displacements in homogeneous media are self-similar processes. This fact greatly enhances our ability to model the displacements.

2. A similarity transformation technique for averaging laboratory coreflood CT data has been developed and demonstrated.

3. The dimensionless response curve obtained by the similarity transformation of coreflood data is a powerful tool for characterizing the performance of the coreflood.

4   The dimensionless scaling groups that control the performance of unstable immiscible and first-contact miscible displacements have been derived and presented.

5. CT experiments have been presented to demonstrate the effect of gravity number on unstable miscible displacements.

6. Significant gravity segregation destroys the self-similarity of unstable displacements thereby making the similarity transformation approach to data averaging less effective than without gravity segregation.

5.1.5 Applications of the Self-Similarity Transformation

There are three immediate applications for the self-similarity transformation approach to data avergaing presented in this section. The methodology of seeking a self-

similar transformation in order to organize experimental results is general and can be applied to most processes. As a general rule, a self-similar transformation aids in the planning and interpretation of experiments and in gaining insights into new processes.

A second application of the self-similarity transformation is in the mathematical modeling of displacement processes in permeable media. It should be apparent that the dimensionless response curve should be matched in order to model and predict the performance of a displacement. Matching the response curve in the porous medium has several advantages over current simulation practices in which the effluent recovery curve is matched. Simulation of the dimensionless response curve simulates the physical processes in the porous medium. This is in contrast to the simulation of the recovery curve, which is patently non unique in its nature. Another advantage is that the dimensionless response curve is a robust indicator of the process with the noise and other perturbing influences suppressed. Thus, the numerical computations can be focused on modeling the true response of the system of interest without distraction by the minor fluctuations that are inevitable in real systems. This is the simulation approach adopted in this research and used in Section 5.3.2 to history-match Experiments 2.2 and 2.3.

A third application of the self-similarity transformation is for scaling laboratory results to other systems. If the response curve for an immiscible displacement in the laboratory can be modeled, then the well-tuned numerical model could be used to predict the prototype behavior by incorporating the correct similarity scaling groups in the model. For example, such a well-tuned model could be used as a design tool to explore the anticipated response in the field under different similarity scaling groups. This application is demonstrated in Section 6 by scaling Experiment 2.3 in a homogeneous sandpack to predict its expected performance in heterogeneous reservoirs.

5.2 Subtask 4.2: Geostatistical Generation of Displacement Parameters

5.2.1 Objective

Petroleum reservoirs are nearly always heterogeneous. In order to use laboratory corefloods in relatively homogeneous media (sandpacks and Berea sandstones) to forecast the expected performance of an enhanced oil recovery process in the field, it is necessary to correct or scale the laboratory results to account for the effect of heterogeneity in the field. This scaling can be done by numerically simulating the laboratory corefloods in porous media with varied degree and structure of heterogeneity.

The objective of this subtask was to generate heterogeneous porous media to be used in scaling our laboratory coreflood experiments to forecast their expected field performance in heterogeneous reservoirs.

5.2.2 Methodology

The heterogeneous permeable media to be used in scaling the laboratory coreflood experiments were generated geostatistically and characterized by two measures of heterogeneity: the Dykstra-Parsons coefficient (DP) and the dimensionless spatial correlation length (Lx). The Dykstra-Parsons coefficient is a measure of the permeability variation in the porous medium (Dykstra and Parsons, 1950). It is defined as:

$$DP = \frac{(k)_{0.5} - (k)_{0.841}}{(k)_{0.5}} \tag{5.103}$$

where $(k)_{0.5}$ is the median of the permeability and $(k)_{0.841}$ is one standard deviation below the median. It is calculated from a set of permeability data arranged in increasing or decreasing order. The data are plotted on a log-probability paper and $(k)_{0.5}$ and $(k)_{0.841}$ are read from a best fit line through the data. When DP is zero, there is no permeability variation with respect to location and the resulting porous medium is homogeneous. As DP increases, the permeability variation increases and the porous medium becomes more and more heterogeneous. When DP is one, the medium is "infinitely" heterogeneous. Thus, a Dykstra-Parsons coefficient between zero and one represents the degree of heterogeneity of the porous medium.

The spatial correlation length is a measure of the distance over which neighboring permeability values are related to one another. The correlation length can be determined from the semivariogram (variogram) which is the variance of the differences between the permeabilities at two locations separated by a distance h (Kerbs, 1986). The variogram is calculated as:

$$\gamma(h) = \frac{Var[k(x) - k(x+h)]}{2} = \frac{[k(x) - k(x+h)]^2}{2N_h} \tag{5.104}$$

Here, $k(x)$ is the permeability at location (x), $k(x+h)$ is the permeability at location $(x+h)$, N_h is the number of data pairs separated by the distance h, and $\gamma(h)$ is the variogram. The distance h is called the lag distance. When the variogram is plotted against the lag distance (h), its value increases with increasing h until a certain distance is reached at which the variogram levels off. The value of h at which the variogram levels off is the correlation length, or the range of influence, and the value of the variogram at this point is called the sill. If the correlation length is zero, then the permeability at a given location is independent of its neighbors and the resulting permeability distribution is fully random. With increasing

-60-

correlation length, the range of influence of one permeability on its neighbors increases up to a distance equal to the correlation length. In the limiting case, when the correlation length approaches infinity, all the permeability values will be the same and a homogeneous medium will result. It should be noted that the correlation length is a directional quantity which can be different in different directions.

In this research, the dimensionless correlation length in the direction of bulk flow (Lx), or the x-direction, was varied, while the dimensionless correlation length in the direction perpendicular to that of the bulk flow (Ly), or the y-direction, was held constant. The correlation lengths were made dimensionless by dividing the correlation length in a given direction by the length of the porous medium in that direction.

The heterogeneous permeability fields were generated geostatistically in two dimensions using a computer program developed at the University of Texas at Austin (Yang, 1990). The computer program is based on the Turning Bands Method (Journel and Huijbregts, 1978) of generating correlated stochastic fields.

5.2.3 Results and Discussion

Twelve stochastic permeability fields were generated to cover a wide range of Dykstra-Parsons coefficient and correlation length. Figure 5.12 shows a schematic layout of the twelve fields together with the average permeability and the standard deviation for each field. Permeability fields were generated at Dykstra-Parsons coefficients of 0.01, 0.55 and 0.87 and dimensionless correlation lengths of 0, 0.2, 0.7 and 2.0. A DP of 0.01 represents a nearly homogeneous medium while a DP of 0.89 represents an extremely heterogeneous medium. Petroleum reservoirs typically have Dykstra-Parsons coefficients that range from 0.6 to 0.8. A correlation length of zero represents an uncorrelated or random permeability distribution; a correlation length of 0.2 represents mild correlation; a correlation length of 2.0 represents extremely strong correlation. Depending on the depositional environment, petroleum reservoirs can have widely different correlation lengths. The value of Ly was constant at 0.2 for the permeability fields generated in this study.

Figure 5.13 shows the permeability maps for the twelve permeability fields generated in this study. Two observations can be made from these maps. First, as the correlation length (Lx) increases, the permeability distributions become more and more stratified. The number of layers is inversely proportional to Ly. In fact, as Lx approaches infinity, for Ly = 0.2, the permeability distribution will consist of exactly five (1/0.2) distinct homogeneous layers. Second, with increasing DP at a given Lx, the contrast in the permeability values increases while their spatial arrangements remain similar. Figure 5.14

shows the permeability histograms which indicate that the permeability fields are log-normally distributed in accordance with observations in sedimentary rocks. Figure 5.15 shows the variograms for the twelve permeability fields which give a visual impression of the degree of correlation in each permeability field.

5.2.4 Conclusion

In this section, twelve heterogeneous porous media with varied degree and structure of hteterogeneity have been generated geostatistically. The simulated porous media will be used in Section 6 to demonstrate a practical application of this research by scaling one of our laboratory waterflood experiements in a sandpack (Experiment 2.3) to predict its expected performance in heterogeneous reservoirs.

5.3 Subtask 4.3: Development of History Match Methodology

5.3.1 Objective

The objective of this subtask was to develop a systematic procedure for history matching the laboratory coreflood experiments with the numerical model. Instead of history matching the oil recovery curves from the experiments as is traditionally done in the literature, our goal was to match the insitu fluid saturation data within the core obtained by CT imaging.

5.3.2 Methodology for Immiscible Displacements

Our approach to modeling the unstable coreflood experiments was to focus on replicating the dimensionless response curves for the experiments. Our simulations were done with UTCHEM using a 2-D, x-y vertical cross-sectional grid to simulate the 3-D coreflood experiments. The saturation images from the corefloods were used qualitatively to ensure that the major displacement mechanisms such as viscous fingering and gravity segregation were included in the numerical model.

In the simulations, the following similarity scaling groups were the same as in the experiments: viscosity ratio (μ_o/μ_w), capillary number (N_c), gravity number (N_g), and stability number (N_s). The adjustable parameters used to accomplish the history-match were the degree of permeability heterogeneity of the porous medium, the relative permeability curves (k_{rw}/k_{ro}), and the capillary pressure curve (dJ/dS). The parameters of the relative permeability and capillary pressure curves were adjusted systematically in the simulations until the response curve of a coreflood was satisfactorily replicated.

We demonstrate our methodology by history matching Experiments 2.2 and 2.3 in the oil-wet and water-wet sandpacks. The best values of the relative permeability and

capillary pressure parameters for history matching the two experiments are shown in Table 5.2. The resulting relative permeability curves are shown in Fig. 5.16. We note that significantly different relative permeability curves were required to simulate the two experiments in the oil-wet and water-wet media. This was so because relative permeability curves are strongly dependent on the wettability of the porous medium.

Results and Discussion

Figure 5.17 shows the saturation images from Experiment 2.2 at 0.05, 0.10, and 0.25 pore volumes injected. These images are 2-D projections of the 3-D coreflood saturation data rather than vertical slices of the 3-D data shown in Section 2. The projection data were used in order to facilitate comparison of the 3-D coreflood data with the 2-D numerical simulation data. The images show the usual evidence of hydrodynamic instability in oil-wet media. Figure 5.18 shows the saturation images from the best numerical simulation at the same times. It can be seen that at early times (0.05 and 0.10 pore volumes injected), there was good qualitative agreement between the experimental and the simulated saturation distributions. However, at late times (0.25 pore volume injected and beyond), the agreement was not so good. It was found that at late times, more gravity underride occurred in the experiment than in the numerical simulation. This is evident in the saturation image at 0.25 pore volume injected, in which the saturation band of 0.10 to 0.20 extends from near the inlet to the outlet in the lower half of the core (Fig. 5.17).

Figure 5.19 compares the experimental and simulated dimensionless response curves for Experiment 2.2. Although the overall agreement is good, the results show better agreement in the early-time data than in the late-time data. At late times, which correspond to low values of x_D/t_D, the model predicted a response curve that was higher than that of the experiment.

Figure 5.20 compares the experimental and the simulated saturation profiles at four times. Once again, we find excellent agreement between the experiment and the simulation at early times, before breakthrough. However, at late times, after breakthrough, there was disagreement between the experimental and the simulated profiles. This is the same disagreement that was observed qualitatively in the saturation images and quantitatively in the dimensionless response functions. It should be noted that although there was disagreement between the experimental and simulated profiles at late times, the simulated profiles passed evenly through the experimental profiles. This indicates that good material balance was maintained in the simulation at all times. Consequently, the experimental and simulated recovery curves will be in good agreement at all times. This is confirmed by Fig. 5.21, which shows excellent agreement in the recovery curves at all times. The fact that the recovery curves can be in excellent agreement even when the in-situ saturation distributions

are not in agreement is a fundamental weakness of the recovery curve as a measure of the quality of the simulation. The recovery curve is a measure of the material balance. Therefore, as long as material balance is maintained in the simulation, the simulated and the experimental recovery curves will agree even when there is a significant disagreement between the simulated and the experimental saturation distribution in the porous medium.

Figure 5.22 shows the projected saturation images for Experiment 2.3 at 0.05, 0.10, and 0.25 pore volumes injected. Compared to the displacement in the oil-wet medium, the saturation images show a more uniform displacement front with saturation bands that stretch with time. Figure 5.23 shows the simulated saturation images for this experiment. Qualitatively, the simulated images are in good agreement with the experimental images.

Figure 5.24 compares the experimental and the simulated dimensionless response curves for Experiment 2.3. The agreement is good over the entire range of x_D/t_D. This is confirmed by Fig. 5.25, which shows excellent agreement between the experimental and the simulated saturation profiles at all times. Figure 5.26 compares the experimental and the simulated recovery curves for Experiment 2.3. The agreement is good. Thus, in the water-wet medium, all aspects of the simulated performance (the response curves, the saturation profiles, and the recovery curves) are in agreement with the experiment. Therefore, the numerical model can be used as a predictive tool with confidence.

Scaling to other Systems

After successfully simulating the laboratory imaging experiments, the well-tuned numerical model can be used to scale the laboratory results to other systems. We demonstrate this novel approach to modeling the performance of EOR processes by scaling the results of the coreflood in the water-wet medium at a viscosity ratio of 91 (Experiment 2.3) to predict the expected performance at a viscosity ratio of 0.5. This could represent an investigation of the benefit to be expected from a successful mobility control measure by use of polymers. The numerical model for the water-wet medium was rerun with the same parameters as before but with the viscosity ratio reduced to 0.5. Thus, only one similarity scaling group, the viscosity ratio, was changed in the simulation.

Figure 5.27 shows the predicted saturation maps if the water-wet experiment conducted at a viscosity ratio of 91 were scaled to a viscosity ratio of 0.5 in a similar porous medium. Qualitatively, it is found that the displacement efficiency improves significantly with this degree of reduction in the mobility ratio. This is evident by the delay in the breakthrough of the injected fluid and by the higher saturation values attained at each time. In fact, the simulation predicts a piston-like displacement with only residual oil left

-64-

behind the front. This prediction is in agreement with experimental saturation images we have obtained in favorable mobility ratio immiscible displacements.

Figure 5.28 compares the predicted dimensionless response curves at the new viscosity ratio with that of the original experiment. Again, the improvement in the displacement performance at the lower viscosity ratio is evident. Figure 5.29 compares the predicted recovery curve with that of the original experiment. The improvement in the displacement performance at the lower viscosity ratio is further demonstrated by the predicted recovery curve. It should be noted that although the ultimate recoveries at the two mobility ratios will be the same, the timing of the recoveries will be significantly different. At a viscosity ratio of 0.5, the ultimate recovery would be obtained after the injection of only 0.6 pore volume, whereas at a viscosity ratio of 91, the ultimate recovery would be obtained after the injection of more than 3 pore volumes. There will therefore be a significant difference in the timing of the economic returns in the two projects.

The scaling of the laboratory results to other systems is not restricted to similar porous media. The results can be scaled to any porous medium. All that is required is an accurate description of the porous medium. For example, the well-tuned numerical model could be implemented in porous media with different spatial heterogeneity structures to investigate the effects of heterogeneity on the performance of the unstable displacements. We demonstrate this approach in Section 6 by scaling Experiment 2.3 to predict its its expected performance in the simulated heterogeneous porous media of Section 5.2.

Conclusions

This section was aimed at developing a procedure for history matching laboratory coreflood experiments with a numerical model. The procedure developed combines numerical modeling with laboratory imaging experiments. The numerical modeling strategy we have developed differs from the traditional approach in that our effort was focused on history-matching the saturation distribution in the porous medium rather than the nonunique recovery curve. Based on the results of this section, the following conclusions may be drawn:

1. Unstable immiscible displacements and their numerical models are self-similar processes that greatly enhance our ability to scale them from one system to another.

2. The similarity transformation developed in this research provides a simple but powerful way to compare exprimental results with numerical simulation results.

3. Unstable immiscible displacements in water-wet and oil-wet media can be modeled accurately by appropriate choice of relative permeability curves.

4. The combination of CT imaging experiments with numerical modeling provides a novel way to scale laboratory results to other systems.

-65-

5.3.3 Methodology for First-Contact Miscible Displacements

The history matching methodology based on the dimensionless response curve was successful for modeling stable, first-contact miscible displacements without gravity segregation. In this case, an analytical model was used in the history matching as shown in Section 2 (Figs. 2.37 and 2.40) for displacements in a sandpack and a Berea sandstone.

The methodology was less successful in modeling unstable miscible displacements with significant gravity segration for two reasons. First, gravity segregation destroys the self-similarity of the displacement, preventing the development of a unique response curve. Second, 2-D numerical simulations could not produce the same degree of gravity segregation observed in our 3-D CT experiments. Significantly higher gravity numbers were needed in the 2-D simulations to reproduce the same degree of gravity segregation observed in our 3-D CT experiments. It would appear that 2-D numerical models may not be adequate for modeling 3-D displacements with significant gravity segregation.

To demonstrate the difficulty of simulating gravity segregation with a 2-D model, we attempted to simulate Experiment 2.1 with UTCHEM at the same gravity number as the experiment. The simulator input are shown in Table 5.3. Figure 5.30 shows the projected solvent concentration images for Experiment 2.1. We note the significant gravity override in the experiment. Figure 5.31 shows the simulated solvent concentration maps at the same times as in Fig. 5.27. We note the absence of gravity override in the simulated results. Clearly, the 2-D model could not reproduce the degree of gravity segregation observed in the experiment. Figure 5.32 compares the experimental and simulated recovery curves. Remarkably, the agreement is good. This observation further points to the inadequacy of the recovery curve as a measure of the quality of the simulation results.

Conclusions

Based on the results of this section, the following conclusions may be drawn:

1. Two-dimensional numerical simulation appears to be inadequate for simulating unstable three-dimensional miscible displacements with significant gravity override.

2. The simulation of unstable laboratory miscible displacements with gravity segration requires further study.

6 PRACTICAL APPLICATION OF RESULTS

6.1 Introduction

The results from this research allows us to predict the performance of EOR processes in the field based on a small-scale laboratory coreflood experiment. We present this practical application of our research by forecasting the expected performance of the waterflood experiment in a water-wet homogeneous sandpack (Experiment 2.3) in heterogeneous reservoirs. We repeated the simulation of the waterflood experiment in each of the twelve simulated porous media of Fig. 5.13. The relative permeability and capillary pressure curves were the same as those used to history match the laboratory experiment in Section 5.3.2. The only parameters that were varied were the degree and structure of the heterogeneity of the porous medium (Dykstra-Parsons coefficient and correlation length).

6.2 Results and Discussion

Figure 6.1 compares the simulated dimensionless response curve for each of the twelve heterogeneous porous media with that of the laboratory waterflood experiment (Experiment 2.3). The following observations can be made from these results. If the heterogeneous media are characterized by low variability in the permeability distributions (low DP), the waterflood response will be essentially the same as in the laboratory sandpack regardless of the structure of the heterogeneity. This is indicated by the agreement between the simulated and the experimental response curves in the first column of Fig. 6.1 (DP = 0.01). If the heterogeneous media are characterized by low correlation in the permeability distributions (low Lx), the waterflood response will be essentially the same as in the laboratory sandpack regardless of the variability in the permeability distributions. This is indicated by the agreement between the simulated and the experimental response curves in the first row of Figure 6.1 (Lx = 0). If the heterogeneous media are characterized by high variability and high correlation in the permeability distributions, the waterflood response could be significantly different from that of the laboratory sandpack. This is most clearly shown by the response in the last permeability field in Figure 6.1 (Lx = 2 and DP = 0.87). In this case, the waterflood effeciency is significantly less in the heterogeneous medium than in the laboratory sandpack. These observations are confirmed by the oil recovery curves of Fig. 6.2 which shows a much lower oil recovery in the heterogenous porous medium with Lx = 2 and DP = 0.87 than in the laboratory sandpack.

To investigate the reason for the significant disparity in performance between the laboratory waterflood in a relatively homogeneous sandpack and in certain kinds of heterogeneous media, we examine the simulated saturation maps. Figures 6.3 and 6.4 show the simulated water saturation maps for each of the twelve heterogeneous reservoirs at 0.10 and 0.25 pore volumes injected. We see that the displacement in the heterogeneous media with high DP and high Lx are dominated by channeling of the injected water due to the permeability stratification. This results in significant bypassing of the oil in unswept layers and consequent low oil recovery. By contrast, the displacement in the media with low DP are characterized by excellent sweep comparable with that observed in the CT images of the laboratory waterflood experiment. This results in a displacement performance that is comparable to the laboratory waterflood experiment in the sandpack.

6.3 Conclusion

We conclude from this section that the performance of an EOR displacement in a heterogeneous reservoir could be significantly lower than in a laboratory experiment depending on the degree and structure of the heterogeneity of the reservoir. This conclusion points to the need for proper scaling when using the results of laboratory coreflood experiments in relatively homogeneous media to forecast the expected performance of an EOR process in heterogeneous reservoirs. The methodology we have developed and presented in this research can be used to accomplish this scaling and prevent erroneous performance forecasts.

7 TECHNOLOGY TRANSFER

The following technical papers, theses, dissertations and oral presentations resulted from this research.

7.1 Technical Papers

Gharbi, R. and E. J. Peters: "Scaling Coreflood Experiments to Heterogeneous Reservoirs," *Journal of Petroleum Science and Engineering*, **10**, (1993) 83-95.

Peters, E. J., R. Gharbi and N. Afzal: "Applications of CT Imaging to Characterize Cores and Fluid Flow in Permeable Media," Paper TT-007, *Proceedings of CONEXPO ARPEL '92*, Third Latin American Petroleum Congress, Rio de Janeiro, Brazil, October 18-23, 1992.

Peters, E. J., R. Gharbi and N. Afzal: "On Scaling Immiscible Displacements in Permeable Media," *Journal of Petroleum Science and Engineering*, **9**, No. 3 (June 1993) 183-205.

Peters, E. J. and R. Gharbi: "Numerical Modeling of Laboratory Corefloods," *Journal of Petroleum Science and Engineering*, **9**, No. 3 (June 1993) 207-21.

Peters, E. J., and R. Gharbi: "Scaling Coreflood Experiments to Heterogeneous Reservoirs," *Proceedings of the 9th Wyoming Enhanced Oil Recovery Symposium*, Casper, Wyoming, May 11-13, 1993.

Peters, E. J., R. Gharbi and N. Afzal: "Measurement of Transport Properties of Heterogeneous Permeable Media by Computed Tomography Imaging," Proceedings of the 1992 Fall Meeting of the American Geophysical Union, San Francisco, California, 1992.

Peters, E. J. and N. Afzal: "Quantitative Characterization of Core Heterogeneities by CT Imaging," *Proceedings of the 8th Wyoming Enhanced Oil Recovery Symposium*, Casper, Wyoming, May 20-21, 1992.

Peters, E. J. and N. Afzal: "Characterization of Heterogeneities in Permeable Media with Computed Tomography Imaging," *Journal of Petroleum Science and Engineering*, **7**, No. 3/4 (May 1992) 283-96.

Khataniar, S. and E. J. Peters: "The Effect of Heterogeneity on the Performance of Unstable Displacements," *Journal of Petroleum Science and Engineering*, **7**, No. 3/4 (May 1992) 263-81.

Khataniar, S. and E. J. Peters: "A Comparison of the Finite Difference and Finite Element Methods for Simulating Unstable Displacements," *Journal of Petroleum Science and Engineering*, **5**, (1991) 205-18.

7.2 Theses and Dissertations Completed

Afzal, N.: Investigation of Heterogeneities and Fluid Displacements in Porous Media Using CT, MS Thesis, The University of Texas at Austin, Austin, Texas, May 1992.

Gharbi, R.: Numerical Modeling of Fluid Displacements in Porous Media Assisted by Computed Tomography Imaging, PhD Dissertation, The University of Texas at Austin, Austin, Texas, August 1993.

Khataniar, S.: A Numerical Study of the Performance of Unstable Displacements in Heterogeneous Media, Ph.D. Dissertation, University of Texas at Austin, Austin, Texas, August 1991.

7.3 Oral Presentations

Waterflooding Viscous Oil Reservoirs: New Results from Computed Tomography Imaging, presented at the Seventh European Symposium on Improved Oil Recovery, October 27 - 29, 1993, Moscow, Russia.

A Novel Approach to Modeling Unstable EOR Displacements, presented at the DOE Bartlesville Project Office and Metairie Site Office Contractor Review Conference, July 18 - 22, 1993, Fountainhead, Oklahoma.

Computer Imaging in Enhanced Oil Recovery, presented to the Society of Petroleum Engineers, Austin Chapter, April 13, 1993.

Peters, E. J., R. Gharbi and N. Afzal: "Scaling Coreflood Experiments to Heterogeneous Reservoirs," presented at the 9th Wyoming Enhanced Oil Recovery Symposium, Casper, Wyoming, May 11-13, 1993.

Measurement of Transport Properties of Heterogeneous Permeable Media by Computed Tomography Imaging, presented at the 1992 Fall Meeting of the American Geophysical Union, San Francisco, CA, December 7-9, 1992.

Applications of CT Imaging to Characterize Cores and Fluid Flow in Permeable Media, presented at CONEXPO ARPEL '92, Third Latin American Petroleum Congress, Rio de Janeiro, Brazil, October 18-23, 1992.

High Tech Comes to the Oil Patch: Applications of CAT Scanning and MRI in Petroleum Engineering Research, presented to the Rotary Club, Round Rock, Texas, September 17, 1992.

Applications of X-Ray Tomography in Modeling Flow in Permeable Media, presented at the Gordon Frontiers of Science Conference on Modeling of Flow in Permeable Media, Plymouth, New Hampshire, August 10-14, 1992.

Applications of CT Imaging to Characterize Cores and Fluid Flow in Permeable Media, presented at the Society of Petroleum Engineers Forum on Special Core Analysis and Applications to Reservoir Engineering, Snowmass Village, Colorado, July 12-17, 1992.

Quantitative Characterization of Core Heterogeneities by CT Imaging, presented at the 8th Wyoming Enhanced Oil Recovery Symposium, Casper, Wyoming, May 20-21, 1992.

An Overview of the Imaging Research Program, presented at the Reservoir & Recovery Research Forum meeting, Tulsa, April 21, 1992.

Applications of X-Ray Computed Tomography (CT) in Modeling Flow in Permeable Media, presented at the Petroleum Engineering Seminar, Texas A&M University, College Station, Texas, February 20, 1992.

Applications of X-Ray Computed Tomography (CT) in Modeling Flow in Permeable Media, presented at the Petroleum Engineering Seminar, University of Tulsa, Tulsa, Oklahoma, February 7, 1992.

Application of Computer Imaging to Enhanced Oil Recovery Research, Petroleum Engineering Seminar, New Mexico Institute of Mining and Technology, Socorro, New Mexico, April 18, 1991.

NOMENCLATURE

A	=	Cross-sectional area
A_i	=	Cross-sectional of streamtube i
C	=	Solvent concentration
C*	=	Wettability number
C_i	=	Inlet solvent concentration
C_{ps}	=	Capillary pressure parameter
C_s, C_o	=	Solvent and Oil Concentrations
D	=	Fractal dimension
D_{ij}	=	Molecular diffusion coefficient of component i in phase j
d	=	Diameter of porous medium
D*	=	Dispersion parameter
D_o	=	Molecular diffusion coefficient
DP	=	Dykstra-Parsons coefficient
ΔP	=	Pressure drop across the porous medium
E_a	=	Areal sweep efficiency
e_{ps}	=	Capillary pressure exponent
F	=	Formation electrical resistivity factor
$\tilde{f}$	=	Dimensionless response function
$\vec{f}$	=	Fractional flow vector
$f(\theta)$	=	Wettability number
$\vec{f}_w$	=	Fractional flow vector for water
g	=	Gravitational acceleration
H	=	Height of porous medium
h	=	Lag distance
IOIP	=	Initial oil in place
J	=	Leverett's J-function
k	=	Absolute permeability
$\vec{k}$	=	Permeability tensor
K_d	=	Distribution coefficient

k_i	=	Absolute permeability for streamtube i
$\vec{K}_{ij}$	=	Dispersion Tensor
K_L	=	Longitudinal dispersion coefficient
K_T	=	Transverse dispersion coefficient
K_{xxij}, K_{yyij}, K_{zzij}	=	Diagonal elements of the dispersion tensor for component i in phase j
K_{xyij}, K_{zxij}, K_{yzij}, K_{zyij}	=	Off-diagonal elements of the dispersion tensor for component i in phase j
k_{jr}	=	End-point relative permeability to phase j
k_{or}	=	End-point relative permeability to oil
k_{rj}	=	Relative permeability of phase j
k_{ro}	=	Relative permeability to oil
k_{rw}	=	Relative permeability to water
k_{wr}	=	End-point relative permeability to water
k_x	=	Permeability in the x direction
k_y	=	Permeability in the y direction
L	=	Length of porous medium
Lx	=	Dimensionless correlation length in the x-direction
Ly	=	Dimensionless correlation length in the y-direction
M^o	=	End-point mobility ratio
M	=	Viscosity ratio
N_h	=	Number of data pairs
N_c	=	Capillary number
N_{cour}	=	Courant number
N_g	=	Gravity number
n_o	=	Oil relative permeability exponent
N_{Pe}	=	Peclet number
N_s	=	Stability number
N_x, N_y	=	Number of grid blocks in the x and y directions
n_w	=	Water relative permeability exponent

pvi	=	Pore volume injected
P	=	Pressure
P_c	=	Capillary Pressure
P_o	=	Pressure in the oil phase
P_w	=	Pressure in the water phase
q	=	Injection rate
q_i	=	Injection rate into streamtube i
$(q_{ij})_{max}$	=	Maximum injection rate of a phase allowed in an injection
q_T	=	Total injection rate
r_d	=	Dimensionless maximum finger radius
R_f	=	Retardation factor
S	=	Normalized water saturation
S_o	=	Oil saturation
S_{or}	=	Residual oil saturation
S_w	=	Water saturation
S_{wi}	=	Initial water saturation
t	=	Time
t_D	=	Dimensionless time
U	=	Constant solvent injection velocity
U_c	=	Critical velocity
$\vec{u}$	=	Darcy velocity vector
$\vec{u}_o$	=	Superficial velocity vector in the oil phase
$\vec{u}_w$	=	Superficial velocity vector in the water phase
u_{xj}, u_{yj}, u_{zj}	=	Phase j flux in x, y and z directions
v	=	Superficial velocity in the y direction
x,y,z	=	Cartesian coordinates
x_D, y_D, z_D	=	Dimensionless Cartesian coordinates
x_{fi}	=	Length of invaded zone along streamtube i

Greek Symbols

α	=	Dip angle

α_L	=	Longitudinal dispersivity
α_T	=	Transverse dispersivity
ΔC_{lim}	=	Maximum allowable concentration change
$\Delta C_{lim,k}$	=	Change in total concentration of component k in grid block i
ΔP	=	Pressure drop across porous medium
$\Delta_x, \Delta_y, \Delta_z$	=	Grid block size
$\Delta \rho$	=	Density difference (solvent minus oil)
$\Delta \mu$	=	Viscosity difference (solvent minus oil)
Δ_t	=	Time-step size in the simulation
ϕ	=	Porosity
∇	=	Gradient operator
Φ_j	=	Flow potential of phase j
γ	=	Semivariogram
γ_j	=	Specific weight of phase j
λ_{rj}	=	Relative mobility of phase j
μ_o	=	Oil viscosity
μ_s	=	Solvent viscosity
μ_w	=	Water viscosity
θ	=	Contact angle
ρ_g	=	Grain density
ρ_o	=	Oil density
ρ_s	=	Solvent density
ρ_w	=	Water density
σ	=	Oil-water interfacial tension
ξ	=	Self-similarity variable
τ	=	Turtuosity
ψ_1	=	CT number of the dry porous medium
ψ_2	=	CT number of the porous medium saturated with the displaced fluid

ψ_3	=	CT number of the porous medium saturated with the displaced and displacing fluids
ψ_a	=	Average CT number of air
ψ_m	=	CT number of the rock matrix
ψ_o	=	Average CT number of the displaced fluid
ψ_w	=	Average CT number of the displacing fluid
∇	=	Gradient operator
$\nabla*$	=	Dimensionless gradient operator

Subscripts

1	=	Core inlet
2	=	Core outlet
D	=	Dimensionless variable
g	=	Grain
i	=	Streamtube
o	=	Oil
s	=	Solvent
T	=	Total
w	=	Water

REFERENCES

Amott, E.: "Observations Relating to the Wettability of Porous Rock," *Trans.*, AIME (1959) **216**, 156-62.

Anderson, G.W.: "Wettability Literature Survey—Part 1: Rock/Oil/Brine Interactions and the Effects of Core Handling on Wettability," *J. Pet. Tech.* (October 1986) **38**, 1125-44.

Anderson, G.W.: "Wettability Literature Survey—Part 2: Wettability Measurement," *J. Pet. Tech.* (November 1986) **38**, 1246-62.

Anderson, G.W.: "Wettability Literature Survey—Part 3: The Effects of Wettability on the Electrical Properties of Porous Media," *J. Pet. Tech.* (December 1986) **38** 1371-78.

Anderson, G.W.: "Wettability Literature Survey—Part 4: Effects of Wettability on Capillary Pressure," *J. Pet. Tech.* (October 1987) **39**, 1283-1300.

Anderson, G.W.: "Wettability Literature Survey—Part 5: The Effects of Wettability on Relative Permeability," *J. Pet. Tech.* (November 1987) **39**,1453-68.

Anderson, G.W.: "Wettability Literature Survey—Part 6: The Effects of Wettability on Waterflooding," *J. Pet. Tech.* (December 1987) 1605-22.

Araktingi, U.G. and F.M. Orr: "Viscous Fingering in Heterogeneous Porous Media," SPE 18095, presented at the 63rd Annual Technical Conference of the Society of Petroleum Engineers, Houston, (Oct. 2-5, 1988).

Araktingi, U.G. and F.M. Orr, Jr.: "Viscous Fingering in Heterogeneous Porous Media," SPE 18095, presented at the 63rd Annual Technical Conference of the Society of Petroleum Engineers, Houston (Oct. 2-5, 1988).

Bahralolom, I. and J. Heller: "Core Sample Heterogeneity from Laboratory Flow Experiments," Quarterly Report, New Mexico Petroleum Recovery Research Center, Socorro (March 1989) .

Baker, W.E., P.S. Westine, and F.T. Dodge: *Similarity Methods in Engineering Dynamics, Theory and Practice of Scale Modelling*, Elsevier, New York (1991).

Barenblatt, G.I., V.M. Entov and V.M. Ryzhik: *Theory of Fluid Flows Through Natural Rocks*, Kluwer Academic Publishers, Boston (1990).

Barenblatt, G.I.: *Similarity, Self-Similarity, and Intermediate Asymptotics*, Consultants Bureau, New York (1979).

Bear, J.: *Dynamics of Fluids in Porous Media*, American Elsevier Publishing Company Inc., New York, 1972.

Benner, F.C., W.W. Riches, and F.E. Bartell: "Nature and Importance of Surface Forces in Production of Petroleum," *API Drill. and Prod. Practice* (1938) 442-46.

Bentsen, R.G.: "Conditions Under Which the Capillary Term May be Neglected," *J. Can. Pet. Tech.* (Oct.-Dec., 1978) **17**, 25-30.

Bergosh, J.L., T.R. Marks and A.F. Mitkus: "New Core Analysis Techniques for Naturally Fractured Reservoirs," SPE 13653, presented at the California Regional Meeting of the Society of Petroleum Engineers, Bakersfield, March 27-29, 1985.

Blackwell, R.J., J.R. Rayne and W.M. Terry: "Factors Influencing the Efficiency of Miscible Displacement," *Trans.*, AIME (1959), **216**, 1-8.

Bobek, J.E., C.C. Mattax, and M.O. Denekas: "Reservoir Rock Wettability—Its Significance and Evaluation," *J. Pet. Tech.* (July 1958) 155-60.

Brown, R.J.S. and I. Fatt: "Measurements of Fractional Wettability of Oilfield Rocks by the Nuclear Magnetic Relaxation Method," *Trans.*, AIME (1956) **207**, 262-64.

Buckley, S.E. and M.C. Leverett: "Mechanism of Fluid Displacement in Sands," *Trans.*, AIME (1942) **146**, 107-16.

Camilleri, D.; A. Fil, G.A. Pope, B.A. Rouse and K. Sepehrnoori: "Improvements in Physical-Property Models Used in Miceller/Polymer Flooding," *SPE Reservoir Engineering* (November 1987), 433-40.

Christie, M.A. and D.J. Bond, D.J. : "Detailed Simulation of Unstable Processes in Miscible Flooding," *SPE Reservoir Engineering* (November 1987), 514-22.

Christie, M.A., A.D.W. Jones and A.H. Muggeridge: "Comparison Between Laboratory Experiments and Detailed Simulations of Unstable Miscible Displacement Influenced by Gravity", paper presented at the North Sea Oil and Gas Reservoirs Conference, Trondheim, Norway (1989).

Christie, M.A.: "High-Resolution Simulation of Unstable Flows in Porous Media," *SPE Reservoir Engineering* (August 1989) **4**, 297-303.

Chuoke, R.L., P. van Meurs and C. van der Poel: "The Instability of Slow, Immiscible, Viscous Liquid-Liquid Displacements in Permeable Media," *Trans.*, AIME (1959) **216**, 188-94.

Clark, I.: *Practical Geostatistics*, Applied Science Publishers, London (1979).

Collins, R. E.: *Flow of Fluids Through Porous Materials*, The Petroleum Publishing Company, Tulsa (1976) 170-75.

Cuiec, L.E.: "Evaluation of Reservoir Wettability and Its Effect on Oil Recovery," *Interfacial Phenomena in Oil Recovery*, N.R. Morrow (ed.), Marcel Dekker, New York (1990) 319-75.

Cuiec, L.E.: "Study of Problems Related to the Restoration of the Natural State of Core Samples," *J. Can. Pet. Tech.* (Oct.-Dec. 1977) **16**, 68-80.

Daccord, G.; J. Nitmann and H.E. Stanley: "Radial Viscous Fingers and Diffusion-Limited Aggregation: Fractal Dimension and Growth Sites," Phys. Rev. Lett., 56, No. 4 (January 1986), 336-39.

David, F.W. and H. Nolle: *Experimental Modelling in Engineering*, Butterworths, Boston (1982).

Demetre, G.P., R.G. Bentsen, and D.L. Flock: "A Multi-Dimensional Approach to Scaled Immiscible Fluid Displacement," CIM Paper No. 81-32-7, presented at the 32nd Annual Technical Meeting of the Petroleum Society of CIM, Calgary, May 3-6, 1981.

Domenico, P.A. and F.W. Schwartz: *Physical and Chemical Hydrogeology*, John Wiley and Sons, New York (1990).

Donaldson, E.C., R.D. Thomas and P.B. Lorenz: "Wettability Determination and Its Effect on Recovery Efficiency," *Soc. Pet. J.* (March 1969) **9**, 13-20.

Dougherty, E.L.: "Mathematical Model of an Unstable Miscible Displacement," *Soc. Pet. Eng. J.* (June 1963) 155-63.

Dougherty, E.L.: "Mathematical Model of an Unstable Miscible Displacement," *Soc. Pet. Eng. J.* (June 1963) 155-63.

Dykstra, H. and R.L. Parsons: "The Prediction of Oil Recovery by Water Flood," *Secondary Recovery of Oil in the United States, Principles and Practice*, 2nd Edition, American Petroleum Institute (1950) 160-74.

Engelberts, W.F. and L.J. Klinkenberg: "Laboratory Experiments on the Displacement of Oil by Water from Packs of Granular Materials," *Proc.*, Third World Petroleum Congress, Sec. II, (1951) 544-54.

Engelberts, W.F. and L.J. Klinkenberg: "Laboratory Experiments on the Displacement of Oil by Water from Granular Materials," *Proc.* Third World Petroleum Congress, Sec. II (1951), 544-54.

Fatt, I. and W.A. Klikoff, Jr.: "Effect of Fractional Wettability on Multiphase Flow Through Porous Media," *J. Pet. Tech.* (Oct. 1959) **11**, 71-76.

Fayers, F.J. and J.W. Sheldon: "The Effect of Capillary Pressure and Gravity on Two-Phase Fluid Flow in a Porous Medium," *Trans.*, AIME (1959) **216**, 147-55.

Fayers, F.J. and T.M.J. Newley: "Detailed Validation of an Empirical Model for Viscous Fingering with Gravity Effects," SPE 15933, presented at the Ninth Symposium on Reservoir Simulation, San Antonio, Feb. 1-4, 1987.

Fayers, F.J.: "An Approximate Model with Physically Interpretable Parameters for Representing Miscible Viscous Fingering," SPE 13166, presented at the 59th Annual Technical Conference of the Society of Petroleum Engineers, Houston, (Sept. 16-19, 1984).

Gardner, J.W. and J.G.J. Ypma: "An Investigation of Phase Behavior-Macroscopic Bypassing Interaction in CO2 Flooding," *Soc. Pet. Eng. J.*, **24**, 1984, 508-20.

Gharbi, R.: Numerical Modeling of Fluid Displacements in Porous Media Assisted by Computed Tomography Imaging, PhD Dissertation, University of Texas at Austin, August 1993.

Giordano, R.M., S.J. Salter. and K.K. Mohanty: "The Effects of Permeability Variations on Flow in Porous Media," SPE 14365, presented at the 60th Annual Technical Conference of the Society of Petroleum Engineers, Las Vegas (Sept. 22-25, 1985).

Graham, J.W. and J.G. Richardson: "Theory and Application of Imbibition Phenomena in Recovery of Oil," *Trans.*, AIME (1959) **216**, 377-381.

Gukhman, A.A.: *Introduction to the Theory of Similarity*, Academic Press, New York (1965).

Hagoort, J.: "Displacement Stability of Water Drives in Water-Wet Connate-Water-Bearing Reservoir," *Soc. Pet. Eng. Jour.*, (February 1974), 63-74.

Handy, L.L.: "Determination of Effective Capillary Pressure for Porous Media from Imbibition Data," *Trans.*, AIME (1960) **219**, 75-80.

Hardham, W.D. : "Computerized Tomography Applied to the Visualization of Fluid Displacements," MS Thesis, University of Texas at Austin (December 1988).

Hassler, G.L., E. Brunner, and T.J. Deahl: "The Role of Capillarity on Oil Production," *Trans.*, AIME (1944) **155**, 155-74.

Hatziavramidis, D.T. : "A New Computational Approach to Miscible Displacement Problem," SPE 16004, presented at the Ninth SPE Symposium on Reservoir Simulation, San Antonio, February 1-4, 1987.

Haugen, J.: "Scaling Criterion for Relative Permeability Experiments on Samples with Intermediate Wettability," *Advances in Core Evaluation*, P.F. Worthington (ed.), Gordon and Breach Science Publishers, *Proc.*, First Society of Core Analysts European Core Analysis Symposium, London, May 21-23, 1990.

Heller, J.P : "Onset of Instability Patterns Between Miscible Fluids in Porous Media," *J. Appl. Phys.* **37** (1966) 1566-79.

Hill, S.: "Channelling in Packed Columns," *Chemical Engineering Science,* **1**, No. 6 (1952) 247-253.

Hohn, M.E.: *Geostatistics and Petroleum Geology*, Van Nostrand Reinhold, New York, 1988.

Honarpour, M.M., K.R. McGee, M.E. Crocker, N.L. Maerefat, and B. Sharma: "Detailed Core Description of a Dolomite Sample From the Upper Madison Limestone Group," SPE 15174, presented at the Rocky Mountain Regional Meeting of the Society of Petroleum Engineers, Billings (May 19-21, 1986).

Hovanessian, S.A. and F.J. Fayers: "Linear Water Flood with Gravity and Capillary Effects," *Soc. Pet. Eng. J.* (March 1961) **1**, 32-36.

Hove, A., J.K. Ringen and P.A. Read: "Visualization of Laboratory Corefloods With the Aid of Computerized Tomography of X-rays," *SPE Reservoir Engineering J.* (May 1987), 148-54.

Hunt, P.K., P. Engler and C. Bajsarowicz: "Computed Tomography as a Core Analysis Tool: Applications, Instrument Evaluation, and Image Improvement," J. Pet. Tech., (September 1988), 1203-10.

Isaaks, E. H. and R. M. Srivastava: *An Introduction to Applied Geostatistics*, Oxford University Press, New York (1989).

Jerauld, G.R., Nitsche, L.C., Teletzke, G.F., Davis, H.T., Scriven, L.E. : "Frontal Structure and Stability in Immiscible Displacements," SPE 12691, presented at the 1984 SPE/DOE Symposium on Enhanced Oil Recovery, Tulsa (April 15-18, 1984).

Journel, A.G. and Huijbregts, Ch. J.: *Mining Geostatistics*, Academic Press, 1978.

Kelkar, M.G. and S.P. Gupta: "A Numerical Studies of Viscous Instabilities: Effect of Controlling Parameters and Scaling Condtions," *SPE Reservoir Engineering* (February 1991) **6**, 121-28.

Kerbs, L.: "GEO-Statistics: The Variogram," Computer Oriented Geological Society Computer Contributions, **2**, No. 2 (August 1986) 54-59.

Khataniar, S. and E.J. Peters: "A Finite Element Method for Simulation of Two-Phase Flow," *Journal of Petroleum Science and Engineering*, **4** (1990) 169-81.

Khataniar, S.: An Experimental Study of the Effect of Instability on Dynamic Displacement Relative Permeability Measurements, MS Thesis, University of Texas at Austin, August 1985.

Khataniar, S. and E.J. Peters: "A Comparison of the Finite Difference and Finite Element Methods for Simulating Unstable Displacements," *Journal of Petroleum Science and Engineering*, 5 (1991) 205-18.

King, M.J. and H. Scher,: "Probabilistic Stability Analysis of Multiphase Flow in Porous Media," SPE 14366, presented at the 60th Annual Technical Conference of the Society of Petroleum Engineers, Las Vegas (September 22-25) 1985.

Koval, E.J.: "A Method for Predicting the Performance of Unstable Miscible Displacement in Heterogeneous Media," *Trans*. AIME, (1963) 228, 145-54.

Kyte, J.R. and Rapoport, R.L. : "Linear Waterflood Behavior and End Effects in Water-Wet Porous Media," *Trans*., AIME (1958) 213, 423-26.

Lake, L.W. and G.J. Hirasaki: "Taylor's Dispersion in Stratified Porous Media," *Soc. Pet. Eng. J.* (August 1981) 21, 459-65.

Lake, L.W.: *Enhanced Oil Recovery*, Prentice Hall, New Jersey, 1989.

Lee, S., K.M.G. Li and W.E. Culham: "Stability Analysis of Miscible Processes," SPE/DOE 12631, presented at the Fourth Symposium on Enhanced Oil Recovery, Tulsa (April 15-18, 1984).

Leverett, M.C.: "Capillary Behavior in Porous Media," *Trans*., AIME (1941) 142, 152-68.

Marle, C.M.: *Multiphase Flow in Porous Media,* Gulf Publishing Company, Houston (1981).

Miller, R.D. and R.E. Miller: "Physical Theory for Capillary Flow Phenomena," *J. App. Phys.* (1956) 27, 324-32.

Morrow, N.R.: *Interfacial Phenomena in Petroleum Recovery*, Marcel Dekker, Inc., New York (1992).

Mui, K.C. and Miller, C.A.: "Stability of Displacement Fronts in Porous Media-Growth of Large Elliptic Fingers," *Soc. Pet. Eng. J.* (April 1985) 255-67.

Mungan, N.: "Enhanced Oil Recovery Using Water as a Driving Fluid, Part 2—Interfacial Phenomena and Oil Recovery: Wettability," *World Oil* (March 1981) 192, 77-83.

Mungan, N.: "Enhanced Oil Recovery Using Water as a Driving Fluid, Part 3—Interfacial Phenomena and Oil Recovery: Capillarity," *World Oil* (May 1981) 192, 149-58.

Mungan, N.: "Interfacial Effects in Immiscible Liquid-Liquid Displacement in Porous Media," *Soc. Pet. Eng. J.* (Sept. 1966) 6, 247-53.

Newcombe, J., J. McGhee, and M.J. Rzasa: "Wettability Versus Displacement in Water Flooding Unconsolidated Sand Columns," *Trans*., AIME (1955) 204, 227-32.

Nittman, J., G. Daccord and H.E. Stanley: "Fractal Growth of Viscous Fingers: Quantitative Characterization of a Fluid Instability," *Nature*, 314 (March 1985), 141-44.

Nittman, J., G. Daccord and H.E. Stanley: "When are Viscous Fingers Fractal?" Fractals in Physics, L. Pietronero and E. Tosatti, eds, (1986) Elsevier, Amsterdam

Odeh, A.S.: "A Proposed Technique for Simulation of Viscous Fingering in One-Dimensional Immiscible Flow," *SPE Reservoir Engineering* (August 1989) **4**, 304-08.

Ogata, A. and R.B. Banks: "A Solution of the Differential Equation of Longitudinal Dispersion in Porous Media," U.S.Geological Survey Professional Paper 411-A, 1961.

Peaceman, D.W. and H.H. Rachford, Jr.: "Numerical Calculation of Multidimensional Miscible Displacement," *Soc. Pet. Eng. J.* (May 1962) 301-17.

Perkins, F.M.: "An Investigation of the Role of Capillary Forces in Laboratory Water Floods," *Trans.*, AIME (1957) **210**, 409-11.

Perkins, F.M. and R.E. Collins: "Scaling Laws for Laboratory Flow Models of Oil Reservoirs," *Trans.*, AIME (1960) **219**, 383-85.

Perrine, R.L.: "A Unified Theory for Stable and Unstable Miscible Displacement," *Soc. Pet. Eng. Jour.*, (September 1963), 205-13.

Peters, E. J. and D.L. Flock: "The Onset of Instability During Two-Phase Immiscible Displacement in Porous Media," *Soc. Pet. Eng. J.* (April 1981), 249-58; *Trans.*, AIME, **271**.

Peters, E. J. and S. Khataniar: "The Effect of Instability on Relative Permeability Curves Obtained by the Dynamic Displacement Method," *SPE Formation Evaluation* (December 1987) 469-74; *Trans.*, SPE (1987) **283**.

Peters, E. J. and W. D. Hardham: "A Comparison of Unstable Miscible and Immiscible Displacements," SPE 19640, presented at the 64th Annual Technical Conference of the Society of Petroleum Engineers, San Antonio, October 8 – 11, 1989.

Peters, E. J. and W. D. Hardham: "Visualization of Fluid Displacements in Porous Media Using Computed Tomography Imaging," *Journal of Petroleum Science and Engineering* (May 1990) **4**, 155-68.

Peters, E. J., J.A. Broman and W.H. Broman, Jr.: "Computer Image Processing: A New Tool for Studying Viscous Fingering in Corefloods," *SPE Reservoir Engineering* (November 1987), 720-28.

Peters, E. J., W.H. Broman, Jr. and J.A. Broman: "A Stability Theory for Miscible Displacement," SPE 13167 presented at the 59th Annual Technical Conference of the Society of Petroleum Engineers, Houston, September 16-19, 1984.

Peters, E.J.: Stability Theory and Viscous Fingering in Porous Media, PhD Dissertation, University of Alberta, Edmonton, Canada (1979).

Peters, E.J. and C.A. Reid: "A Microcomputer-Based Imaging System for the Visualization of Fluid Displacements," *J. Pet. Tech.* (May 1990) 558-63.

Peters, E.J. and E. Kasap: "Simulation of Unstable Miscible Displacements by Finite Element Method," SPE 15597, presented at the 61st Annual Technical Conference of the Society of Petroleum Engineers, New Orleans (October 5-8, 1986).

Peters, E. J., R. Gharbi and N. Afzal: "On Scaling Immiscible Displacements in Permeable Media," *Journal of Petroleum Science and Engineering*, **9**, No. 3 (June 1993) 183-205.

Peters, E. J. and R. Gharbi: "Numerical Modeling of Laboratory Corefloods," *Journal of Petroleum Science and Engineering*, 9, No. 3 (June 1993) 207-21.

Peters, E.J. and S.R. Cavalero: "The Fractal Nature of Viscous Fingering," SPE 20491, Proceedings of the 65th Annual Technical Conference of the Society of Petroleum Engineers, New Orleans, September 23-26, 1990.

Peters, E. J., R. Gharbi and N. Afzal: "On Scaling Immiscible Displacements in Permeable Media," *Journal of Petroleum Science and Engineering*, 9, No. 3 (June 1993) 183-205.

Peters, E.J.: "Stability Theory and Viscous Fingering in Porous Media," Ph.D. Thesis, University of Alberta, Calgary (January 1979) 12-40.

Pope, G.A., Lake, L.W. and Sepehrnoori, K.: "Modelling and Scale-Up of Chemical Flood: Third Annual and Final Report for the Period October 1987—September 1988," prepared for the U.S. Department of Energy under contract No. AC1985BC10846, Bartlesville, OK (March 1990).

Rachford, H.H.: "Instability in Water Flooding Oil from Water-Wet Porous Media Containing Connate Water," Trans., AIME (1964) 231, 133-48.

Raza, S.H., L.E. Treiber, and D.L. Archer: "Wettability of Reservoir Rocks and Its Evaluation," *Producers Monthly* (April 1968) 32, 2-7.

Richardson, J.G: "Flow Through Porous Media," *Handbook of Fluid Dynamics, Section 16*, Edited by V.L. Streeter, McGraw-Hill, New York 1961.

Saad, N.: Field Scale Simulation of Chemical Flooding, PhD Dissertation, The University of Texas at Austin, 1989

Schowalter, W.R.: "Stability Criteria for Miscible Displacement of Fluids from a Porous Medium," *AIChE Jour.*, 11, 1965, 99-105.

Shook, M., Li, D. and Lake, L.W.: "Scaling Immiscible Flow Through Porous Media by Inspectional Analysis," In Situ, 16, No. 3 (1992) 311-349.

Stalkup, F.I.: Miscible Displacement, SPE Monograph, 8, 1983.

Szucs, E.: *Similitude and Modelling*, Elsevier Scientific Publishing, New York (1980).

Tan, C.T. and G.M. Homsy: "Simulation of Non-Linear Viscous Fingering in Miscible Displacement," *Physics of Fluids*, 31 (1988) 1330-38.

Tan, C.T. and G.M. Homsy: "Stability of Miscible Displacements in Porous Media," *Physics of Fluids*, 29 (1986) 3549-69.

Treiber, I.E., D.L. Archer, and W.W. Owens: "A Laboratory Evaluation of the Wettability of Fifty Oil Producing Reservoirs," *Soc. Pet. Eng. J.* (Dec. 1972) 12, 531-40.

van Damme, H.; F. Obrecht, P. Levitz, L. Gartineau and C. Laroche: "Fractal Viscous Fingering in Clay Slurries," *Nature*, 320 (April 1986) 731-33.

Vinegar, H.J.: "X-Ray CT and NMR Imaging of Rocks," *J. Pet. Tech.* (March 1986) 257-59.

Vinegar, H.J. and S.L. Wellington: "Tomographic Imaging of Three-Phase Flow Experiments," *Rev. Sci. Instrum.* (January 1987), 58, 96-107.

Wang, S.Y., S. Ayral, F.S. Castellana and C.C. Gryte: "Reconstruction of Oil Saturation Distribution Histories During Immiscible Liquid-Liquid Displacement by Computer-Assisted Tomography," *AIChE J.*, (July 1984) **30**, 642-46.

Wang, S.Y., S. Ayral. and C.C. Gryte: "Computer-Assisted Tomography for the Observation of Oil Displacement in Porous Media," *Soc. Pet. Eng. J.* (February 1984) 53-55.

Wellington, S.L. and H.J. Vinegar: "CT Studies of Surfactant-Induced CO2 Mobility Control," SPE 14393, presented at the 60th Annual Technical Meeting of the Society of Petroleum Engineers, Las Vegas (Sept. 22-25, 1985).

Wellington, S.L. and H.J. Vinegar: "X-Ray Computerized Tomography," *J. Pet. Tech.* (August 1987), 885-98.

Withjack, E.M.: "Computed Tomography for Rock Property Determination and Fluid-Flow Visualization," SPE 16951, presented at the 62nd Annual Technical Conference of the Society of Petroleum Engineers, Dallas, (Sept. 27-30, 1987).

Withjack, E. M., S. K. Graham, and C. T. Young: "Determination of Heterogeneities and Miscible Displacement Characteristics in Corefloods by CT Scanning," Paper SPE 20490, presented at the 65th Annual Technical Conference of the Society of Petroleum Engineers, New Orleans, September 23-26, 1990.

Withjack, E.M. and I. Akervoll: "Computed Tomography Studies of 3-D Miscible Displacement Behavior in a Laboratory Five-Spot Model," SPE 18096, presented at the 63rd Annual Technical Conference of the Society of Petroleum Engineers (Houston, Oct. 2-5, 1988).

Yang, A.P.: "Stochastic Heterogeneity and Dispersion, " Ph.D. Dissertation, The University of Texas at Austin, 1990.

TABLE 2.1

Properties of Experiments 2.1, 2.2 and 2.3

	Symbol	Units	Experiment 2.1	Experiment 2.2	Experiment 2.3
Type of Displacement			First-Contact Miscible	Immiscible	Immiscible
Porous Medium					
Type			Unconsolidated Sandpack	Unconsolidated Sandpack	Unconsolidated Sandpack
Length	L	cm	54.2	54.1	54.5
Diameter	d	cm	4.8	4.8	4.8
Absolute Permeability	k	darcies	9.5	10.4	9.3
Porosity	ϕ	%	31.7	31.5	30.9
Initial Water Saturation	S_{wi}	%	0.0	0.0	15.0
Wettability type	—	—	—	Oil-Wet	Water-Wet
Fluids					
Displacing Fluid			Distilled Water + 14.9% BaCl$_2$ + 7.7% NaCl	Distilled Water + 10% BaCl$_2$	Distilled Water + 10% BaCl$_2$
Density	ρ_o	g/cm^3	1.191	1.088	1.088
Viscosity	μ_o	cp	1.63	1.14	1.14
Displaced Fluid			Glycerin + Distilled Water	Mineral Oil	Mineral Oil
Density	ρ_w	g/cm^3	1.215	0.966	0.966
Viscosity	μ_w	cp	88.2	103.4	103.4
Interfacial Tension	σ	dynes/cm	—	26.7	26.7
Wettability Number	C*	—	—	5.45	306.25
Dispersion Parameter	D*	cm^3/s	1.159×10^{-4}	—	—
Darcy Velocity	U	cm/s	8.5×10^{-3}	8.5×10^{-3}	8.5×10^{-3}
Viscosity Ratio	M	—	54	91	91
Stability Number	N_s	—	3293	16643	271
Gravity Number	N_g	—	-2.7×10^{-5}	1.1×10^{-5}	9.8×10^{-6}
Breakthrough Recovery		%IOIP	25.8	16.2	31.9

TABLE 2.2

Properties of Experiments 2.4 and 2.5

	Experiment 2.4	Experiment 2.5
Porous Medium		
Type	Unconsolidated Sandpack	Berea Sandstone
Length (cm)	54.2	60.2
Diameter (cm)	4.8	5.1
Absolute Permeability (Darcies)	6.4	0.160
Average Porosity from CT (%)	29.7	17.3
Fluids		
Displacing Fluid	Distilled Water + 13% NaCl	Distilled Water + 10% NaI
Density of Displacing Fluid (g/cm^3)	1.089	1.078
Viscosity of Displacing Fluid (mPa.s)	1.262	1.029
Displaced Fluid	Distilled Water + 10% BaCl$_2$	Distilled Water + 1.4% NaCl + 10% KCl
Density of Displaced Fluid (g/cm^3)	1.089	1.078
Viscosity of Displaced Fluid (mPa.s)	1.127	1.028
Viscosity Ratio	0.9	1.0
Darcy Velocity (cm/s)	3.037×10^{-3}	2.742×10^{-3}
Interstitial Velocity (cm/s)	1.023×10^{-2}	1.714×10^{-2}
Breakthrough Recovery (%)	95.0	84.4

TABLE 2.3

Summary of Results for Experiments 2.4 and 2.5

	Experiment 2.4	Experiment 2.5
Porous Medium	Unconsolidated Sandpack	Berea Sandstone
Longitudinal Dispersion Coefficient with Heterogeneity (cm^2/s)	100x10^{-5}	600x10^{-5}
Longitudinal Dispersivity with Heterogeneity (cm)	0.098	0.379
Longitudinal Dispersion Coefficient without Heterogeneity (cm^2/s)	82x10^{-5}	431x10^{-5}
Longitudinal Dispersivity without Heterogeneity (cm)	0.080	0.272
Distribution Coefficient (cm^3/g)	0.0057	0.0087
Retardation Factor	1.04	1.11
Peclet Number	554	159

TABLE 3.1

Summary of Experiments in a Quarter Five-Spot Model

Experiment	Type	Model Orientation	ϕ %	q cc/hour	M	S_{wi} %	$\rho_w - \rho_o$ g/cc
3.1	Miscible	Horizontal	40.38	320	100	—	-0.226
3.2	Miscible	Horizontal	40.57	200	100	—	-0.226
3.3	Miscible	Horizontal	43.05	100	100	—	-0.226
3.4	Miscible	Horizontal	40.38	320	50	—	-0.210
3.5	Miscible	Horizontal	40.38	200	50	—	-0.210
3.6	Miscible	Horizontal	43.43	100	50	—	-0.210
3.7	Miscible	Vertical	39.45	320	100	—	-0.226
3.8	Miscible	Vertical	42.67	200	100	—	-0.226
3.9	Miscible	Vertical	40.67	100	100	—	-0.226
3.10	Miscible	Vertical	41.90	320	50	—	-0.210
3.11	Miscible	Vertical	38.77	200	50	—	-0.210
3.12	Miscible	Vertical	40.76	100	50	—	-0.211
3.13	Immiscible	Horizontal	38.40	320	100	0	0.029
3.14	Immiscible	Horizontal	41.10	320	100	5	0.029

TABLE 4.1

Input Data for Example Simulation of an Unstable Immiscible Displacement (Run 4.1)

Nx	53
Ny	122
Porosity	0.296
Average permeability	9.26 darcies
Dykstra-Parsons coefficient	0.55
Displacing fluid viscosity	1.1276 cp
Displaced fluid viscosity	103.4 cp
Injected rate	0.15 cm^3/s
Displaced fluid density	0.9655 gm/cc
Displacing fluid density	1.0882 gm/cc
Initial water saturation	0.15

TABLE 4.2

Input Data for Example Simulation of an Unstable First-Contact Miscible Displacement (Run 4.2)

Nx	53
Ny	122
Porosity	0.32
Average permeability	9.5 darcies
Dykstra-Parsons coefficient	0.05
Displacing fluid viscosity	1.663 cp
Displaced fluid viscosity	88.15 cp
Injected rate	0.76 cm^3/s
Displaced fluid density	1.216 gm/cc
Displacing fluid density	1.191 gm/cc
α_L	0.3 cm
α_T	0.0 cm

TABLE 5.1

A Comparison of the Properties of Experiments 2.1 and 5.1

	Symbol	Experiment 2.1	Experiment 5.1
Oil		84% Glycerin +15% Water	85% Glycerin +15% Water
Solvent		Water + 14.87% NaCl + 7.74% BaCl$_2$	Water +10% BaCl$_2$
Length (cm)	L	54.2	54.3
Height (cm)	H	4.8	4.8
Porosity (%)	ϕ	30.39	31.15
Permeability (Darcies)	k_x, k_y	9.50	10.28
Oil Viscosity (cp)	μ_o	88.15	92.78
Solvent Viscosity (cp)	μ_s	1.63	1.11
Oil Density (g/cm^3)	ρ_o	1.216	1.218
Solvent Density (g/cm^3)	ρ_s	1.191	1.089
Injection Velocity (cm/s)	U	0.008504	0.008504
Longitudinal Peclet Number	N_{PeL}	1820	1779
Dispersion Number	N_d	3.57	3.58
Aspect Ratio	A_r	0.089	0.088
Dip Angle	N_α	0	0
Effective Aspect Ratio	R_L	11.3	11.3
Gravity (Buoyancy) Number	N_g	-2.7×10^{-5}	-1.4×10^{-4}
Density Number	N_ρ	-0.02	-0.16
Viscosity Ratio	M	54	84

TABLE 5.2

Simulation Input Data for Experiments 2.2 and 2.3
(Runs 5.1 and 5.2)

	Run 5.1	Run 5.2
Dimensions Grid Blocks Length Cross-Sectional Area	53 x 122 54.08 cm 18.29 cm^2	53 x 122 54.53 cm 18.29 cm^2
Dykstra-Parson Coefficient	0.576	0.050
Relative Permeability Data S_{wi} S_{or} k_{wr} k_{or} n_w n_o	0.0 0.0 1.0 1.0 2.0 2.0	0.15 0.20 0.90 0.90 3.5 0.49
Fluids ρ_w μ_w ρ_o μ_o μ_o/ρ_o	1.0882 g/cc 1.138 cp 0.9655 g/cc 103.4 cp 91	1.0882 g/cc 1.1276 cp 0.9655 g/cc 103.4 cp 91
N_c N_g	2.16×10^{-8} 1.30×10^{-3}	1.91×10^{-8} 1.30×10^{-3}
Capillary Pressure	$-0.01 \, (S_n)^2$	$0.01 \, (1-S_n)^2$
Darcy's Velocity	8.5×10^{-3} cm/s	8.5×10^{-3} cm/s

TABLE 5.3

Simulation Input Data for Experiment 2.1
(Run 5.3)

	Simulation data
Grid blocks	53 x 122
Length	54.17 cm
Cross-sectional area	18.29 cm^2
Average ϕ	31.7%
α_L	0.15 cm
α_T	0.003 cm
Fluids	
Density of displacing fluid	1.191 g/cc
Viscosity of displacing fluid	1.633 cp
Density of displaced fluid	1.216 g/cc
Viscosity of displaced fluid	88.15 cp
μ_o/μ_s	54
Darcy velocity	8.5x10^{-3} cm/s
N_g	-3.1x10^{-4}

Longitudinal Vertical Plane

Longitudinal Horizontal Plane

Axial Plane
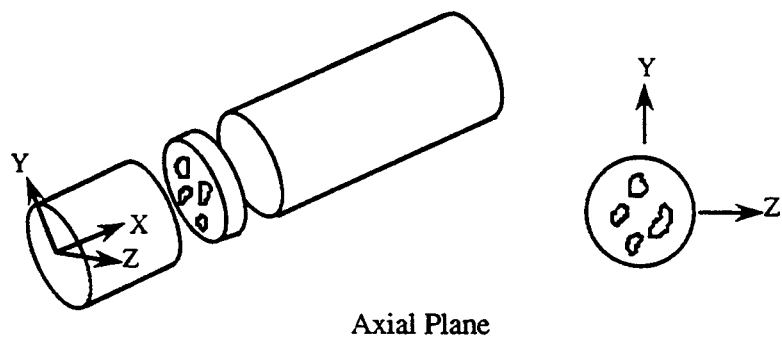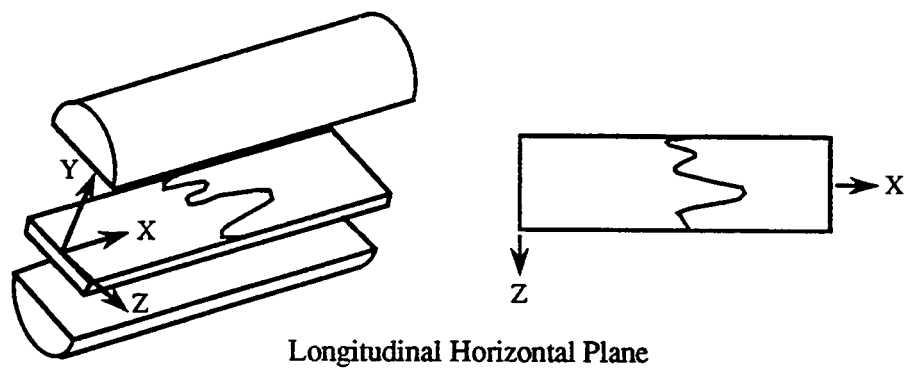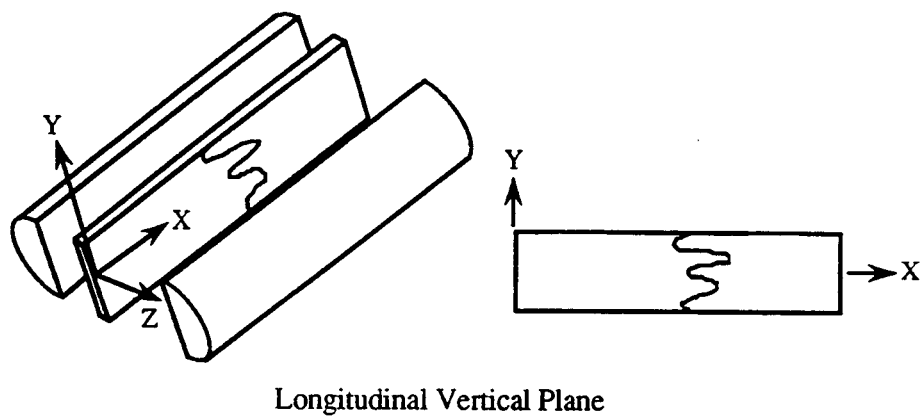
Figure 1.1.   Principal viewing planes of CT images of a core.
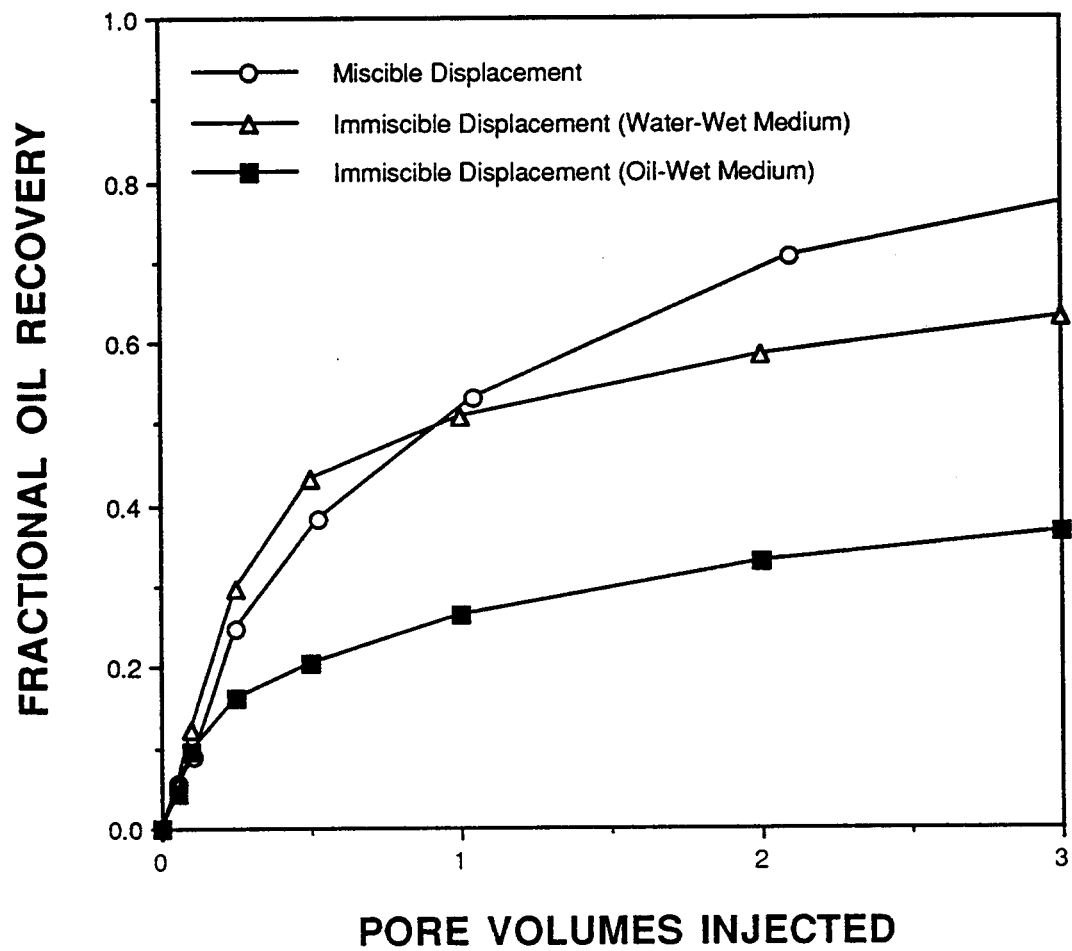
Figure 2.1. Oil recovery curves for typical unstable first-contact miscible and immiscible displacements (Experiments 2.1, 2.2 and 2.3).
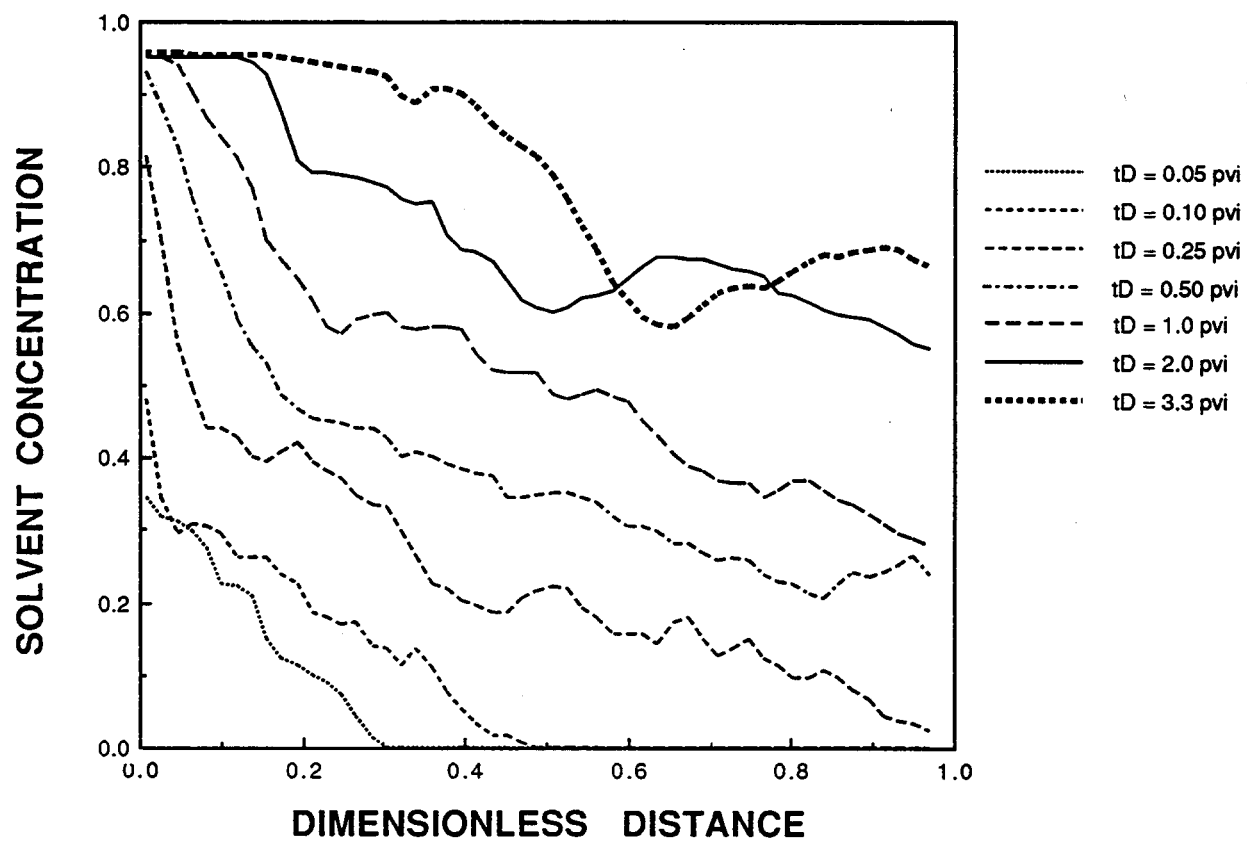
Figure 2.2. Solvent concentration profiles for a typical unstable first-contact miscible displacement at a viscosity ratio of 54 (Experiment 2.1).
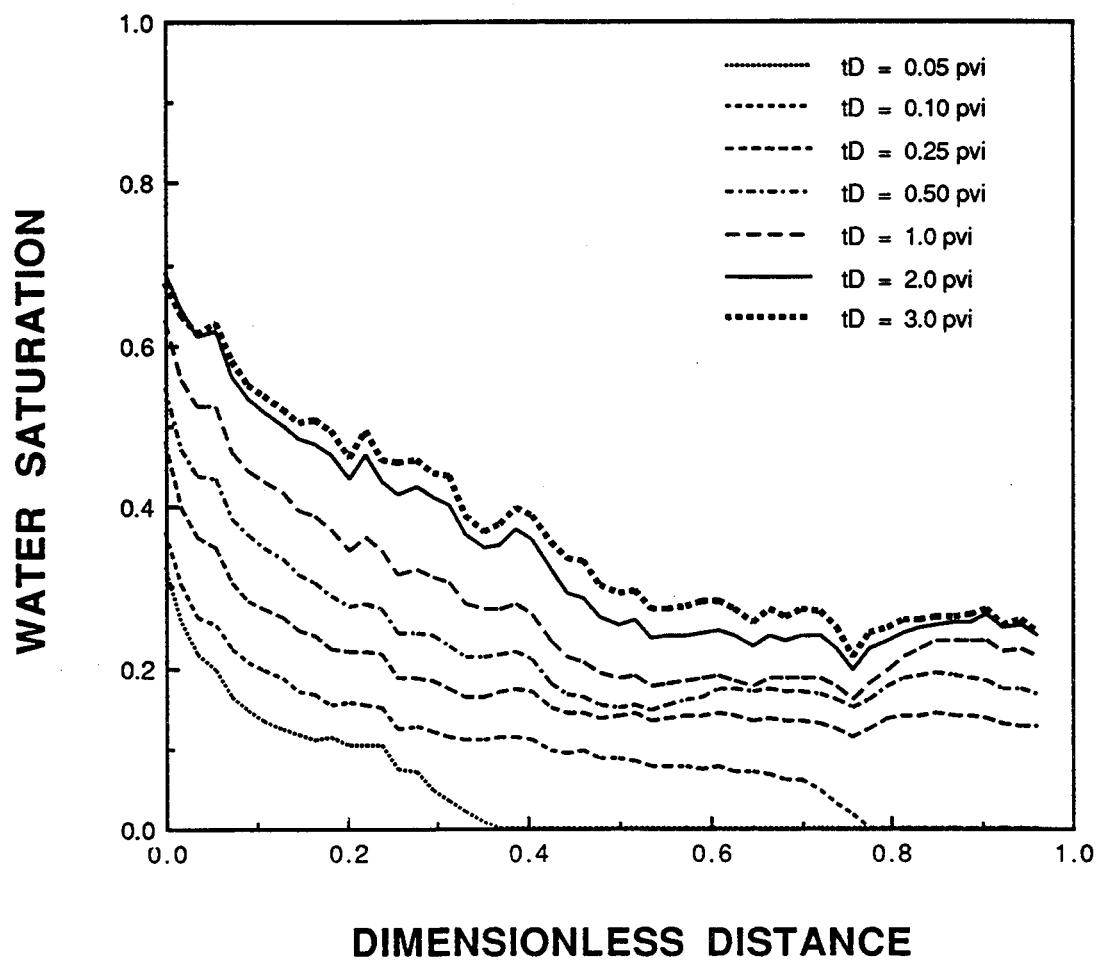
Figure 2.3. Saturation profiles for a typical unstable immiscible displacement in an oil-wet sandpack at a viscosity ratio of 91 (Experiment 2.2).
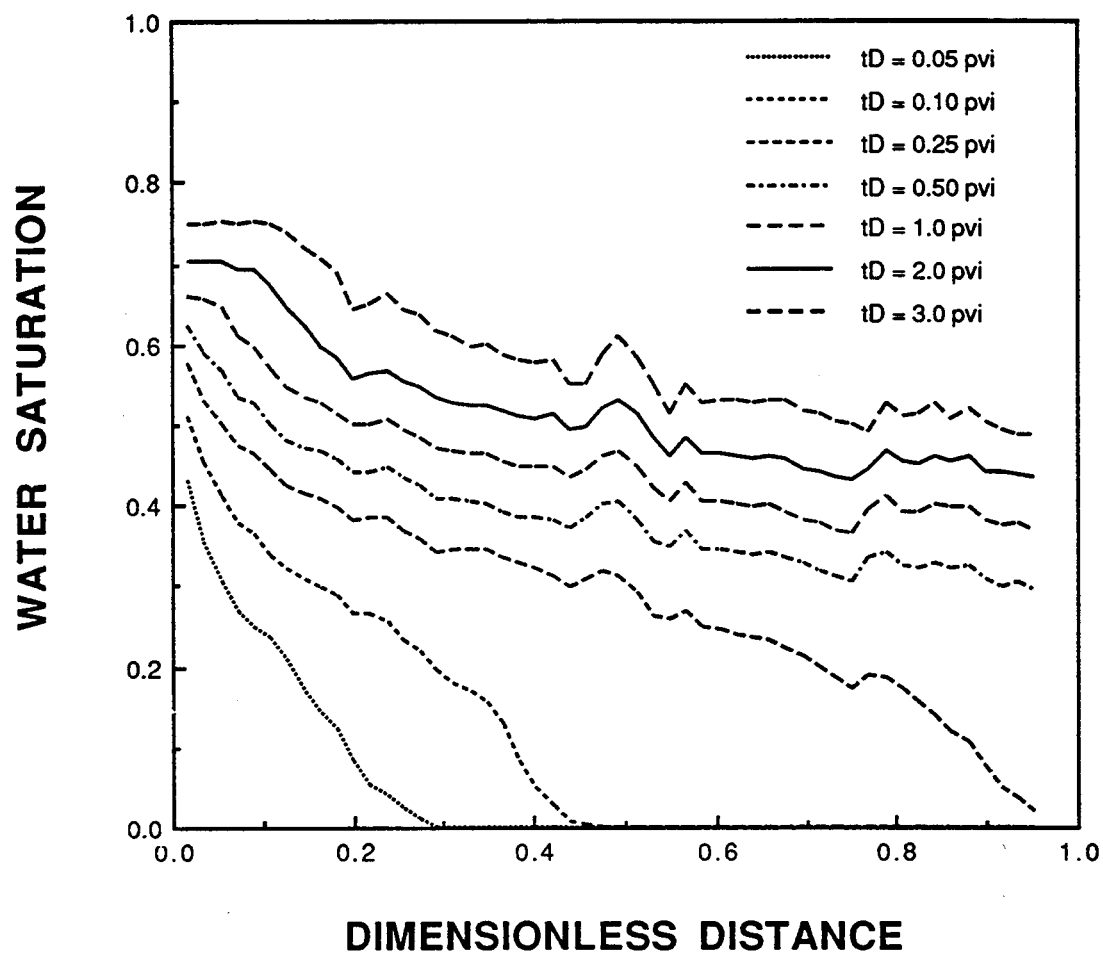
Figure 2.4. Saturation profiles for a typical unstable immiscible
displacement in a water-wet sandpack at a viscosity ratio
of 91 (Experiment 2.3).
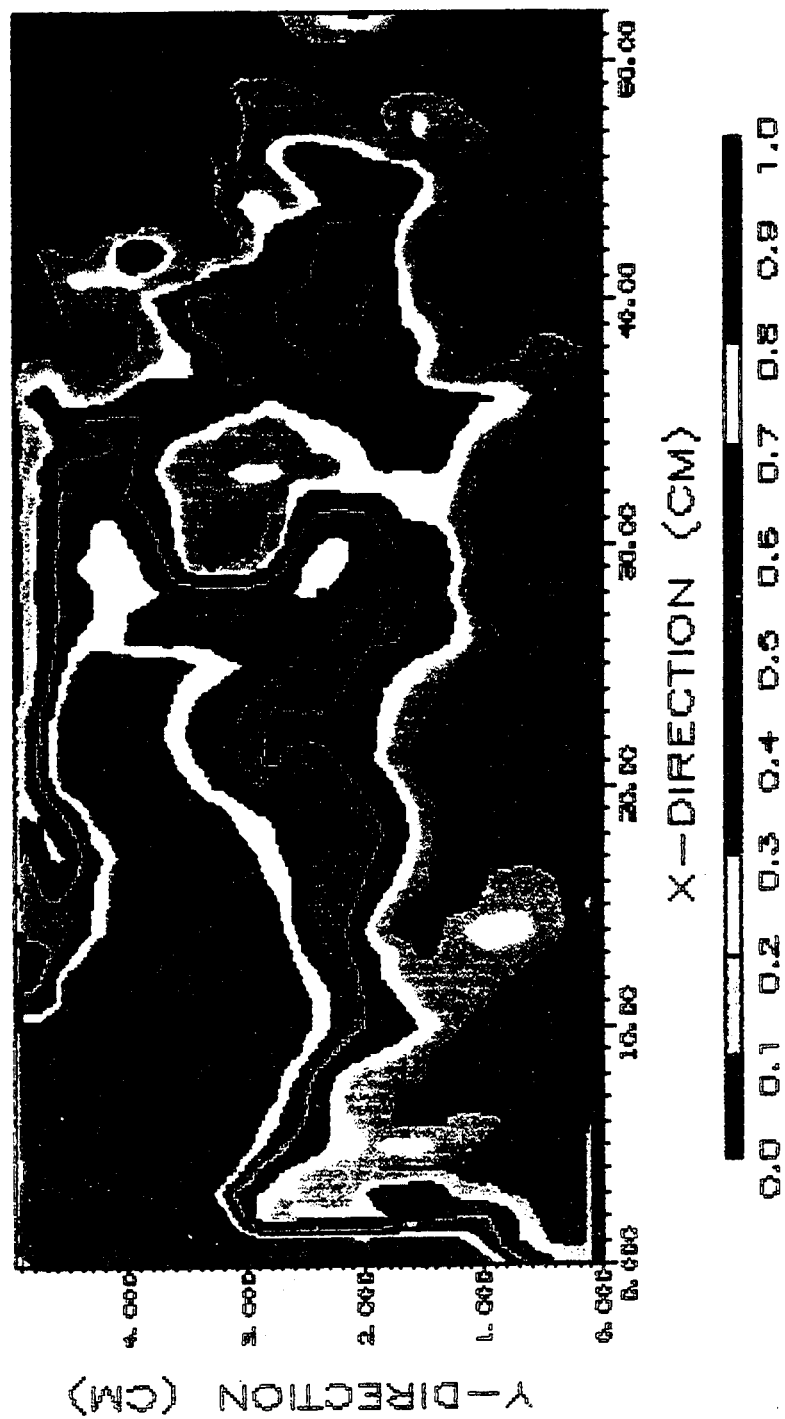
Figure 2.5. Solvent concentration image for a typical unstable first-contact miscible displacement at 0.25 pore volume injected (Experiment 2.1).
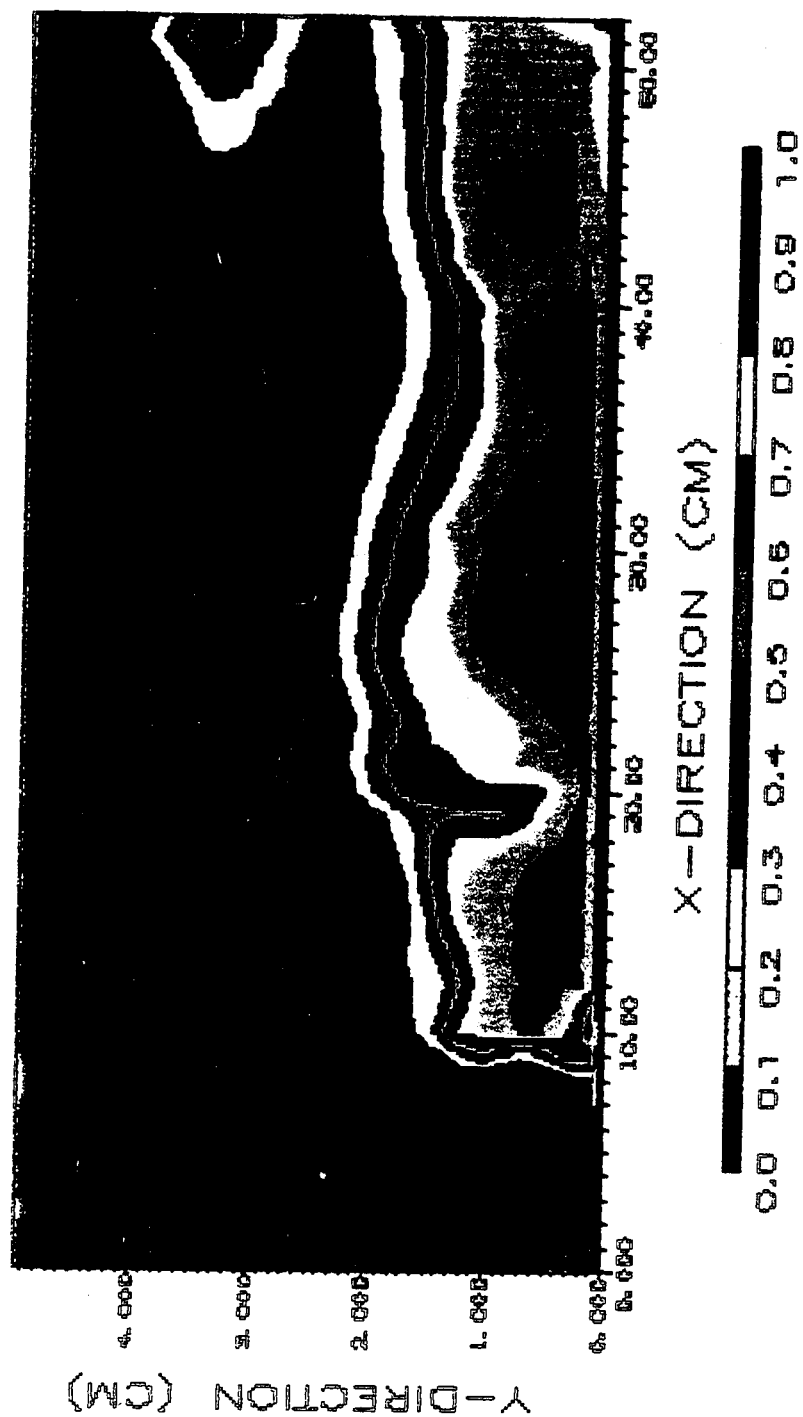
Figure 2.6. Solvent concentration image for a typical unstable first-contact miscible displacement at 2.0 pore volumes injected (Experiment 2.1).
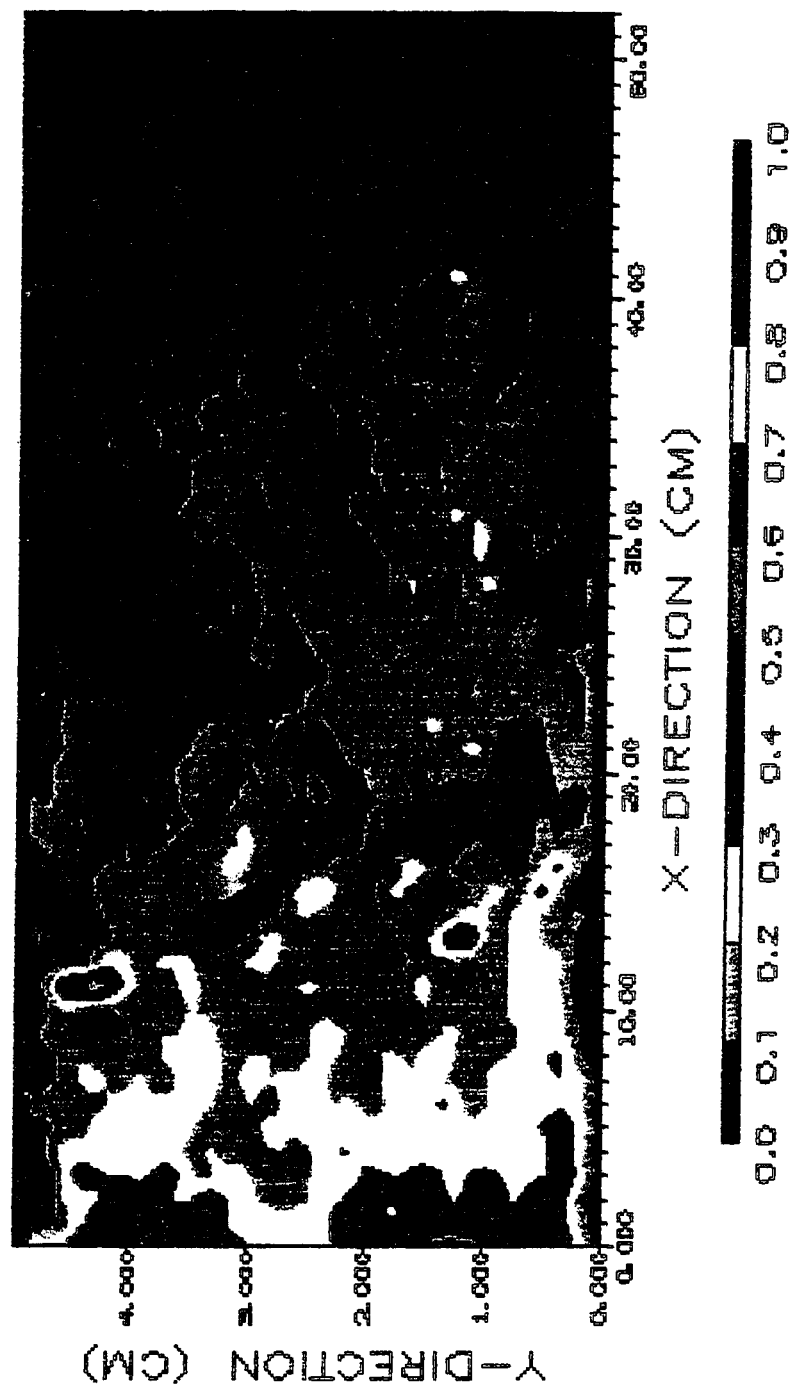
Figure 2.7. Saturation image for a typical unstable immiscible displacement in an oil-wet sandpack at 0.10 pore volume injected (Experiment 2.2).
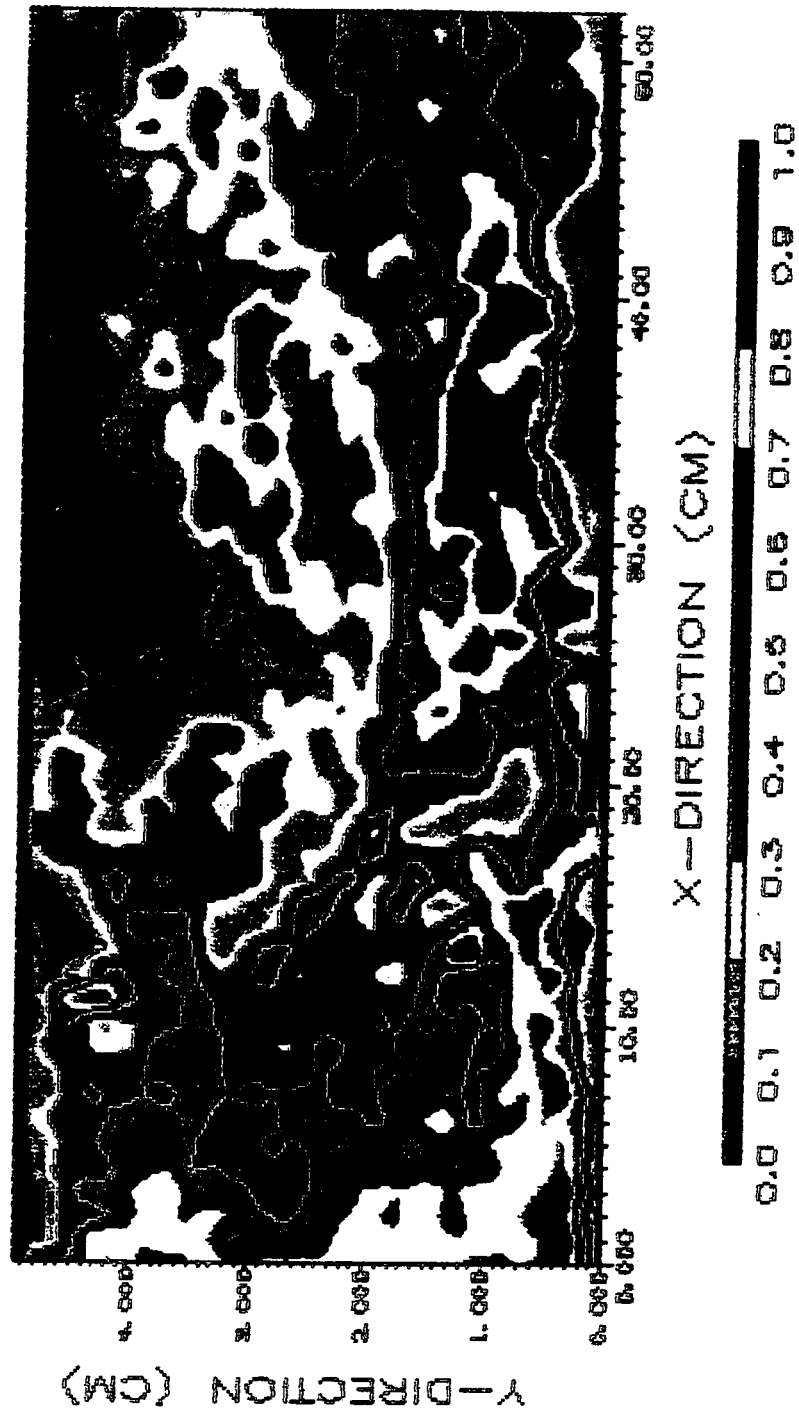
Figure 2.8. Saturation image for a typical unstable immiscible displacement in an oil-wet sandpack at 2.0 pore volumes injected (Experiment 2.2).
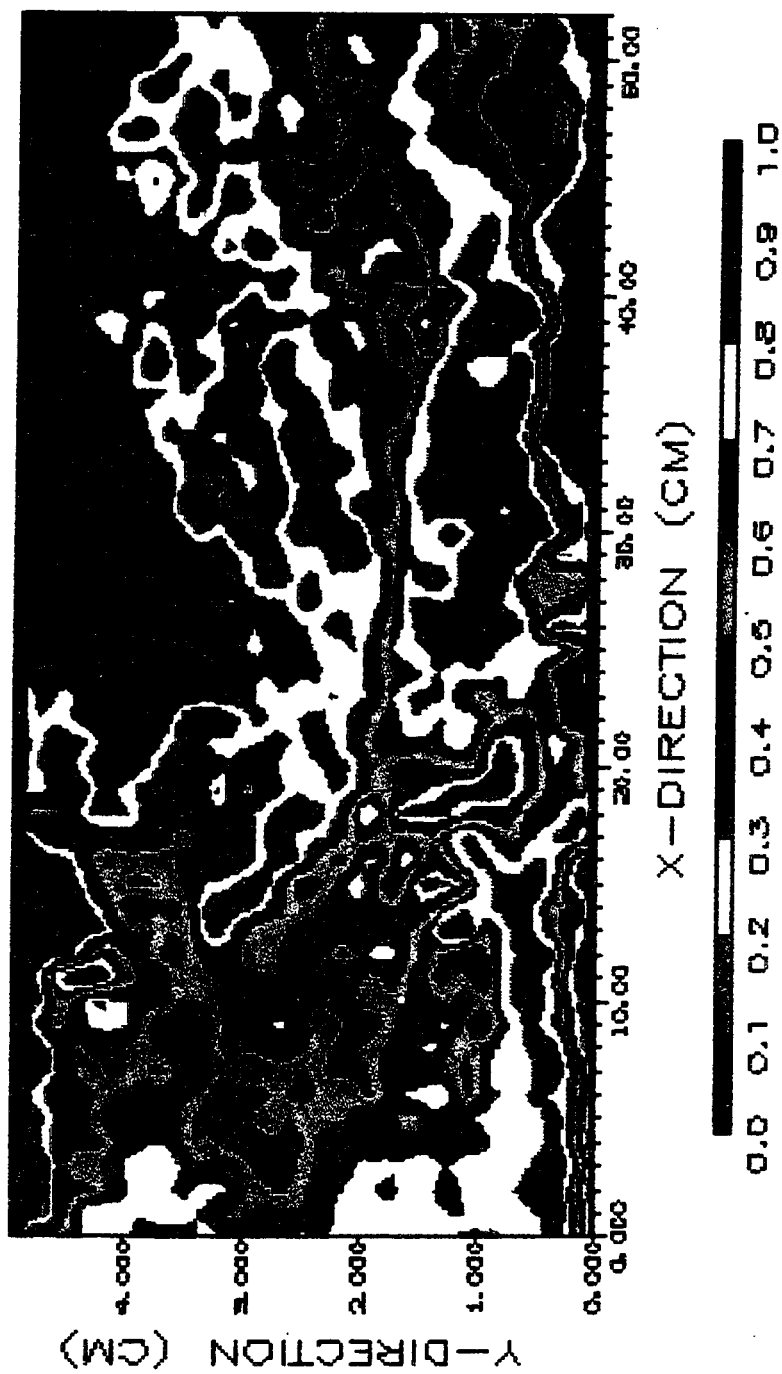
Figure 2.9. Saturation image for a typical unstable immiscible displacement in an oil-wet sandpack at 3.0 pore volumes injected (Experiment 2.2).
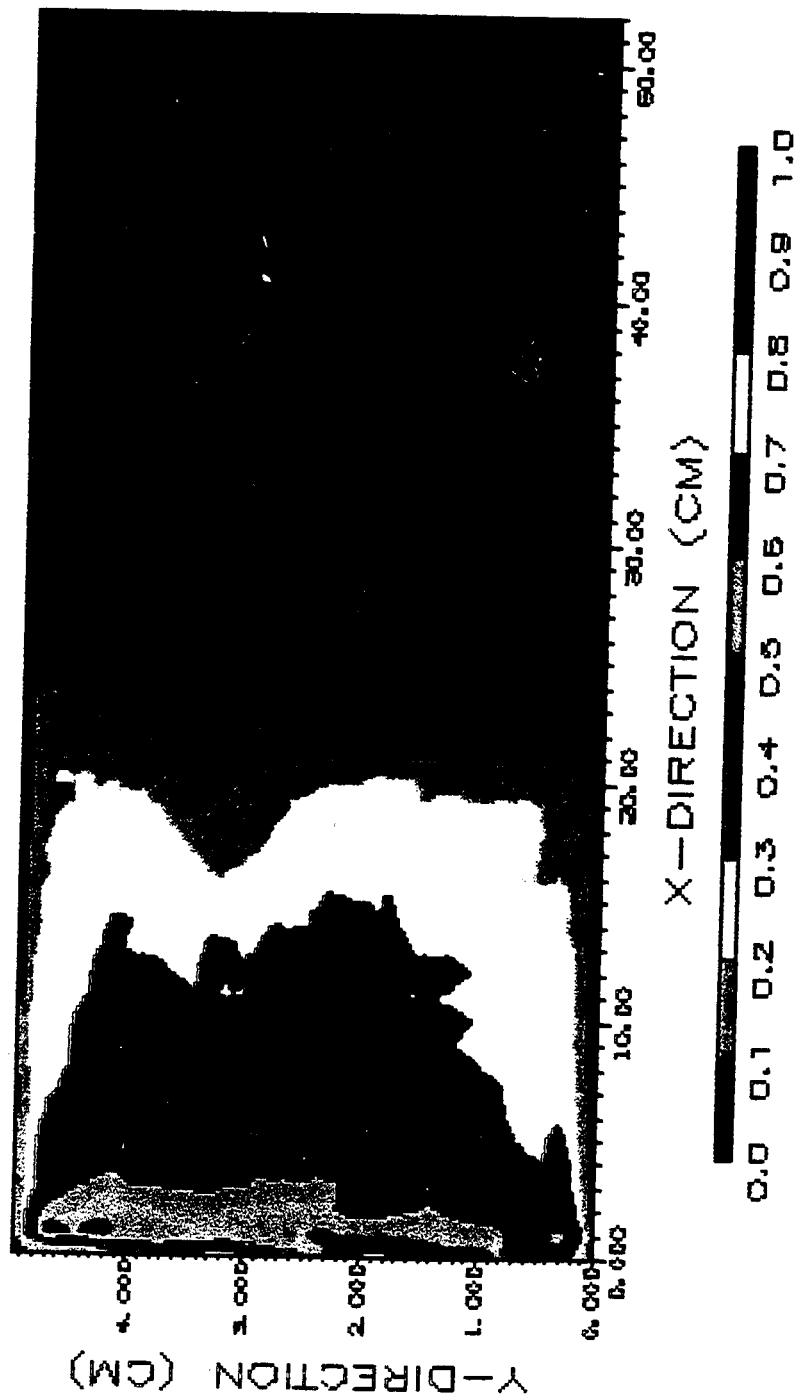
Figure 2.10. Saturation image for a typical unstable immiscible displacement in a water-wet sandpack at 0.10 pore volume injected (Experiment 2.3).
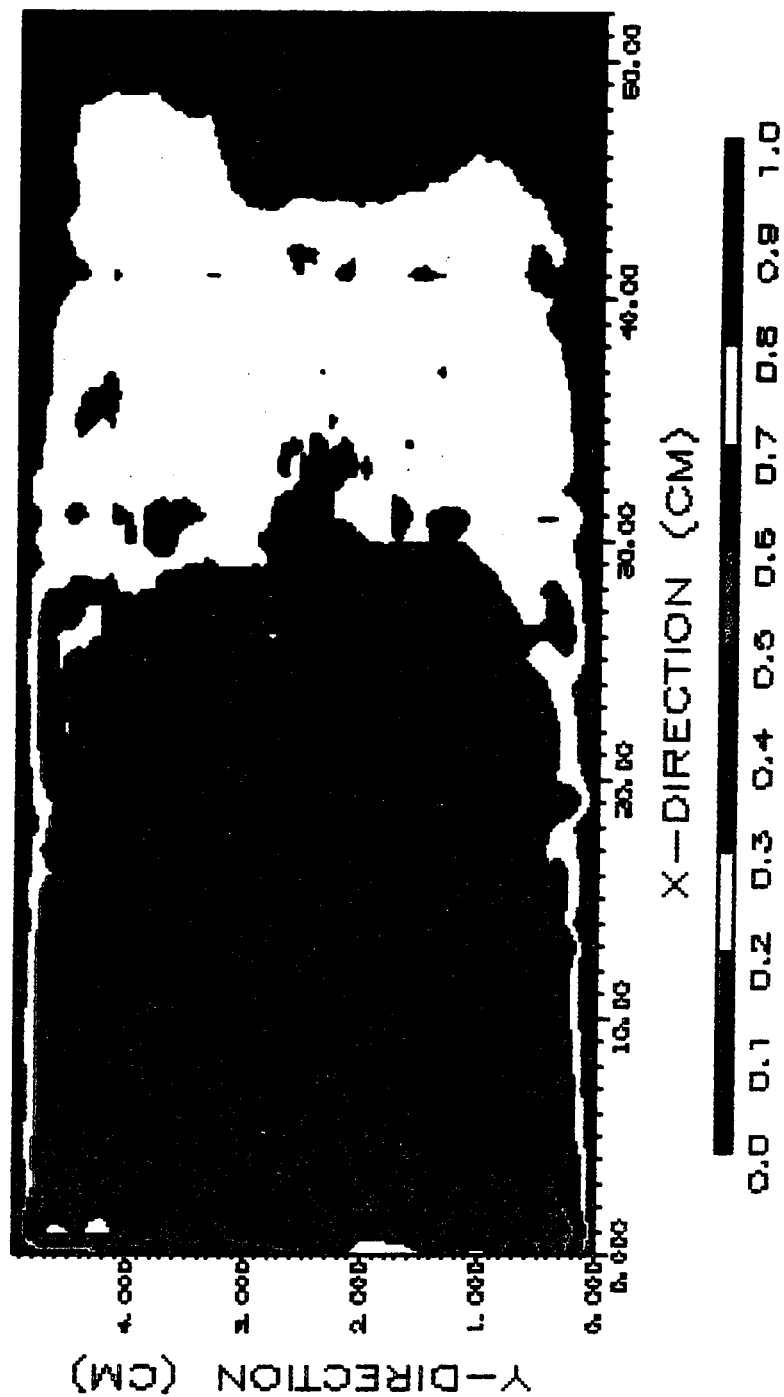
Figure 2.11. Saturation image for a typical unstable immiscible displacement in a water-wet sandpack at 0.25 pore volume injected (Experiment 2.3).

128 pixels

128 pixels

50 slices
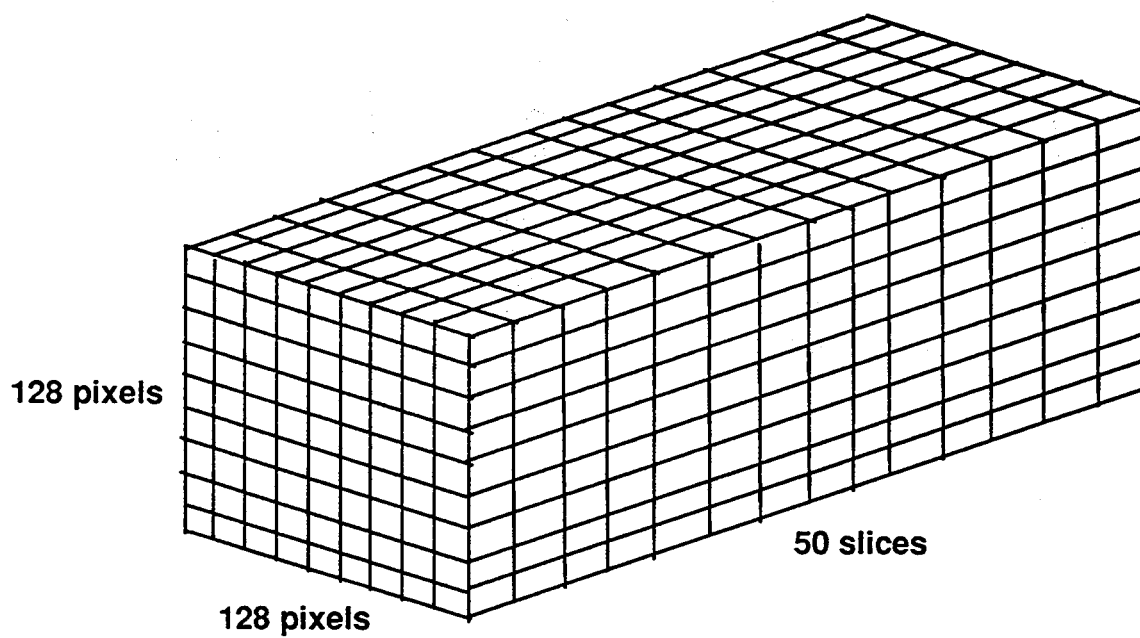
Figure 2.12. Voxels and streamtubes in a laboratory core.
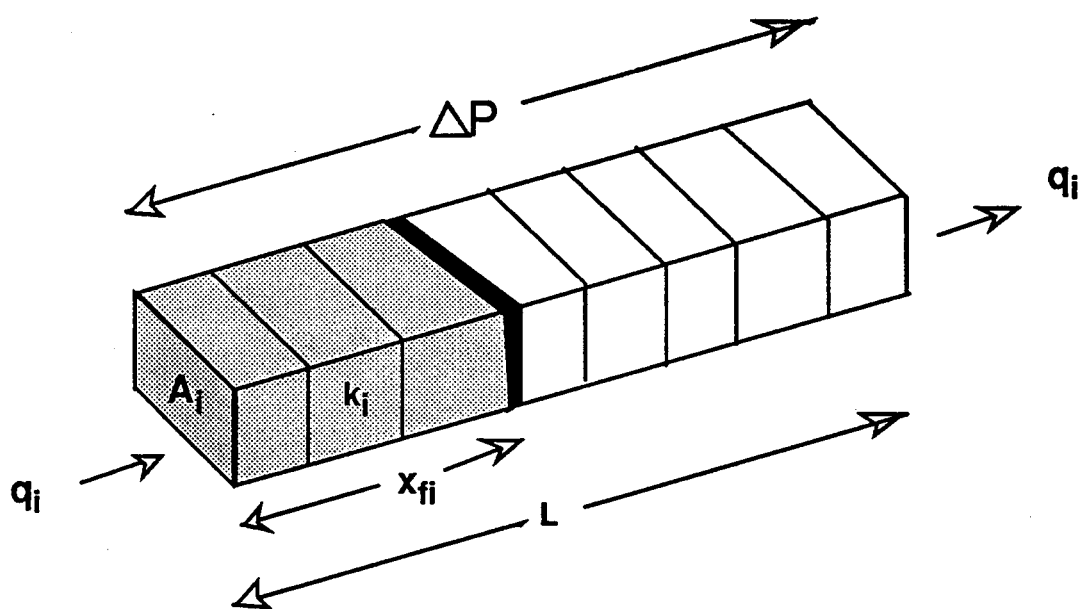
Figure 2.13. Position of flood front in a typical streamtube
before solvent breakthrough.

2300 2320 2340 2360 2380 2400 2420 2440 2460 2480 2500
CT number
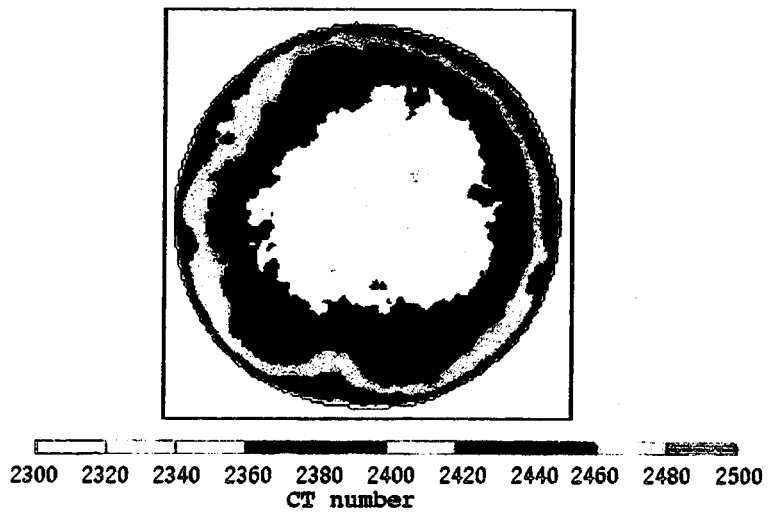
Figure 2.14. CT image of a dry sandpack at a typical cross-section
(Experiment 2.4).

Figure 2.15. CT image of a vertical slice through the center of a dry sandpack (Experiment 2.4).
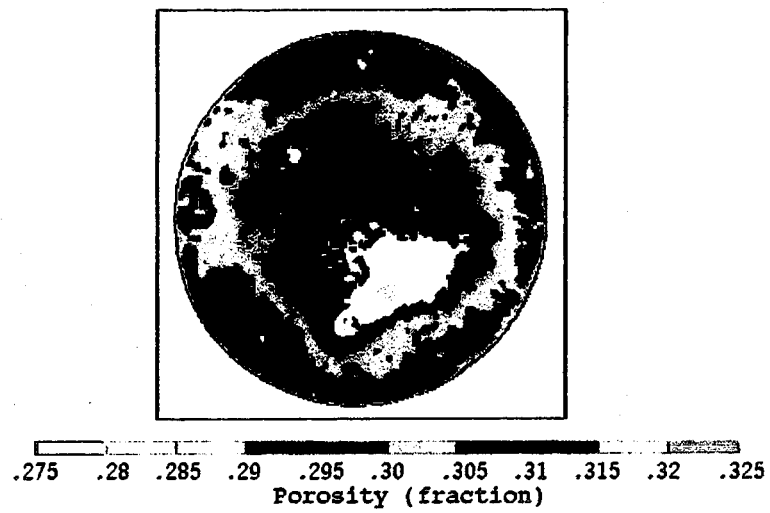
Figure 2.16. Porosity image of a typical cross-section of a sandpack (Experiment 2.4).
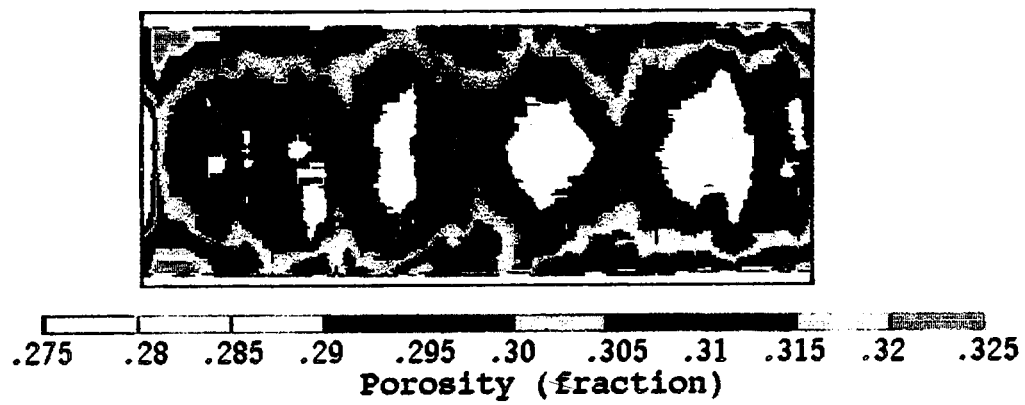
Figure 2.17. Porosity image of a vertical slice through the center of a sandpack (Experiment 2.4).

A

B

0.0   0.1   0.2   0.3   0.4   0.5   0.6   0.7   0.8   0.9   1.0
Saturation
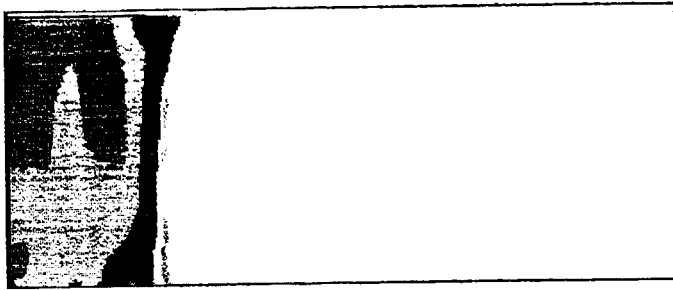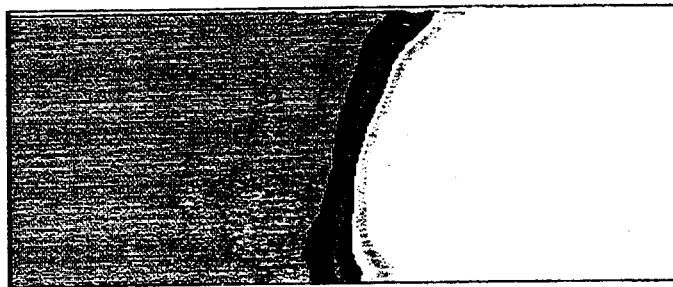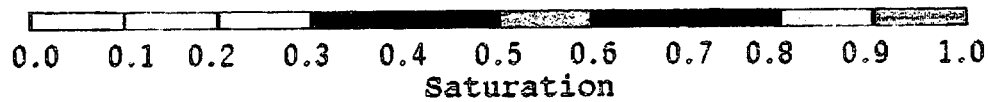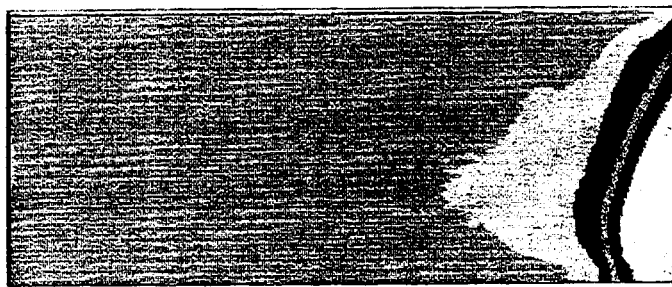
C

Figure 2.18. Solvent concentration images for a tracer test in a sandpack at
(A) 0.2 pore volume injected; (B) 0.5 pore volume injected
and (C) 0.9 pore volume injected (Experiment 2.4).

-112-

3.6 3.9   4.2   4.5   4.8   5.1   5.4   5.7   6.0   6.3   6.6
Permeability (darcy)
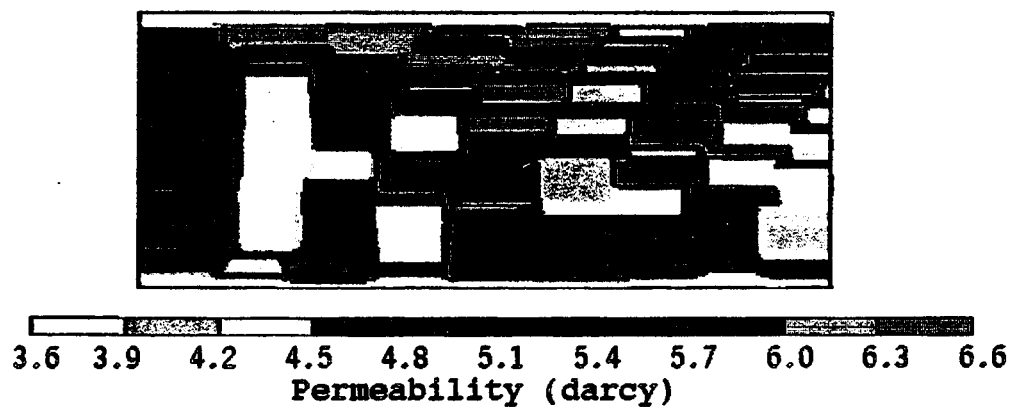
Figure 2.19. Computed permeability image of vertical slice through the center of a sandpack (Experiment 2.4).
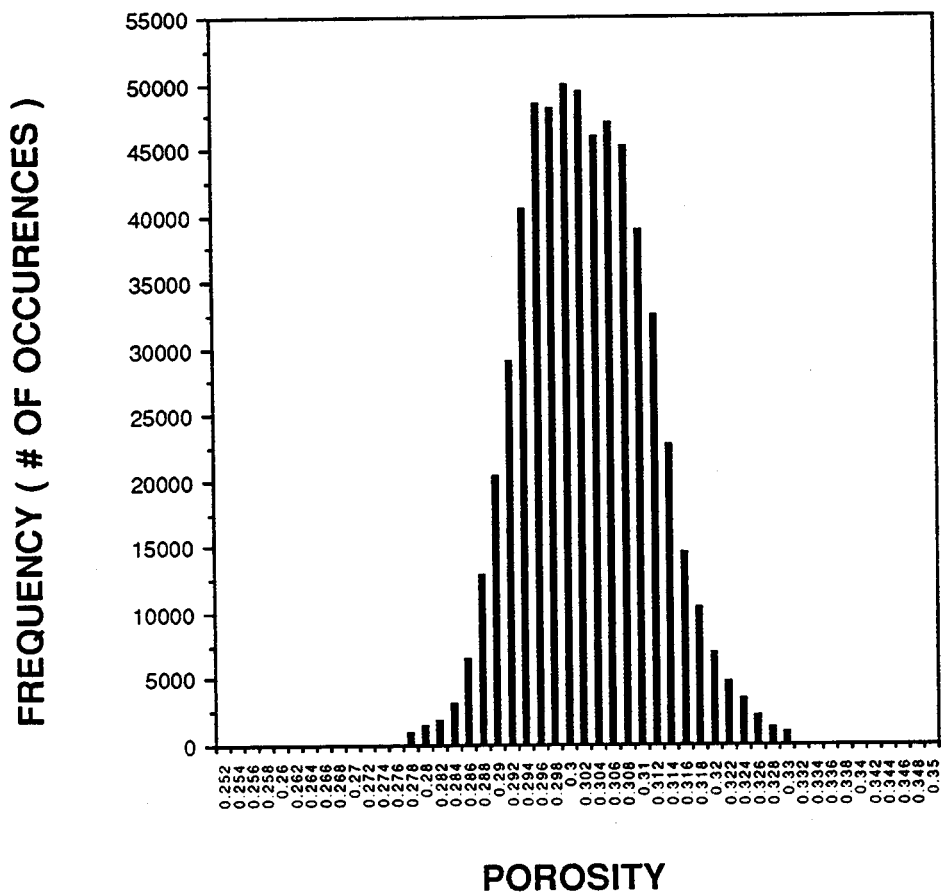
Figure 2.20. Porosity histogram for a sandpack (Experiment 2.4).
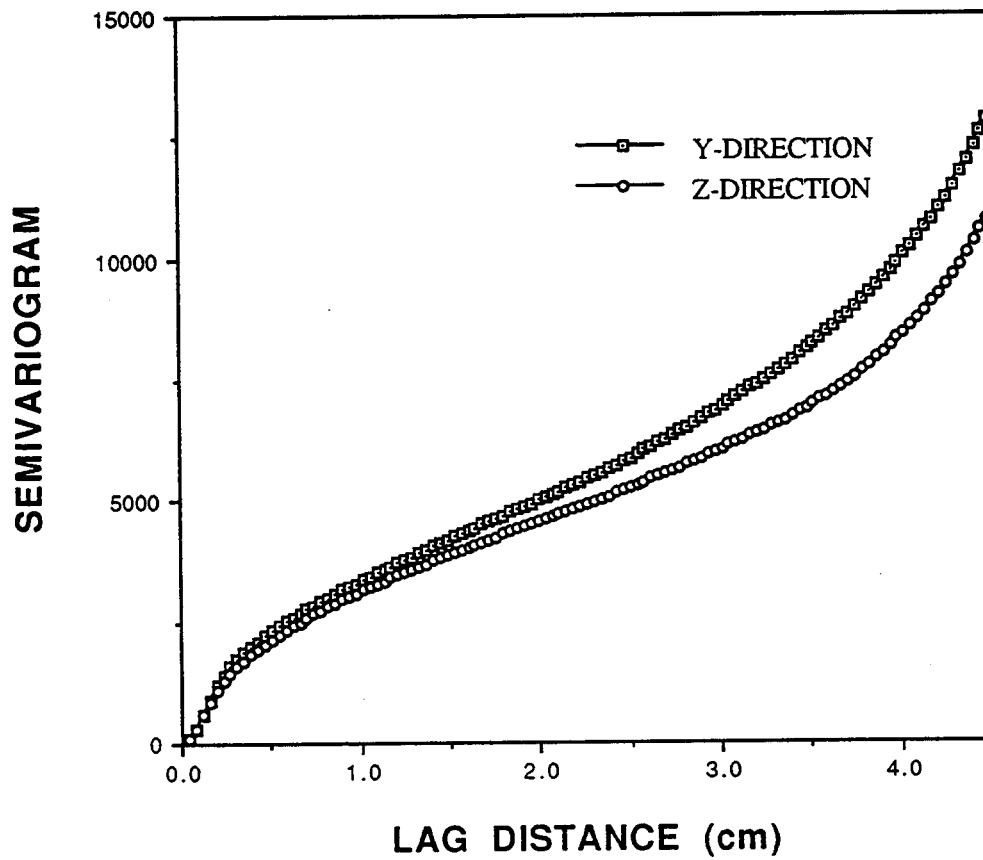
Fig. 2.21. Semivariograms of CT numbers in the transverse directions
of a dry sandpack (Experiment 2.4).
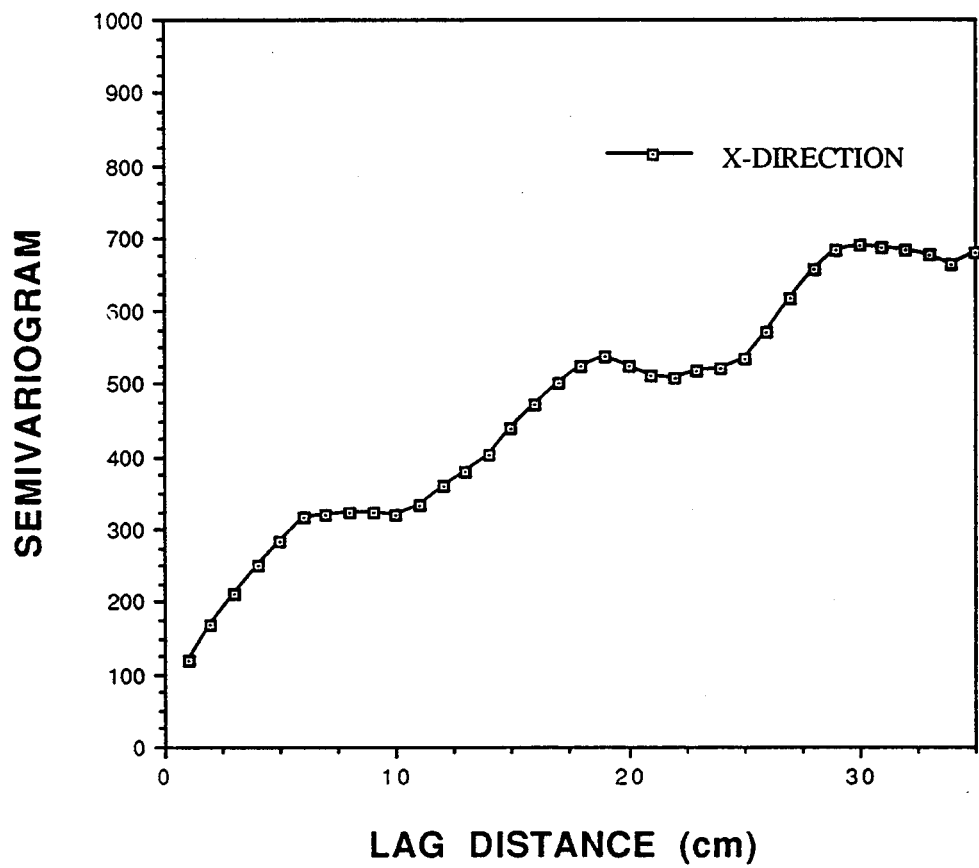
Figure 2.22. Semivariogram of CT numbers in the longitudinal direction of a dry sandpack (Experiment 2.4).
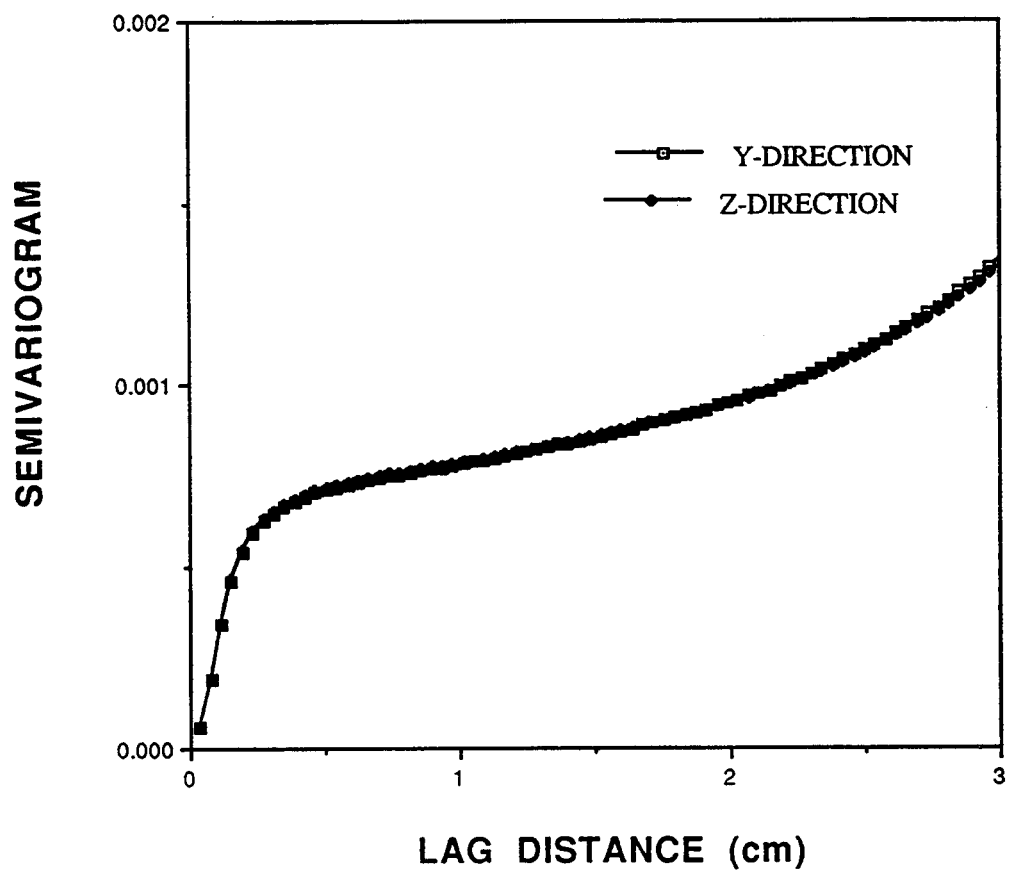
Figure 2.23. Porosity semivariograms in the transverse directions of a sandpack (Experiment 2.4).
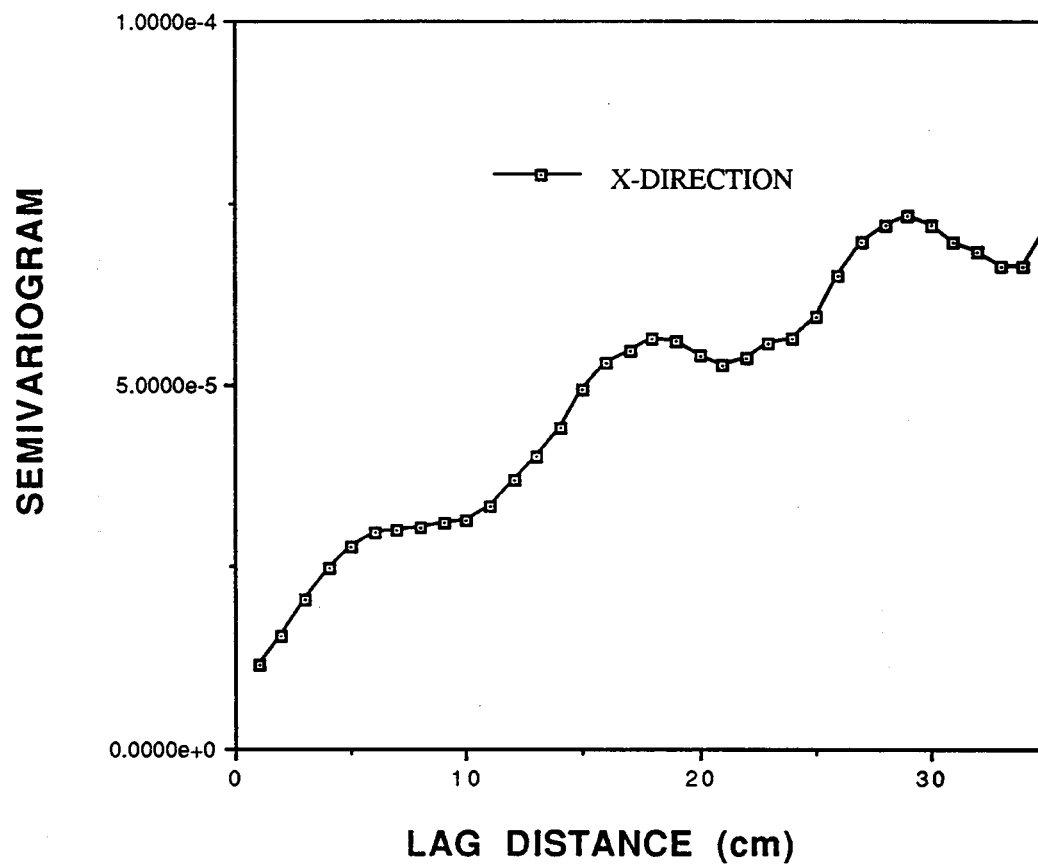
Figure 2.24. Porosity semivariogram in the longitudinal direction
of a sandpack (Experiment 2.4).
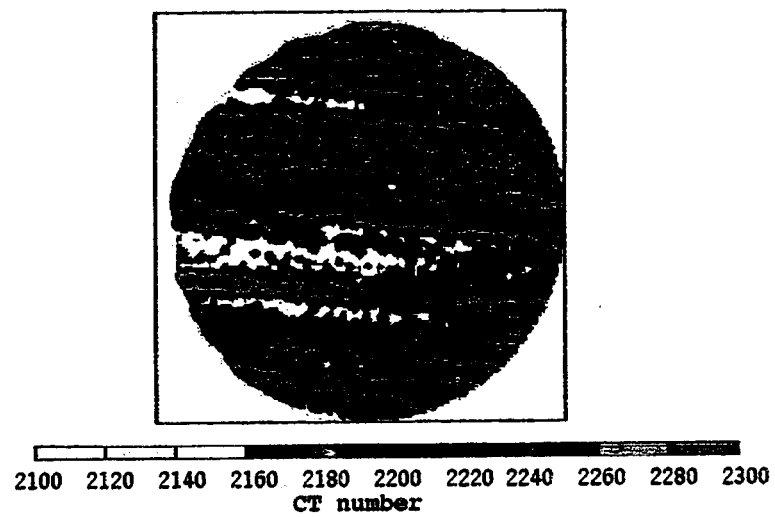
Figure 2.25. CT image of a dry Berea sandstone at a typical cross-section (Experiment 2.5).
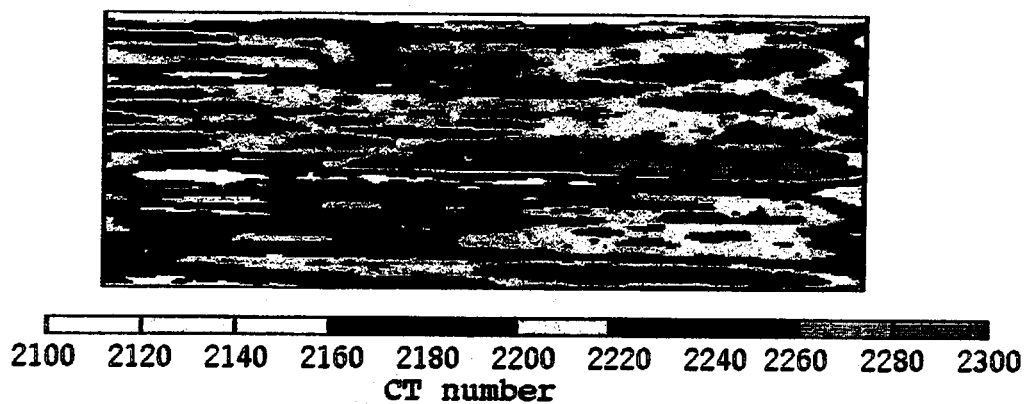
Figure 2.26. CT image of a vertical slice through the center of a dry Berea
sandstone (Experiment 2.5).

.145   .15   .155   .16   .165   .17   .175   .18   .185   .19   .195
                          Porosity (fraction)
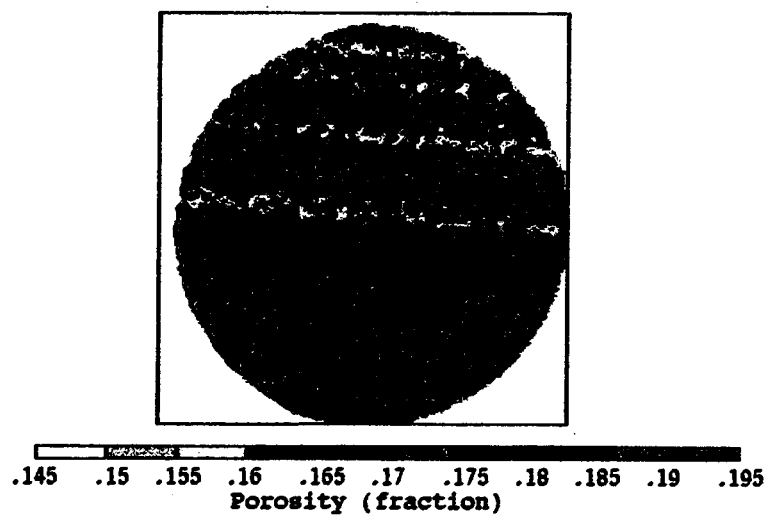
Figure 2.27. Porosity image of a typical cross-section of a Berea sandstone
             (Experiment 2.5).
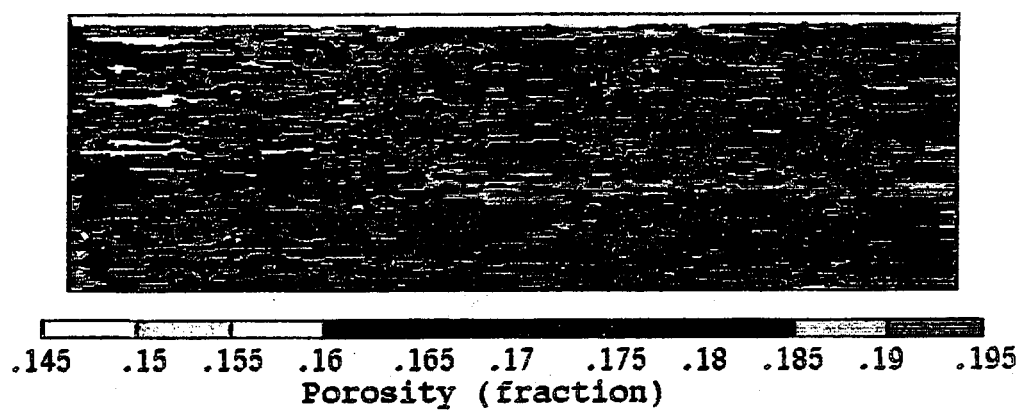
Figure 2.28. Porosity image of a vertical slice through the center of a Berea
sandstone (Experiment 2.5).
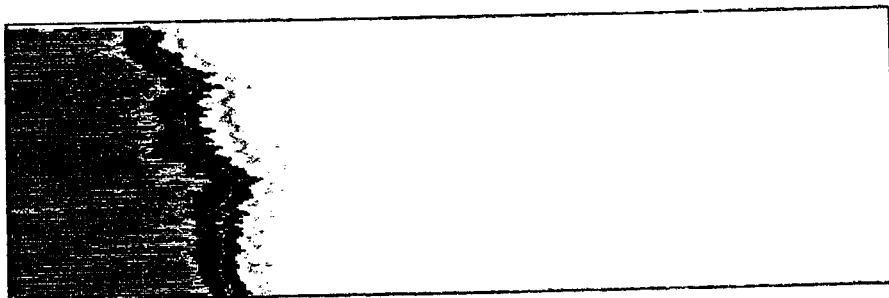
A
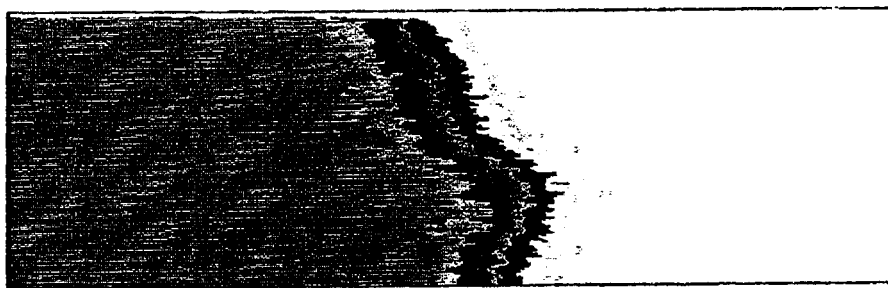
B
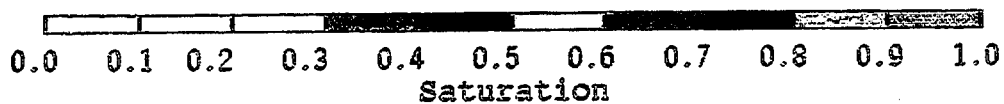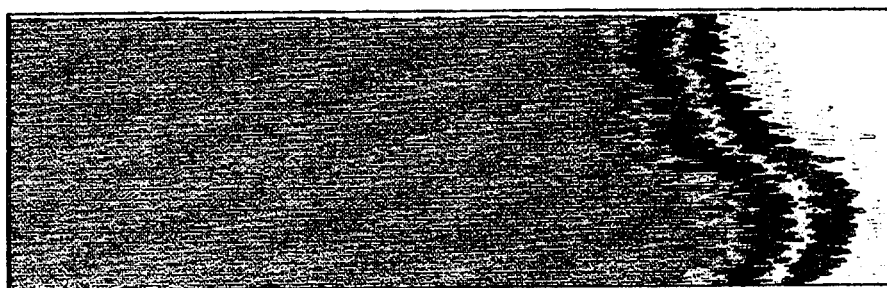
C

Figure 2.29. Solvent concentration images for a tracer test in a Berea
sandstone at (A) 0.2 pore volume injected; (B) 0.5 pore
volume injected and (C) 0.8 pore volume injected
(Experiment 2.5).
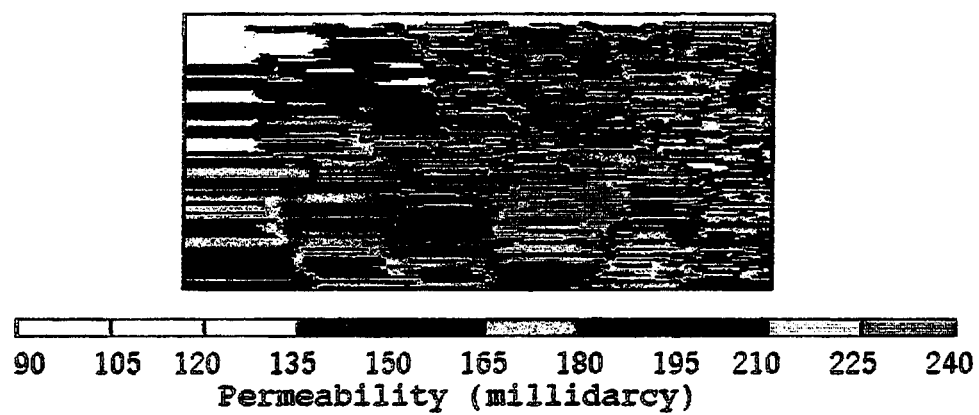
Figure 2.30. Computed permeability image of vertical slice through the center of a Berea sandstone (Experiment 2.5).
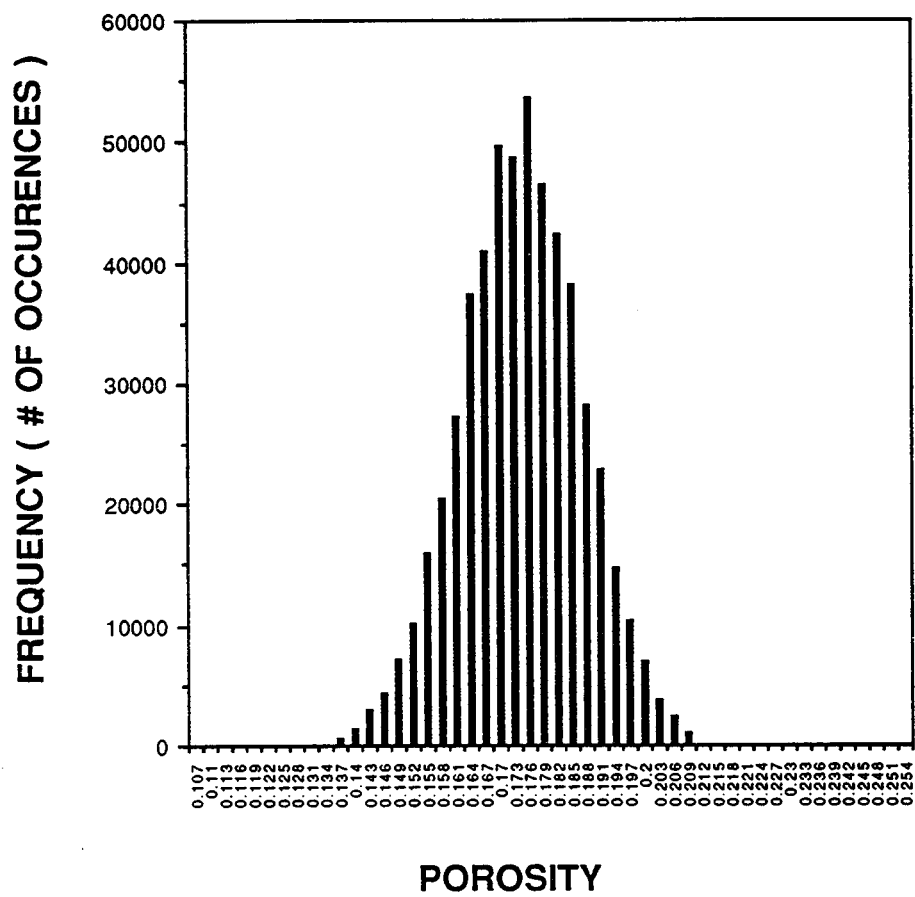
Figure 2.31. Porosity histogram for a Berea sandstone (Experiment 2.5).
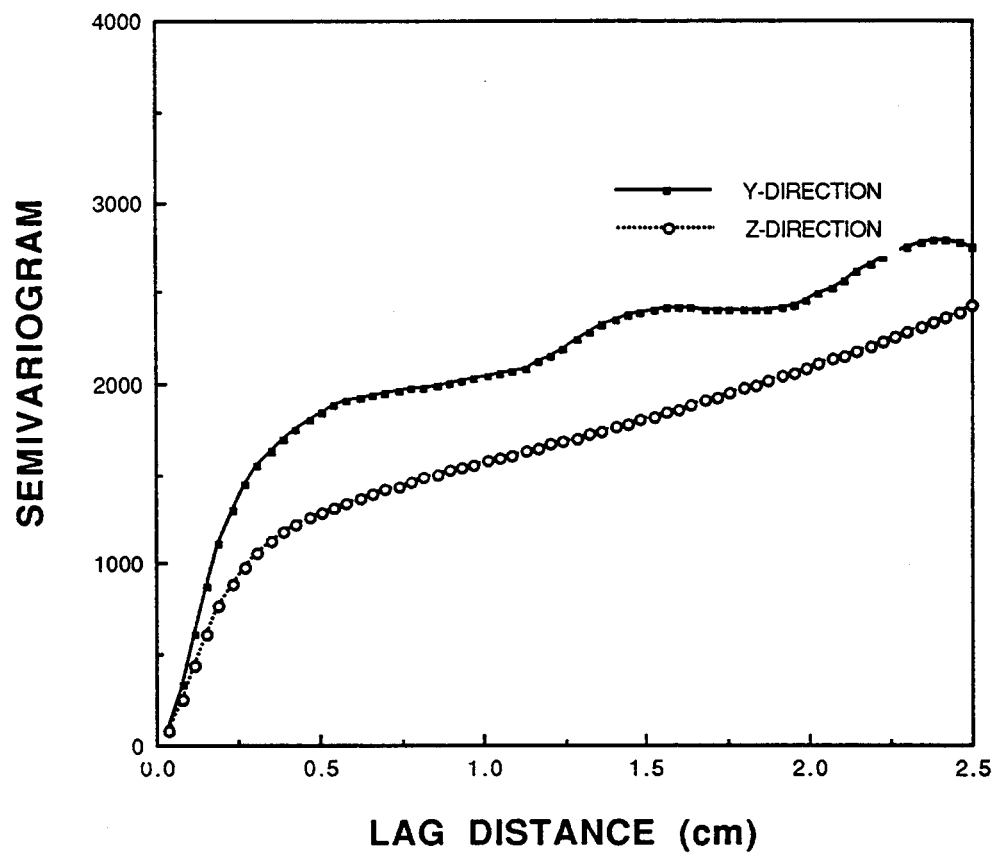
Figure 2.32. Semivariograms of CT numbers in the transverse directions of a dry Berea sandstone (Experiment 2.5).
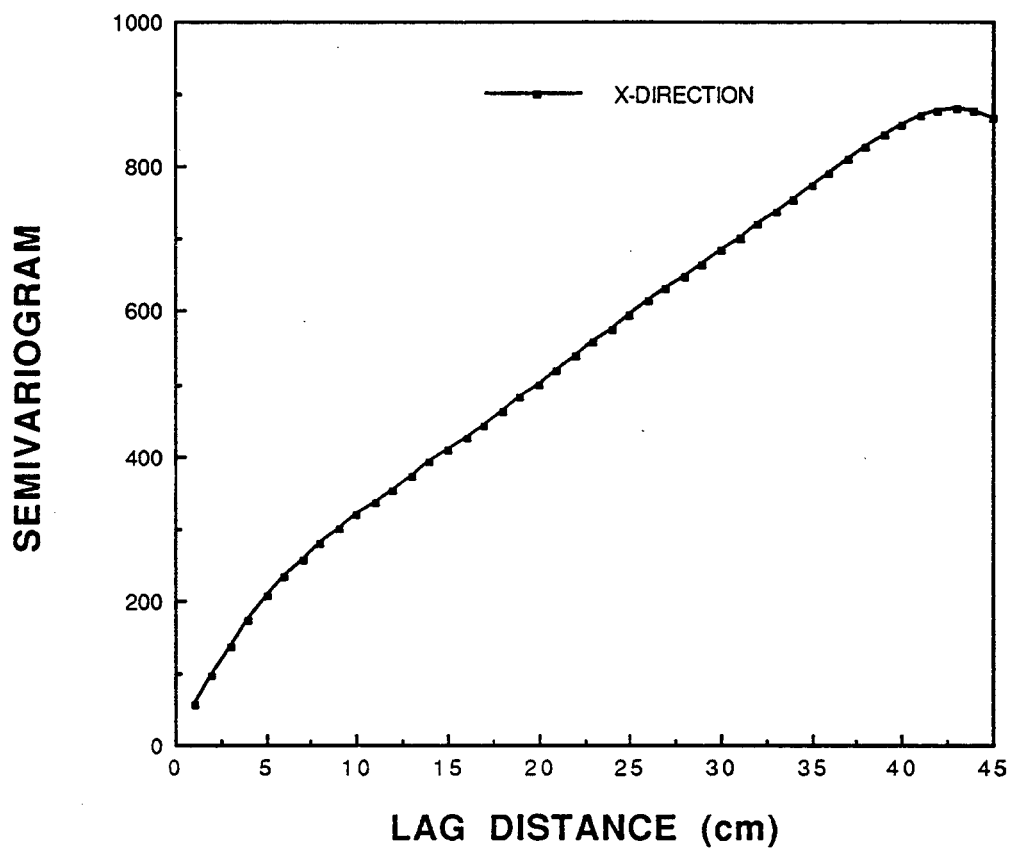
Figure 2.33. Semivariogram of CT numbers in the longitudinal direction
of a dry Berea sandstone (Experiment 2.5).
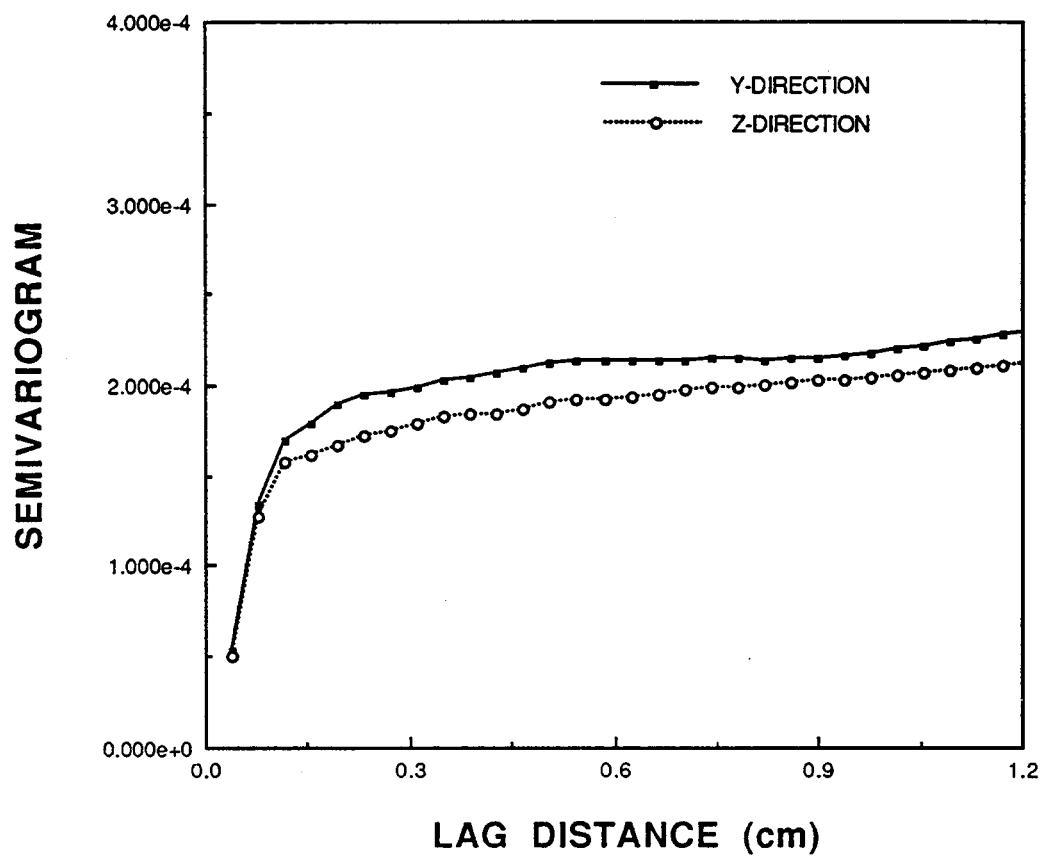
Figure 2.34. Porosity semivariograms in the transverse directions
of a Berea sandstone (Experiment 2.5).
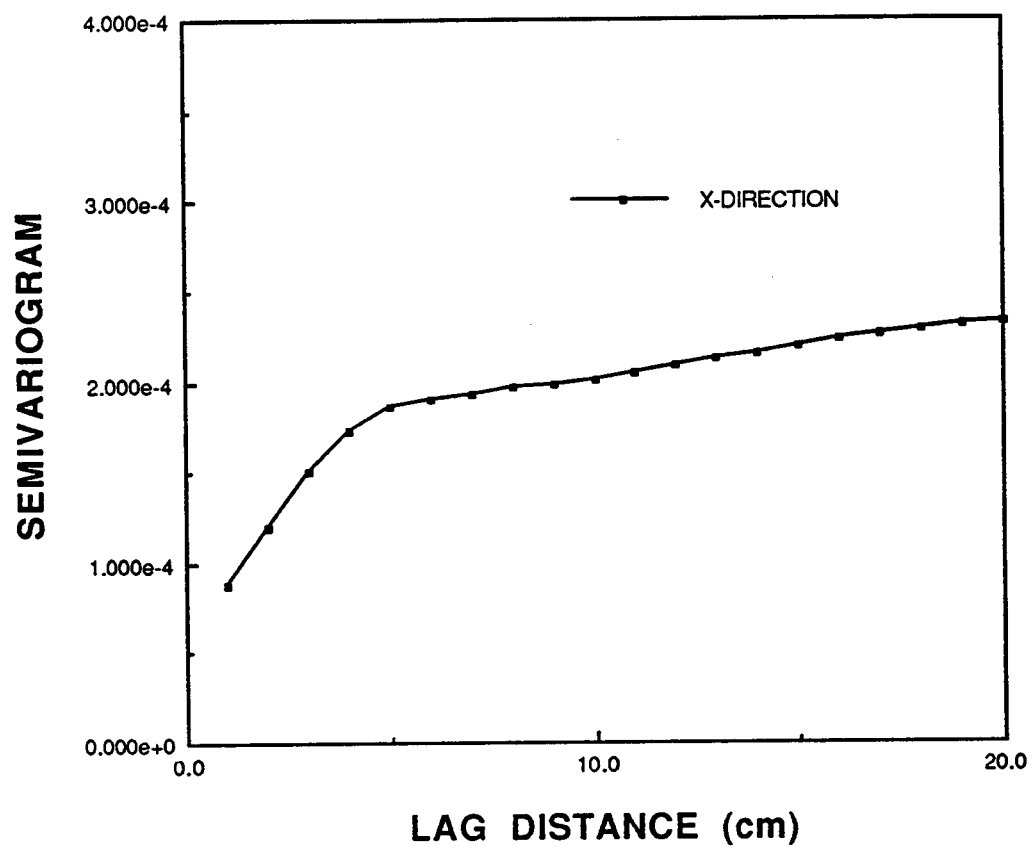
Figure 2.35. Porosity semivariogram in the longitudinal direction of a Berea sandstone (Experiment 2.5).
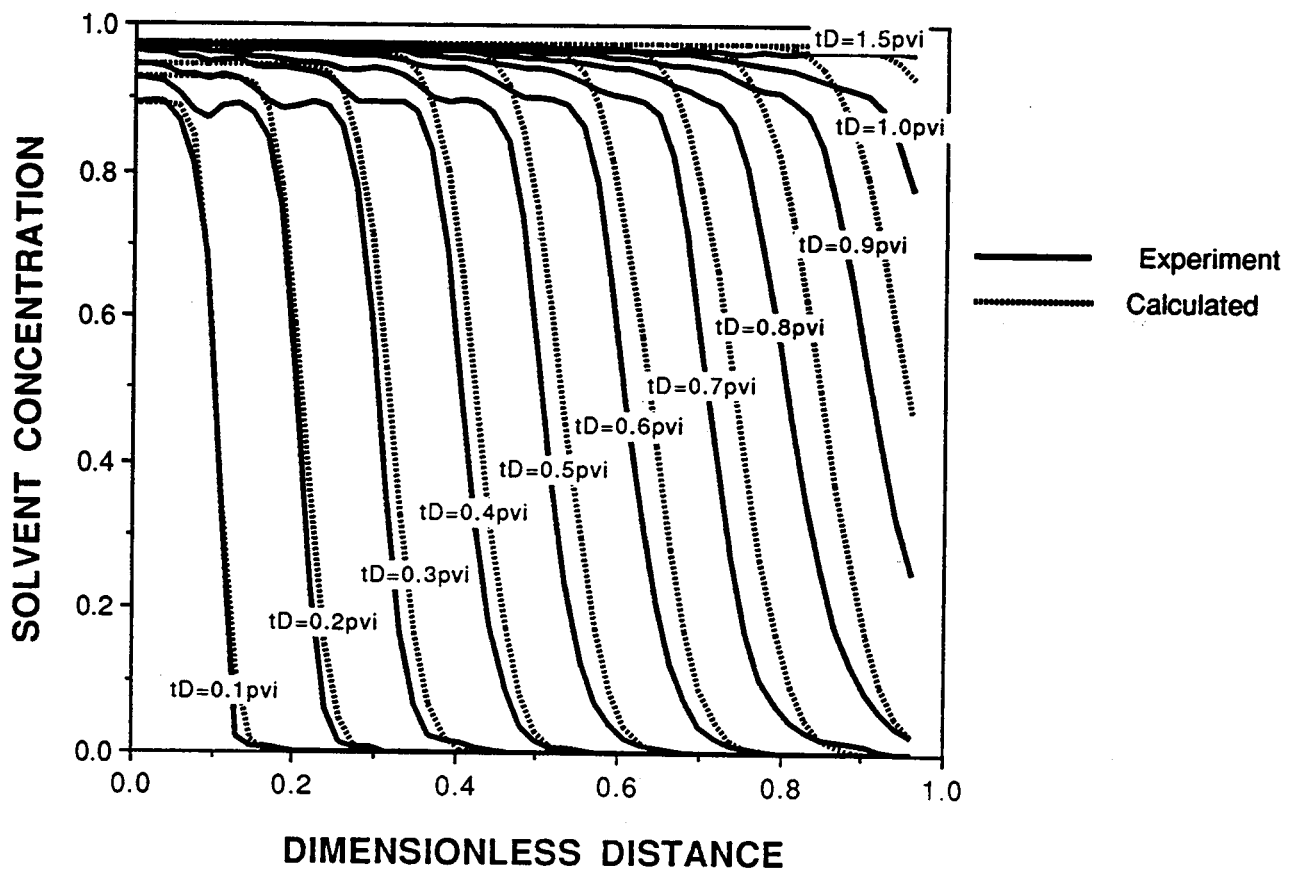
Figure 2.36. Experimental versus computed solvent concentration profiles for tracer test in a sandpack. $D_L = 100 \times 10^{-5}$ cm^2/s, $R_f = 1.00$ (Experiment 2.4).
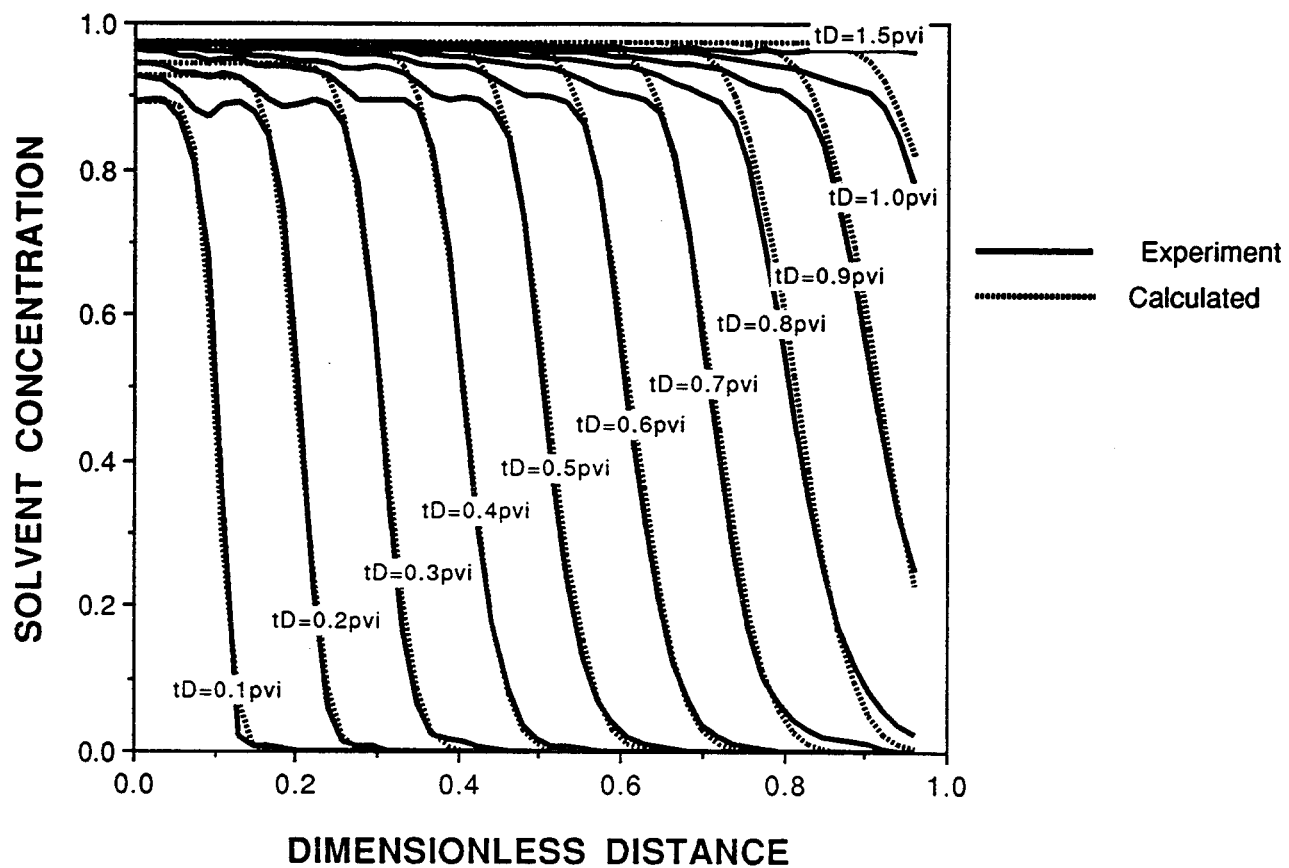
Figure 2.37. Experimental versus computed solvent concentration profiles for tracer test in a sandpack. $D_L = 100 \times 10^{-5}$ cm^2/s, $R_f = 1.04$ (Experiment 2.4).
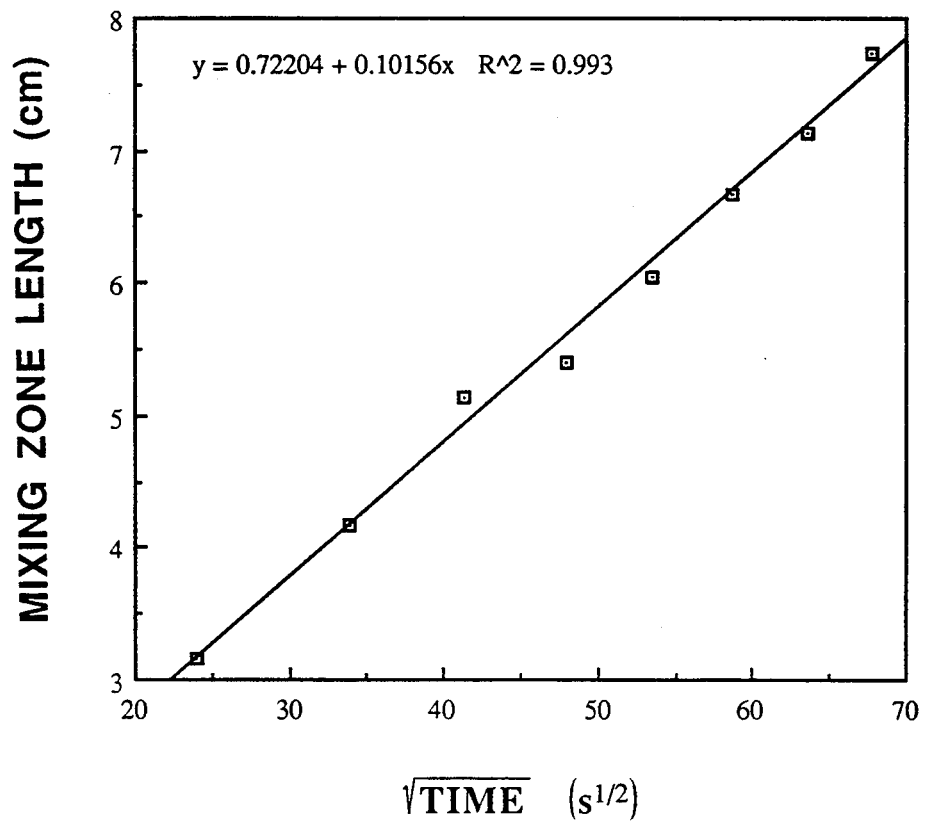
Figure 2.38. Growth of mixing zone length with time for a tracer test in a sandpack (Experiment 2.4).
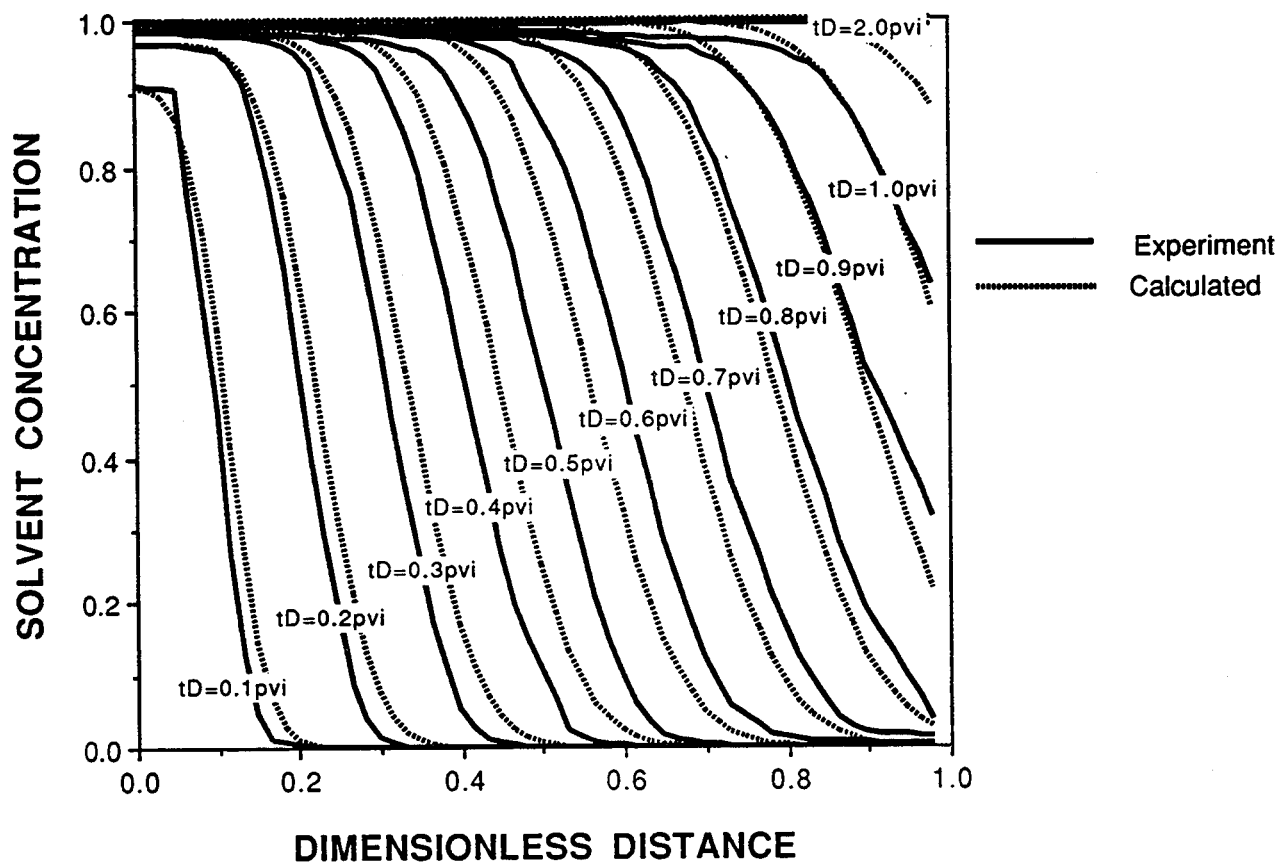
Figure 2.39. Experimental versus computed solvent concentration profiles for tracer test in a Berea sandstone. $D_L = 600 \times 10^{-5}$ cm^2/s, R_f = 1.00 (Experiment 2.5).
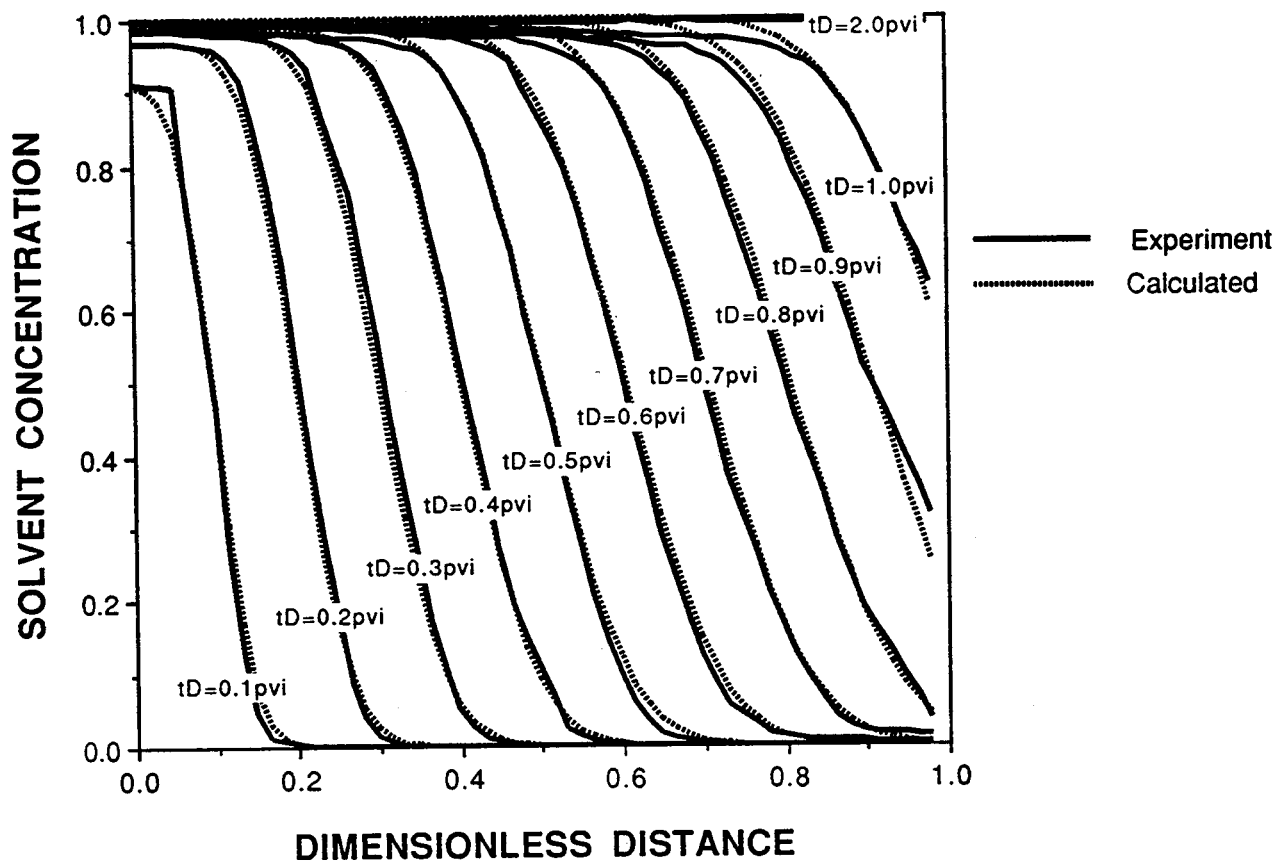
Figure 2.40. Experimental versus computed solvent concentration profiles for tracer test in a Berea sandstone. $D_L = 600 \times 10^{-5}$ cm^2/s, R_f = 1.11 (Experiment 2.5).
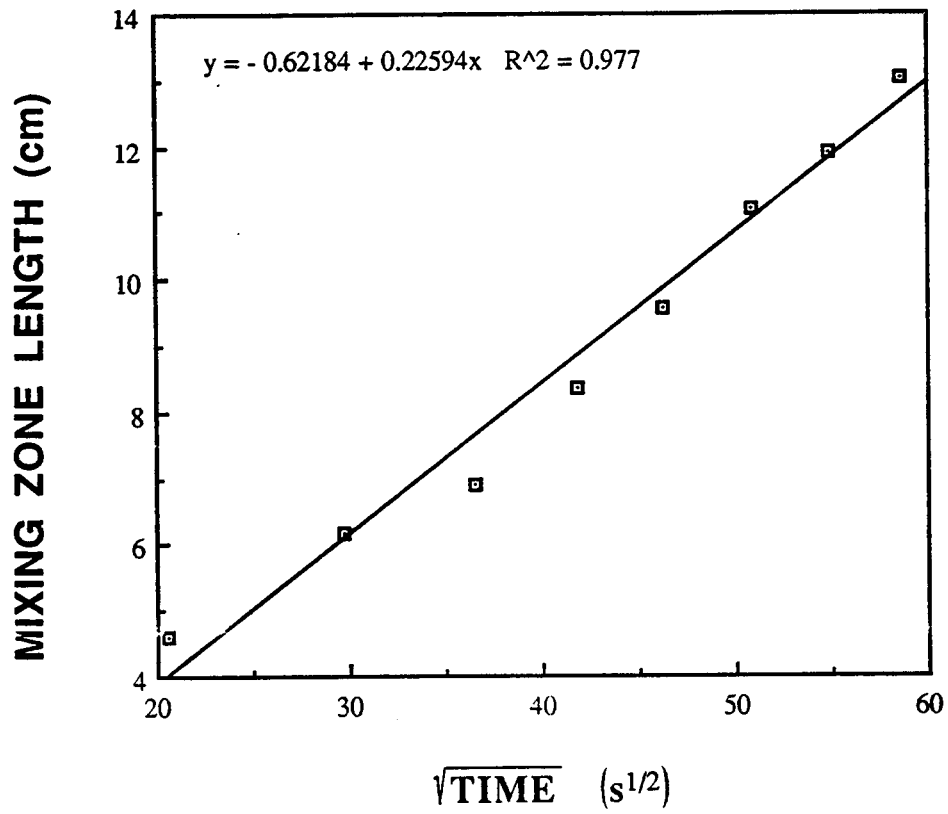
Figure 2.41. Growth of mixing zone length with time for a tracer test in a Berea sandstone (Experiment 2.5).
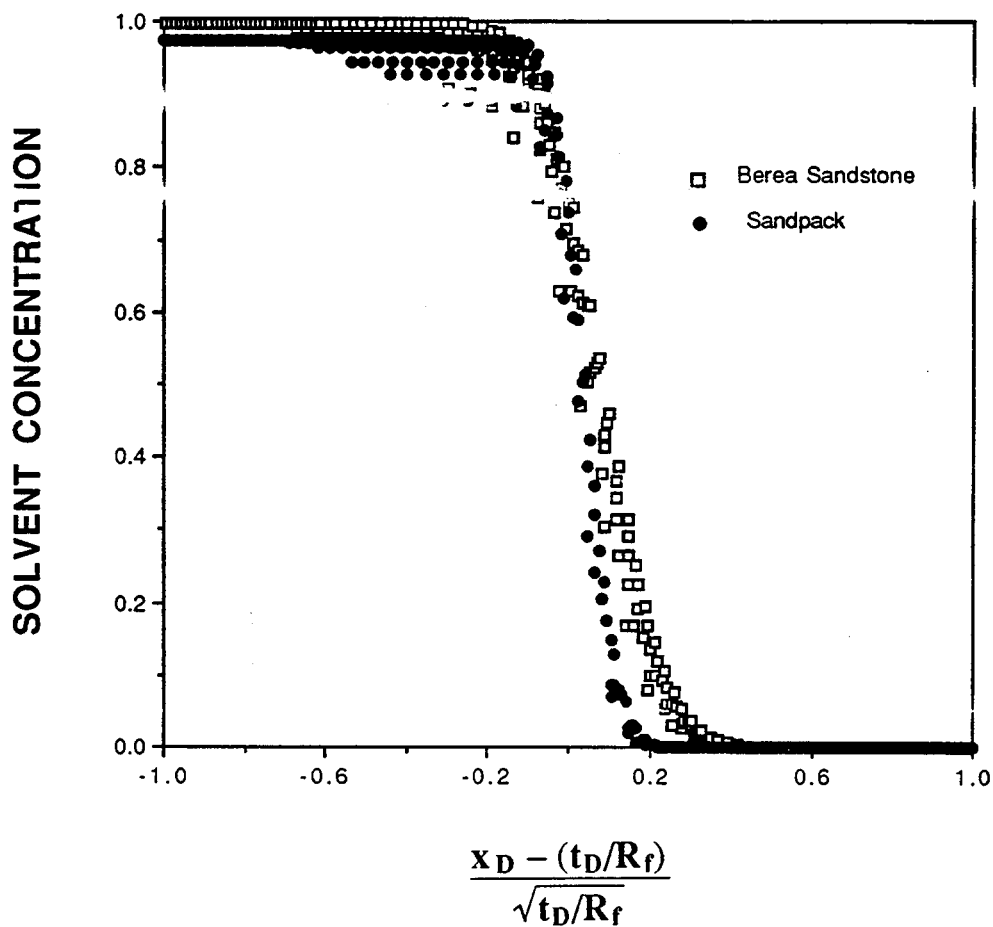
Figure 2.42. Similarity transformation of solvent concentration profiles for
tracer tests in a sandpack and a Berea sandstone (Experiments
2.4 and 2.5).

Viscosity   Ratio

100   50

320

Expt 3.1   Expt 3.4

Injection   Rate   (cc/hour)

200

Expt 3.2   Expt 3.5

100

Expt 3.3   Expt 3.6
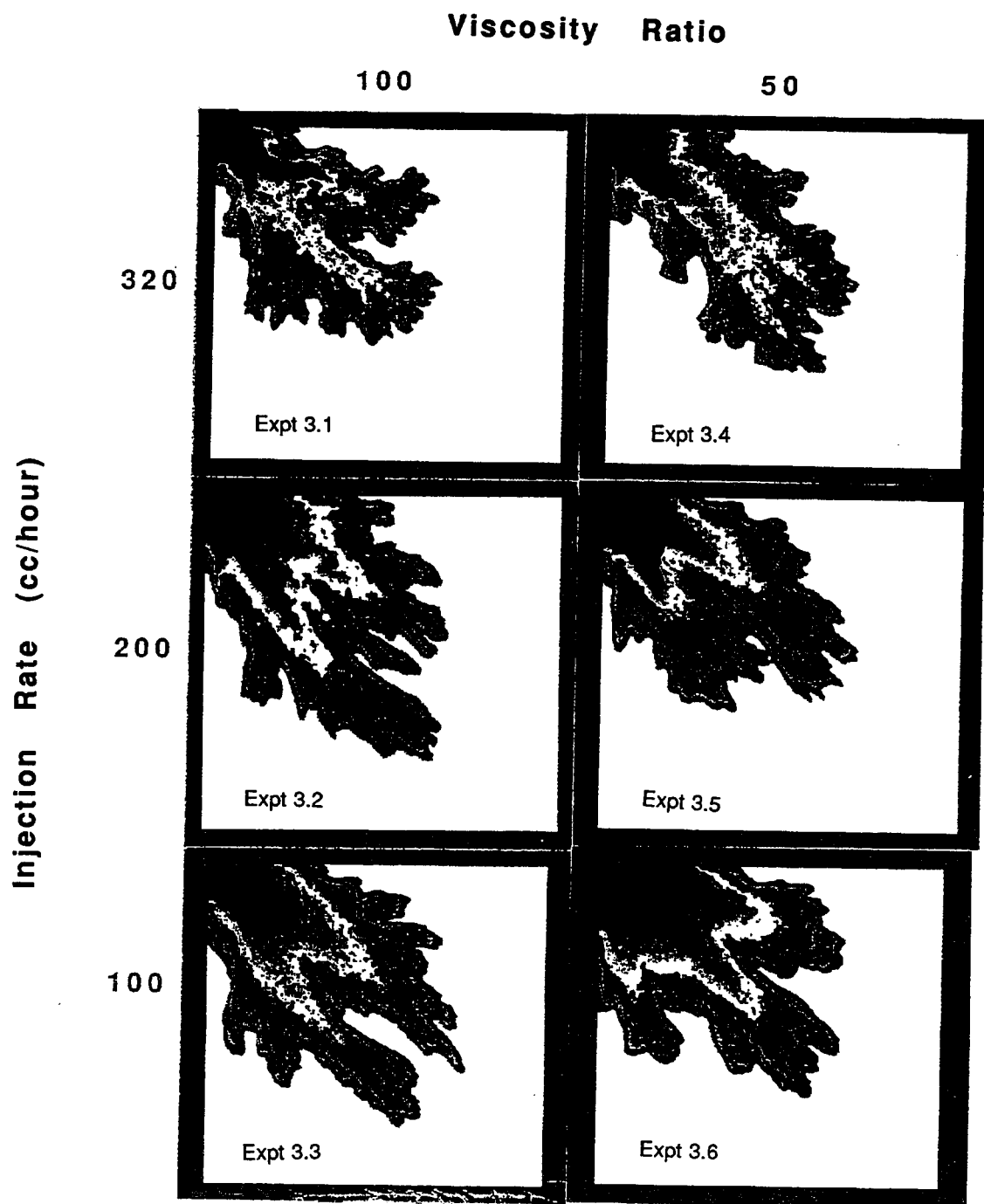
Figure 3.1.   Solvent concentration images for six unstable first-contact
miscible displacements in a horizontal quarter five-spot model
at 0.10 pore volume injected.

-137-

Viscosity   Ratio

100   50

320   Expt 3.1   Expt 3.4

Injection   Rate   (cc/hour)

200   Expt 3.2   Expt 3.5

100   Expt 3.3   Expt 3.6
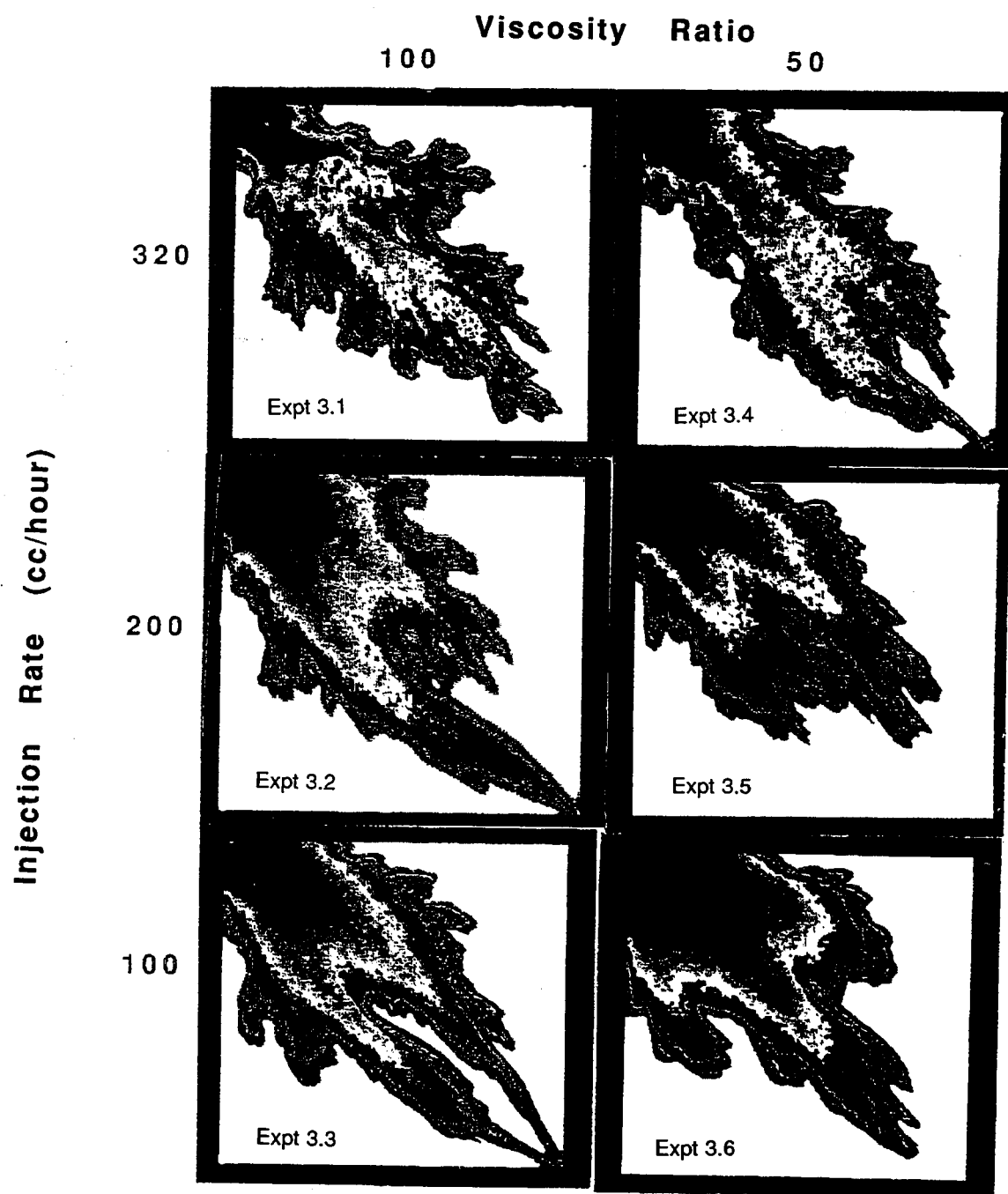
Figure 3.2.   Solvent concentration images for six unstable first-contact
               miscible displacements in a horizontal quarter five-spot model
               at 0.15 pore volume injected.

-138-

Viscosity Ratio
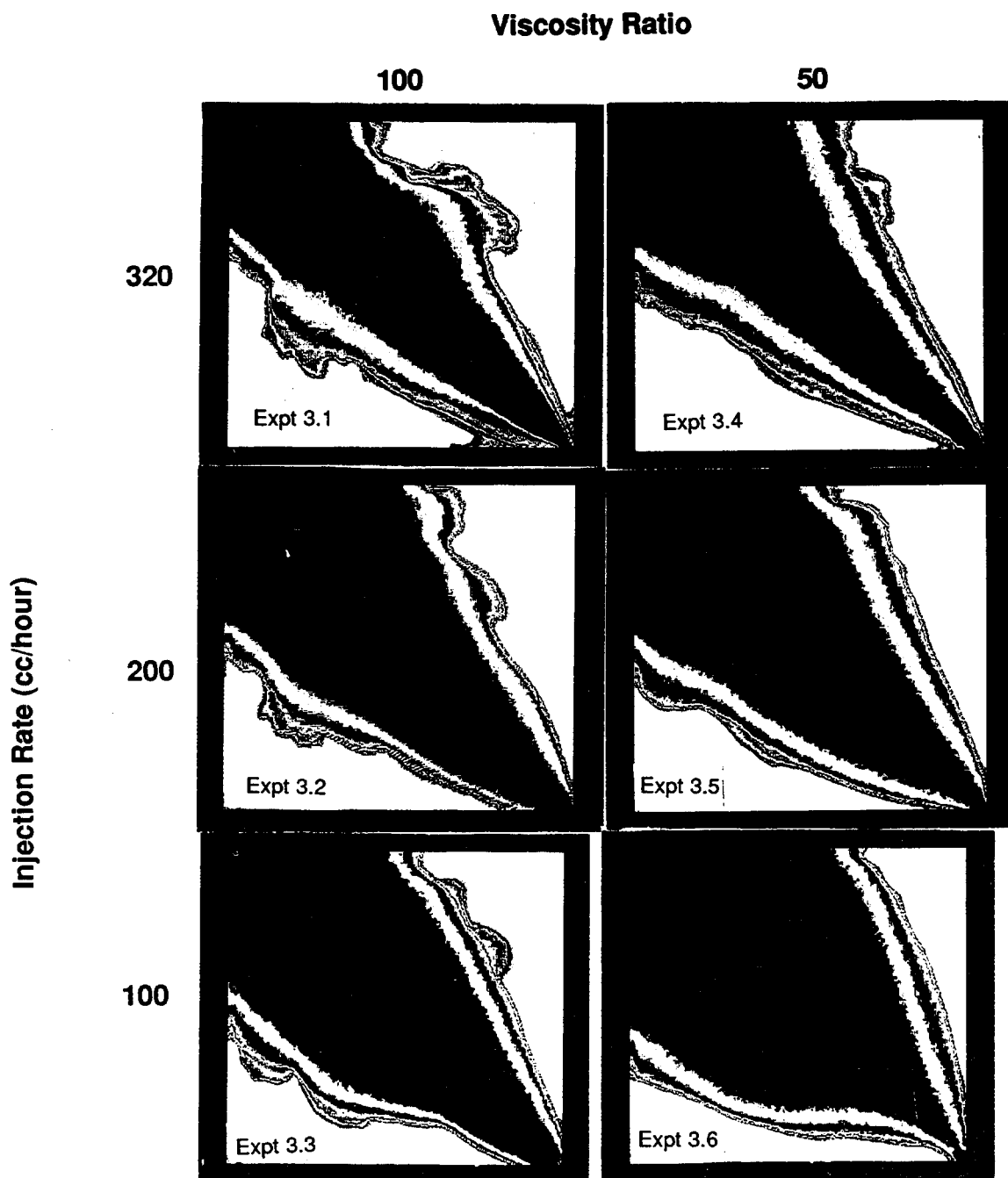
Figure 3.3. Solvent concentration images for six unstable first-contact miscible displacements in a horizontal quarter five-spot model at 1.0 pore volume injected.
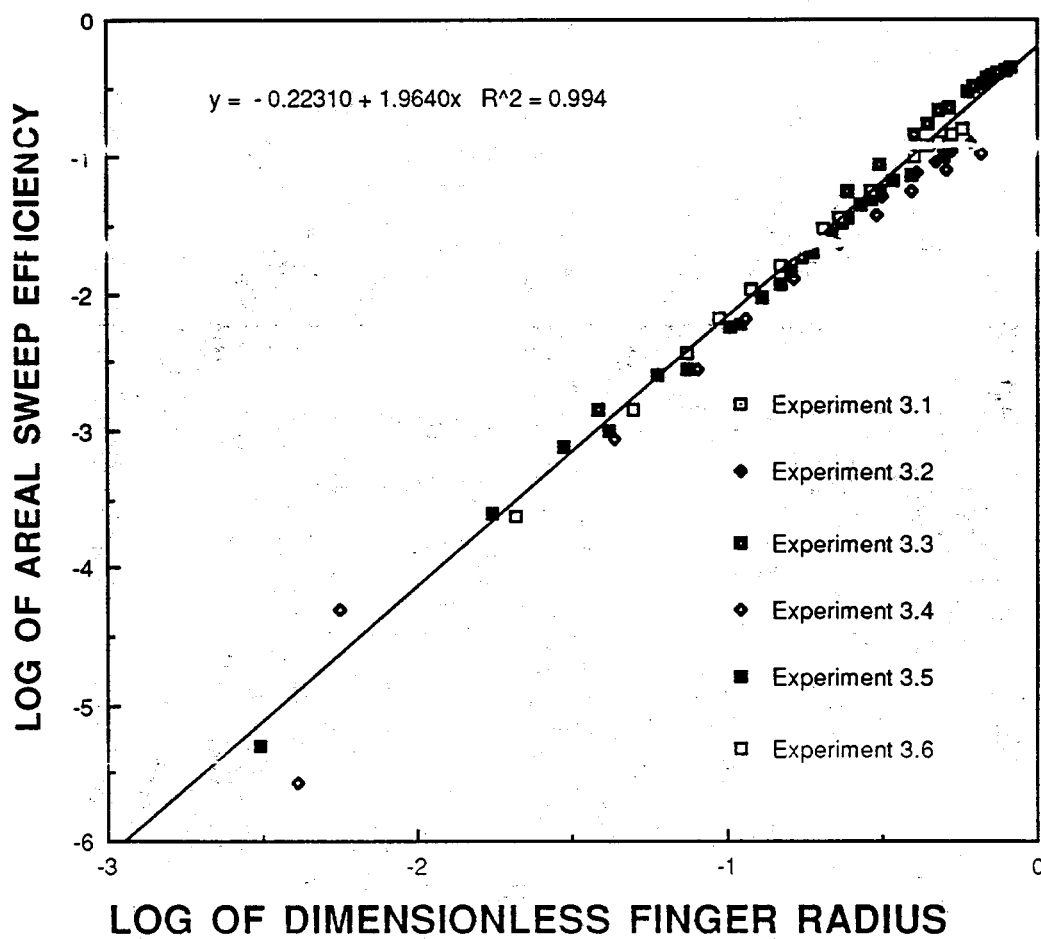
Figure 3.4. Log-log plots of areal sweep efficiency versus maximum finger radius for six unstable first-contact miscible displacements in a horizontal quarter five-spot model.
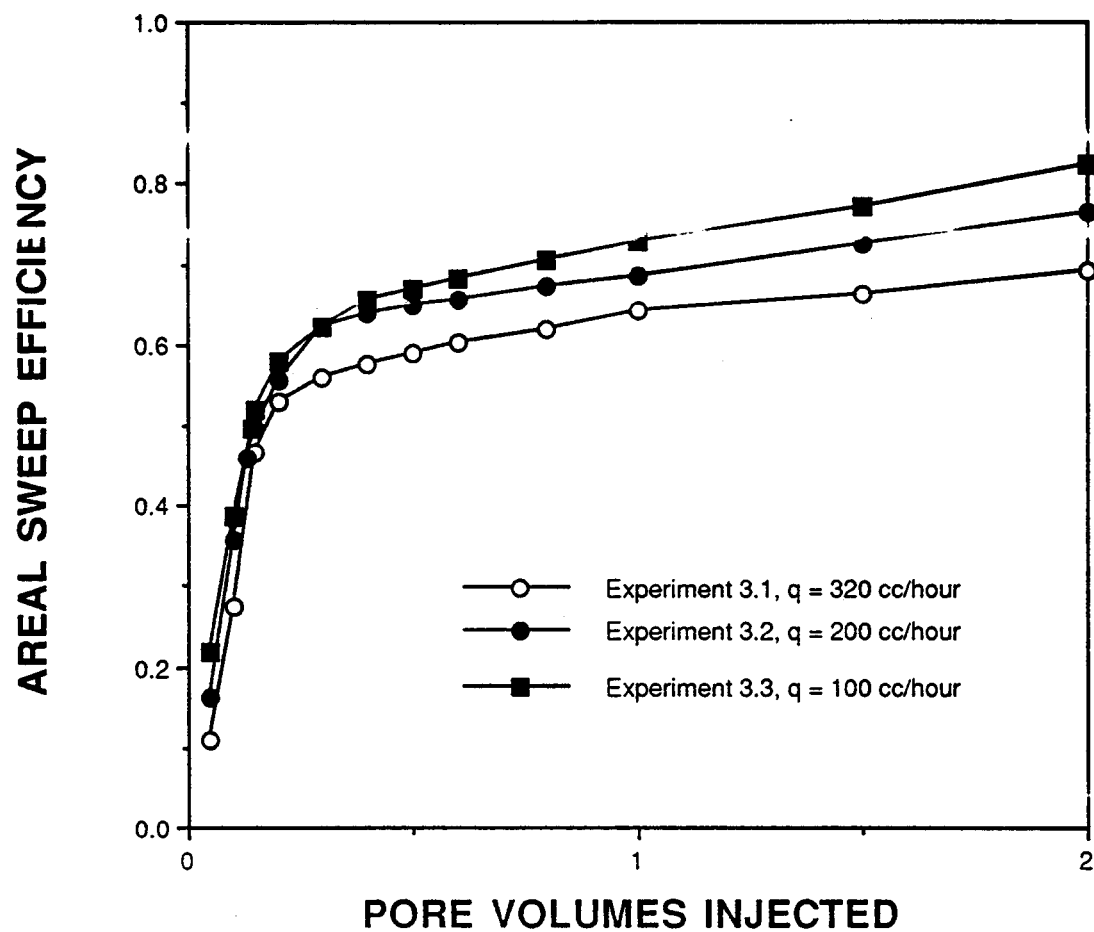
Figure 3.5. Effect of injection rate on the areal sweep efficiency for unstable first-contact miscible displacements in a horizontal quarter five-spot model at a viscosity ratio of 100.
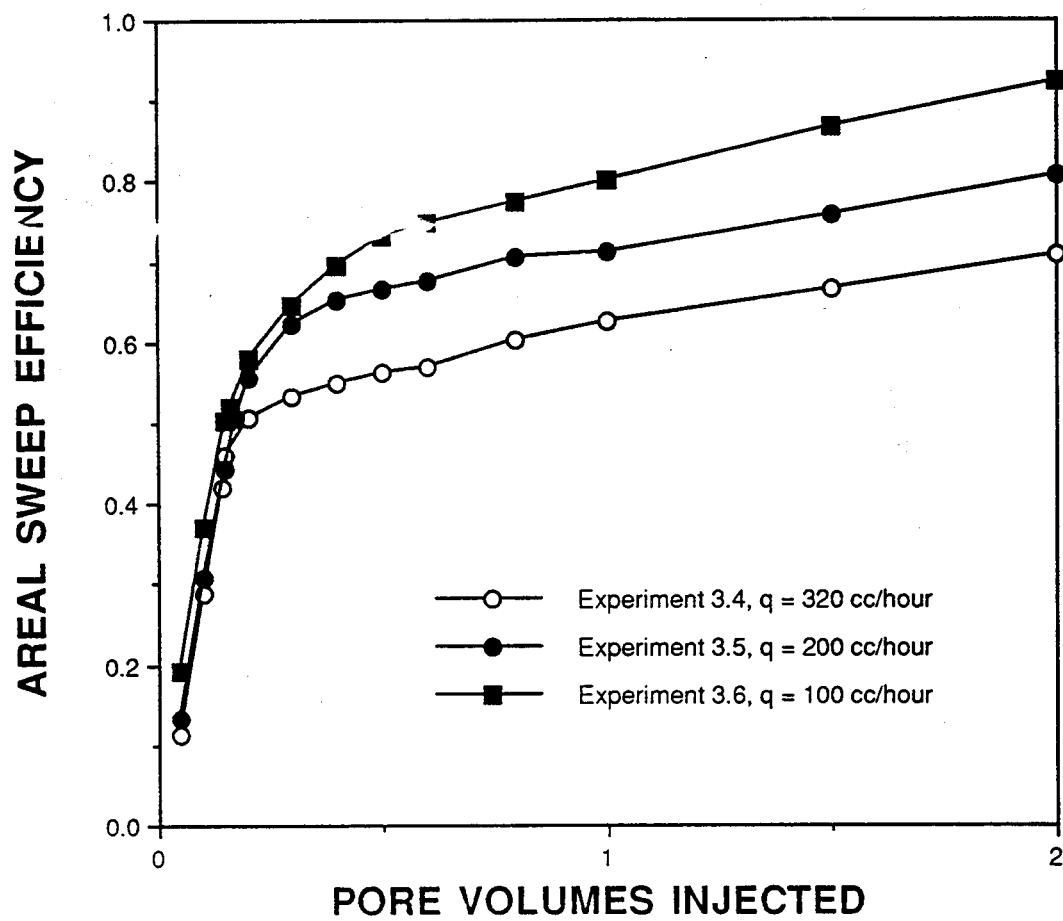
Figure 3.6. Effect of injection rate on the areal sweep efficiency for unstable first-contact miscible displacements in a horizontal quarter five-spot model at a viscosity ratio of 50.
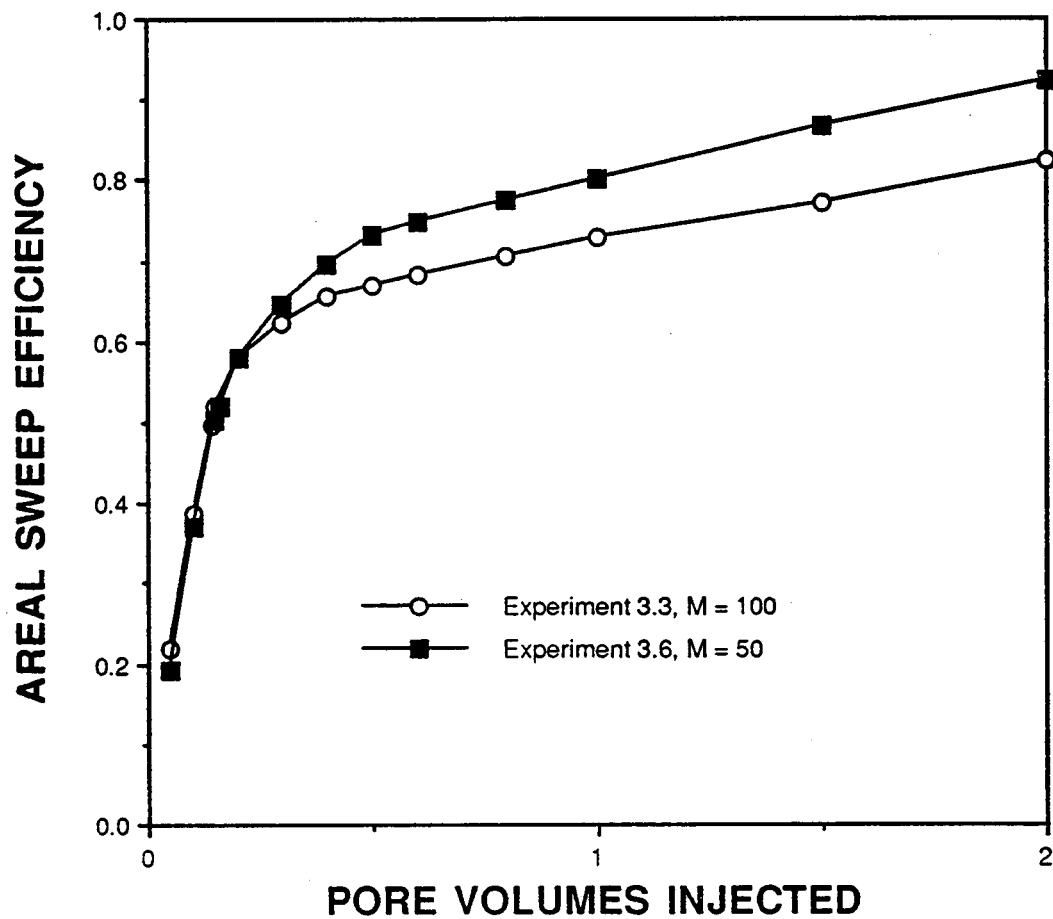
Figure 3.7. Effect of viscosity ratio on the areal sweep efficiency for
unstable first-contact miscible displacements in a horizontal
quarter five-spot model at an injection rate of 100 cc/hour.
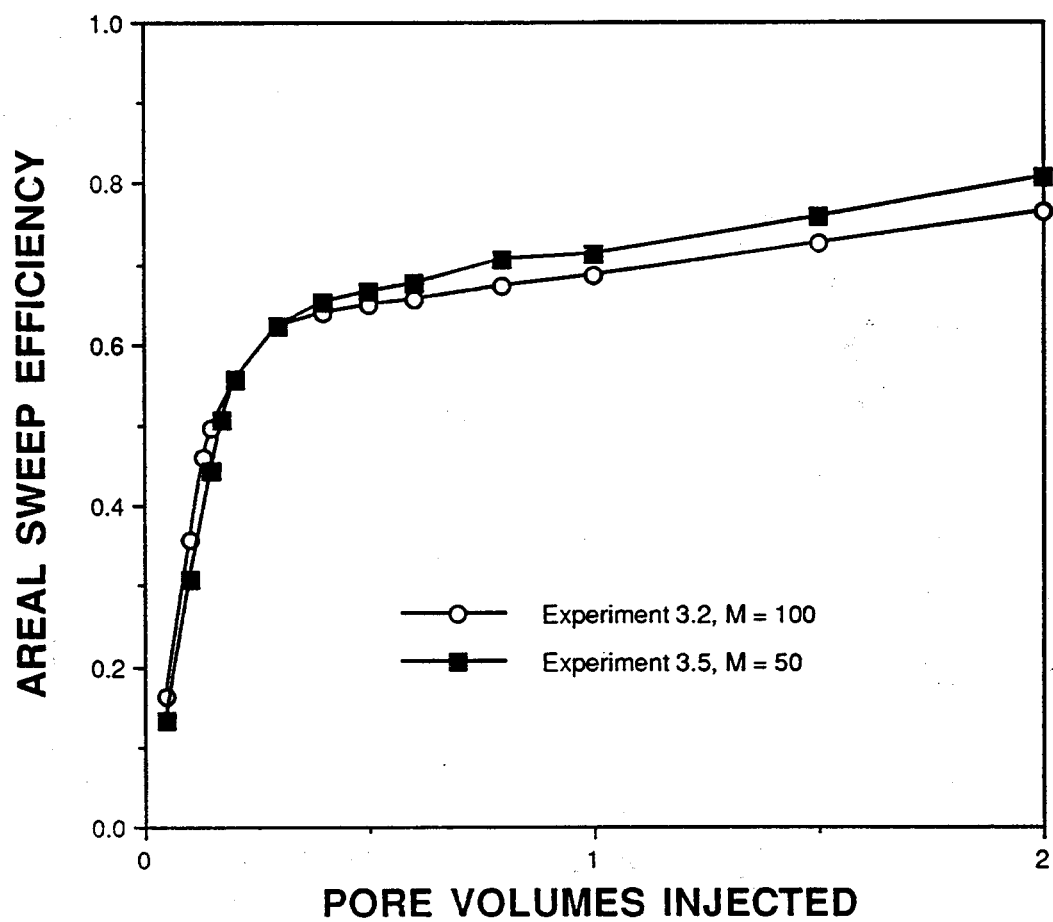
Figure 3.8. Effect of viscosity ratio on the areal sweep efficiency for unstable first-contact miscible displacements in a horizontal quarter five-spot model at an injection rate of 200 cc/hour.
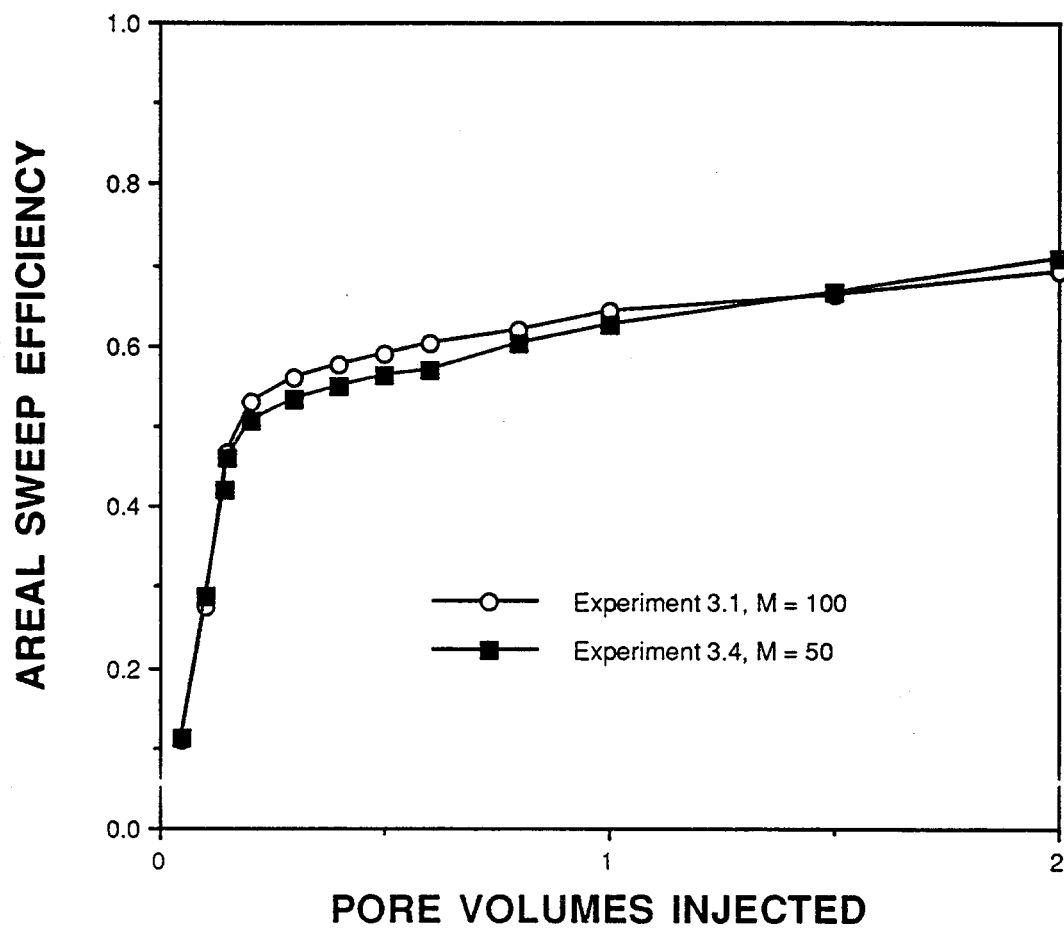
Figure 3.9. Effect of viscosity ratio on the areal sweep efficiency for
unstable first-contact miscible displacements in a horizontal
quarter five-spot model at an injection rate of 320 cc/hour.

Viscosity Ratio
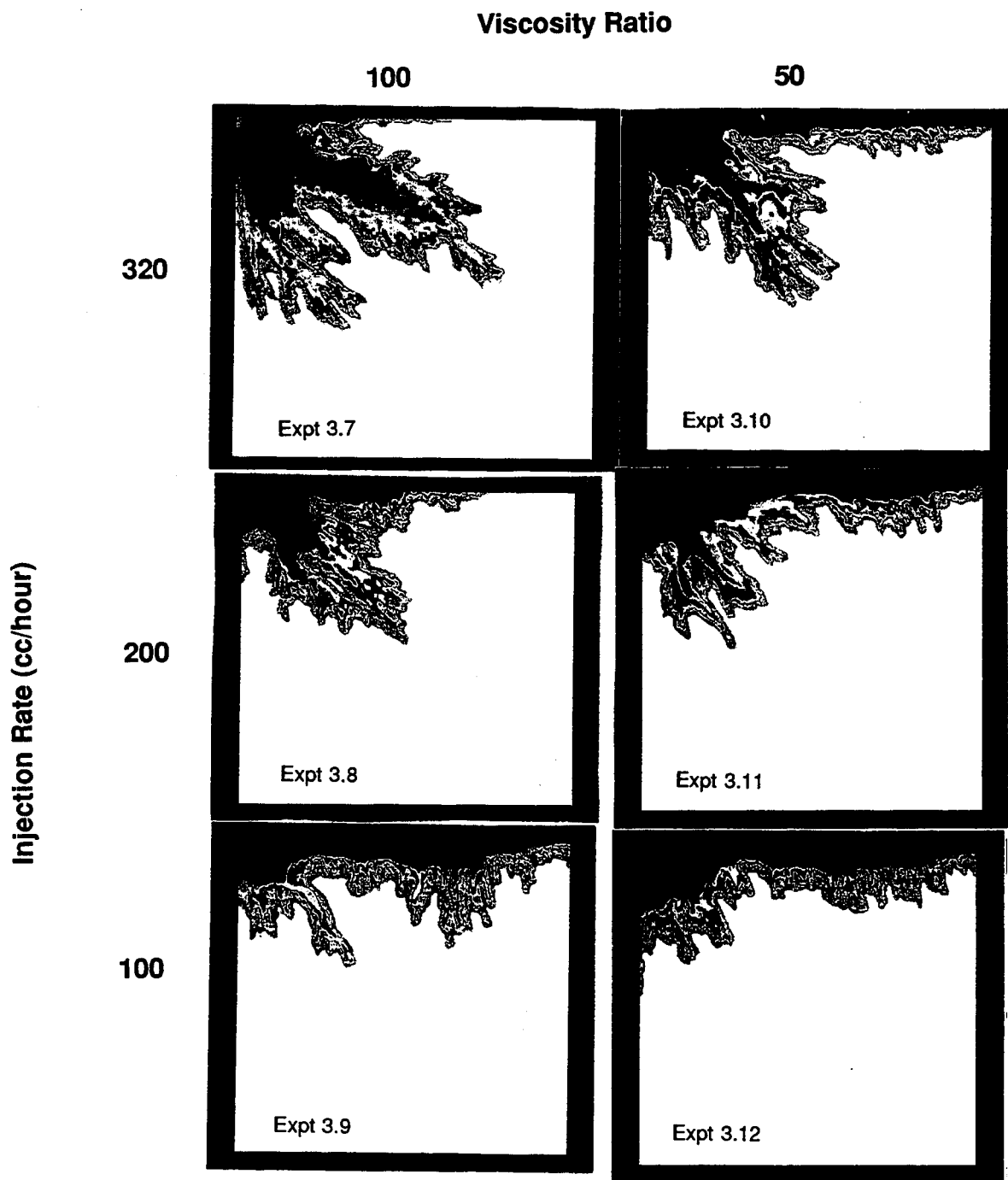
Figure 3.10. Solvent concentration images for six unstable first-contact
miscible displacements in a vertical quarter five-spot model
at 0.10 pore volume injected.

Viscosity Ratio
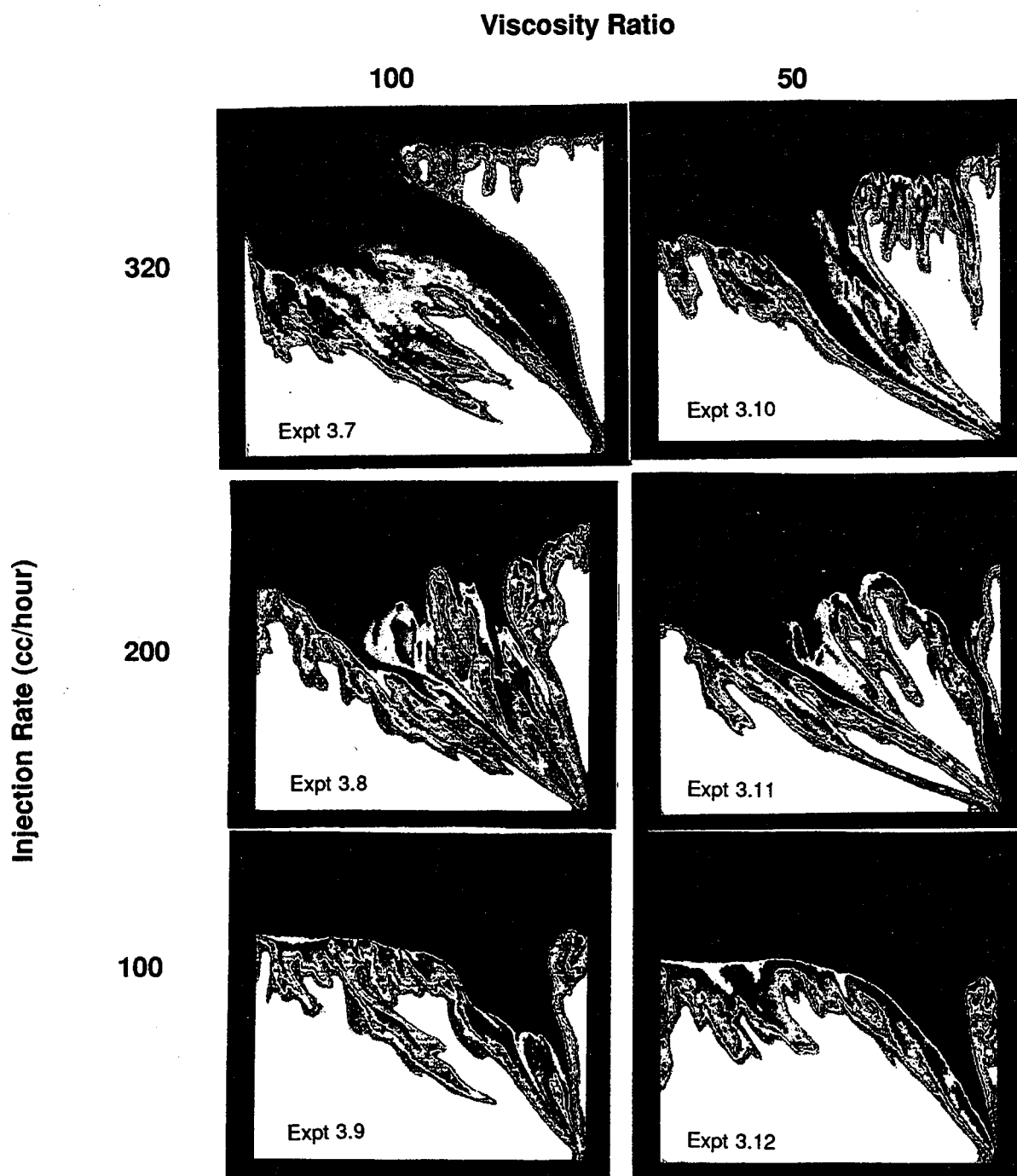
Figure 3.11. Solvent concentration images for six unstable first-contact miscible displacements in a vertical quarter five-spot model at 0.50 pore volume injected.

Viscosity Ratio

100   50
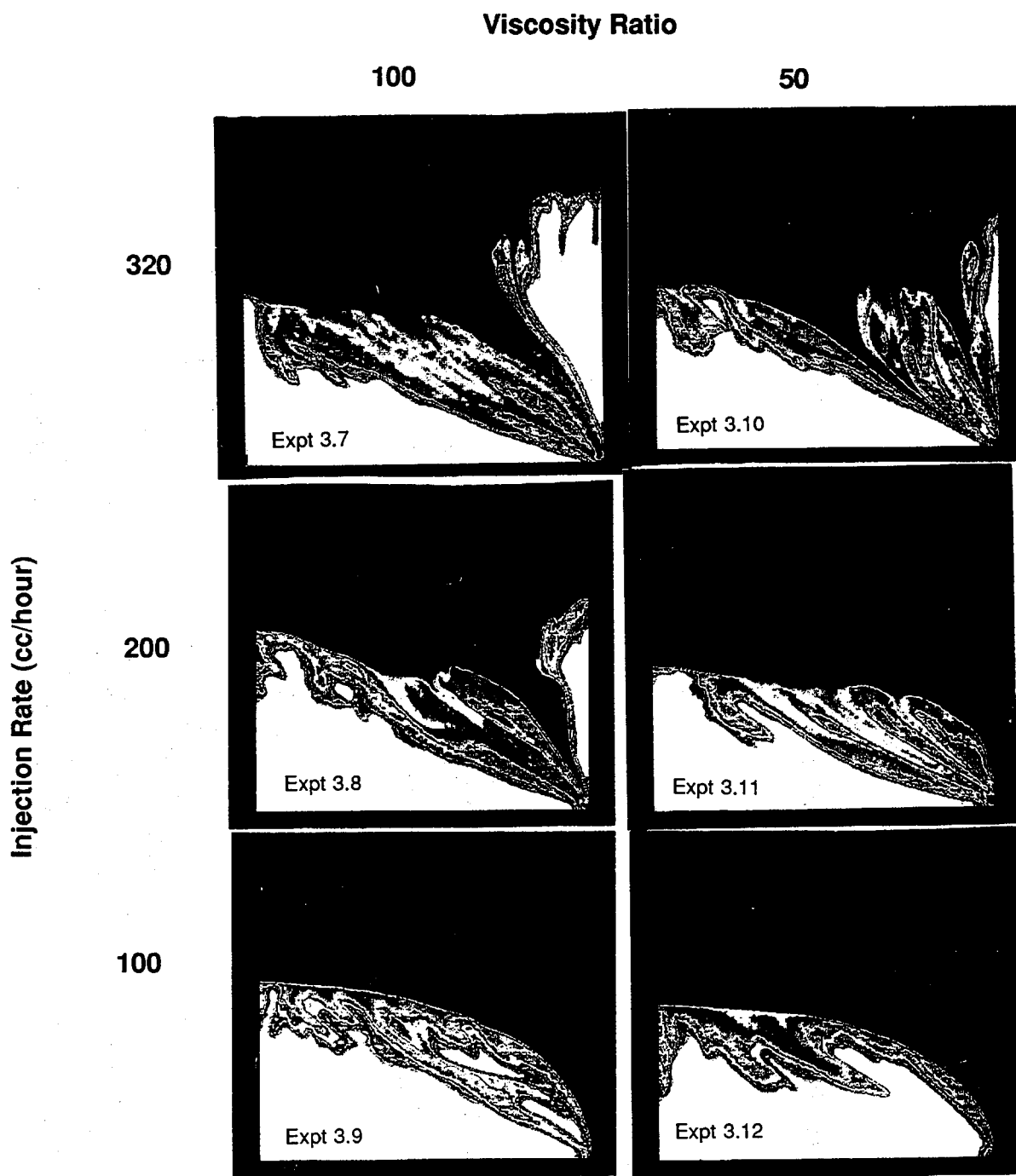
Figure 3.12. Solvent concentration images for six unstable first-contact miscible displacements in a vertical quarter five-spot model at 1.0 pore volume injected.
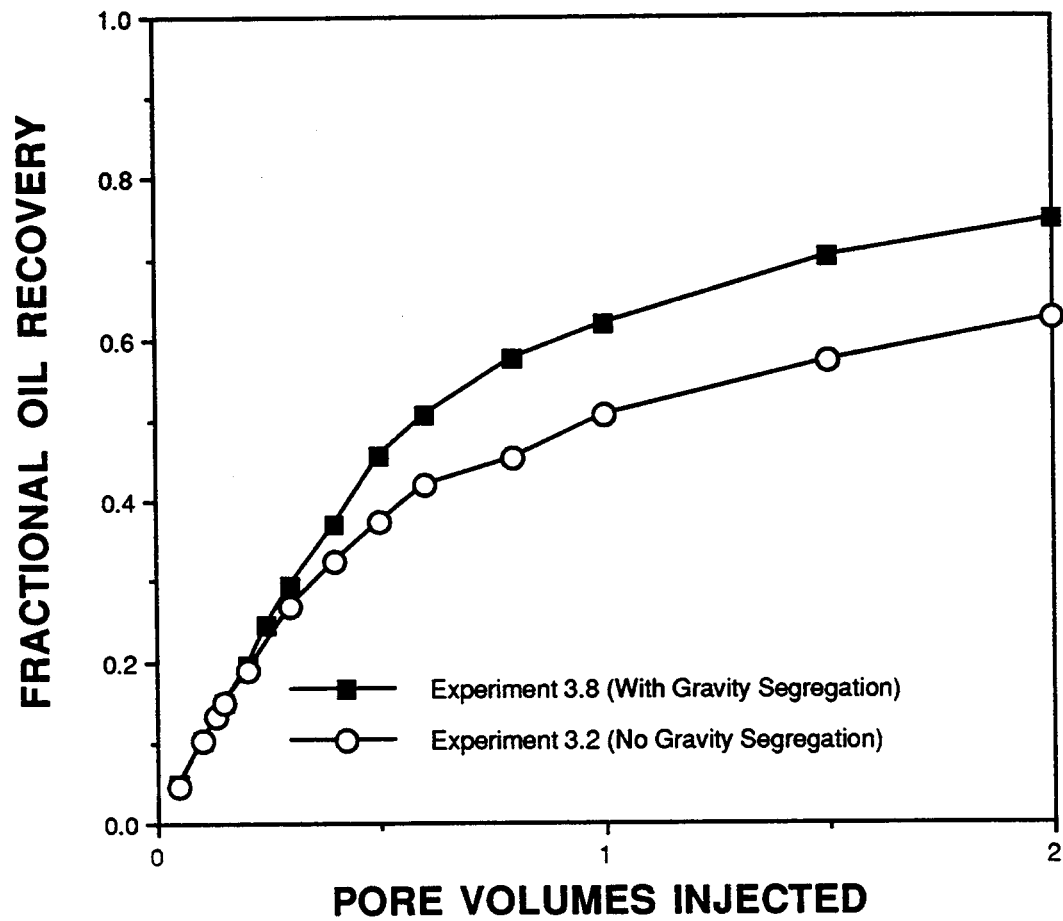
Figure 3.13. Effect of gravity segregation on the performance of unstable first-contact miscible displacements at a rate of 200 cc/hour and a viscosity ratio of 100.
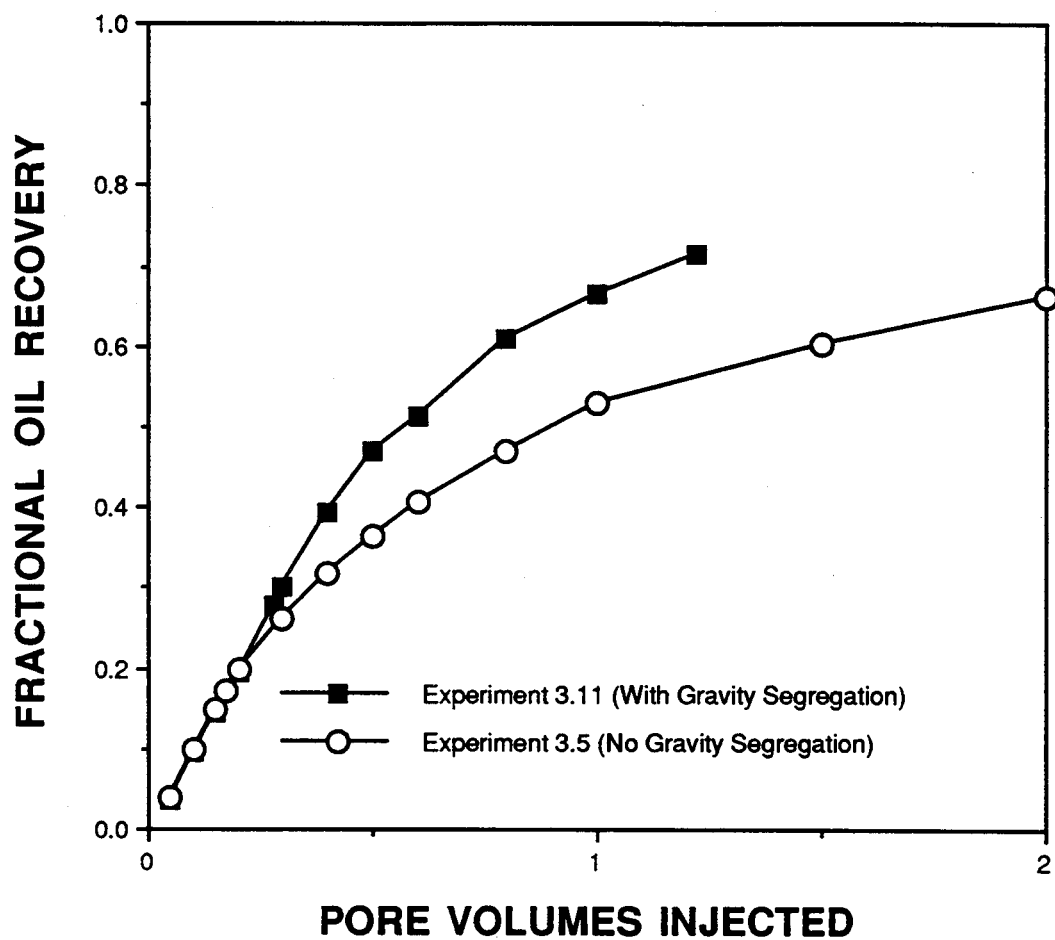
Figure 3.14. Effect of gravity segregation on the performance of unstable first-contact miscible displacements at a rate of 200 cc/hour and a viscosity ratio of 50.
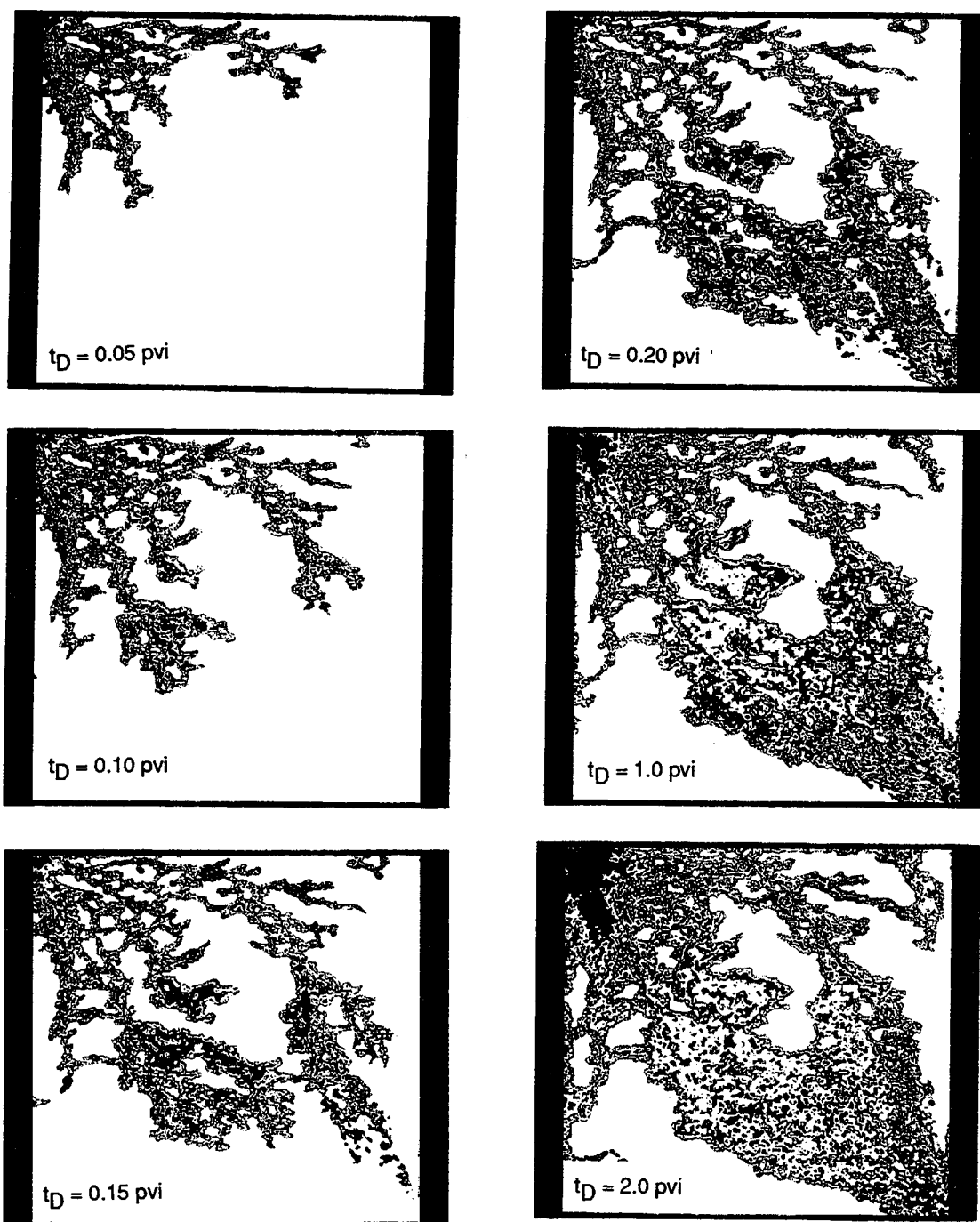
Figure 3.15. Saturation images for an unstable immiscible displacement in an oil-wet horizontal quarter five-spot model (Experiment 3.13).
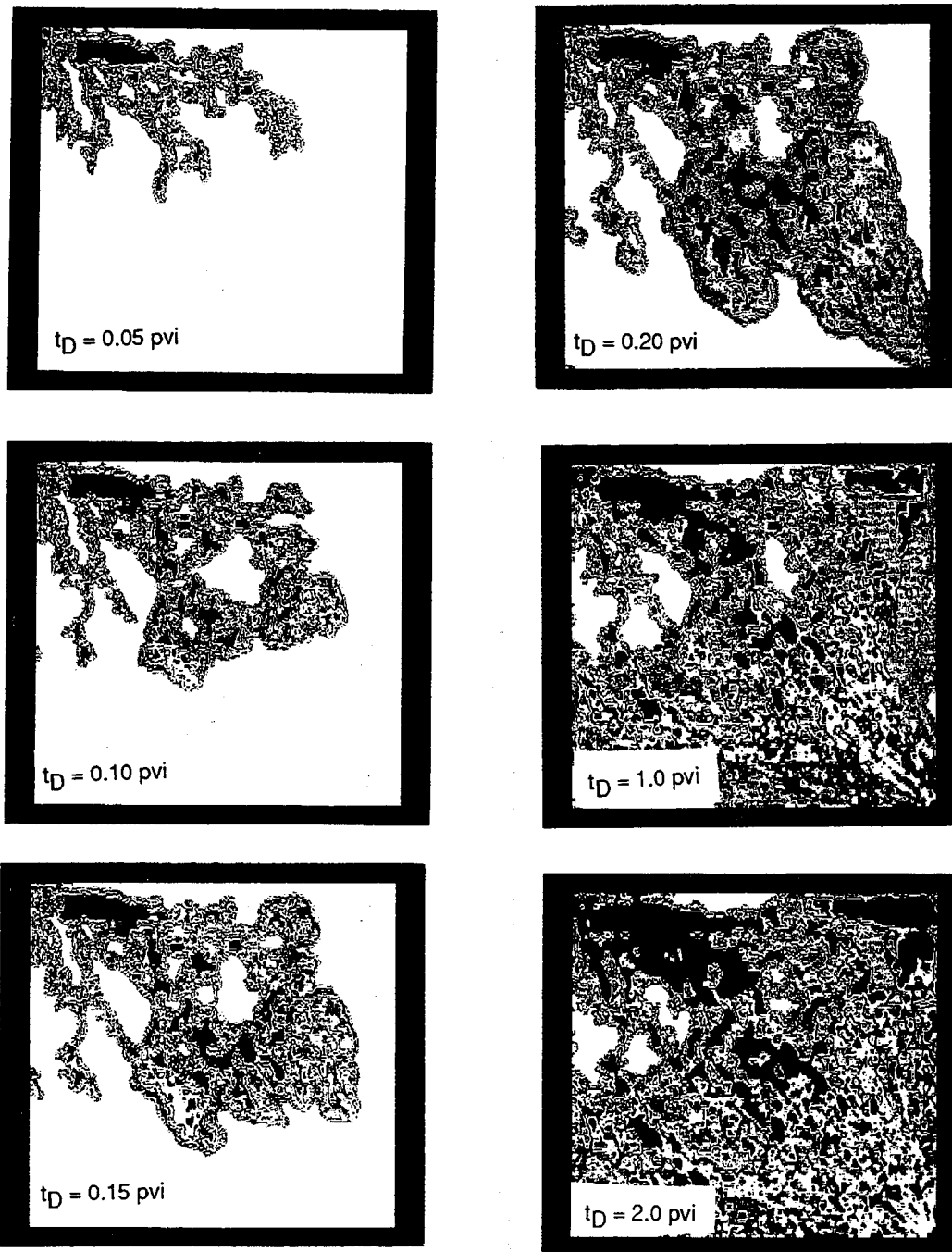
Figure 3.16. Saturation images for an unstable immiscible displacement in a
water-wet horizontal quarter five-spot model (Experiment 3.14).
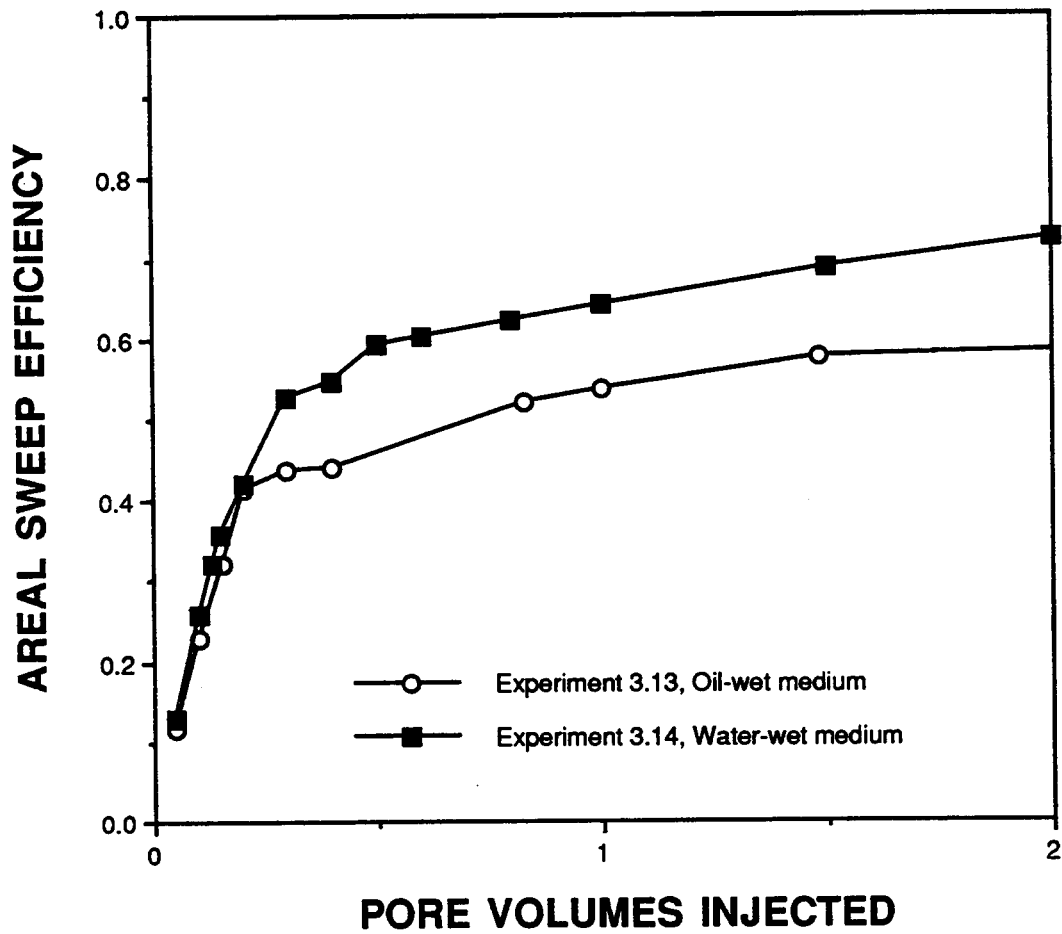
Figure 3.17. A comparison of the areal sweep efficiencies for unstable immiscible displacements in an oil-wet and a water-wet quarter five-spot model.
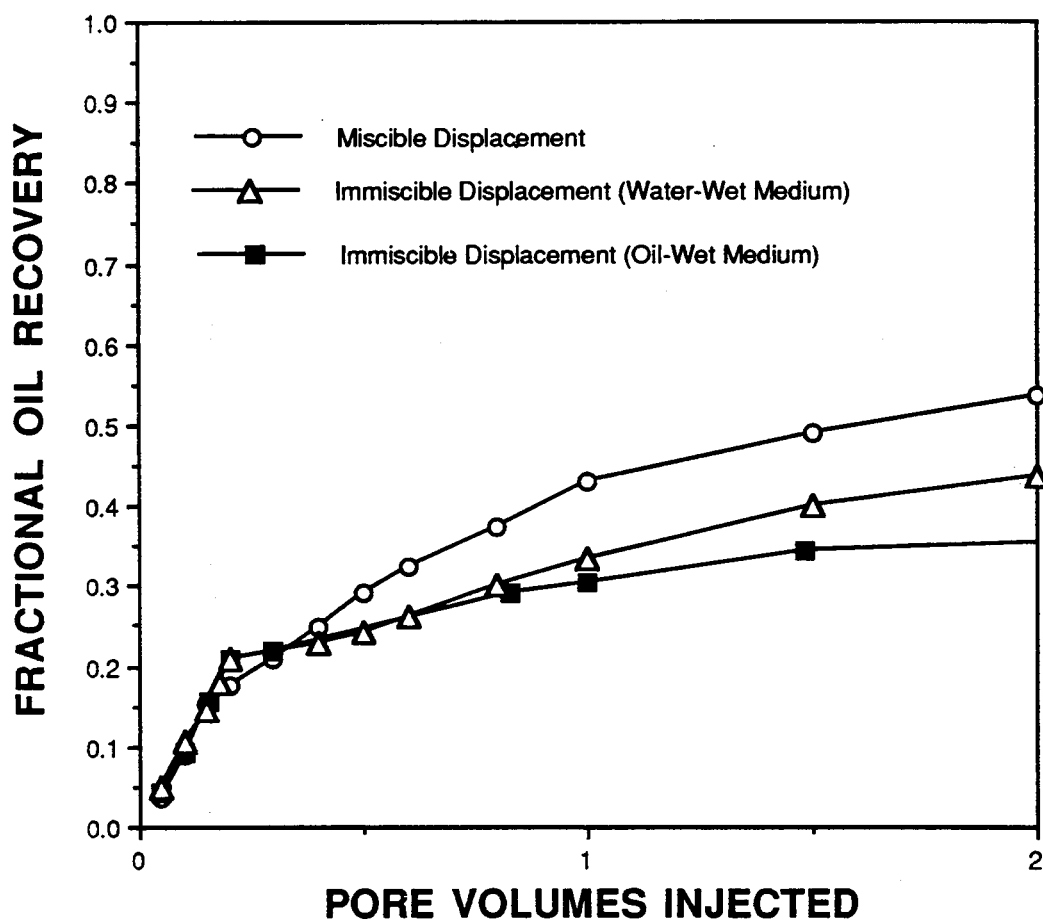
Figure 3.18. A comparison of the oil recovery curves for unstable first-contact miscible and immiscible displacements in a quarter five-spot model at a rate of 320 cc/hour and a viscosity ratio of 100.
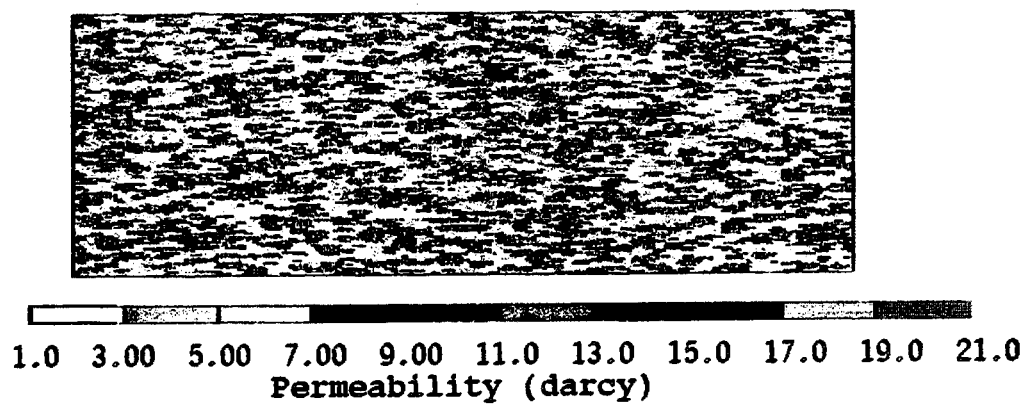
Figure 4.1. Permeability map for example numerical simulations (Runs 4.1 and 4.2).
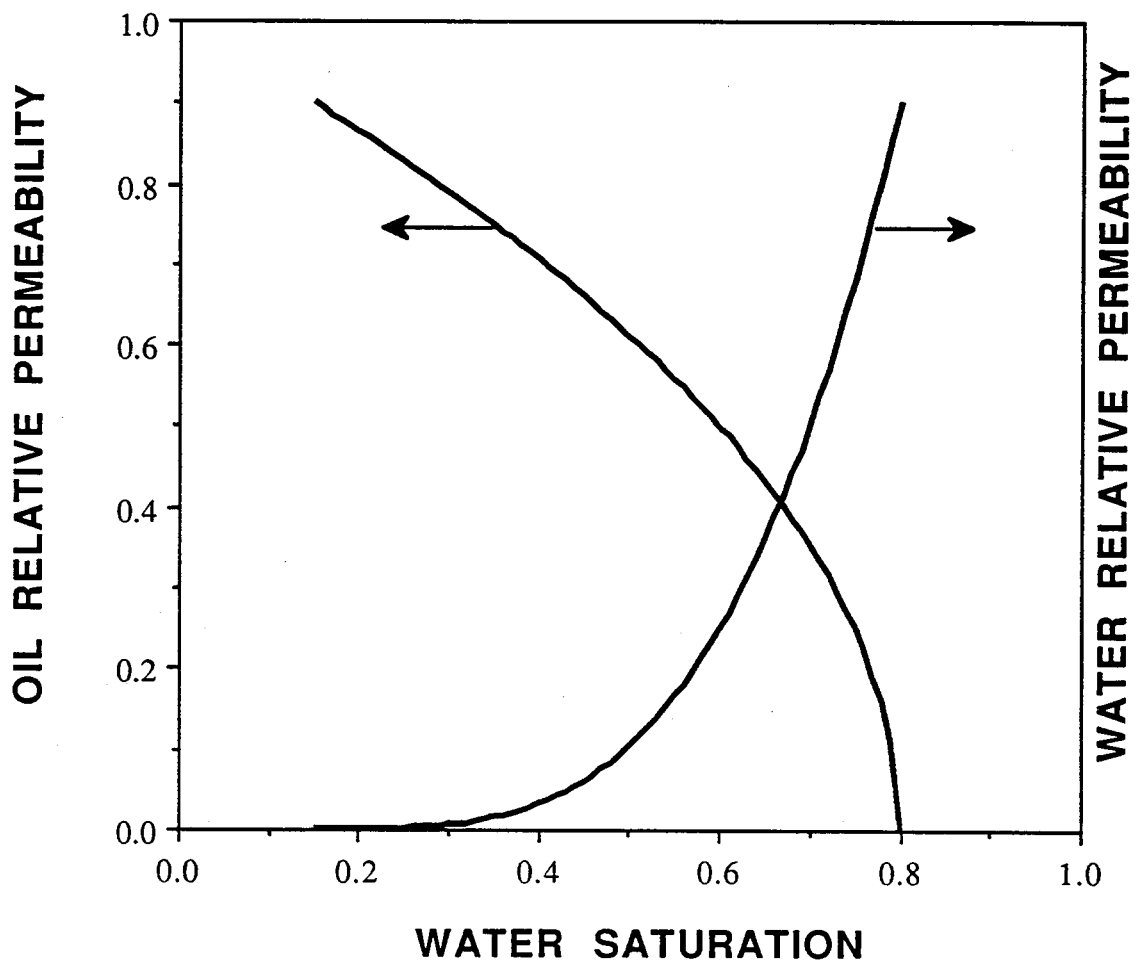
Figure 4.2. Oil-water relative permeability curves for example numerical
simulation of an unstable immiscible displacement (Run 4.1).
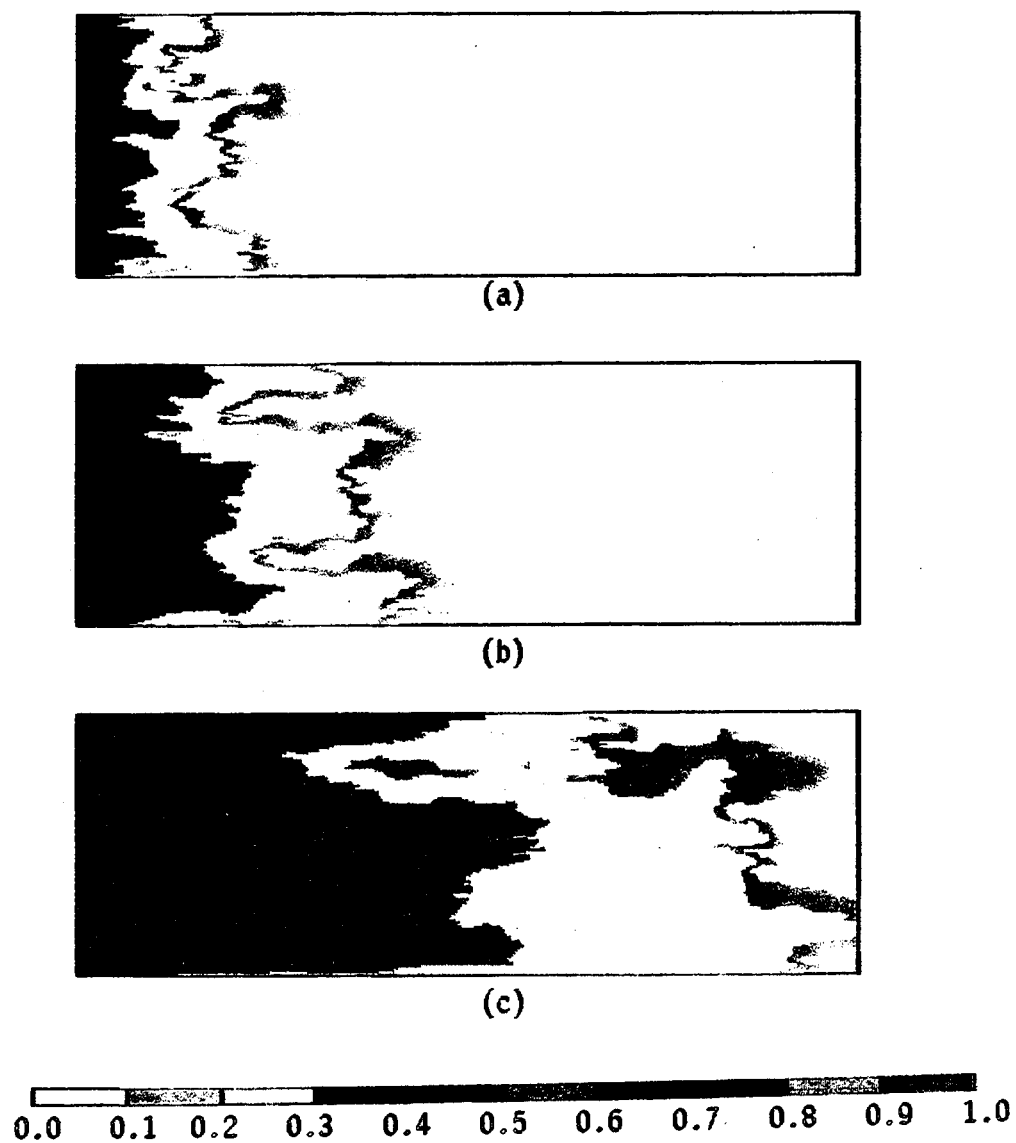
Figure 4.3.   Water saturation maps for example numerical simulation of an
             unstable immiscible displacement at (a) 0.05 pore volume
             injected; (b) 0.10 pore volume injected and (c) 0.25 pore
             volume injected (Run 4.1).
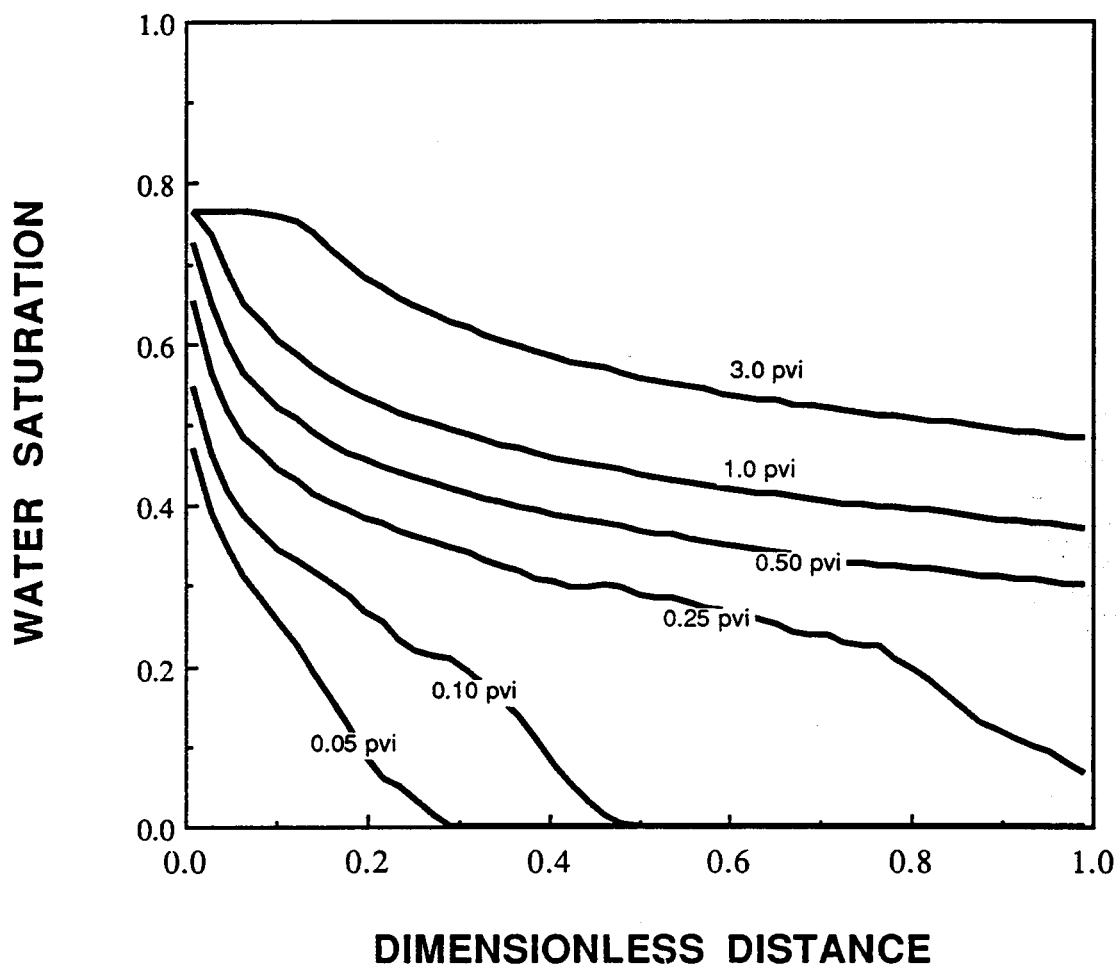
Figure 4.4. Water saturation profiles for example numerical simulation of
an unstable immiscible displacement (Run 4.1).
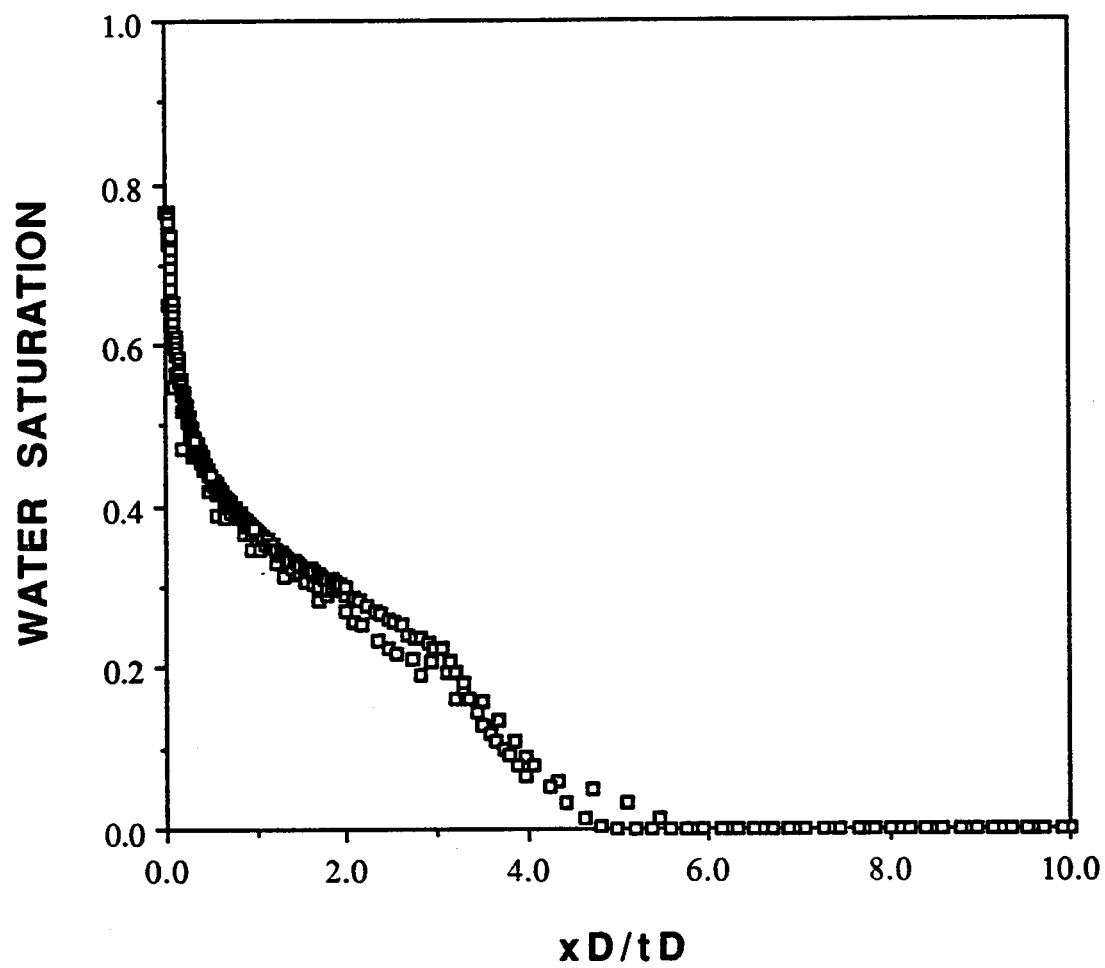
Figure 4.5. Dimensionless response curve for example numerical
simulation of an unstable immiscible displacement (Run 4.1).
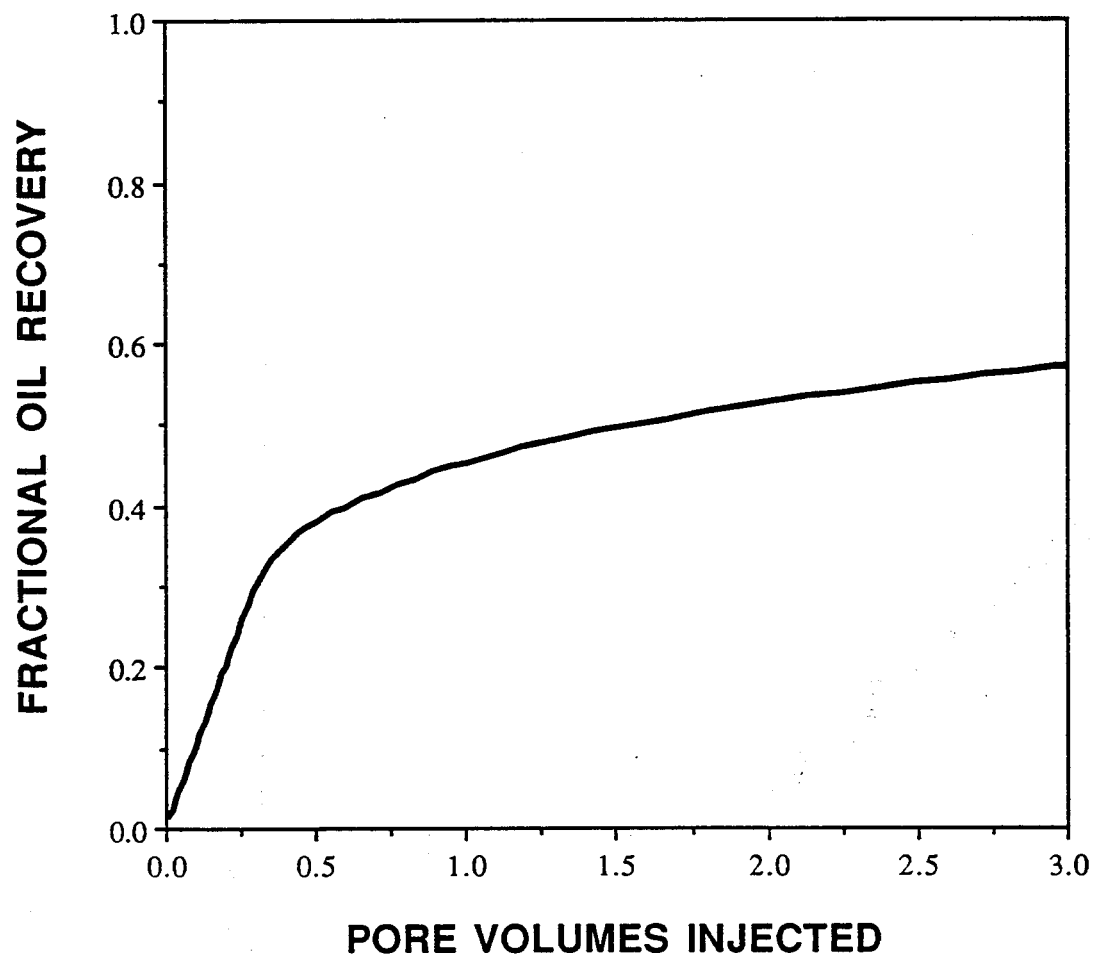
Figure 4.6. Oil recovery curve for example numerical simulation of an unstable immiscible displacement (Run 4.1).

(a)

(b)

(c)

0.0   0.1   0.2   0.3   0.4   0.5   0.6   0.7   0.8   0.9   1.0
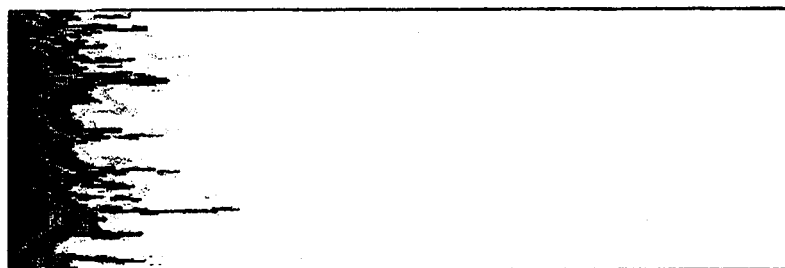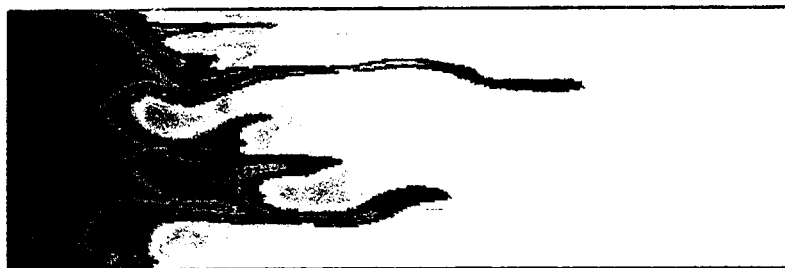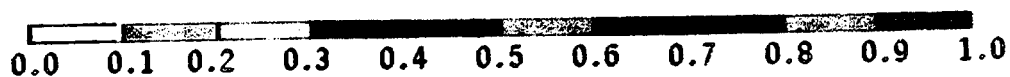
Figure 4.7.   Solvent concentration maps for example numerical simulation
of an unstable first-contact miscible displacement at (a) 0.05
pore volume injected; (b) 0.10 pore volume injected and (c)
0.25 pore volume injected (Run 4.2).
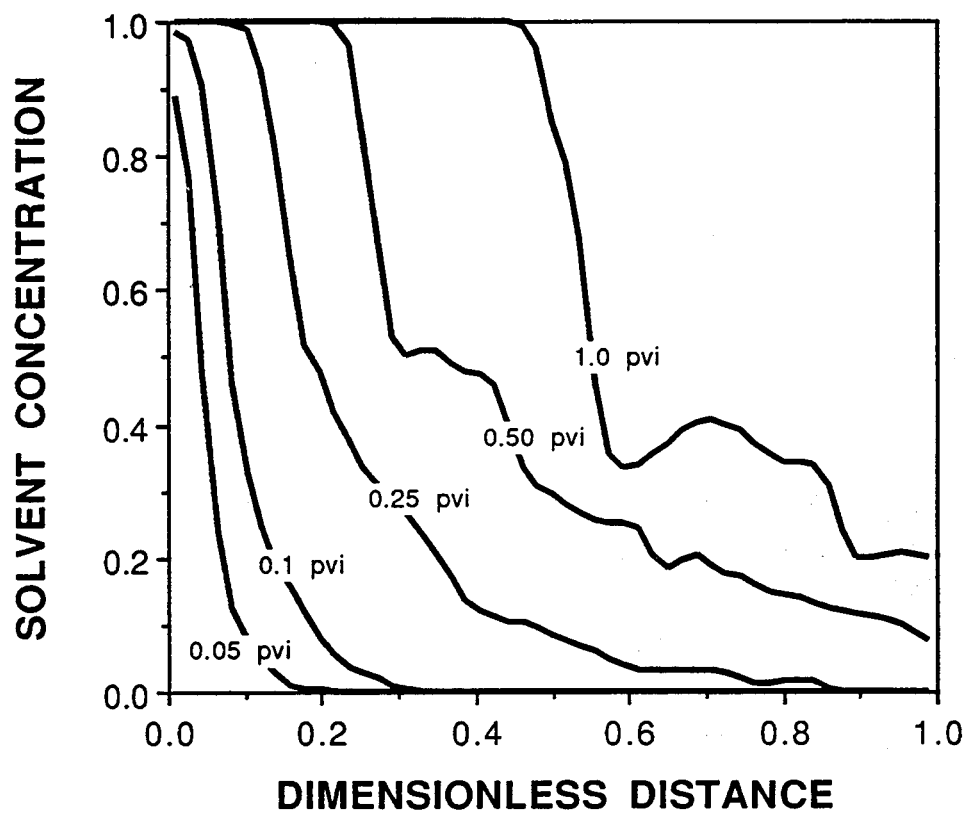
Figure 4.8. Solvent concentration profiles for example numerical simulation of an unstable first-contact miscible displacement (Run 4.2).
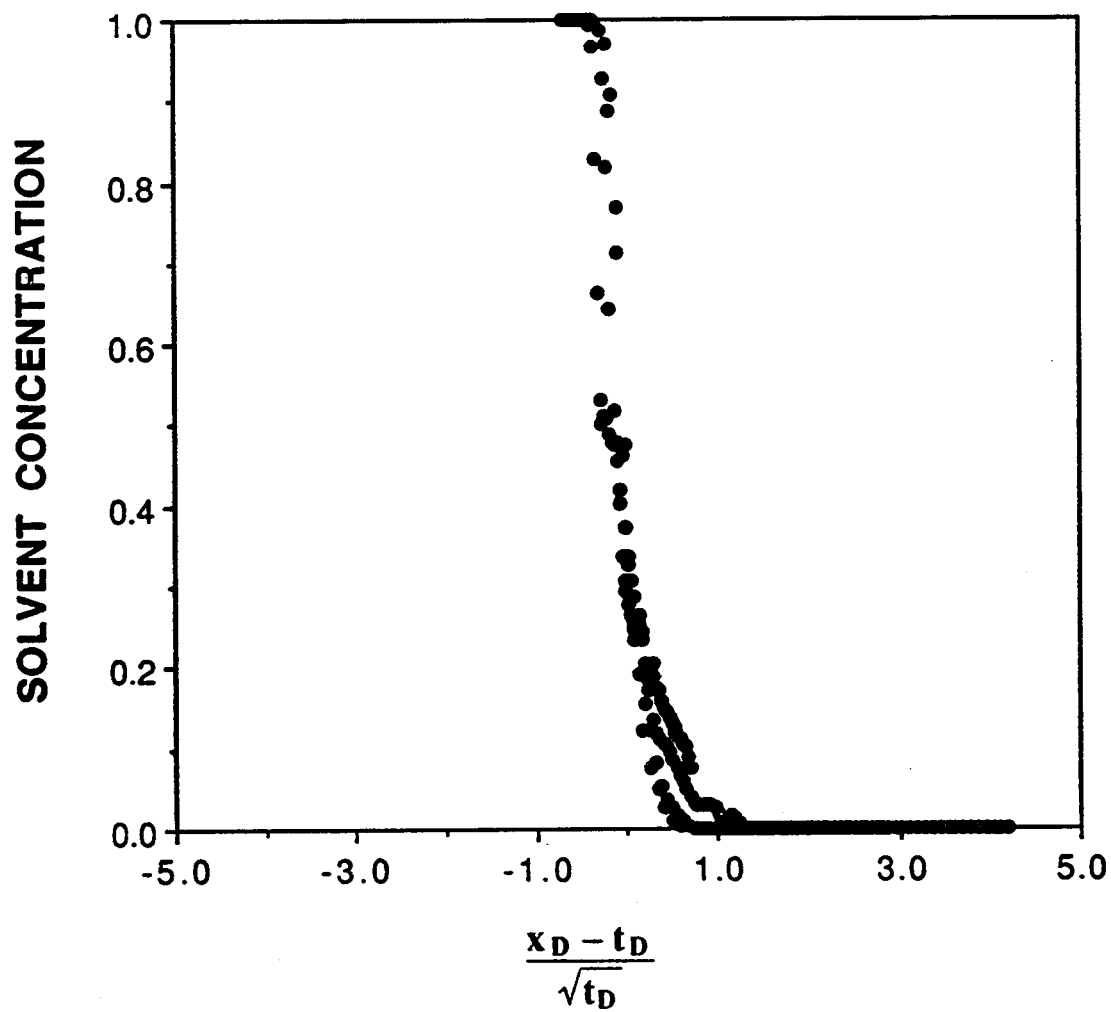
Figure 4.9. Dimensionless response curve for example numerical
simulation of an unstable first-contact miscible
displacement (Run 4.2).
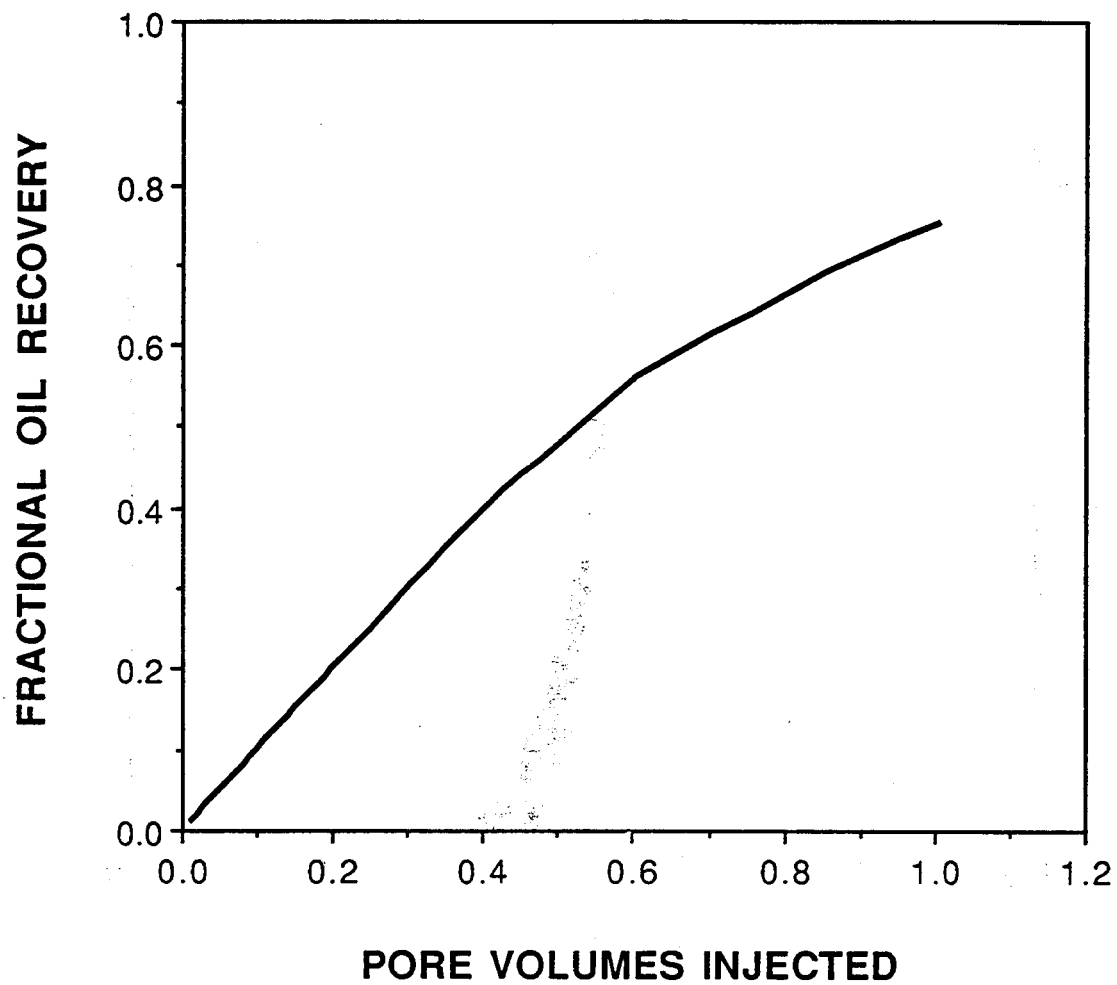
Figure 4.10. Oil recovery curve for example numerical simulation of
an unstable first-contact miscible displacement (Run 4.2).
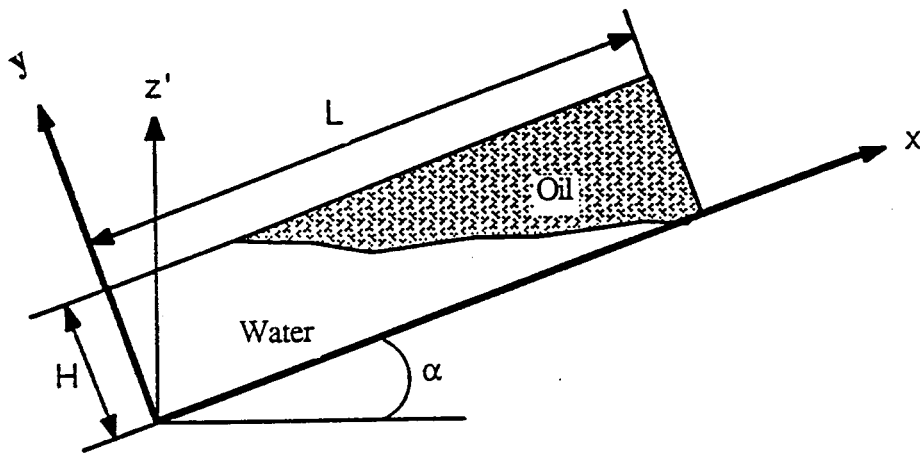
Figure 5.1. Displacement of oil by water in a two-dimensional porous medium.
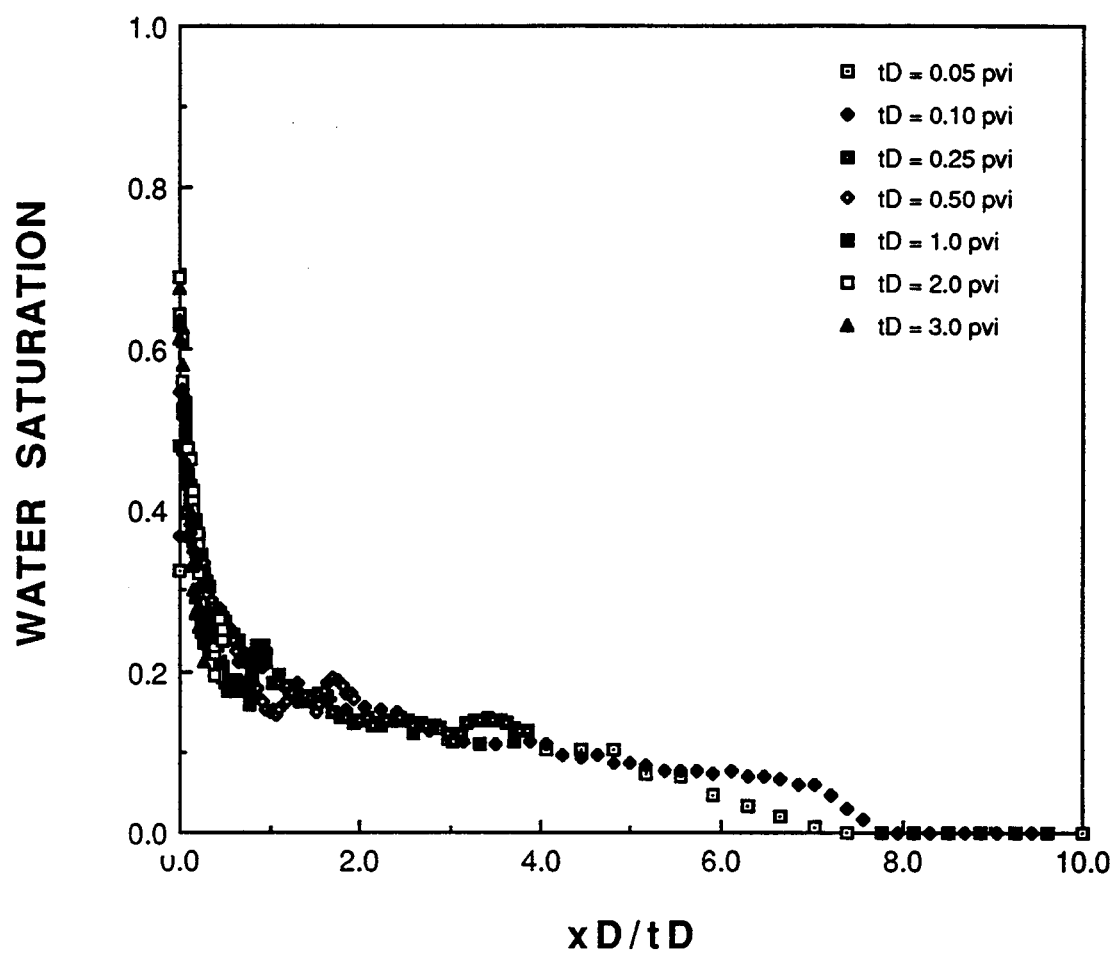
Figure 5.2. Dimensionless response curve for an unstable immiscible displacement in an oil-wet sandpack (Experiment 2.2).
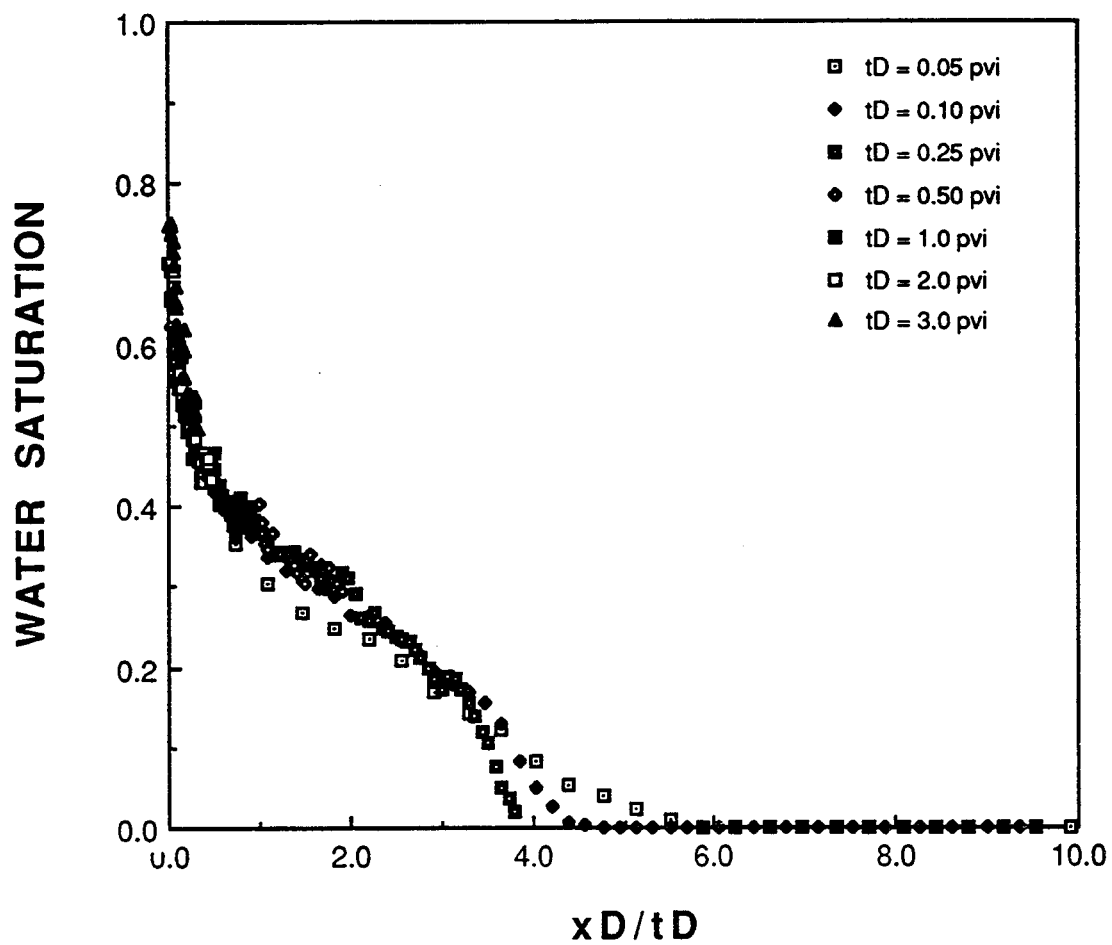
Figure 5.3. Dimensionless response curve for an unstable immiscible displacement in a water-wet sandpack (Experiment 2.3).
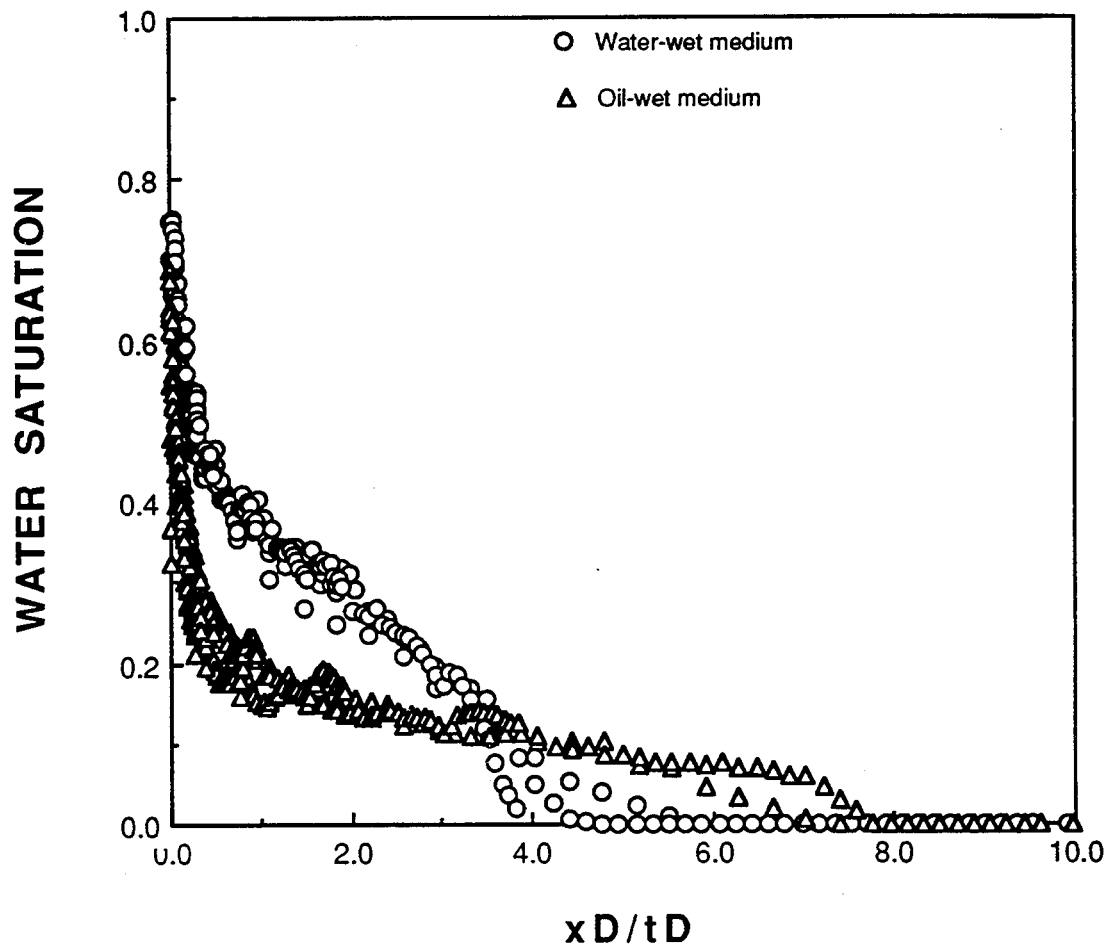
Figure 5.4. A comparison of the dimensionless response curves for unstable immiscible displacements in an oil-wet and a water-wet sandpack (Experiments 2.2 and 2.3).
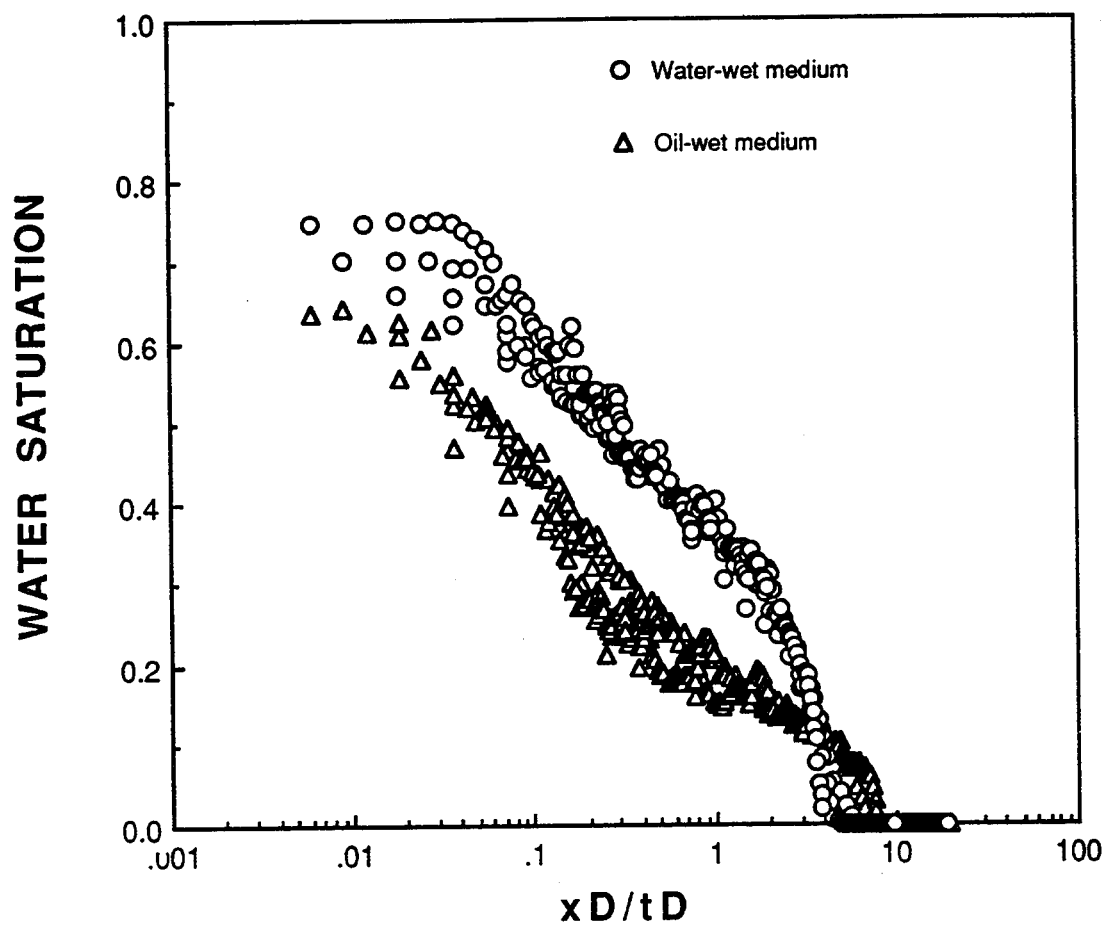
Figure 5.5. Semilog plots of the dimensionless response curves for
unstable immisicible displacements in an oil-wet and a
water-wet sandpack (Experiments 2.2 and 2.3).
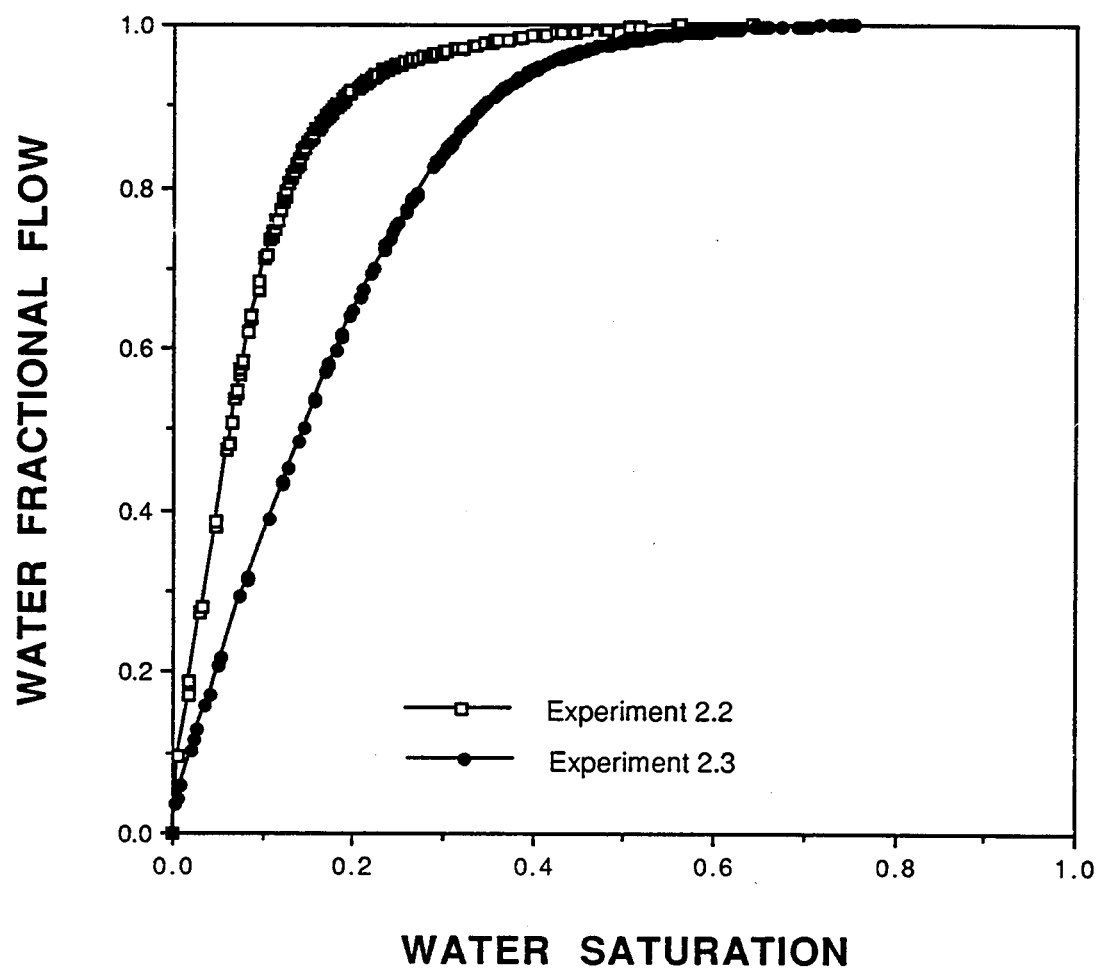
Figure 5.6. Fractional flow curves for unstable immiscible displacements in an oil-wet and a water-wet sandpack (Experiments 2.2 and 2.3).
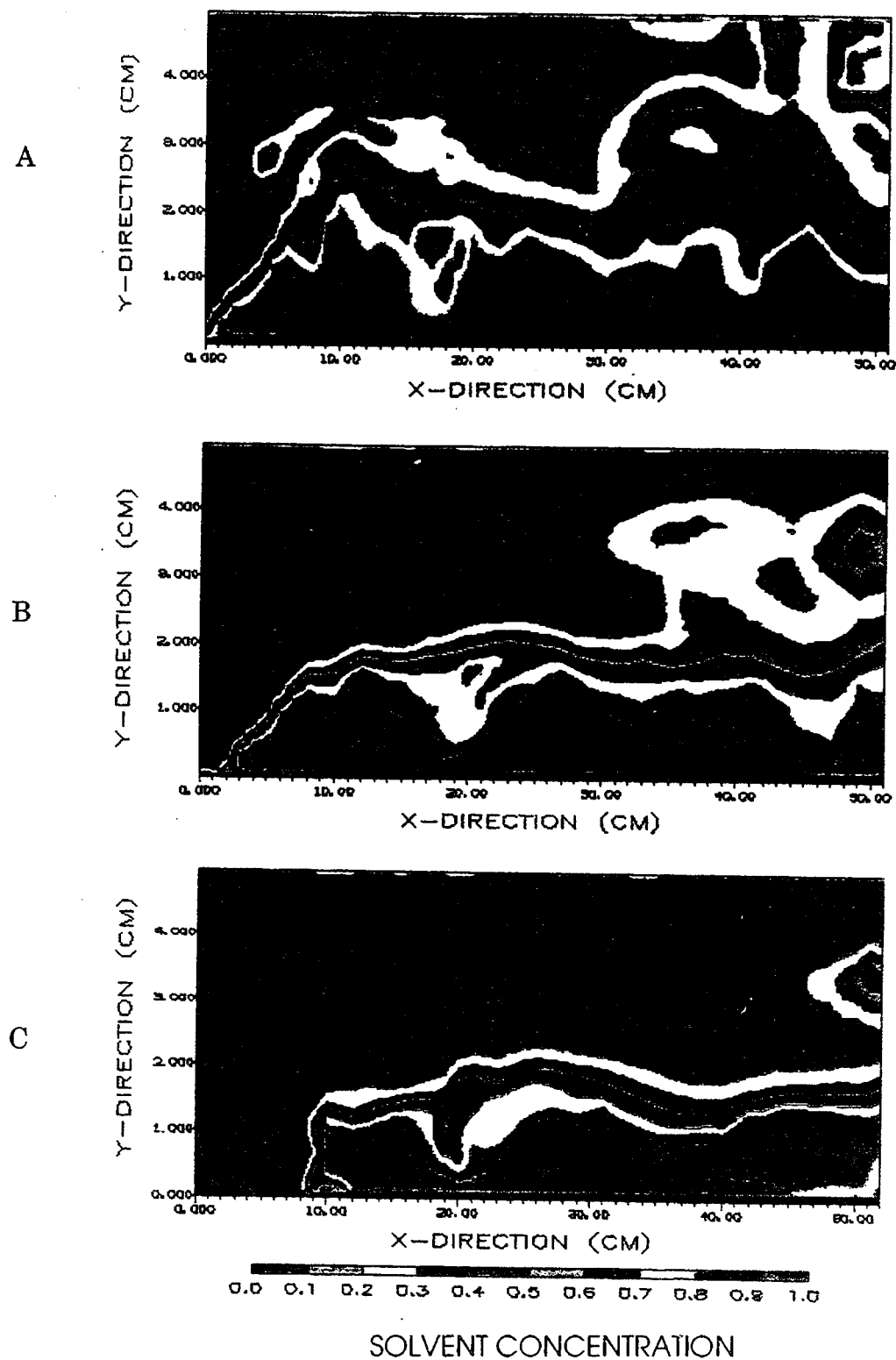
Figure 5.7.   Solvent concentration images for an unstable first-contact
miscible displacement at (A) 0.5 pore volume injected; (B)
1.0 pore volume injected and (C) 2.0 pore volume injected
(Experiment 2.1).

-171-
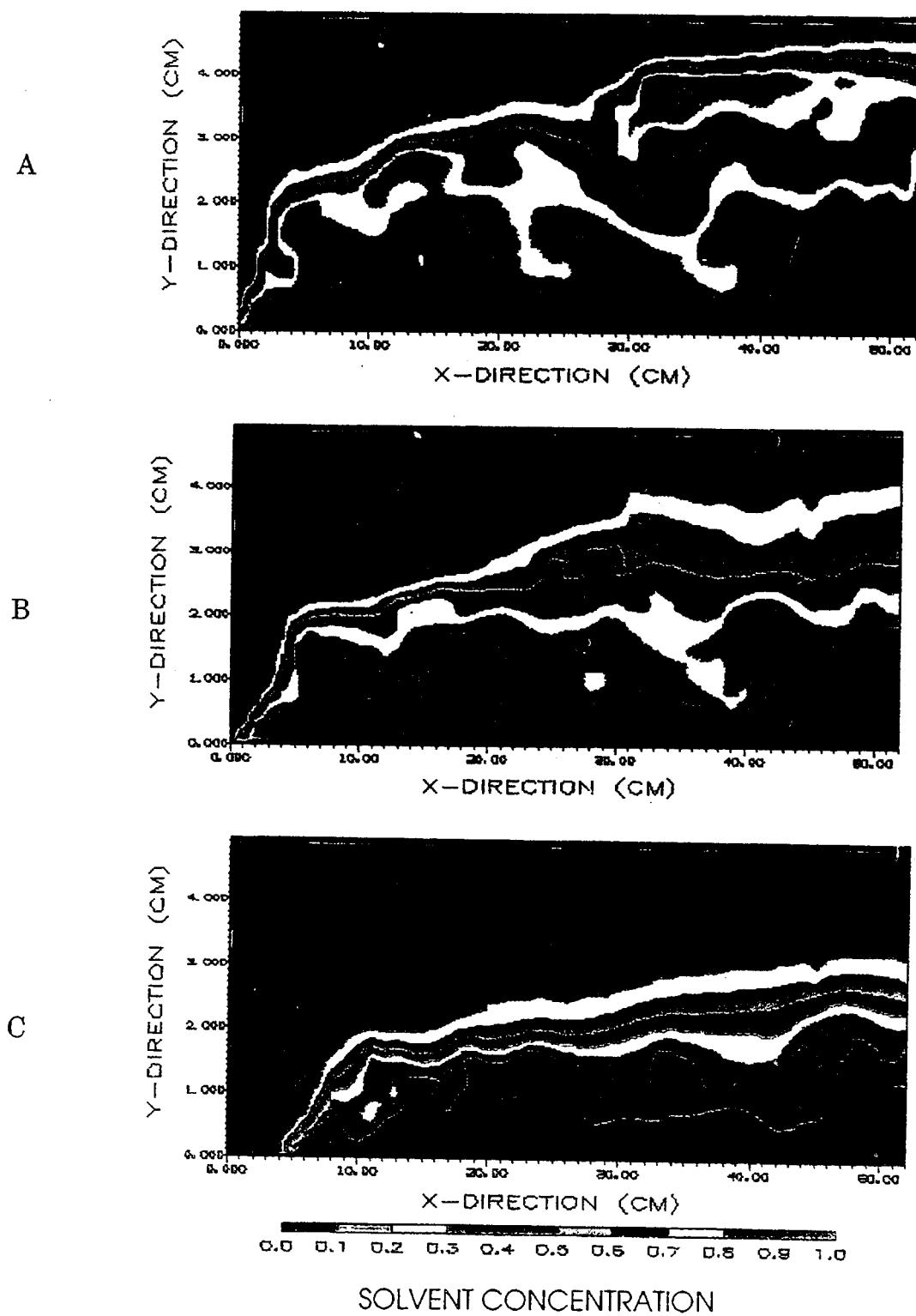
Figure 5.8. Solvent concentration images for an unstable first-contact
             miscible displacement at (A) 0.5 pore volume injected; (B)
             1.0 pore volume injected and (C) 2.0 pore volume injected
             (Experiment 5.1).

-172-
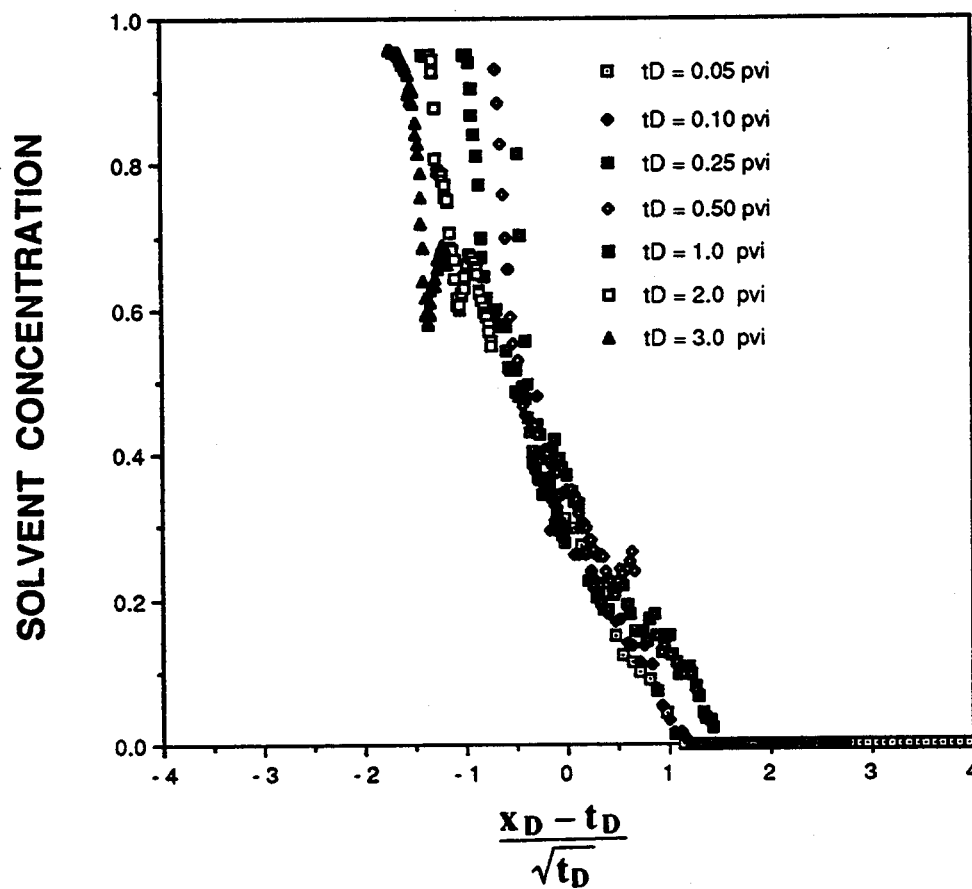
Figure 5.9. Similarity transformation of the solvent concentration profiles
for an unstable first-contact miscible displacement
(Experiment 2.1).
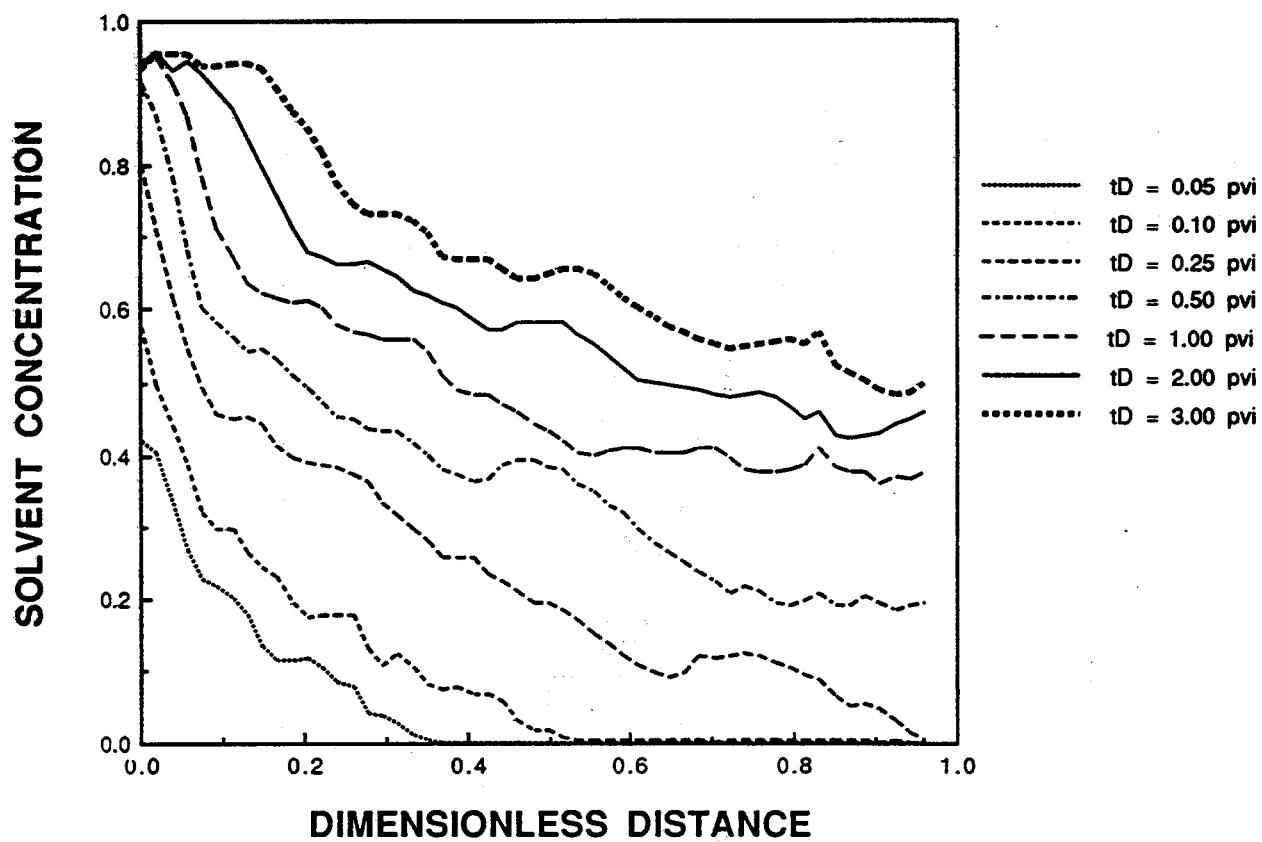
Figure 5.10. Solvent concentration profiles for an unstable first-contact
miscible displacement (Experiment 5.1).
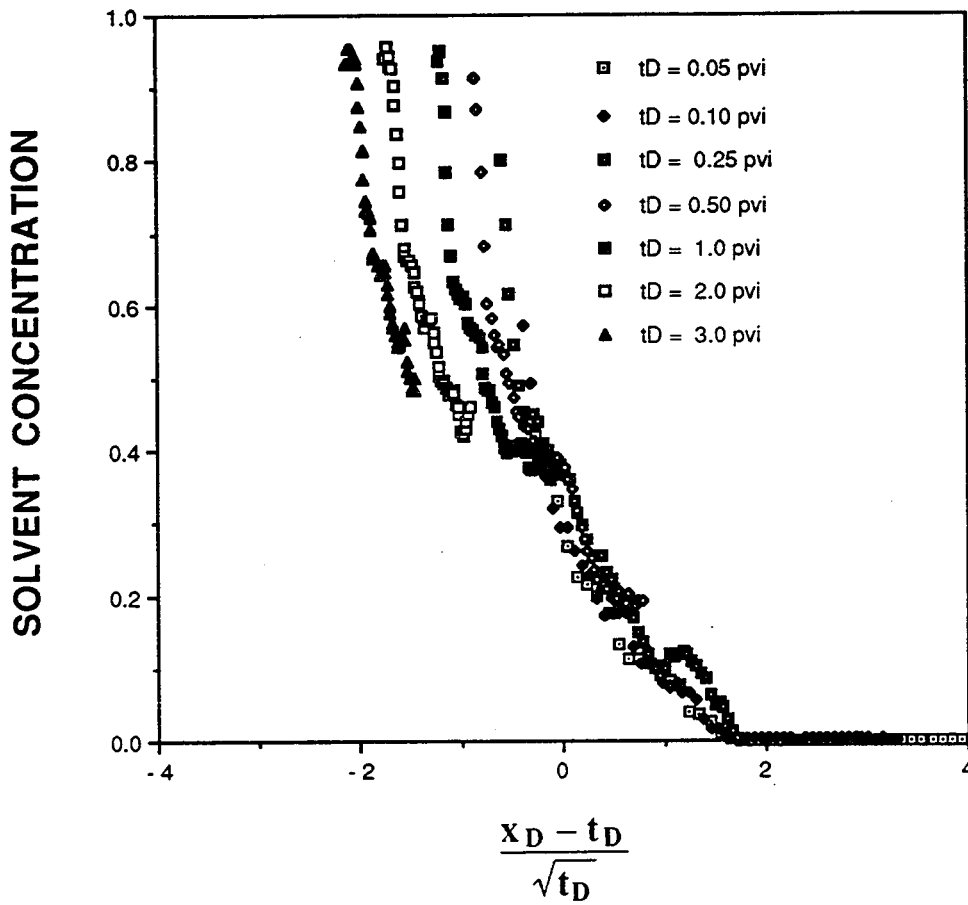
Figure 5.11. Similarity transformation of the solvent concentration profiles for an unstable first-contact miscible displacement (Experiment 5.1).

	DP = 0.01	**DP = 0.55**	**DP = 0.87**
Lx = 0.0	$\mu = 9.261$ D $\sigma = 0.101$ D	$\mu = 9.350$ D $\sigma = 8.652$ D	$\mu = 9.242$ D $\sigma = 40.94$ D
Lx = 0.2	$\mu = 9.266$ D $\sigma = 0.095$ D	$\mu = 9.354$ D $\sigma = 8.408$ D	$\mu = 7.400$ D $\sigma = 26.167$ D
Lx = 0.7	$\mu = 9.239$ D $\sigma = 0.104$ D	$\mu = 7.845$ D $\sigma = 6.310$ D	$\mu = 4.705$ D $\sigma = 9.758$ D
Lx = 2.0	$\mu = 9.230$ D $\sigma = 0.105$ D	$\mu = 7.469$ D $\sigma = 6.444$ D	$\mu = 4.622$ D $\sigma = 10.753$ D

Figure 5.12. Schematic layout of the simulated permeability fields in which
μ = mean permeability and σ = standard deviation of the log
of the permeability.
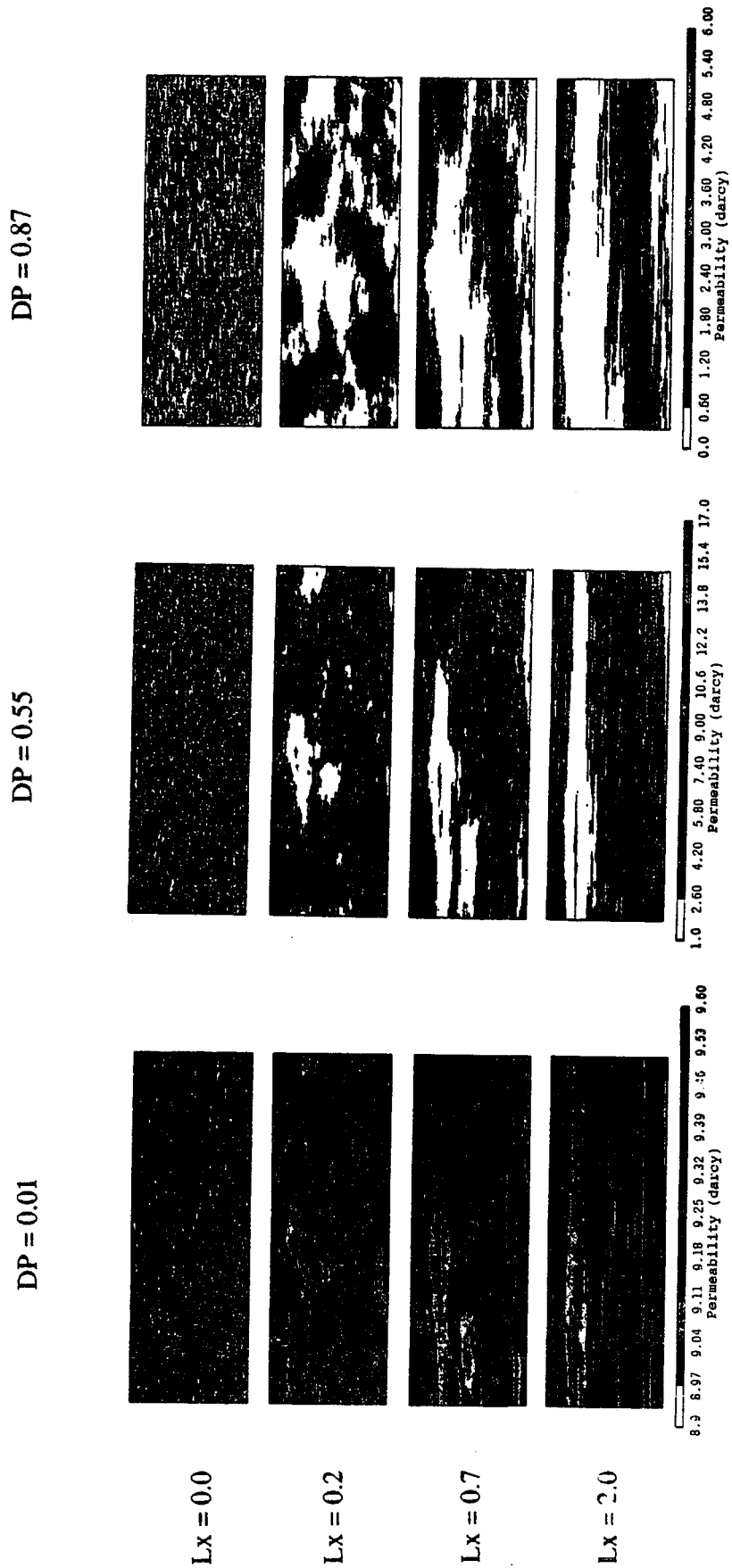
Figure 5.13. Simulated permeability maps.
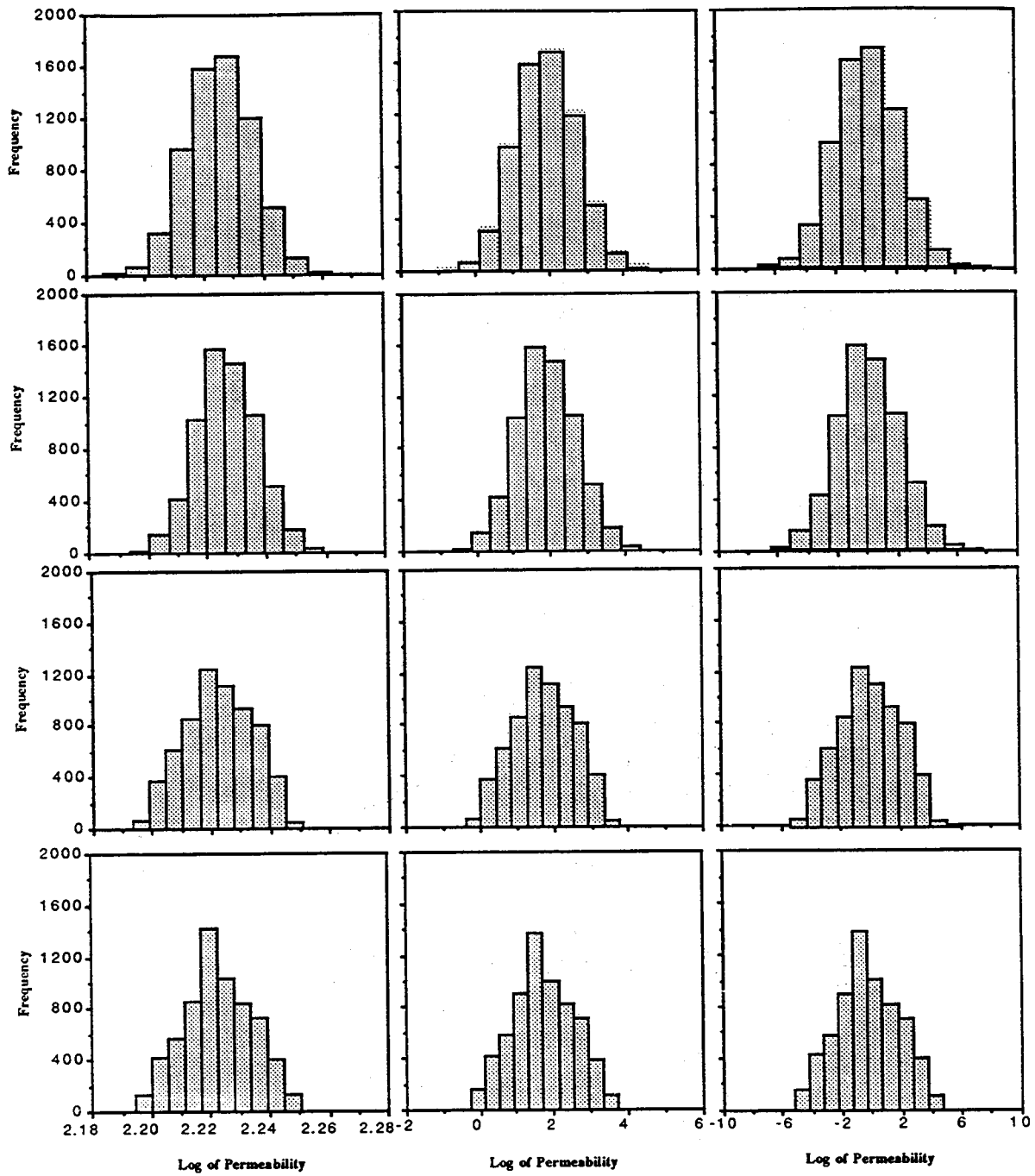
Figure 5.14. Simulated permeability histograms.

-178-
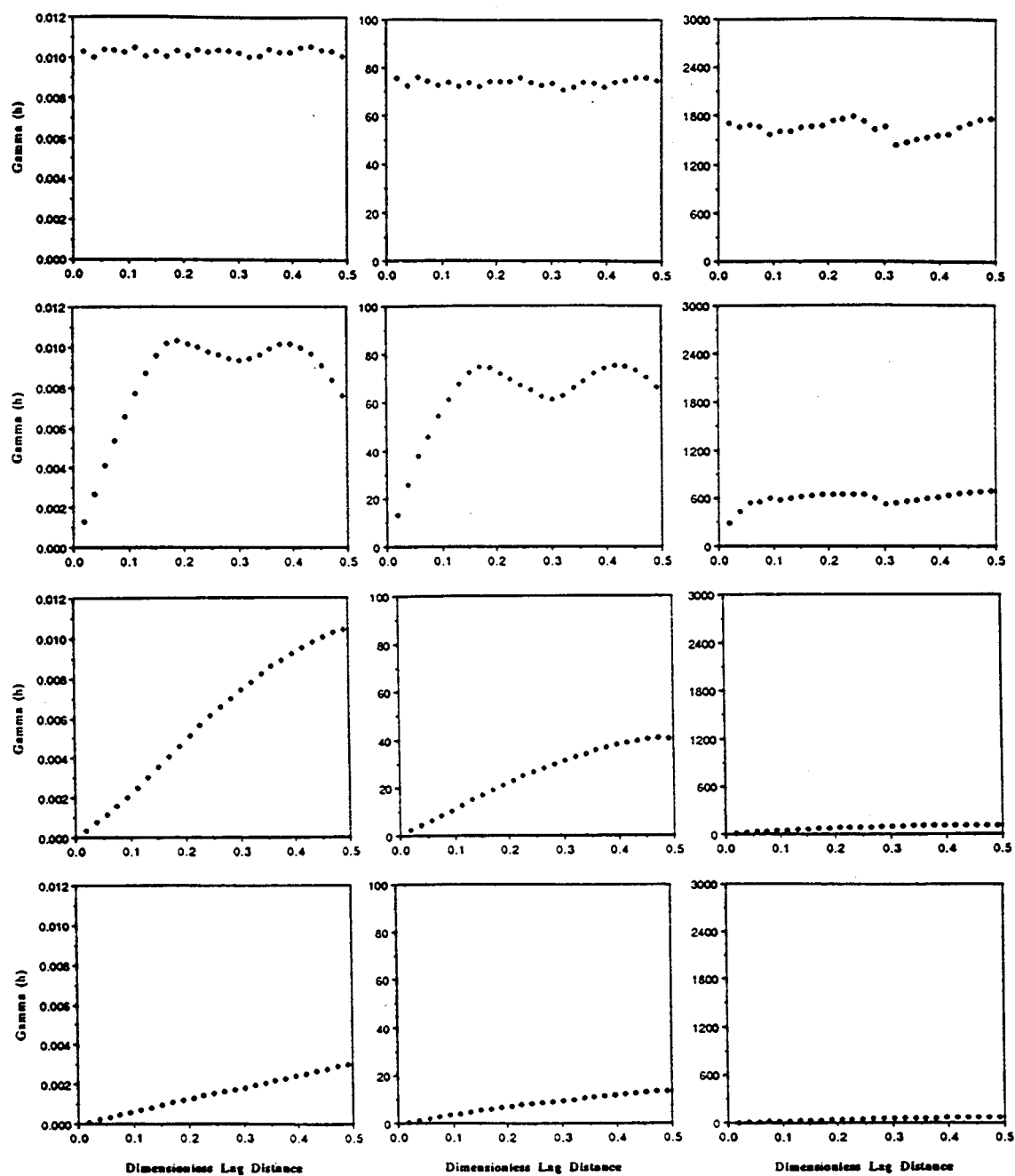
Figure 5.15. Simulated permeability semivariograms in the direction of bulk flow.
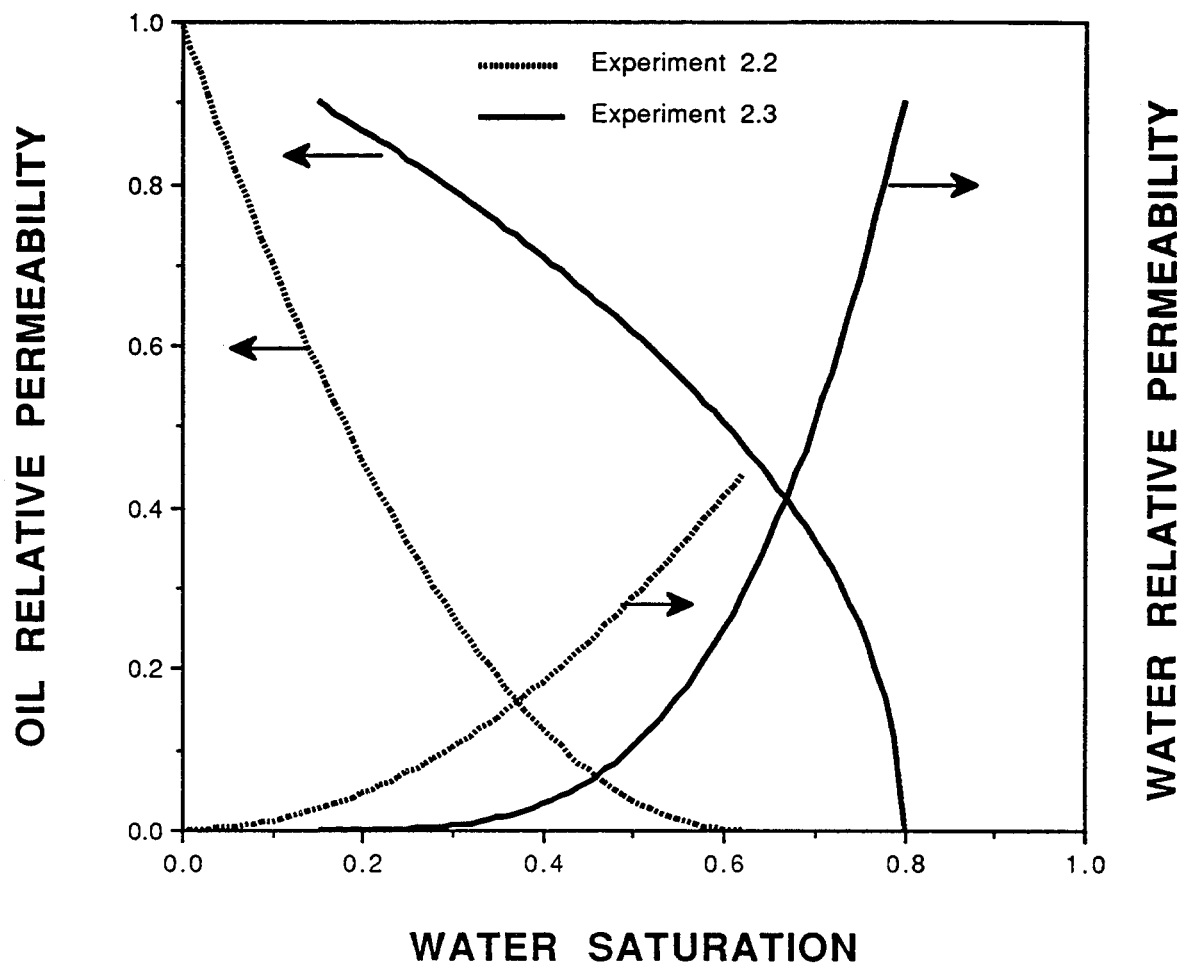
Figure 5.16. Oil-water relative permeability curves used to simulate
unstable immiscible displacements in an oil-wet and
water-wet sandpack (Experiments 2.2 and 2.3).

(a)

(b)

(c)

0.0　0.1　0.2　0.3　0.4　0.5　0.6　0.7　0.8　0.9　1.0
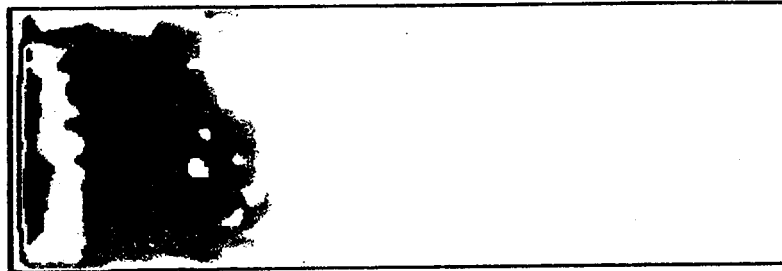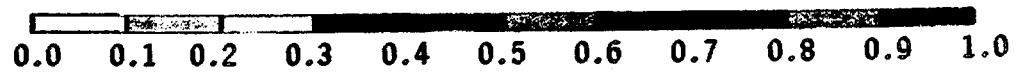
Figure 5.17. Projected water saturation maps for Experiment 2.2 at (a)
0.05 pore volume injected; (b) 0.10 pore volume injected and
(c) 0.25 pore volume injected.

(a)

(b)

(c)

0.0 0.1 0.2 0.3 0.4 0.5 0.6 0.7 0.8 0.9 1.0
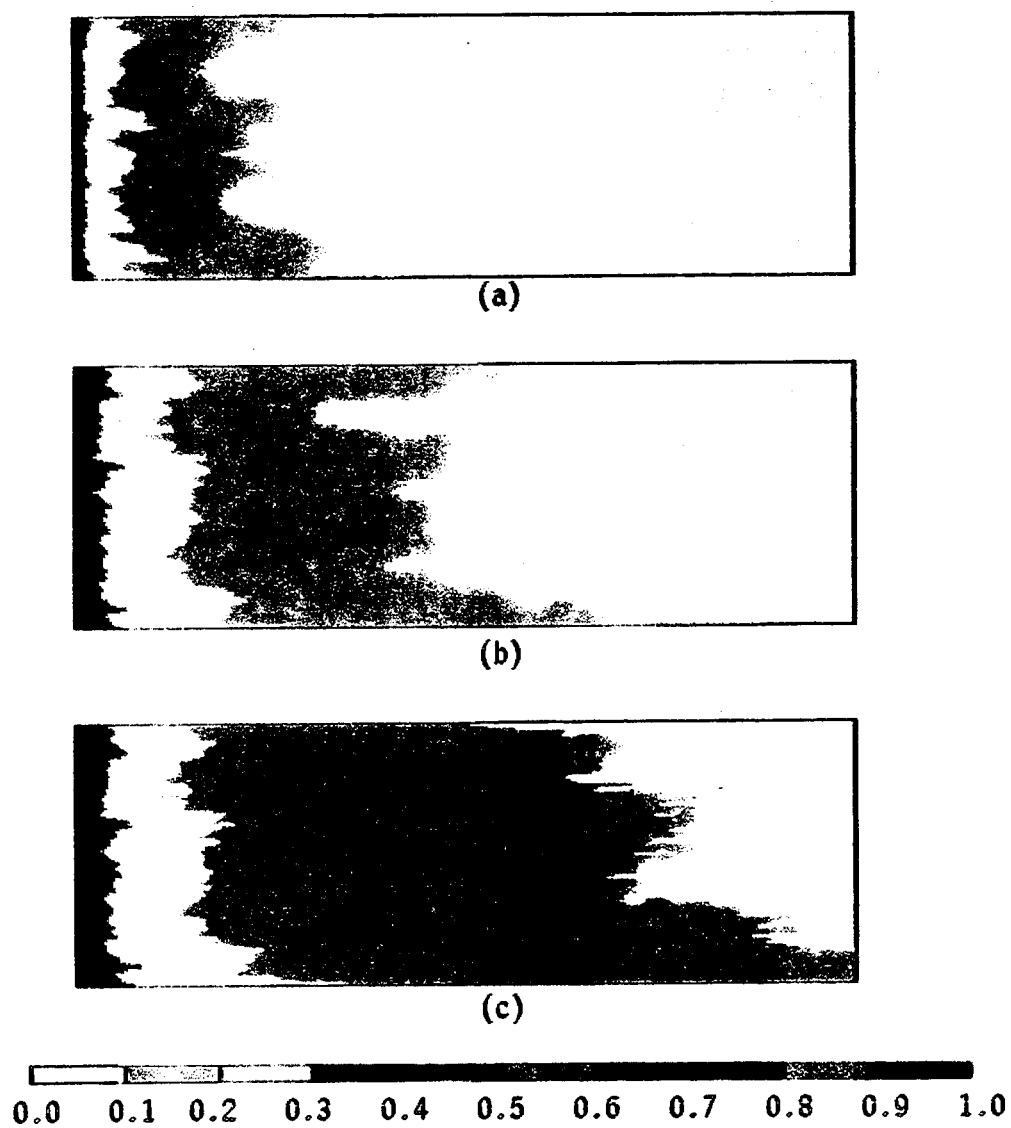
Figure 5.18. Simulated water saturation maps for Experiment 2.2 at (a) 0.05 pore volume injected; (b) 0.10 pore volume injected and (c) 0.25 pore volume injected (Run 5.1).
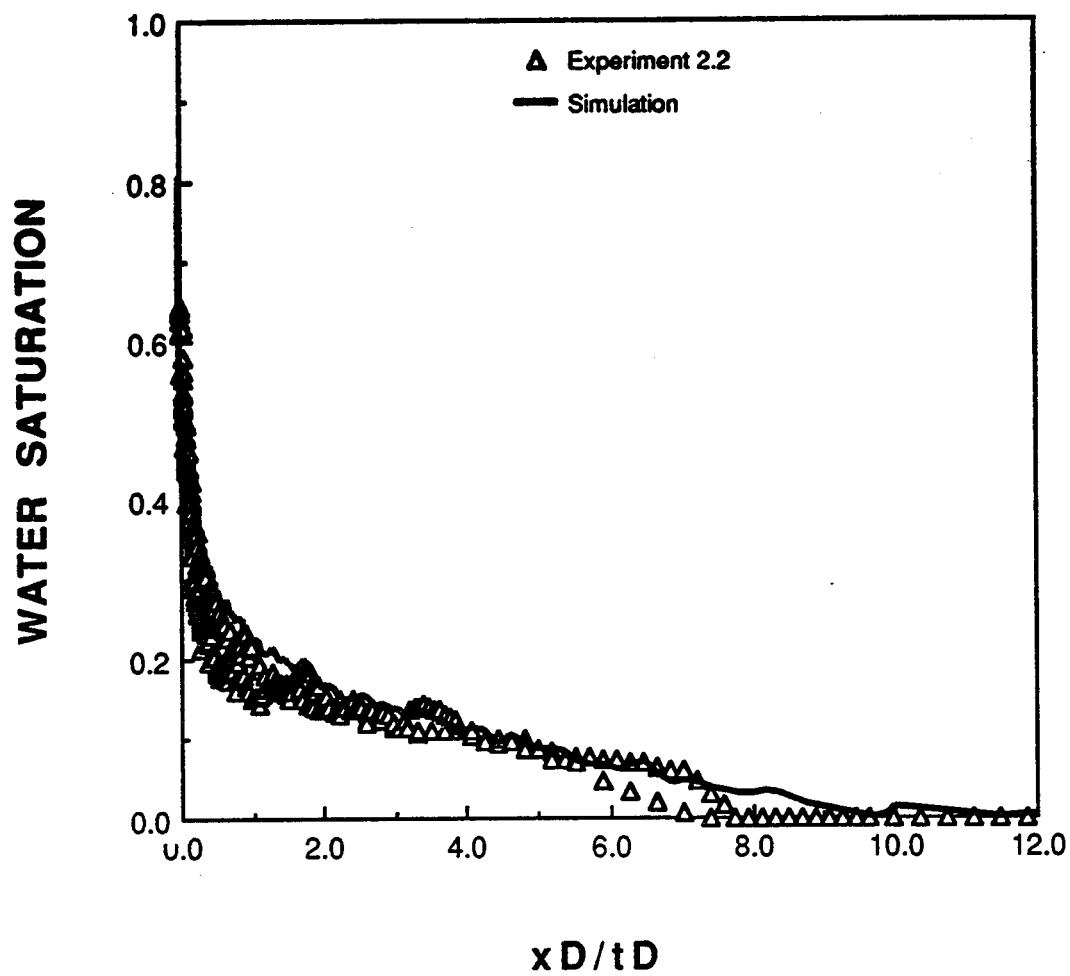
Figure 5.19. A comparison of the experimental and simulated
dimensionless response curves for Experiment 2.2.
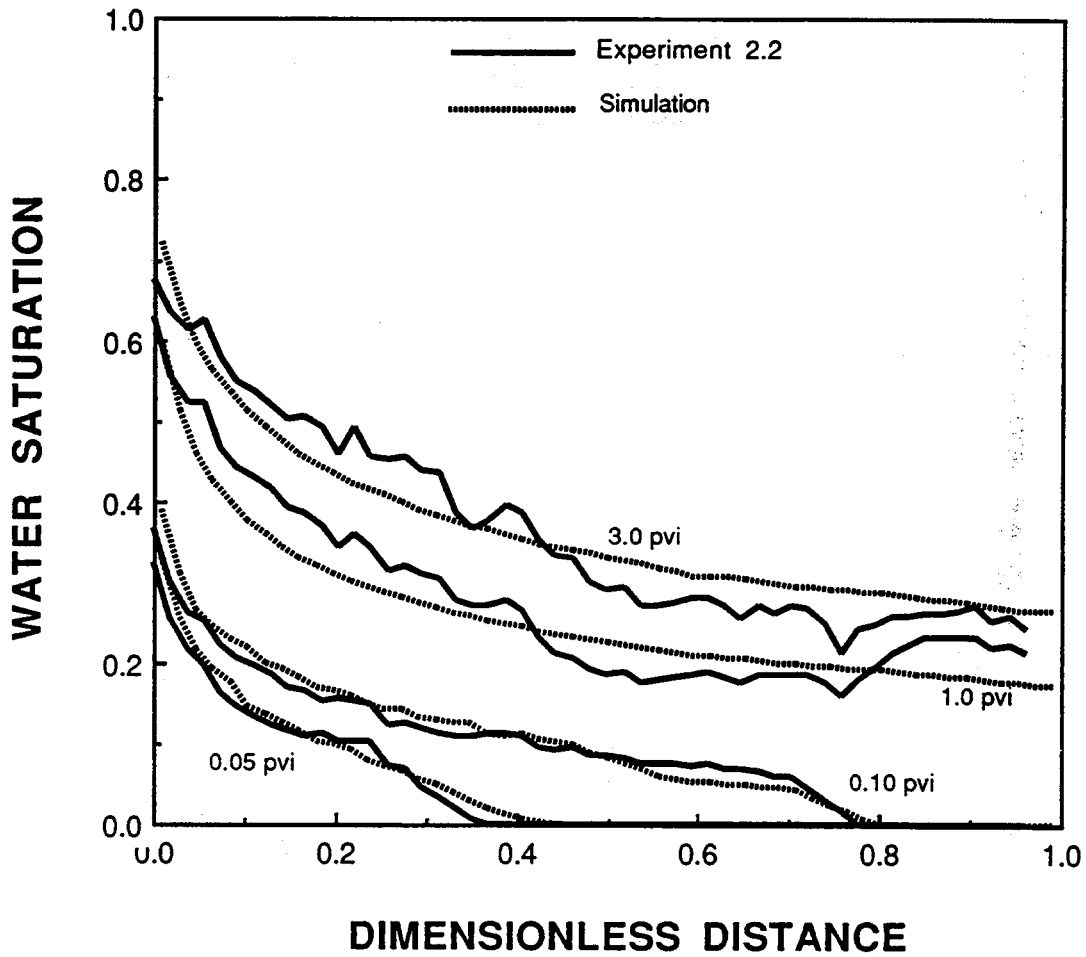
Figure 5.20. A comparison of the experimental and simulated
saturation profiles for Experiment 2.2.
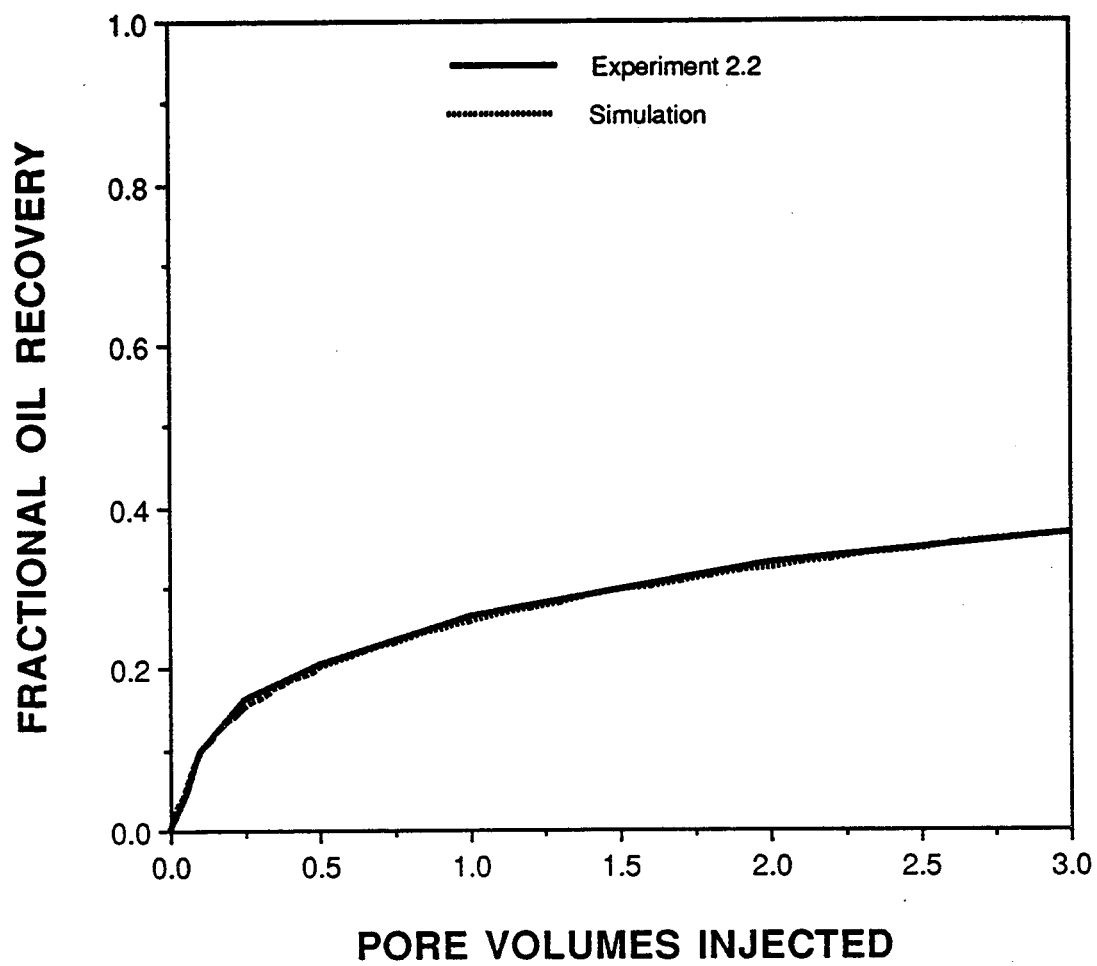
Figure 5.21. A comparison of the experimental and simulated oil
recovery curves for Experiment 2.2.
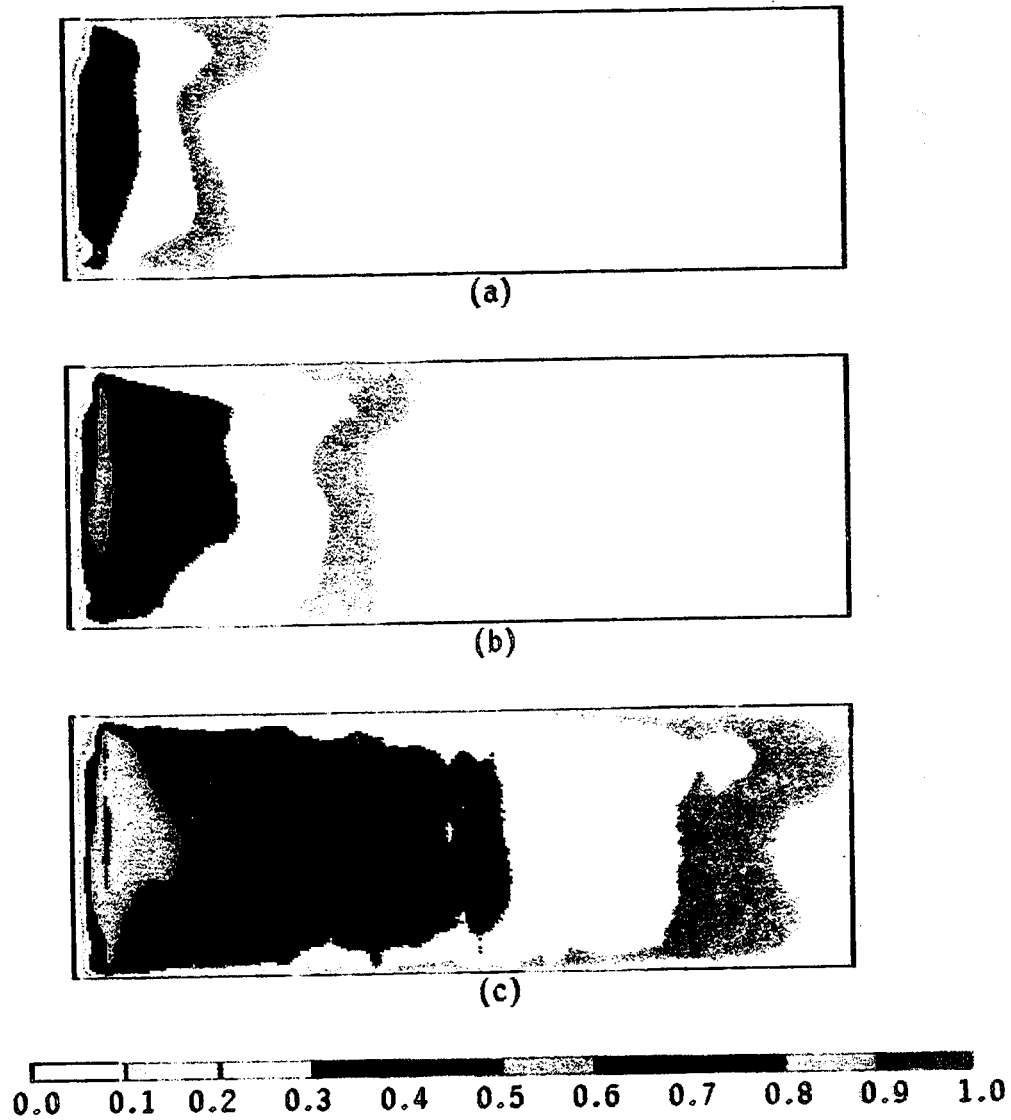
Figure 5.22. Projected water saturation maps for Experiment 2.3 at (a) 0.05 pore volume injected; (b) 0.10 pore volume injected and (c) 0.25 pore volume injected.
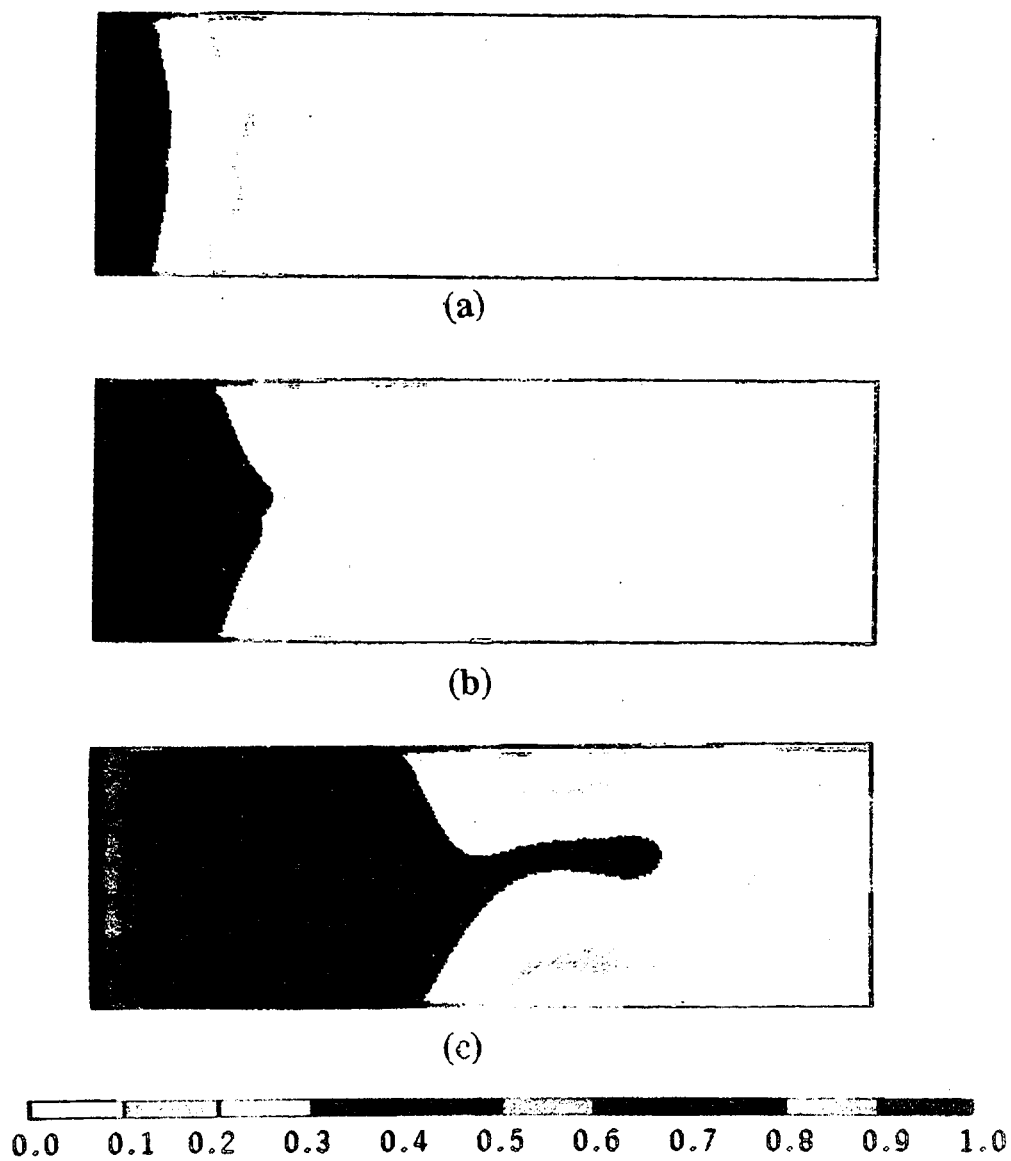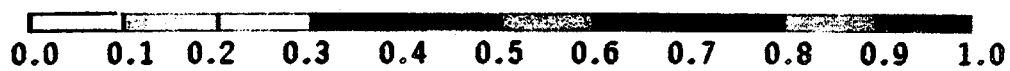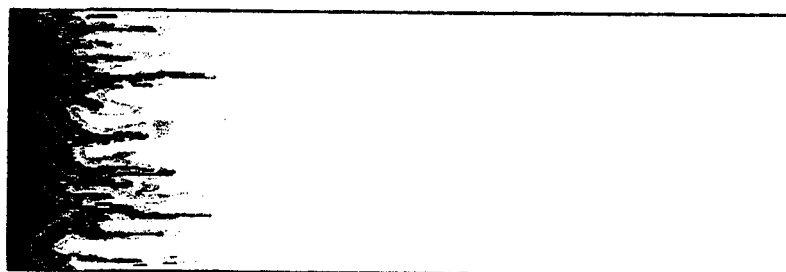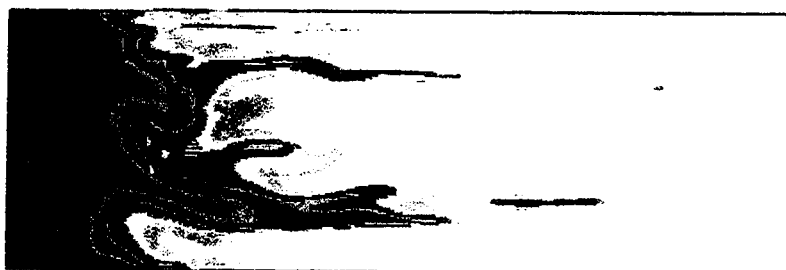
Figure 5.23. Simulated water saturation maps for Experiment 2.3 at (a)
0.05 pore volume injected; (b) 0.10 pore volume injected and
(c) 0.25 pore volume injected (Run 5.2).
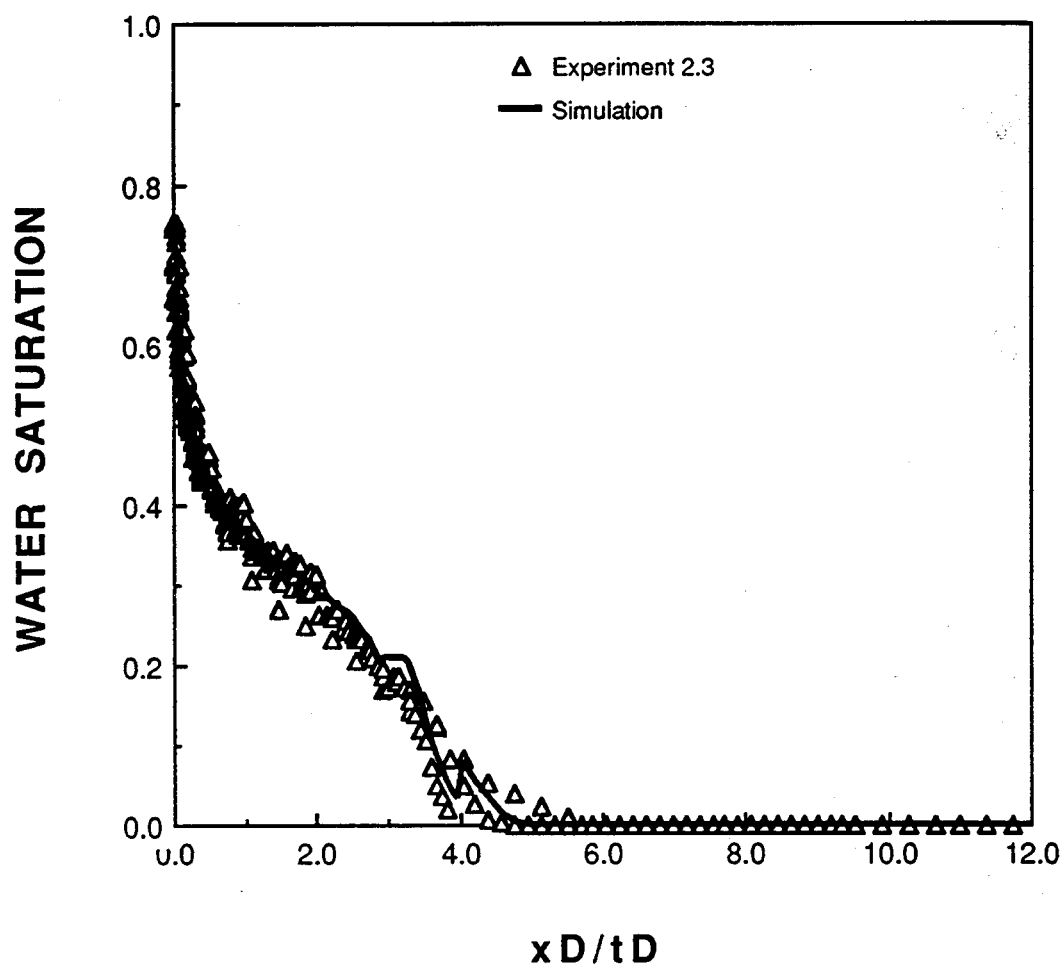
Figure 5.24. A comparison of the experimental and simulated
dimensionless response curves for Experiment 2.3.
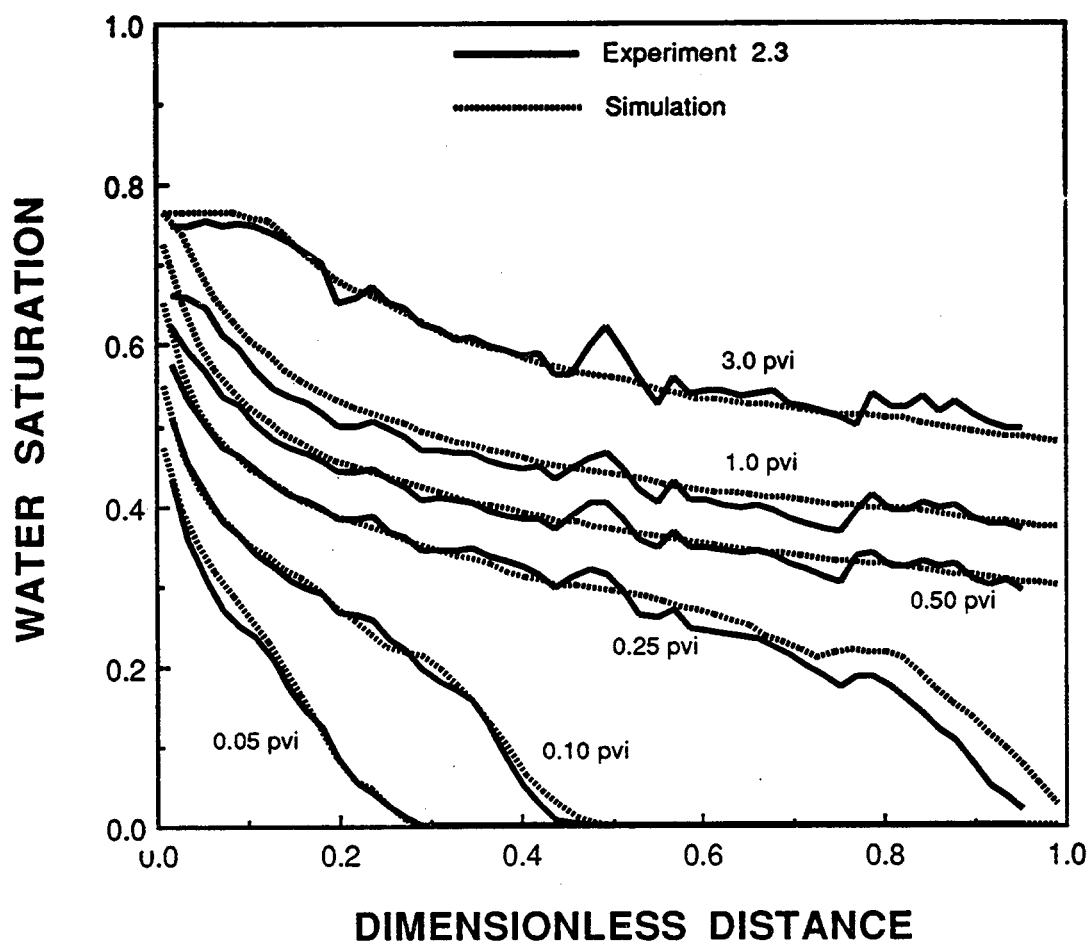
Figure 5.25. A comparison of the experimental and simulated
saturation profiles for Experiment 2.3.
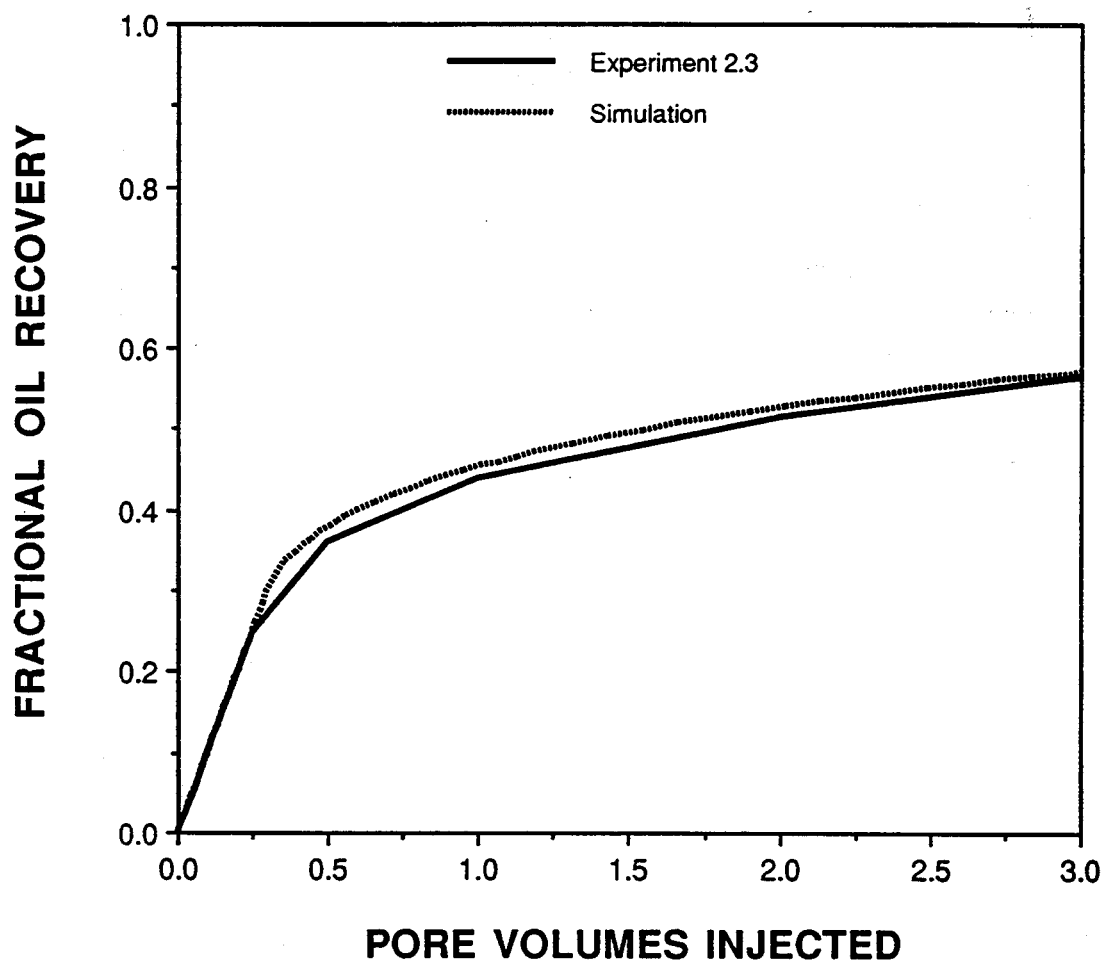
Figure 5.26. A comparison of the experimental and simulated oil recovery curves for Experiment 2.3.

(a)

(b)

(c)

0.0   0.1   0.2   0.3   0.4   0.5   0.6   0.7   0.8   0.9   1.0
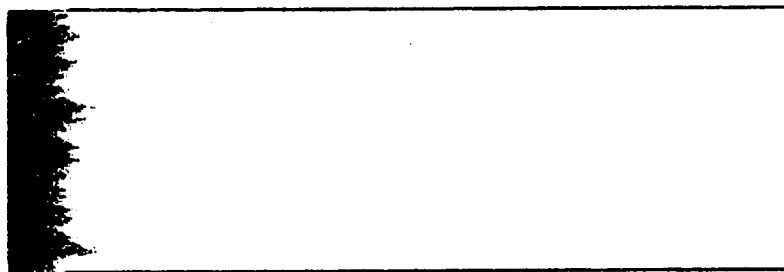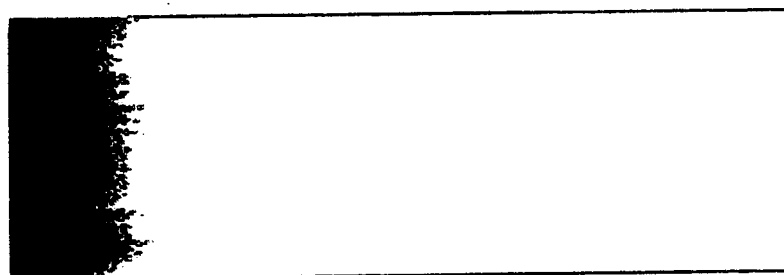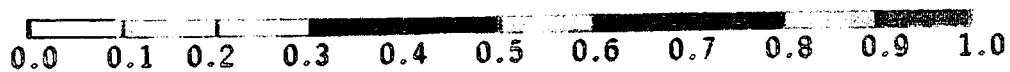
Figure 5.27. Predicted water saturation maps for an immiscible displacement at a viscosity ratio of 0.5 at (a) 0.05 pore volume injected; (b) 0.10 pore volume injected and (c) 0.25 pore volume injected.
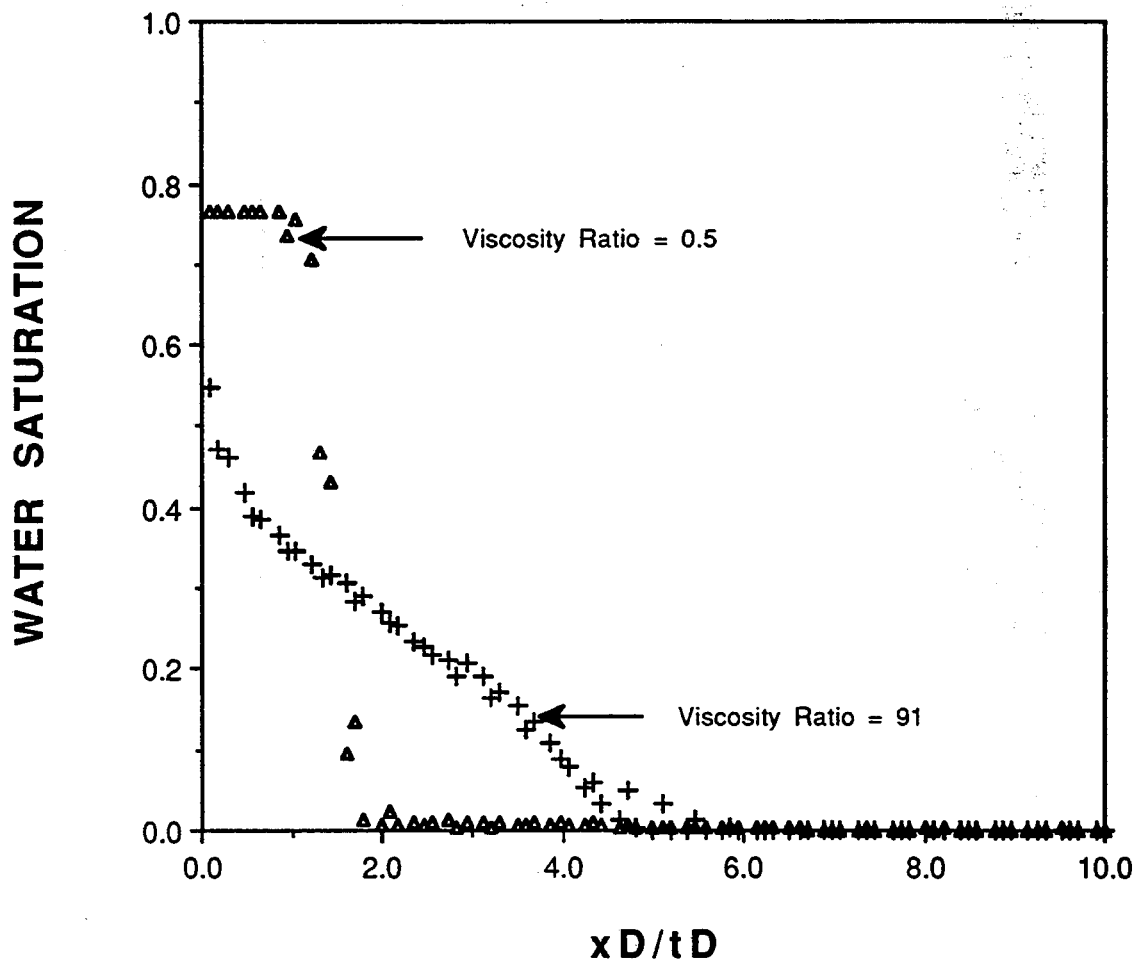
Figure 5.28. A comparison of the predicted response curve at a viscosity ratio of 0.5 and the experimental response curve at a viscosity ratio of 91.
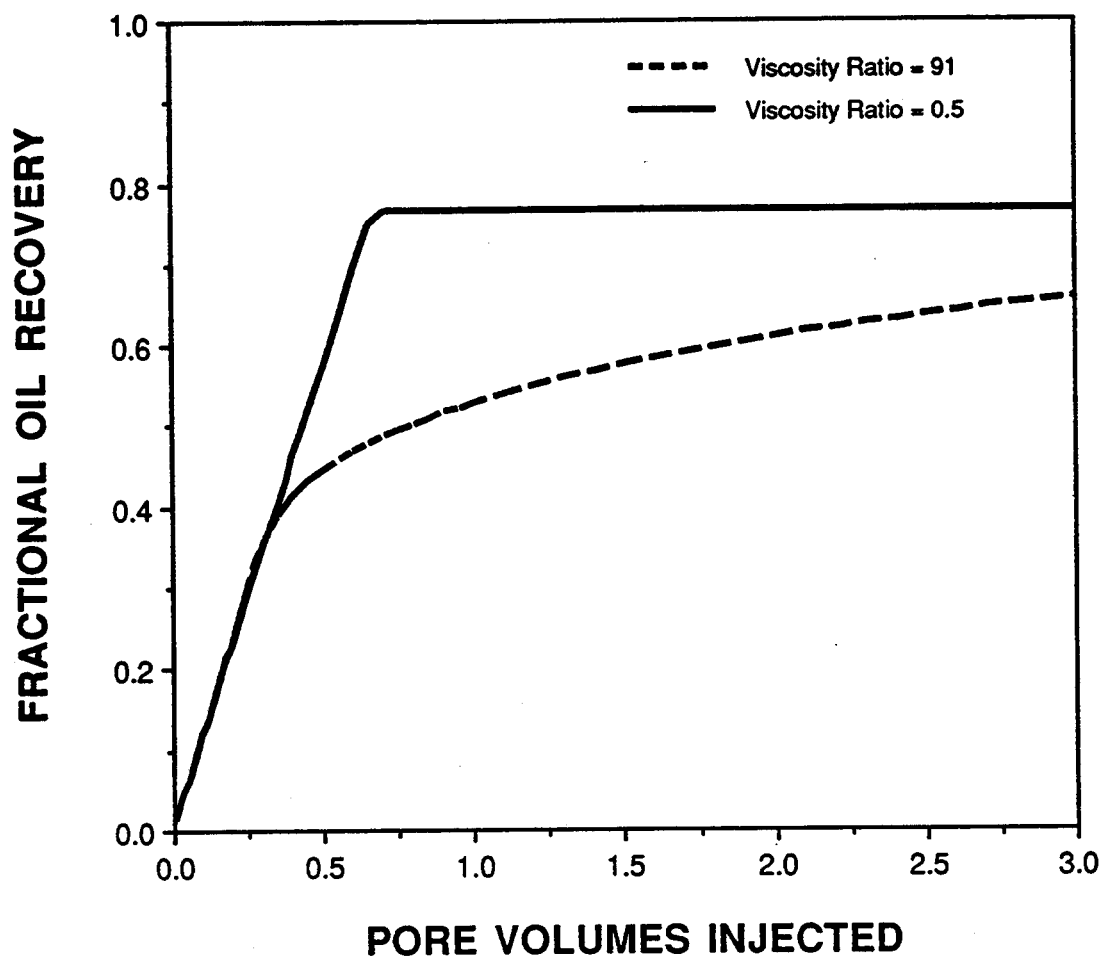
Figure 5.29. A comparison of the predicted oil recovery curve at a
viscosity ratio of 0.5 and the experimental oil recovery
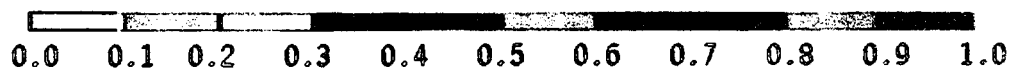curve at a viscosity ratio of 91.
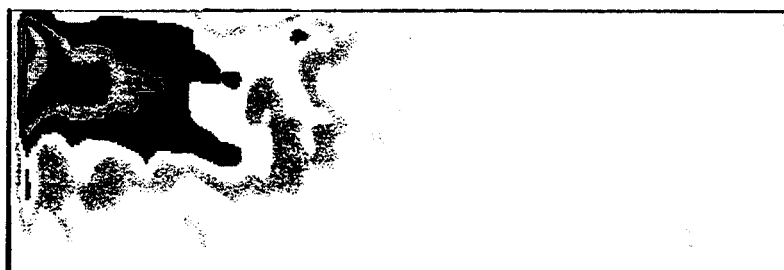
Figure 5.30. Projected solvent concentration maps for Experiment 2.1 at
(a) 0.10 pore volume injected; (b) 0.25 pore volume injected
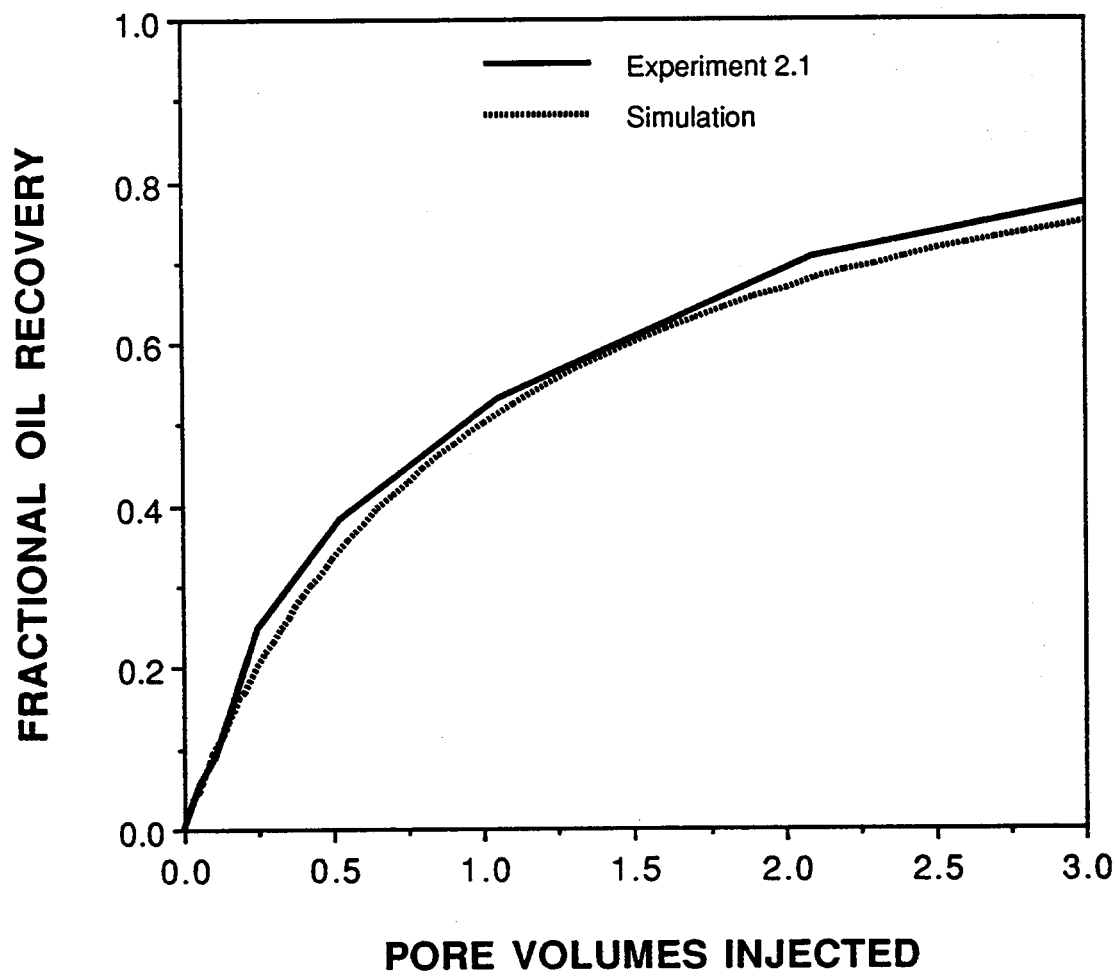and (c) 0.50 pore volume injected.

(a)

(b)

(c)

0.0 0.1 0.2 0.3 0.4 0.5 0.6 0.7 0.8 0.9 1.0

Figure 5.31   Simulated solvent concentration maps for Experiment 2.1
at (a) 0.10 pore volume injected; (b) 0.25 pore volume
injected and (c) 0.50 pore volume injected.

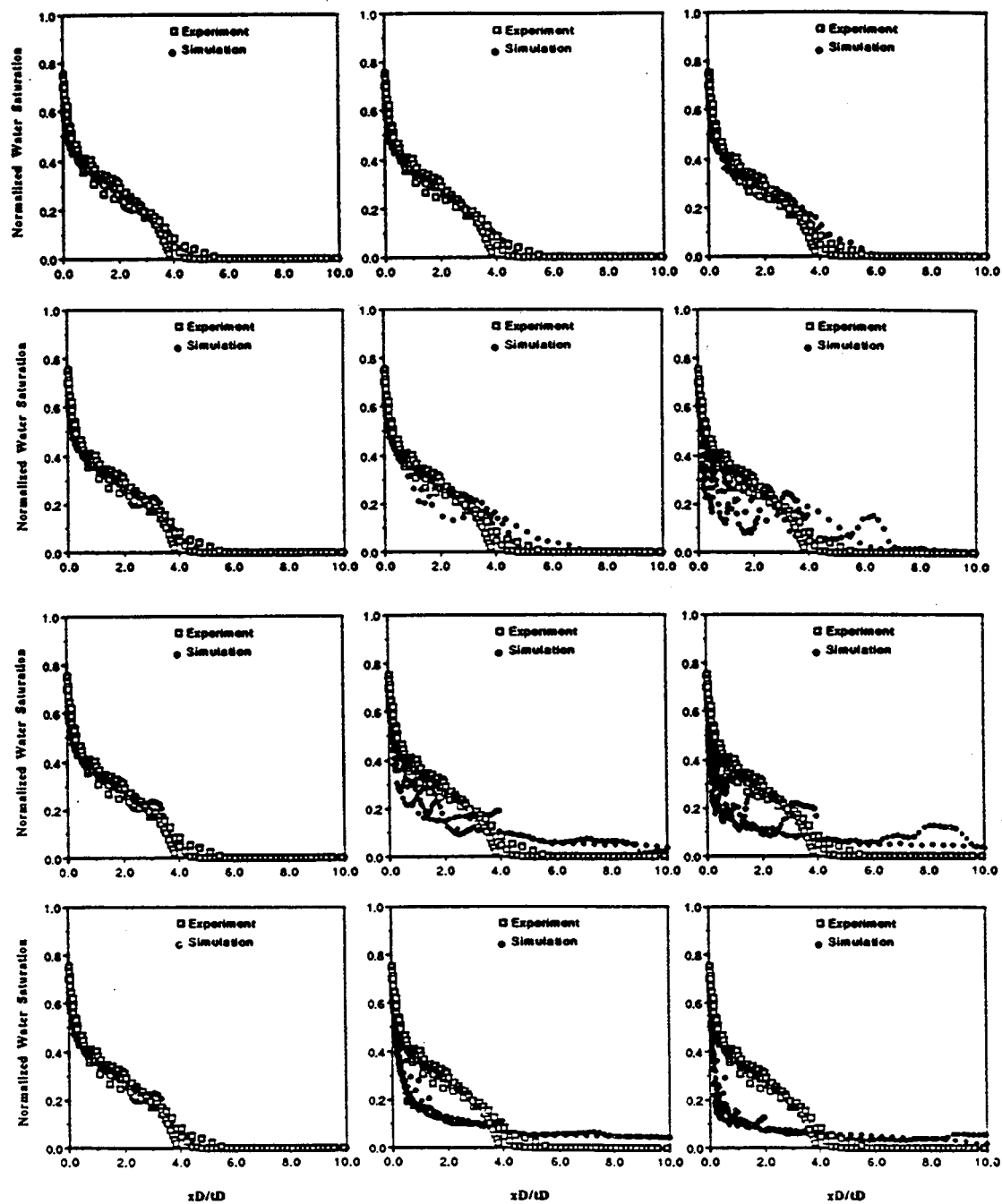Figure 5.32. A comparison of the experimental and simulated oil recovery curves for Experiment 2.1.

Figure 6.1. A comparison of the experimental and simulated response functions for Experiment 2.3 in twelve heterogeneous porous media.
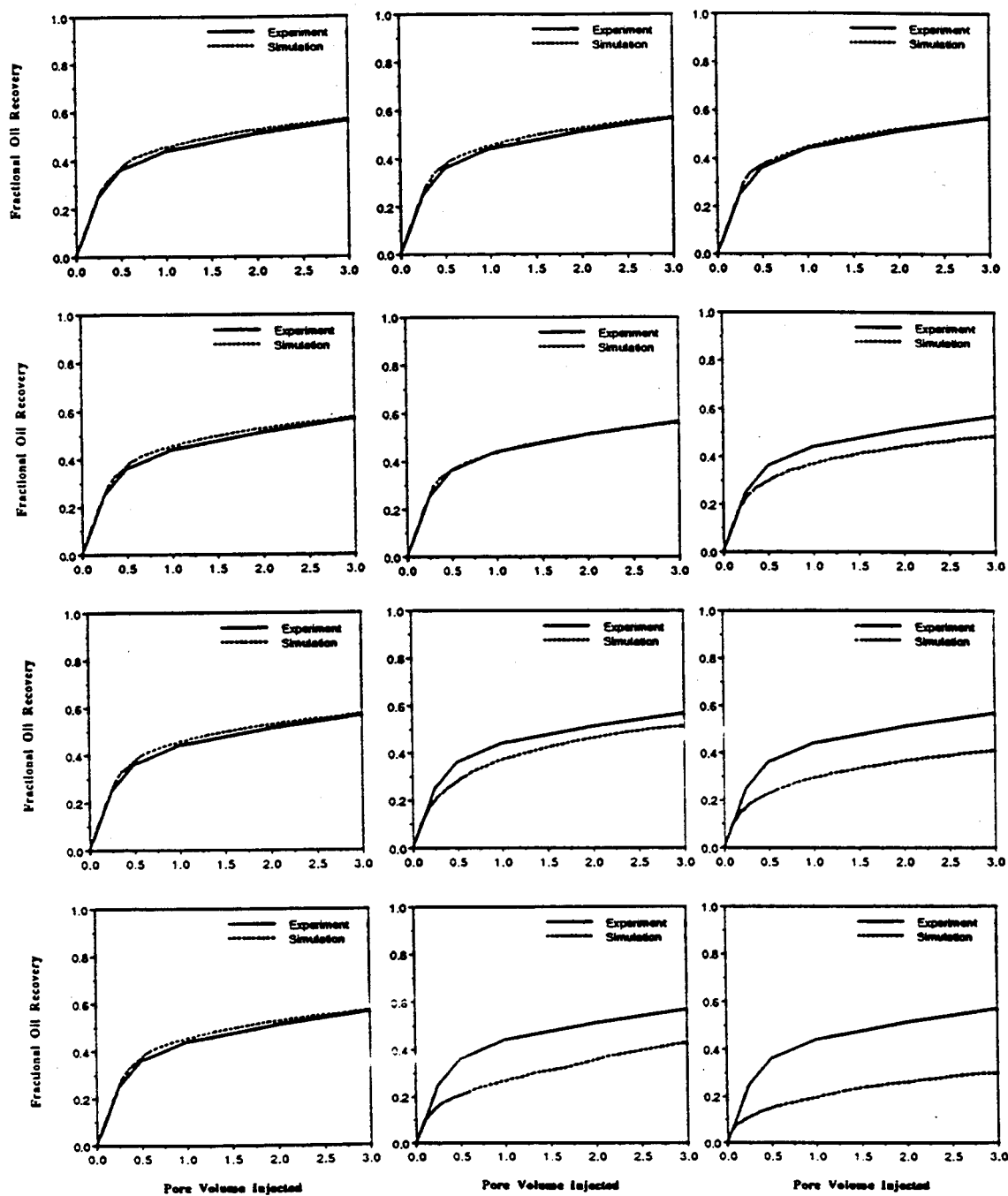
Figure 6.2. A comparison of the experimental and simulated oil recovery curves for Experiment 2.3 in twelve heterogeneous porous media.
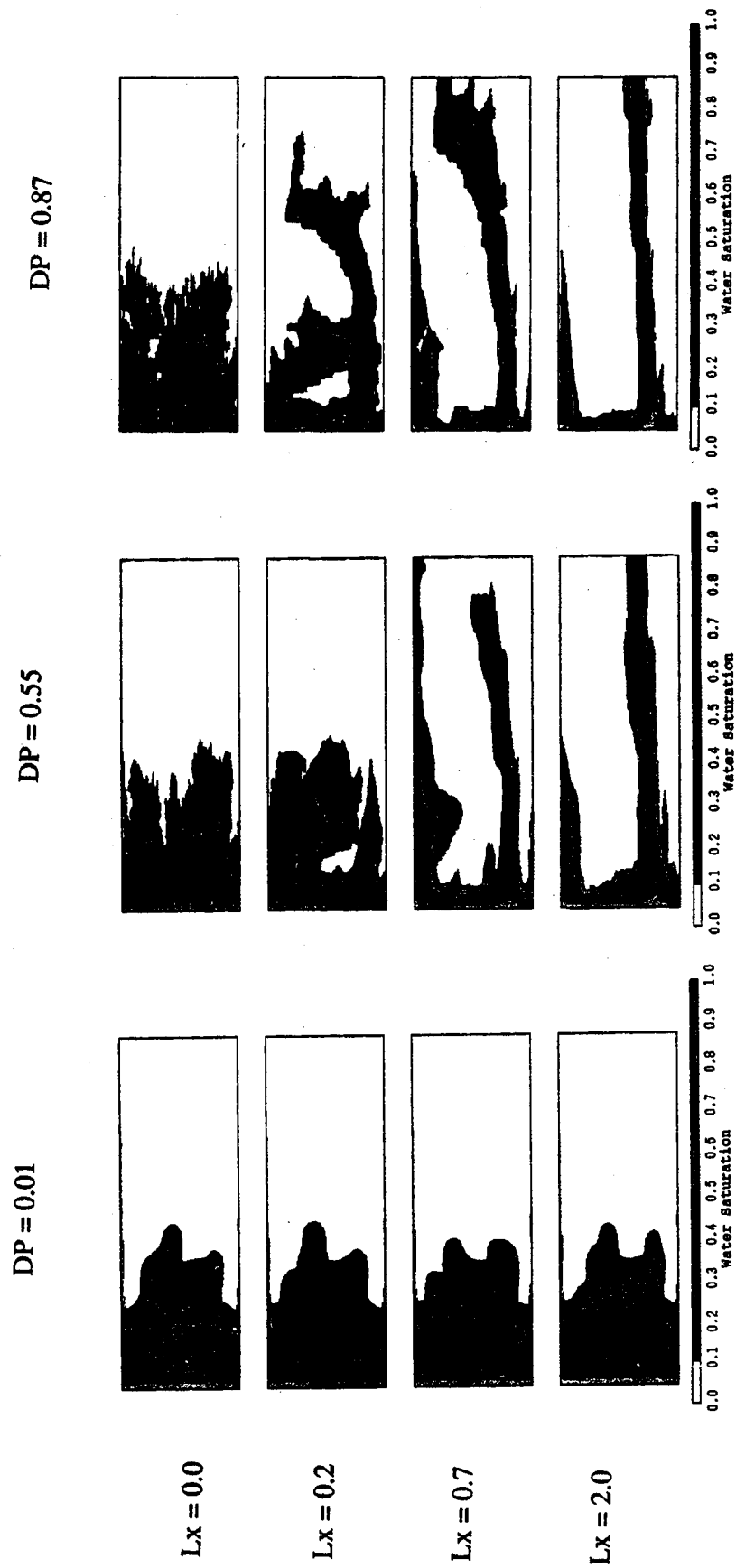
-198-

DP = 0.01   DP = 0.55   DP = 0.87

Lx = 0.0

Lx = 0.2

Lx = 0.7

Lx = 2.0

Figure 6.3.   Simulated water saturation maps at 0.10 pore volume injected
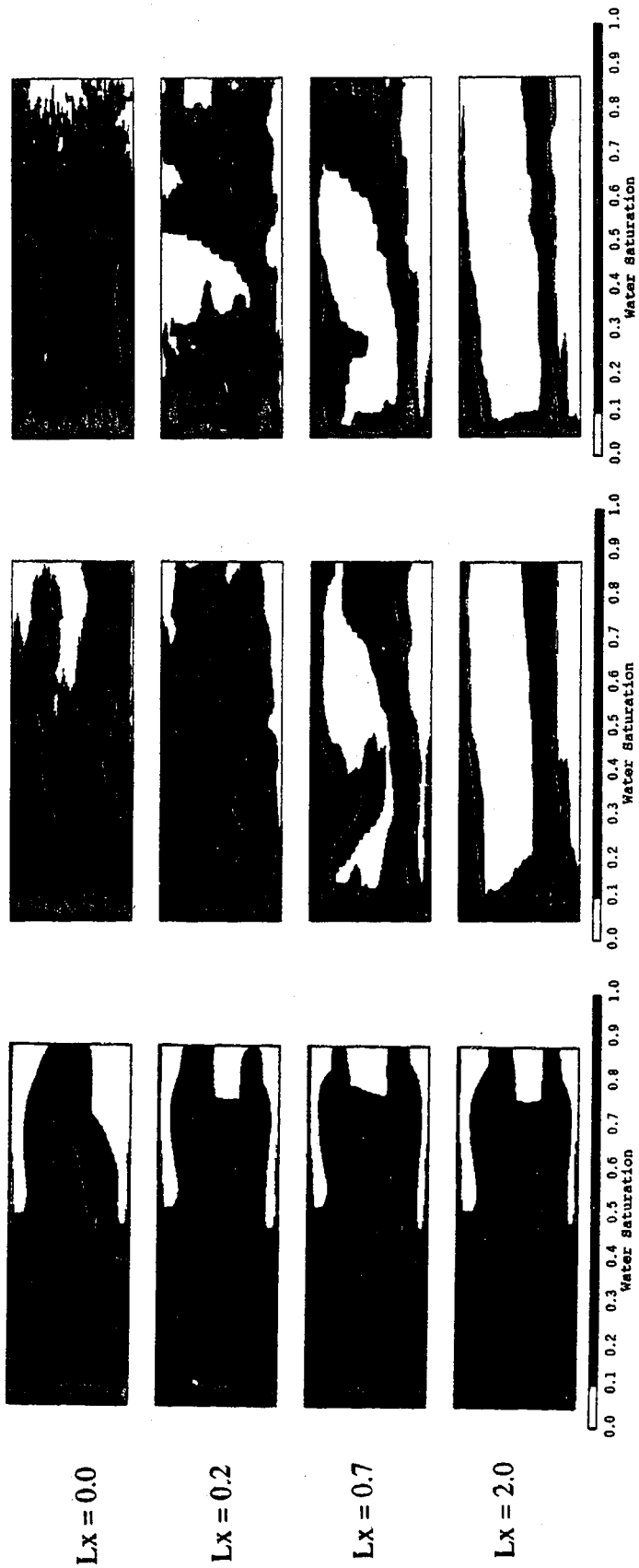in twelve heterogeneous porous media.

Figure 6.4. Simulated water saturation maps at 0.25 pore volume injected in twelve heterogeneous porous media.